

# Fundamentals of the Planetary Spectrum Generator 2022 Edition

**Villanueva**, Geronimo Luis  
NASA Goddard Space Flight Center  
Greenbelt, MD, USA

## **PSG Team:**

**Liuzzi**, Giuliano  
**Faggi**, Sara  
**Protopapa**, Silvia  
**Kofman**, Vincent  
**Fauche**, Thomas J.  
**Stone**, Shane W.  
**Mandell**, Avi M.

Electronic version publicly available at: <https://psg.gsfc.nasa.gov/help.php>  
Documentation funded by NASA's Sellers Exoplanet Environments Collaboration (SEEC),  
Goddard Fellows Innovation Challenge (GFIC) and Goddard's ExoSpec Project.

ISBN 978-0-578-36143-7  
Library of Congress Control Number: 2022901290  
Greenbelt, Maryland, United States of America





# Table of contents

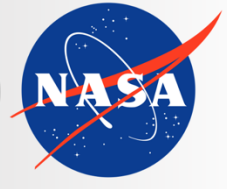
<b>Chapter 1: Introduction</b> .....	7
1. About the Planetary Spectrum Generator .....	8
2. Initializing and running PSG .....	9
3. Modules and outputs of the PSG architecture.....	11
4. Main sections of the web interface.....	14
<b>Chapter 2: Geometry and orbital modeling</b> .....	21
1. Geometry modeling .....	22
2. Orbital modeling of solar system objects.....	22
3. Orbital modeling of exoplanets.....	23
4. Orbital and spectroscopic velocities .....	24
5. Types of stellar hosts .....	25
6. Definition of the modeling geometries: angles and sub-sampling .....	26
6.1 Looking up / Looking up to the Sun / Looking to an object / Dome view .....	26
6.2 Limb / Solar occultation / Stellar occultation .....	27
6.3 Nadir.....	27
6.4 Observatory .....	28
7. Description and modeling of the field-of-view (FOV) .....	29
<b>Chapter 3: Atmospheres, exospheres and comets</b> .....	31
1. Types of atmospheres.....	32
2. Vertical structure of an atmosphere in hydrostatic equilibrium.....	33
3. Earth atmosphere .....	34
4. Mars atmosphere .....	35
5. Gas giants / Dense and hazy atmospheres.....	35
6. Cometary atmospheres.....	36
7. Exoplanet atmospheres .....	39
8. Three-dimensional characterization (GCM) of the atmosphere and surface .....	39

<b>Chapter 4: Radiative transfer modeling.....</b>	<b>43</b>
1. Radiative transfer modeling in PSG .....	44
2. Raytracing in a spherical and refractive atmosphere.....	47
3. Atmospheric opacities.....	49
3.1 Line-by-line modeling .....	50
3.2 Correlated-k calculations.....	55
3.3 Molecular cross-sections and UV modeling.....	56
3.4 Rayleigh and Raman scattering.....	57
3.5 Collision-Induced-Absorption (CIA) and the Water Continuum (MT_CKD) .....	58
4. Non-Local Thermodynamical-Equilibrium (non-LTE) modeling.....	60
5. Cometary modeling (CEM module) .....	61
<b>Chapter 5: Multiple Scattering Atmospheric Modeling .....</b>	<b>65</b>
1. Atmospheric scattering modeling in PSG .....	66
2. Theory of radiative transfer in a scattering medium .....	67
2.1 Discretization of the azimuthal intensities, Fourier series and Legendre polynomials .....	67
2.2 Discretization of the polar angles, Gaussian quadrature angles .....	70
2.3 Solving the whole system, applying boundary conditions.....	71
2.4 Scattering numerical algorithm.....	72
3. Mie scattering and calculation of the aerosol models .....	73
4. Selection of the number of stream pairs (NMAX) and Legendre terms (LMAX).....	73
<b>Chapter 6: Surface Scattering Modeling.....</b>	<b>79</b>
1. Surface modeling in PSG .....	80
2. Lambert model: isotropic scattering .....	80
3. Hapke model: parametric surface modeling.....	81
4. Lommel-Seeliger: dark and weakly scattering Lunar/asteroid/comet surfaces.....	85
5. Cox-Munk model: glint and ocean's reflections .....	88
6. Cometary dust/icy grains.....	89
7. Mixing compositions.....	90
8. Calculation of the single scattering albedo .....	90
9. Disk integrated quantities: albedos and phase integrals.....	92



<b>Chapter 7: Mass spectrometry .....</b>	<b>95</b>
1. Mass spectrometry and its implementation in PSG .....	96
2. Fragmentation model and an accurate high-resolution mass database.....	97
3. Simulating mass spectrometry and its noise.....	100
4. Mass spectrometry retrievals and complex organics identification.....	101
<b>Chapter 8: Instruments and Noise Modeling.....</b>	<b>105</b>
1. Principles of noise modeling.....	106
2. Field-Of-Views (FOVs), diffraction limits and planetary filling factors.....	108
3. Spectral grids, sampling and convolutions .....	110
4. Radiation and intensity output units .....	111
5. Zodiacal light, exozodii, telluric and background sources.....	112
6. Coronagraphic modeling .....	115
7. AOTF and grating modeling.....	117
<b>Chapter 9: Retrieval Methods.....</b>	<b>119</b>
1. Retrievals general elements.....	120
2. Optimal Estimation .....	120
3. Implementation of OE in PSG .....	123
4. Retrieval of vertical profiles.....	128
5. Nested retrievals: principles .....	130
6. MultiNest and its implementation: PSGnest .....	134
<b>Chapter 10: Application Program Interface (API) and Installation .....</b>	<b>137</b>
1. Application Program Interface.....	138
2. Calling the API.....	138
3. Installing a personal version of PSG in your computer .....	139
4. Types of planetary spectra and special keywords .....	141
6.1 Structurer of the AWS console and instances.....	146
6.2 Accessing the instances .....	150
6.2 Configuring AWS on the ssh.....	151
6.2 Cloning an instance.....	152





**Planetary Spectrum Generator**  
National Aeronautics and Space Administration

# Chapter 1: **Introduction**

**Villanueva, Faggi and  
PSG team**



## 1. About the Planetary Spectrum Generator

The Planetary Spectrum Generator (PSG, <https://psg.gsfc.nasa.gov>) is a radiative transfer model suite for synthesizing and retrieving planetary spectra (atmospheres and surfaces) for a broad range of wavelengths (50 nm to 100 mm, UV/Vis/near-IR/IR/far-IR/radio) from any observatory (e.g., JWST, ALMA, Keck, SOFIA), any orbiter (e.g., MRO, ExoMars), or any lander. PSG also permits to synthesize/retrieve mass-spectrometry data of orbiters, landers and laboratory instrumentation. This is achieved by combining several state-of-the-art radiative transfer models, spectroscopic databases and planetary databases (i.e., climatological and orbital). The tool first became online in 2015, with a first paper reporting the suite capabilities reported in (Villanueva et al., 2018a).

The latest version of PSG has the following general capabilities:

- A 3D (three-dimensional) **orbital calculator** for most bodies in the solar system, and all confirmed exoplanets. Possible observing geometries include observatory, full sky view, nadir, limb, solar/stellar occultation, transit, etc. The orbital calculator provides all possible geometry parameters needed for computing spectroscopic fluxes.
- The program can ingest **billions of spectral lines of almost 1,000 species from several spectroscopic repositories** (e.g., HITRAN, JPL, CDMS, GSFC-Fluor, ExoMol). For mass-spectrometry, PSG operates with a high-resolution (mDa) fragmentation pattern database for +20,000 species calibrated with the NIST public library.
- **Atmospheric models** (e.g., equilibrium chemistry, cometary models), databases (e.g., Mars GCMs, Earth/NASA-MERRA2) and templates (vertical profiles of temperature and abundances) are available for the main atmospheres (Venus, Earth, Mars, Titan, Neptune, Uranus), and general atmospheric and surface parameters are available for the other bodies.
- Radiative transfer analysis can be performed with several models:
  - **Multiple scattering spherical modeling**, PUMAS.
  - Line-by-Line (LTE) **Cometary Model**, CEM.
  - Line-by-Line (non-LTE) **Cometary Fluorescence Model**, CEM.
  - **Generalized Continuum Model**, CONTINUUM.
  - **Mass spectrometry modeling**, MASS.
- The code synthesizes spectra in **any desired radiance unit** (spectral radiance, spectral intensity, spectral flux, radiant energy density, irradiance, spectral irradiance, magnitude, etc.) and transmittance output.
- It includes the possibility to integrate **stellar templates** by adopting the Kurucz 2005 stellar templates (0.15-300  $\mu\text{m}$ ), which is complemented at short wavelengths ( $<0.4 \mu\text{m}$ ; X-ray, EUV, FUV) with the MUSCLES Treasury Survey. When considering the G-type template, the spectrum is complemented with the ACE solar spectrum (2-14  $\mu\text{m}$ ) in the infrared and with the LISIRD template ( $<0.4 \mu\text{m}$ ) in the UV.
- It includes a **realistic noise calculator** for a broad range of instruments, including heterodyne instruments in the radio, interferometers, AOTF systems, LIDAR instruments, coronagraphs, orbital cameras. The noise module includes a broad range of background and systematic sources of noise.

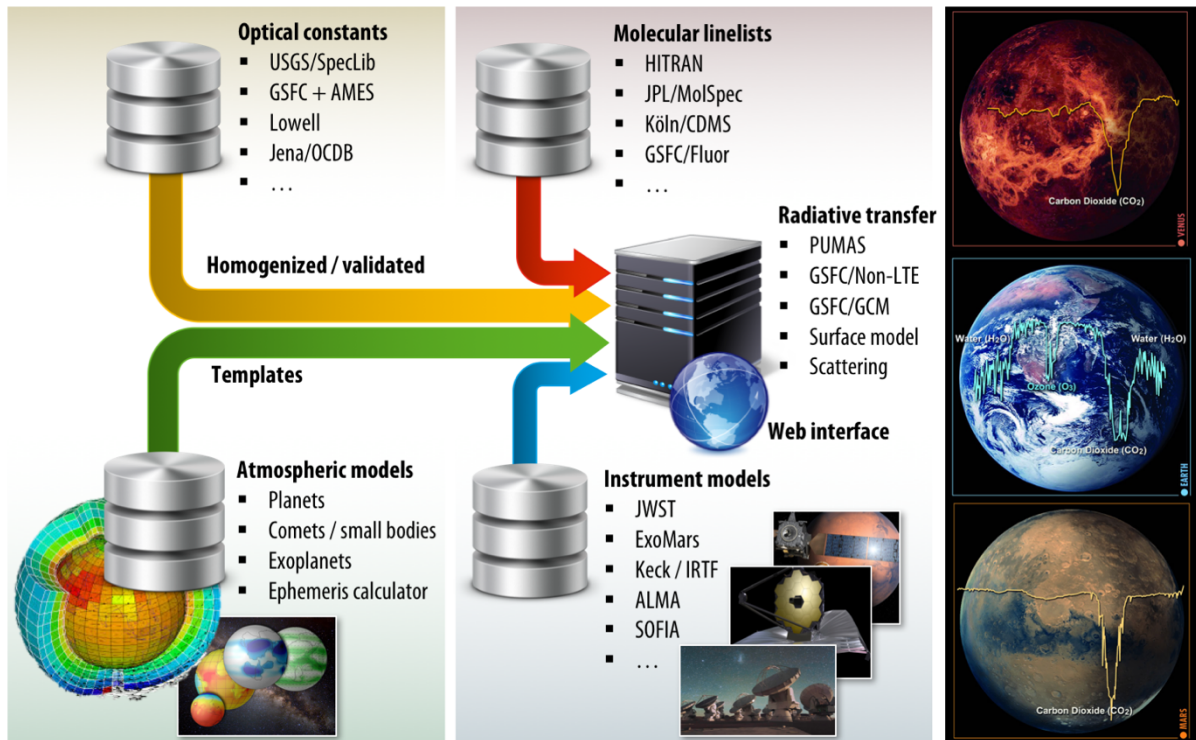


**Figure 1:** By combining several modern and versatile online radiative transfer models that access state-of-the-art spectroscopic databases, the PSG tool can synthesize a broad range of planetary spectra and regimes, as measured with a broad range of instruments and observatories.

## 2. Initializing and running PSG

The tool can be operated in several ways: via a web interface (<https://psg.gsfc.nasa.gov>, see Figure 2), via a flexible application program interface (API, <https://psg.gsfc.nasa.gov/api.php>) accessible from any scripting language (e.g., python, MATLAB, IDL), and it can be also operated by an installable suite via the Docker virtualization system. Parameters of PSG are defined for all modules and elements via a single configuration file, typically called “config”, which is formatted in a type of relaxed XML format.

The easiest way to start a simulation is by loading a configuration template file from the website; these templates are pre-saved configuration text files that are read by the radiative transfer modules when requesting an on-demand calculation. The configuration files are listed in the “Select Template” menu below the three main online sections of PSG (see Figure 2). Once a template configuration file is selected, and after clicking the “Load Template” button, all the parameters for the selected simulation are defined. Several templates targeting the main objects in the solar system are available, and any parameter of the run can be modified by clicking on the “Change” buttons, which will redirect into the three PSG modules, and then “Save settings”. The user can also decide to not change any parameter after exploring the module by clicking “Cancel” or clicking “Reset” on the main page.

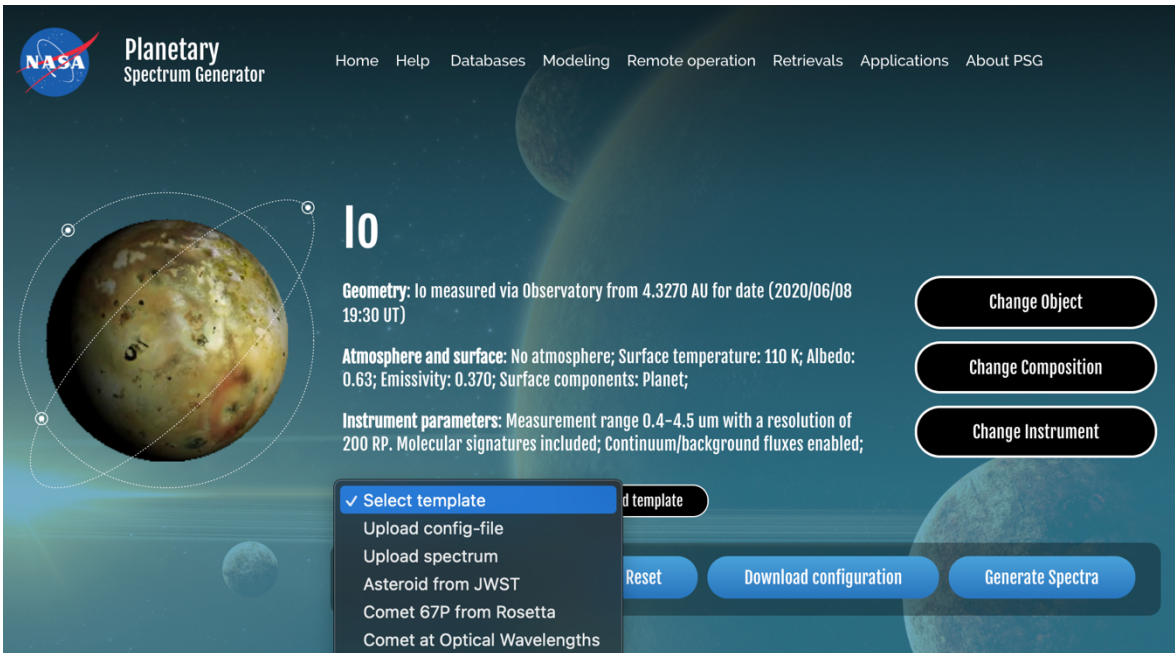


**Figure 2:** Home screen of the PSG interface, where the results of the calculations are plotted, and in which the main parameters of the simulation are summarized.

Essentially, the full purpose of the online web-interface GUI is to read/edit/save the configuration file before calling the PSG server requesting for a simulation. This file can also be downloaded and saved in your own computer for future operations by clicking the “Download configuration” button. In the same list-menu that reports the template files, it is possible to select “Upload config-file” option, which allows the user to upload pre-defined/saved files.

Once the configuration of the parameters is ready, one can start the calculation by clicking on "Generate Spectra". This will first verify the geometric parameters and pre-calculate geometric and atmospheric parameters. These will be fed together with the input configuration file to the radiative transfer modules for analysis. The output of these modules (and most databases accessed by PSG) are easy-to-read text files formatted as multi-column tables with a header defined by the # symbol. These output tables are read by the graphics module to produce the spectral plots.

When accessing the public PSG server (web and API), every user is identified by a cookie and their IP address, and has a unique configuration file associated to this ID. A limit of 100 API calls per day to the public server is defined for every ID, yet the user may obtain a higher limit (up to 100,000 simulations / day) by requesting a personal key (please send us an email). One can forgo any restrictions by installing PSG in any personal machine or computational cluster (e.g., AWS) via the free Docker architecture (see chapter 10).



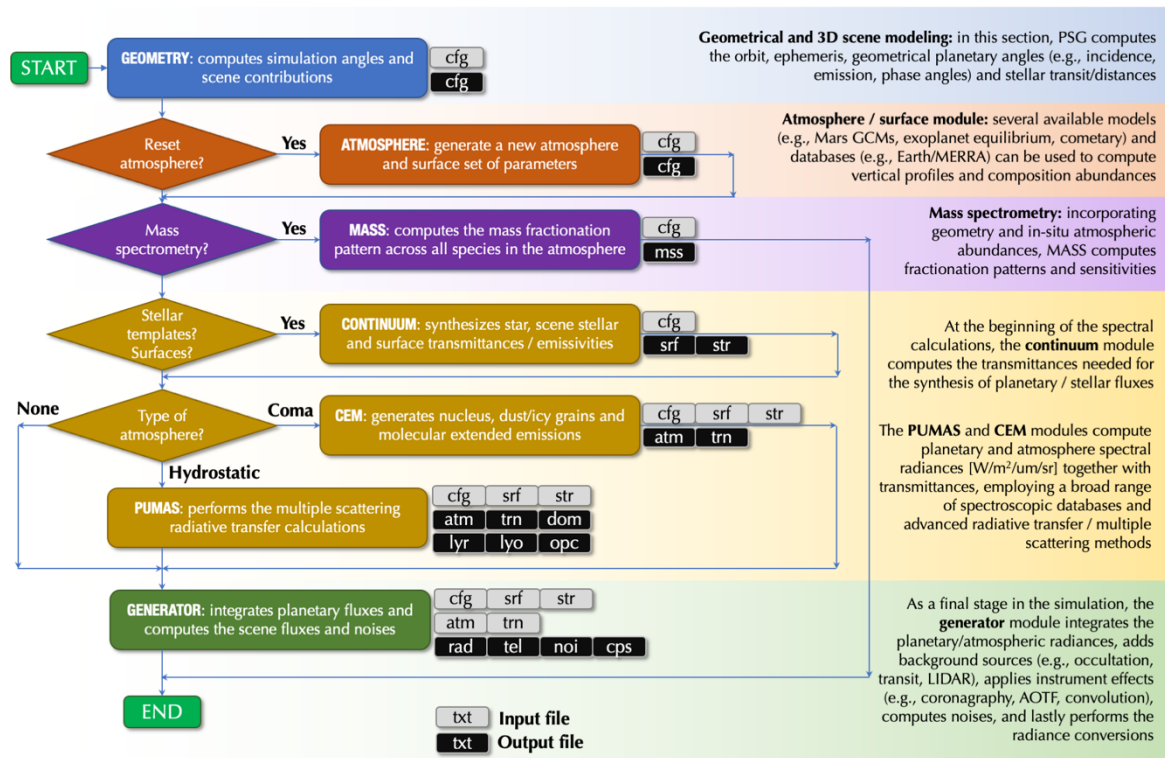


**Figure 3:** Architecture of the main modules of PSG and their interrelationship. The codes share inputs/outputs by accessing the corresponding output files/parameters from the preceding modules. All the modules are parameterized by the “config” cfg file, and the main output of PSG is captured in the rad file.

### 3. Modules and outputs of the PSG architecture

The generation of spectra is done by following a specific sequence of operations. These are done internally in PSG, in which every module takes a set of input files and produces another set of output files. Understanding this sequence is of relevance when scripting and debugging operational issues. In particular, when interfacing with PSG we may want to only to run a specific module and not all of them, as done by the web/API server. For instance, the geometry section of PSG website only calls the “GEOMETRY” module, and similarly the atmosphere section only operates with the “ATMOSPHERE” module. One can choose which module to operate in the API call by establishing the required output and operational modules of the call.

In Figure 3 the sequence of operations performed by PSG is shown, in which the interplay between the different modules (e.g., GEOMETRY, ATMOSPHERE, MASS, CONTINUUM, CEM, PUMAS, GENERATOR) is presented. The retrieval module (see chapter 9) operates above this diagram, and effectively calls PSG as a “wrapper” to compute forward spectra and to determine Jacobians. Similarly, most PSG apps (e.g., GlobES) operate as “wrappers” to this architecture, so once the user understands the core modules of PSG (Figure 3), it is then possible to understand the full structure of the modules operating in the PSG suite.



*The input/output files contents are as following:*

**cfg** This is the configuration file that defines the operations of all the modules. A single line is provided for each parameter, in which the parameter name is defined first in the line and given in brackets as <KEYWORD>. Following '>', the value is provided for that keyword (parameter), which can be a string, a number, or a set of comma separated values. The keywords and their formats (S# defines a string of length #) are listed at <https://psg.gsfc.nasa.gov/helpapi.php#parameters>. Empty lines and strings not starting in '<' are skipped, while if the keyword is provided many times in the file, the latest entry in the file is taken as the desired value. The user can also upload column-formatted data within the “config” file, by bracketing the data in between the following keywords: <DATA>, which define where the data start and </DATA> which define the end- this input is then transferred to the “dat” file (the input file used only by the retrieval module, see Chapter 9). Binary data (e.g., GCM data for GlobES) can be uploaded by bracketing it in between the <BINARY> and </BINARY> keywords - this input is then transferred to the “bin” file. User-defined spectroscopy (e.g., laboratory measurement) can be also provided with the “config” file by adding a line as <SPEC>name\_T#\_USER (name is the component name and # is the spectroscopic type of the data <https://psg.gsfc.nasa.gov/helpatm.php#profiles>) and then bracketing with </SPEC> - these inputs are then transferred to individual files for each database, and only accessible to that ID/user.

**rad** This is the main output of PSG, and it is the spectrum used by the retrieval/apps wrappers. This is a text file with headers defined by the # letter with values provided in a multi-column format, organized in rows for each spectral point. The first column of the data is the wavelength/frequency, the following column is the total radiance, then noise (if asked) and then the columns for each sub-component of the radiation. In these files, the line “# Spectral unit:” defines the unit of the first column, while “# Radiance unit:” defines the unit for all the following columns. The line “# Wave/freq ...” defines the name/type of all the columns. If the simulations include a star in the scene (see chapter 2), a column “Stellar” will appear, and/or in LIDAR mode the column “Laser” will appear. For transit observations, the column “Transit” describes the stellar flux lost due to the planetary transit (probably the mostly used column), while “Total” will incorporate this loss but also add the self-emission thermal emission of the planet (i.e., Total = Transit + planet\_self\_emission).

**mss** This is the main output of MASS module, and it is the mass spectrometry simulated spectra at the desired mass range and resolution. The natural intensity of the MASS module is [molecules/cm<sup>3</sup>], yet the MASS module can convert to any desired units (e.g., [counts/second]) by integrating information about the efficiency of the instrument and the sampling strategy considered.

**str** A key element in any spectral simulation is the properties of the host star impinging spectrum and that of any stellar spectra within the observational scene. In PSG, the stellar fluxes are computed as a multiplication of an underlying blackbody, with an effective temperature and stellar radius, and a stellar “transmittance” (1.0 is as blackbody). In a simulation, two types of stellar sources should be considered, the star from which the planet revolves around and therefore it is the main source of shortwave radiation arriving to the planet – in our solar system, that would be the Sun. The second is any star within the observational scene, as in a stellar occultation or when observing an exoplanet in which the star is within the field (e.g., coronagraphy, transit, see details at





<https://psg.gsfc.nasa.gov/help.php#doppler>). Each source can have different relative velocities and may also have different stellar properties (e.g., type, temperature), and as such different transmittances. The “str” file contains three columns, the first is the simulation wavelength, and the following are star transmittance (star of the planet host) and then stellar transmittance (if any star is within the field).

**srf** As discussed in chapter 6, the surface properties, independent of scattering model and geometry, are characterized by the single scattering albedo and emissivity. The user can compute reflected/emitted fluxes at a variety of phases and geometries by choosing a model and by knowing these parameters. The CONTINUUM module of PSG computes these two variables and saves them into the “srf” file as a three columns file (wavelength/frequency single\_scattering\_albedo emissivity). These parameters are integrated into the cometary (CEM), planetary (PUMAS) and radiative integrator (GENERATOR) to compute planetary/cometary fluxes.

**atm** This file contains the main outputs of the planetary/cometary modules (e.g., PUMAS, CEM), containing spectral radiances [ $\text{W}/\text{m}^2/\mu\text{m}/\text{sr}$ ], which are used to compute scene fluxes by the radiative integrator (GENERATOR). The radiation reported in the atm file specifically pertains to the planet (i.e., reflected, scattered, thermal emissions), surface, atmosphere and to the dust/icy grains for comets, for the selected geometry and coverage of the field-of-view. The GENERATOR module will add these radiances to any background sources to produce the Total observed radiances as reported in the “rad” file – The values in the “rad” file are also converted from [ $\text{W}/\text{m}^2/\mu\text{m}/\text{sr}$ ] in the “atm” file to any desired output unit.

**trn** This file contains the planetary transmittances (i.e., exponential of the integral of opacities) at the observational emission angle. For transit simulations, this file reports the combined transit transmittances across all layers in transit and for all atmospheric constituents. The file is formatted as a multi-column table, in which the first column is wavelength/frequency and then the total value for all components, followed by columns for each sub-component. This output is only used by GENERATOR module when computing transit and occultation fluxes.

**lyr** This file reports the input layer information as ingested by the PUMAS module, together with the computed Curtis-Godson effective layer parameters and the corresponding column densities. The header of the file reports additional information pertaining to the radiative transfer simulations, such as the inclusion of CIAs / UV cross sections and the collisional regime assumptions. The upper section of the file reports the parameters at the specific layer points as defined by the <ATMOSPHERE-LAYER-#> keywords in the config file. These boundary values are then taken by the PUMAS module and integrated across the curved path of radiation to define the effective Curtis-Godson P/T/abundances within the layer. Those appear at the bottom part of the file.

**lyo** When selecting the “Layering” mode in the processes section of the atmosphere (field ATMOSPHERE-CONTINUUM), PUMAS will output the total opacities at each layer as employed by the radiative transfer module. The values are provided as a 2D table (wavelength vs layers) in units of [ $\tau/\text{km}$ ]. The per ‘km’ unit refers to the fact that the opacity values are divided by



the height of the layer. The altitude of the layers (including TOA) are provided after the “# Wave/freq” keyword in the header.

**opc** When operating in the “Cell” mode (defined in the geometry section and via OBJECT keyword), the PUMAS module will provide the cell opacities in this file. This mode of operation and output is of relevance when operating PSG to compute opacities at specific P/T conditions.

**dom** When running full sky 3D simulations, this file contains the spectral radiances at the different azimuth and zenith angles. The output is formatted as a 2D table of  $(A \times Z) + 1$  columns: A is the number of azimuth angles, defined in the header by the keyword “# Azimuths”, while Z is the number of zenith angles, defined by the keyword “# Zeniths”. The output radiances are always reported in units of spectral radiance  $[W/m^2/um/sr]$ .

**tel** PSG can apply telluric effects (e.g., background atmospheric emission and extinction) to ground-based astronomical simulations by operating with a database of pre-computed telluric transmittances. The database includes telluric transmittances for 5 altitudes and 4 columns of water for each case. The altitudes include that of Maunakea/Hawaii (4200 m), Paranal/Chile (2600 m), SOFIA (14,000 m) and balloon observatories (35,000 m), while the water vapor column was established by scaling the tropical water profile by a factor of 0.1, 0.3 and 0.7 and 1. The “tel” file reports in a 2-column file the extracted telluric transmittances for the selected case.

**noi** The noise module of GENERATOR can compute sensitivity values for a broad range of instruments and observatories. This file reports the total noise (as reported in the 3<sup>rd</sup> column of the rad file) and the individual components that led to this noise, which is particularly relevant when exploring the limiting sensitivity factors affecting a simulation. The file reports the components in 6 columns: Wave/freq Total Source Detector Telescope Background.

**cps** When computing high-contrast coronagraphy simulations, a valuable metric when exploring sensitivities is the count rates, or counts being measured by the detector for the different noise components. These values are collected in the “noi” output, and they can be used to compute and compare sensitivities with other numerical methods.

#### 4. Main sections of the web interface

The configuration file and web interface can be organized into four main blocks or sub-sections. First, we have the definition of the object and the geometry, parameterized via the OBJECT and GEOMETRY fields in the configuration file, and accessed on the website via the “**Change Object**” button (first block). Second, there are the parameters referring to the atmosphere and surface of the object, defined in the config via the ATMOPHERE and SURFACE fields, and accessed on the website via the “**Change Composition**” button (second block). Thirdly comes the parameters referring to the instrument/observatory (e.g., wavelength range, resolution), defined via the GENERATOR fields and accessed on the website via the “**Change Instrument**” button (third block). Lastly, accessed on top of the website via the “**Retrievals**” button, we have the retrieval interface (fourth block), with its parameters saved on the config via the RETRIEVAL keywords.

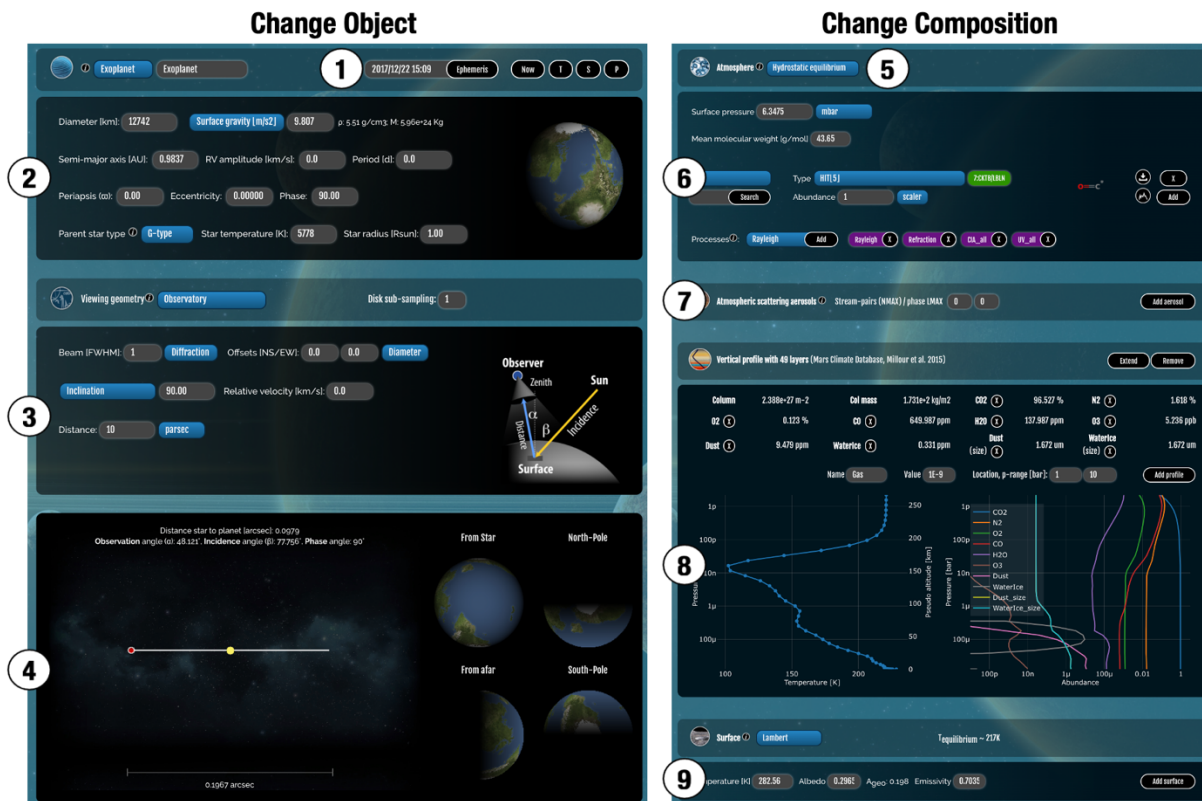


**Figure 4:** Website graphical user interface (GUI) for the object/geometry and atmosphere/surface sections. The different numbers indicate the main blocks within these interface windows.

The number of parameters (<https://psg.gsfc.nasa.gov/helpapi.php#parameters>) can in principle appear daunting, but PSG will select defaults appropriate for each case, ensuring a simplified parameter entry. Also, there are only 4 interfaces to learn, and once these are understood, the full capabilities of the tool can be accessed and controlled.

**Figure 4** shows the interfaces of the “Change Object” and “Change Composition”, in which the main components are:

1. In the upper bar of the geometry section, one can select the type of object (e.g., planet, moon, exoplanet, comet, asteroid, cell), and perform several ephemeris operations. By entering a date (format YYYY/MM/DD HH:MM), and clicking “Ephemeris”, PSG will search the object among its database of solar system objects and exoplanets (extracted from the NASA exoplanet archive every 48 hours) and perform a realistic orbital calculation for that date and viewing geometry. If the solar system object is not in the PSG database, PSG will perform an API request to the JPL/Horizons system. The “Now” button will calculate ephemeris for the current date/time. The next 3 buttons are object dependent. If an exoplanet has been selected, the letters T, S and P will appear, which permit to search for the next primary transit (T), secondary transit (S) and periastron (P). The date will change to the next date when this event occurs, and the planet will be set to this particular orbital phase. If



a solar system object has been selected, the symbols < and > will appear, which permit to run ephemeris -1 day (<) and +1 day (>).

2. The upper fields of the geometry section define the properties of the planet (e.g., diameter, gravity) and its relationship to its host star. This includes parameters of the planetary orbit (e.g., periapsis, eccentricity) and importantly the phase/season along this orbit. For exoplanets, the phase of an orbit defines the planet/star location relative to the observer, in which 180 is the planet is in front of the star (primary transit), 0 is secondary eclipse, and 90/270 the planet is at quadrature. For solar system objects, season identifies the angle with respect to equinox, relevant when defining the season/weather on the planet. If performing a theoretical simulation of a solar system object from afar (>0.1 parsec), then season relates to the orbital phase as with exoplanets.
3. The lower fields of the geometry section define how this planetary system is being observed, and specifically the location of the observer with respect to the planet. As discussed in chapter 2, the simulations could be done assuming the observer is within/nearby the planet (e.g., looking from the surface, occultation inside its atmosphere, mass spectrometry, orbital nadir), looking from afar but within the same planetary system (e.g., observatory looking at solar system objects), or looking at the whole planet and star from afar (>0.1 parsec), in which the host star is also included in the simulation (e.g., transit, coronagraphy). In particular, if one wants to calculate transit/coronagraphy simulations, the distance has to be >0.1 parsec in order to properly capture the proper geometry conditions.
4. The bottom panel of the geometry section shows 3D simulations as computed by the GEOMETRY module. The full disk simulations include a realistic treatment of the surface scattering properties (see chapter 6) and showcase the orbital configuration as computed with the orbital model of PSG. PSG also includes a full and interactive 3D model of the solar system, accessible for solar system objects by clicking on the “Show orbit” button.
5. In the upper bar from the atmosphere section, the user can select from several precompiled atmosphere/surface templates and atmospheric models (e.g., equilibrium models, Mars GCMs, Earth NASA/MERRA). In this section, one can also upload user defined spectroscopic databases, such as aerosol scattering models, molecular cross-sections, and surface single scattering albedos. These databases are only accessible to the current user.
6. This is the main section of the atmosphere section. It defines where the surface pressure level (or cometary activity) and the molecules to be considered for the simulation (and for the retrieval). Only the molecules listed here will be considered in the simulation/retrieval, independently of the profiles shown/reported in block 8. The connection between the profiles in section 8 and molecules listed in this section, is done via the “scaler” abundance unit. A scaler of 1 indicates that the values as in the profile shown in 8 will be used, while any other unit (e.g., ppm, ppb) indicates a constant mixing ratio (w.r.t., to the local wet density) with altitude. If a scaler is selected for a constituent for which no profile exists in block 8, PSG will consider a scaler relative to an abundance of 100%. The surface pressure indicates where the atmosphere starts, again independently of the profile pressures shown in block 8. The surface pressure is where the surface starts, and where the diameter and gravity values provided in block 2 relate to in the vertical structure of the planet. Continuum



processes and special keywords can be activated by adding them via the “Processes” dropdown list.

7. This block pertains to scattering aerosols and scattering parameters (LMAX/NMAX, see chapter 5). Similarly to block 6, only aerosols listed here will be considered in the simulation, while the scaler unit is the method to relate and scale to the profiles presented in block 8. If NMAX=0, the fast single scattering approximation is employed (see chapter 4), which is only recommended for weakly scattering media.
8. The vertical profile of the atmosphere as provided by the ATMOSPHERE-LAYER keywords is reported in this block. The total column density is the integral of the densities across all the reported layers, while the column mass is that number multiplied by the molar mass. The reported abundances are the average column abundances, so each column density is that reported abundance times the total column density. In this block, the user can also add arbitrary layers of gases/aerosols via the “Add profile” button. The “Extend” button will extend the vertical profiles up to 1 pbar by copying the temperature and mixing ratios of the last layer, which may be useful when exploring weak upper atmosphere signatures, and when performing transit or Solar occultation simulations. The reported profiles are not included in the simulation by default, they are only included when added in blocks 6 and 7.
9. The bottom block permits to provide surface properties (SURFACE keywords) and to alter the composition (areal mixing) by selecting reflectance and optical constants parameters. The user can also choose the method in which the surface is being modelled with (e.g., Hapke).

The main components of the “Change Instrument” and “Retrieval” website graphical user interfaces as presented in **Figure 5** are:

1. The upper bar of the instrument section allows to select from a selection of pre-defined instrument templates. These templates are simply text files with the GENERATOR keywords filled to match the properties of these instrument/observatories. The user is free to modify these and to create their own simulation / instrument setup. These instrument models are approximations to the real instruments - they do not account neither for overheads nor subtleties of the instruments/detectors - and the user is advised to work with the official modeling tools of these instruments if available.
2. The main parameters of the simulation are provided in these fields, which include wavelength range, spectral resolution and intensity unit. The resolution defined here refers to the sampling resolution of the output grid. If the “Gaussian” kernel is selected, the sampling resolution is defined to be 10 times the actual resolution, and the spectra is convolved with a Gaussian having a Full-Half-Width-Maximum (FWHM) that of the selected resolution. PSG will internally compute the spectra at the needed spectral resolution to ensure spectral accuracy (see chapter 4), and then bin down to the desired output sampling/convolution resolution. The flag “**Include molecular signatures**” enable/disable the PUMAS/CEM modules, while a disabled flag “**Include continuum fluxes**” removes a synthetic model spectrum from the simulated spectra. The flag “**Integrate stellar templates**” enables/disables the use of stellar templates in the computation of stellar spectra – a disabled flag implies to simply use black-bodies for the stars. If modeling astronomical ground-based observations,





**Figure 5:** Website graphical user interface (GUI) for the instrument and retrieval sections. The different numbers indicate the main blocks within these interface windows.

one can enable telluric effects with the “**Terrestrial transmittance**” flags. The flag “**Apply**” implies that the noise will include telluric transmittances and telluric background sources, but the planetary spectra will not be affected. The flag “**Multiply**” will multiply the simulated spectra by telluric transmittances. As discussed before in the description of the “atm” and “rad” files, the planetary modules compute spectra in spectral radiance [ $\text{W}/\text{m}^2/\mu\text{m}/\text{sr}$ ], and the GENERATOR module will convert the fluxes to any unit as selected in this block.

3. Spectra can be simulated for a broad range of instrument types, in which a simple and standard simulation without any complex effect would mean “single dish”. The field-of-view (FOV) setting is important for establishing the amount of planetary flux encompassed by the FOV (see chapter 2), and if and how much stellar background sources should be added to the simulation (e.g., transit, coronagraphy). The telescope diameter is only relevant when computing noise (collecting area) or when defining a diffraction limited simulation.
4. PSG includes a realistic noise calculator, and in this section one can enter the detector parameters. Parameters needed for all simulations include integration time per exposure and number of exposures. The number of pixels refer to how many detector pixels of the instrument are encompassed in each simulation spectral pixels (as selected in block 2). In this block, the user may also provide wavelength dependent detector values as tables via the “**Table**” button. More details regarding the noise parameters can be found in chapter 8.
5. In the upper bar of the retrievals window, the user can upload data. The data should be a 2 or 3 columns file, with the first column is wavelength/frequency (in units as defined in block 6), second column is data (in units as defined in block 6), and noise (this is optional and PSG will assume 5% of the signal if this information is missing). By default, PSG assumes that the wavelength points refer to the center of pixel, with a width as defined by the spacing of the points. If the first column is in the format A:B, then PSG will interpret that the pixel spans from A to B in wavelength. Regarding the second column, if the values are in format C/D, PSG will interpret that the reported values refer to ground-based observations, in

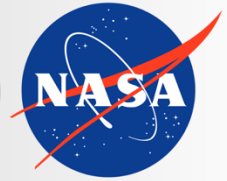


which  $D$  is the effective transmittance for the signal at  $C$ , and the value of TOA for this pixel is  $C/D$ .

6. In this block, the user enters the units and general parameters for the retrieval (see chapter 9). The resolution refers to the convolved resolution of the data in the “dat” file, while the scaling factor is a numerical scaler to the provided data.
7. PSG can correct for several typical issues affecting spectroscopic data, and with these flags the user can enable these corrections. Enabling more features adds degeneracy to the retrieval, so a mindful selection of parameters is required. These fitted synthetic effects are later reported in the output “dat” file as additional columns.
8. This is the main block of the retrieval section, in which the retrieval parameters are defined. The initial, minimum and maximum values for each parameter as used when determining the initial covariance matrix and the a-priori background values. They also ensure that the fit remains within physical bounds. More information regarding retrieval variables and their parameterization is presented in chapter 9.







**Planetary Spectrum Generator**  
National Aeronautics and Space Administration

# Chapter 2: **Geometry and orbital modeling**

**Villanueva and  
PSG team**

## 1. Geometry modeling

Any spectroscopic simulation of planets requires a precise description of the geometry being considered. For that purpose, PSG is integrated with a three-dimensional (3D) geometry calculator which includes any object in the solar system and all confirmed exoplanets. By setting the appropriate observational geometry, PSG can synthesize spectra for practically any observer and target configuration. In the first step, PSG computes the orbit and orientation of the planet relative to the star in the observer's reference frame. Based on the selected viewing geometry and distance to the planet, PSG then switches between three general geometrical regimes (Figure 1), the first one is the “orbital and in-situ”, for simulations nearby the planet (e.g., nadir, occultation, looking up from the surface, in-situ), and in which the simulated field-of-view samples a finite patch on the planet / sky. On such cases, the observational incidence and emission angles are unique and finite. The other two geometrical regimes are “observatory view” and they are distinguished by the observatory being within 0.1 parsec or beyond 0.1 parsec to the planet. In the first case, PSG does not include the host-star, and the FOV can encompass a broad range of emission and incidence angles on the planet, or even the whole planet. In the second case, at larger distances ( $>0.1$  parsec), PSG considers the location and contribution of the host-star with respect to the planet in the FOV, with the possibility of transit or inclusion of the stellar fluxes in the scene. Transit, eclipse and coronagraphy simulations are therefore only possible when defining distances greater than 0.1 parsec.

## 2. Orbital modeling of solar system objects

The GEOMETRY module in PSG is the one responsible for computing ephemeris, orbital parameters, and establishing the geometrical angles needed for the radiative transfer simulation. For the main bodies in the solar system (e.g., Mars, Neptune, Europa, etc.), PSG relies on pre-computed ephemeris tables from 1960 to 2050 calculated with the JPL/Horizons ephemerides system (<https://ssd.jpl.nasa.gov/horizons.cgi>) at a cadence of 1 hour, and later interpolated to the observational time, establishing the geometrical location and orientation of the object with respect to the observer. These tables tabulate heliocentric distance, heliocentric velocity, geocentric distance, geocentric velocity, sub-solar latitude, sub-solar longitude, sub-observer latitude and sub-observer longitude. For small bodies (e.g., comets, asteroids) and planetary ephemerides of orbiters, PSG dynamically extracts orbital parameters from the JPL-Horizons ephemerides system by connecting via their API. For small bodies with no sub-solar / sub-observer latitudes and longitudes, PSG defines them based on the ecliptic angles.

A key climatological parameter is the solar longitude, or position of the object across its orbital path (true anomaly) with respect to the northern hemisphere spring equinox (time when the planet's equatorial plane is equal to the orbital plane,  $L_s=0$ ).  $L_s=90$  corresponds to northern summer solstice,  $L_s=180$  marks the northern autumn equinox and  $L_s=270$  indicates northern winter solstice. This parameter is particularly relevant when querying information from general-circulation-models (GCM) or climatological databases of planets, since it is a fundamental factor in describing the structure and dynamics of the atmosphere. From the previously described ephemerides tables, which also include the true anomaly quantity, we determined the  $L_s=0$  for each object and used this information to establish the seasonal state and climatology of the planet. When defining the

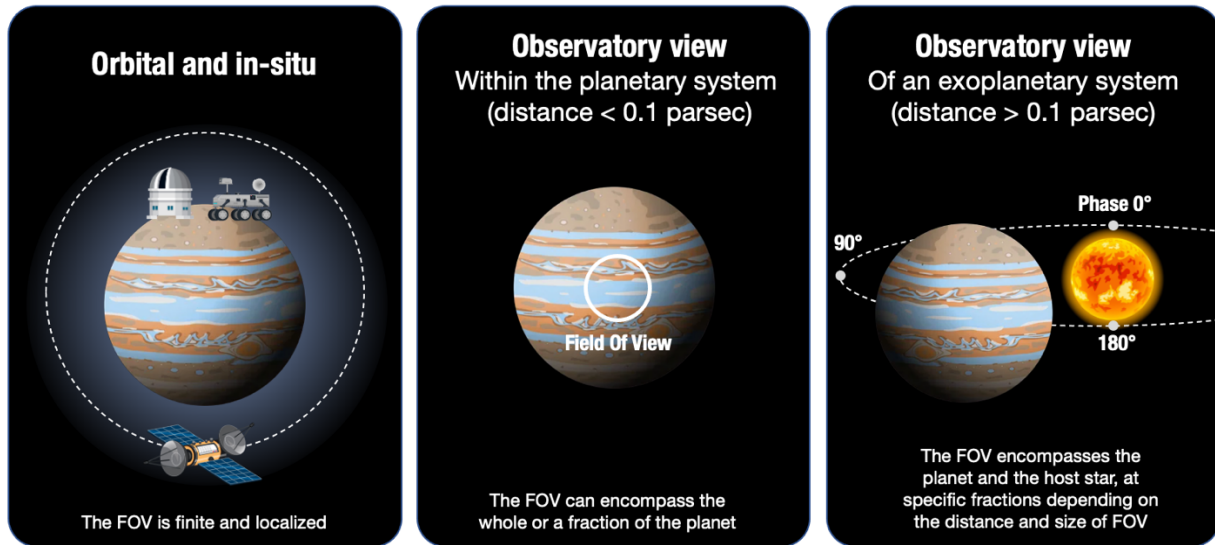


**Figure 1:** Based on the selected viewing geometry and distance to the planet, PSG switches between three general geometrical regimes: (1) all non-observatory geometries (e.g., nadir, occultation, looking up from the surface, in-situ) are considered to be local to the planet, (2) observatory geometries within 0.1 parsec do not include the host-star, and (3) observatory geometries including host-star are for >0.1 parsec simulations. For exoplanets (or solar system objects simulated beyond 0.1 parsec), the “season” defines the orbital phase, in which 180° is in front of the host-star, 0° behind the star, and 90/270° in quadrature.

reference point (i.e., location of the observer), PSG typically assumes an Earth-centered position, yet detailed spacecraft information has been integrated into PSG for many orbiters (e.g., MRO, Mars Express, ExoMars/Trace Gas Orbiter, MAVEN, Mars Odyssey, Cassini, Juno) and hundreds of points of interest (e.g., Maunakea, Paranal, Chajnantor, Arecibo, Viking, MSL/Curiosity, MER landers).

### 3. Orbital modeling of exoplanets

Transit detection and radial velocity characterization of exoplanet orbits provide constraints on the orbital parameters of planets detected around other stars. This information can be used to construct a three-dimensional view of the system and is used by PSG to predict the time of future primary and secondary transits. The NASA Exoplanet Archive (<https://exoplanetarchive.ipac.caltech.edu>) is an excellent repository of the constantly growing database of exoplanet orbital parameters. For exoplanets, PSG does not employ ephemerides tables, but computes the orbital integration of the Keplerian orbit using parameters obtained from the NASA Exoplanet Archive (via their API). This ensures that PSG uses the latest and most accurate orbital parameters, and that newly discovered exoplanets can be properly handled by PSG. Unfortunately, Kepler’s equation that relates the true anomaly (T, position on the elliptical orbital path) and the mean anomaly (M, proportional to time) does not have a closed-form solution (i.e., transcendental equation), and the orbital calculation requires an iterative solver. PSG employs the iterative Newton–Raphson algorithm to determine the true anomaly (T), constrained to an eccentric anomaly (E) precision of 1e-6 radians and to a maximum of 30 iterations. This computation employs the longitude of periapsis (w), orbital

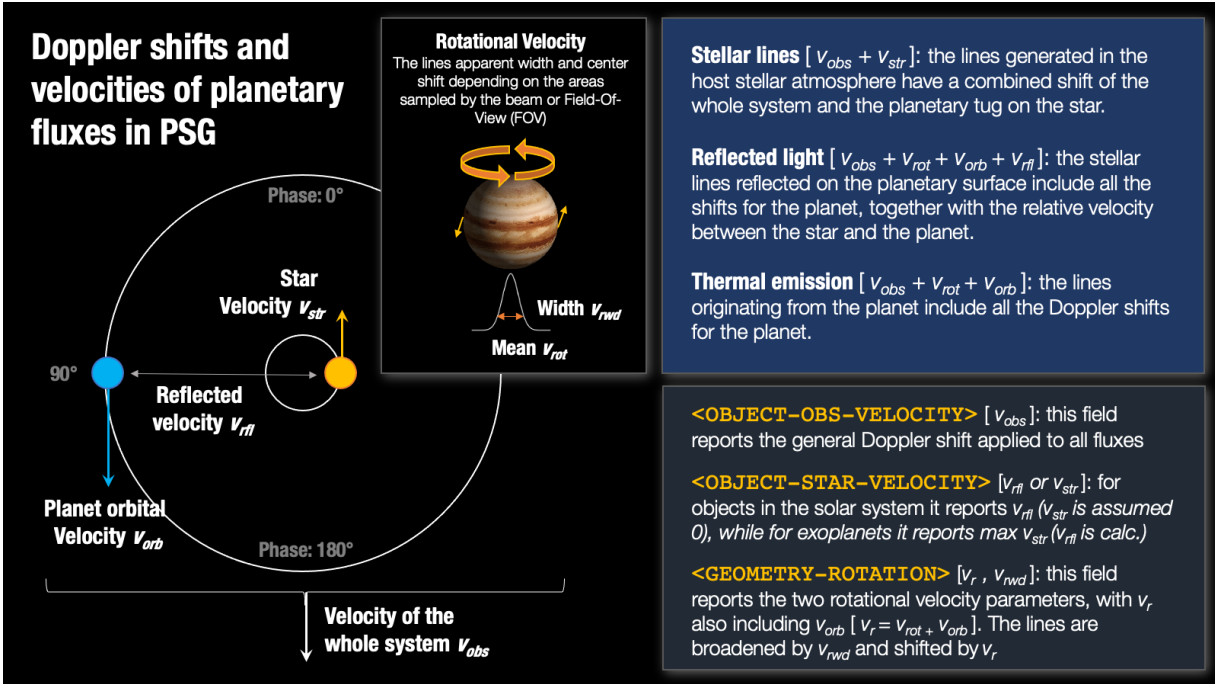


**Figure 2:** The motion of the planets across their orbit introduces spectroscopic shifts on the planetary and stellar fluxes. This motion also perturbs or "tugs" the host-star, introducing a Doppler shift on the stellar signatures. In PSG, all these effects are taken into account when synthesizing spectra, and are described via three fields: OBJECT-OBS-VELOCITY, OBJECT-STAR-VELOCITY and GEOMETRY-ROTATION. This figure describes how these three fields (calculated by PSG's Geometry module) encode the Doppler information of the motions for the whole system.

eccentricity ( $e$ ) and time of transit (TT) or time of periastron (TP). Even for highly eccentric orbits, such a method is sufficient to accurately determine the location of the exoplanet along its orbit, and this together with knowledge of the orbital inclination, permits PSG to construct an accurate three-dimensional view of the system (within the known certainty of these variables). Determining the actual sub-solar and sub-observer latitudes/longitudes requires knowledge of the rotational period and obliquity of the planet. Such parameters are rarely known for exoplanets, so when computing exoplanet ephemerides PSG assumes that the planets are tidally locked with no obliquity and that the sub-solar latitudes/longitudes are set at the center of the planet. The phase identifies the true anomaly relative to that one of the secondary transit (with a phase of 180 corresponding to the primary transit). Arbitrary or user-defined sub-solar and sub-observer values can be edited manually in the configuration file, or via an API request.

#### 4. Orbital and spectroscopic velocities

When performing high-resolution spectroscopic simulations, a detailed and accurate description of the different velocities is of great importance. In PSG, these parameters are specifically captured via three fields: OBJECT-OBS-VELOCITY, OBJECT-STAR-VELOCITY and GEOMETRY-ROTATION. Each sub-component of the sources sampled by the field-of-view (FOV) will have a

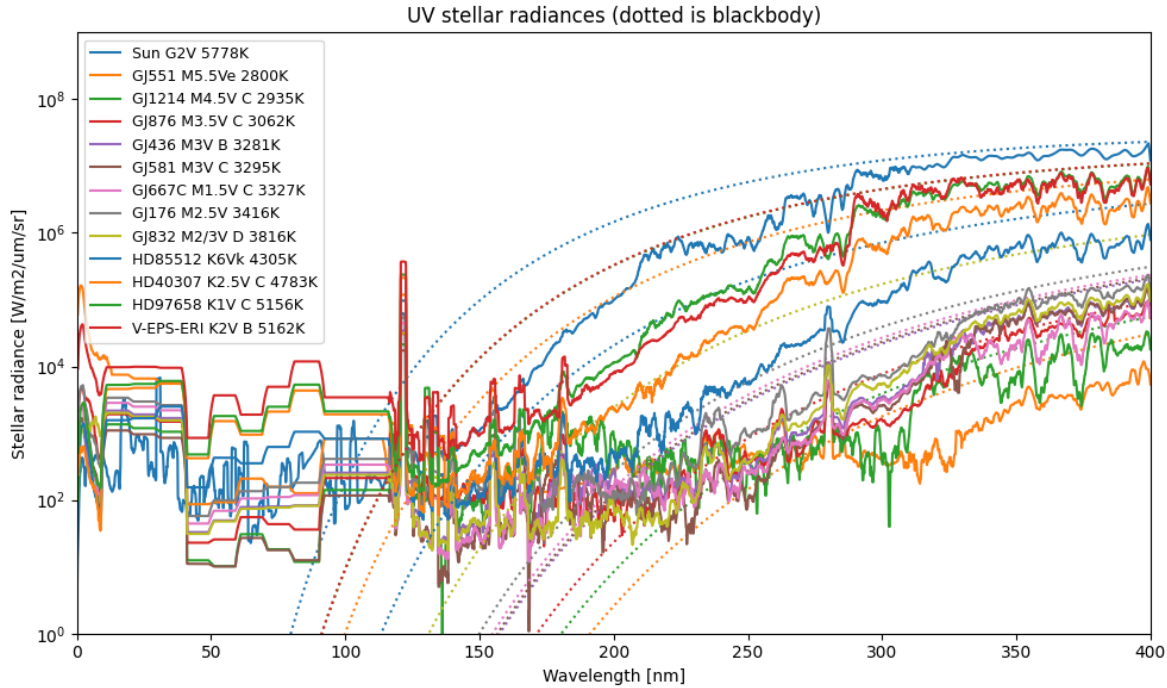


**Figure 3:** PSG allows to integrate a broad range of stellar templates, with the UV templates shown in this figure. The UV templates ( $<0.4 \mu\text{m}$ ) are based on the MUSCLES Treasury Survey (France et al., 2016), with the UV solar template derived from the LISIRD tool (LASP). The templates at longer wavelengths (i.e.,  $0.15\text{-}300 \mu\text{m}$ , optical, IR and radio) are based on the Kurucz spectral templates, which is complemented with the ACE solar spectrum ( $2\text{-}14 \mu\text{m}$ ) for the G-type.

particular Doppler shift associated to the object's rotation and orbital parameters. As summarized in Figure 2, the stellar fluxes will have a Doppler shift that integrates the full system velocity and that of the star as being affected by the planet. This "tug" of the star by the orbiting planets is now of the prime methods used to characterize the properties of exoplanets.

The integration of all these Doppler effects is particularly relevant when employing the cross-correlation method in exoplanetary research. This method compares residual planetary spectra at different phases with a synthetic set of templates shifted following the orbital motion of the planet (and all the associated Doppler shifts). This is the prime method to characterize exoplanets using ground-based observatories, since telluric signatures are static spectroscopically, yet the planetary signatures shift by km/s across the planetary orbit. In PSG as shown in Figure 2, the planetary and stellar velocities are computed based on the orbital phase and orbital parameters.

## 5. Types of stellar hosts

PSG includes the possibility to integrate stellar templates by adopting the (Kurucz, 2009) stellar templates ( $0.15\text{-}300 \mu\text{m}$ ), which is complemented at short wavelengths ( $<0.4 \mu\text{m}$ ; X-ray, EUV, FUV) with the MUSCLES Treasury Survey (France et al. 2016). When considering the G-type template, the spectrum is complemented with the ACE solar spectrum ( $2\text{-}14 \mu\text{m}$ ) in the infrared and

with the LISIRD template in the UV ( $<0.4 \mu\text{m}$ ). PSG picks the template based on the stellar type and temperature, and all fluxes are scaled to the actual effective stellar temperature of the star. The stellar information is used to compute reflected stellar/solar fluxes, and also to compute the total observable exoplanet fluxes, when the (exo)planet and star are within the field-of-view (FOV).

The Kurucz template for the A-type star is based on the Vega model, the K-type is based on the HD189733 model, and the M-type model is based on the M5-3170 model. In the UV, the stellar templates include: Sun (G2V, 5778K), HD85512 (K6Vk, 4305K), HD40307 (K2.5V, 4783K), HD97658 (K1V C, 5156K), V-EPS-ERI (K2V B, 5162K), GJ551 (M5.5V, 2800K), GJ1214 (M4.5V, 2935K), GJ876 (M3.5V, 3062K), GJ436 (M3V B, 3281K), GJ581 (M3V C, 3295K), GJ667C (M1.5V, 3327K), GJ176 (M2.5V, 3416K), GJ832 (M2/3V, 3816K). The fluxes as shown in Figure 3 are in units of spectral radiance in  $[\text{W}/\text{m}^2/\mu\text{m}/\text{sr}]$ , and in order to compute the actual spectral irradiance  $[\text{W}/\text{m}^2/\mu\text{m}]$  received by the planet one needs to multiply by the solid angle encompassed by star as seen from the planet ( $\Omega = 6.807\text{e-}5 \cdot (\text{Rstar}/\text{Dstar})^2 [\text{sr}]$ ), where Rstar is the star size with respect to our Sun [1.0 for Sun], and Dstar is the distance to the star in AU [1.0 for Earth].

## 6. Definition of the modeling geometries: angles and sub-sampling

The definition of the direction of incidence and emission plays an important role in the calculation of the radiant intensities. As summarized in the equations of chapters 4 to 6, all terms include a direction quantifier (e.g.,  $\mu$ ,  $\phi$ ), which can be challenging to establish when the observed scene includes many incidence / emission angles, as when we observe a planet from afar. In PSG, the angles are computed by the geometry module, which are then fed to the radiative transfer module. There are several possible geometries (Figure 4), which can be grouped as “Looking up”, “Limb or Stellar/solar Occultation”, “Nadir”, “Observatory”.

### 6.1 Looking up / Looking up to the Sun / Looking to an object / Dome view

This is the geometry configuration that describes when the observer is located at a specific altitude from the surface, looking up in the sky. The observational zenith angle  $\mu$  and the solar azimuth angle  $\phi - \phi_0$  are user inputs. From here on we will define  $\phi$  to be the solar zenith angle, and therefore  $\phi_0$  is set to 0. The incidence solar zenith angle  $\mu_0$  is calculated from the observer’s longitude ( $\lambda$ ) and latitude ( $\varphi$ ) as:

$$\mu_0 = \sin \varphi \sin \varphi_0 + \cos \varphi \cos \varphi_0 \cos(\lambda - \lambda_0) \quad (1)$$

where  $\lambda_0$  and  $\varphi_0$  are the sub-solar longitude and latitude respectively. On a similar form, the cosine of the phase angle ( $\theta$ ) is calculated as:

$$\cos \theta = \mu \mu_0 + \sin(\cos^{-1} \mu) \sin(\cos^{-1} \mu_0) \cos \phi \quad (2)$$

In the “Looking to the Sun” mode the angles are further set to be  $\mu_0=\mu$ ,  $\phi=0$ ,  $\theta=0$ , and the Sun is the background source, while in “Looking up to an Object” the background source is a point source (a



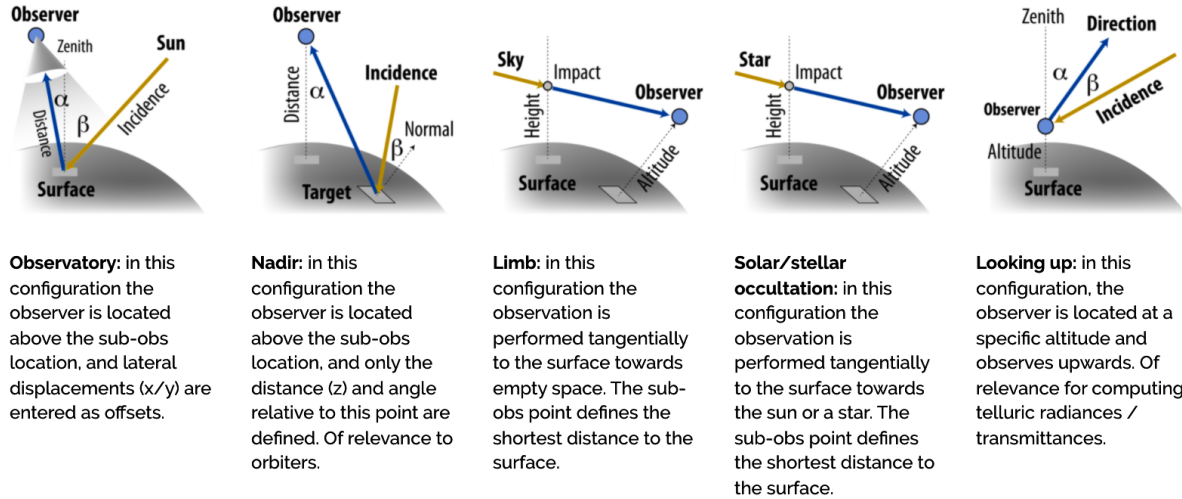


**Figure 4:** PSG allows for several observational geometries, in which the geometry module computes the zenith, azimuth and phase angles to be employed by the radiative transfer module.  $\alpha$  is the observer's zenith angle ( $\mu = \cos\alpha$ ), while  $\beta$  is the incidence solar zenith angle ( $\mu_0 = \cos\beta$ ).

star) of a user defined brightness and temperature / spectral type. In these geometries there is only one set of incidence and emission angles and the path of radiation is computed from TOA to the altitude of the observer. The “Dome” mode is a  $360^\circ$  3D view of the sky and it is an adaption of the looking up geometry, in which the diffuse radiation field is solved following the discrete ordinates method and intensities are computed at  $(2N+1)$  azimuths and  $(2N+1)$  zenith angles. If  $N=10$ , then 441 intensities are computed across the whole sky as:  $\phi$  from  $0$  to  $360^\circ$  with  $\Delta\phi=18^\circ$  and zenith angles  $\alpha$  from  $0$  to  $90^\circ$  with a spacing of  $4.5^\circ$ .

## 6.2 Limb / Solar occultation / Stellar occultation

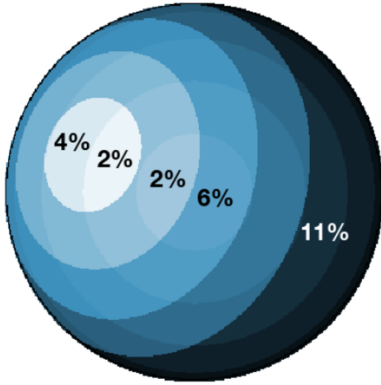
These are observation geometries in which the observer is located at a specific altitude in the atmosphere and is observing towards a specific impact height (lowest altitude of the radiation path) of the atmosphere. The possible background source variables ingested by PSG are: **space** for selecting “limb”, **Sun** for “solar occultation” and a **star** of an user defined brightness and temperature / spectral type for “stellar occultation”. By definition, the cosine of the observing zenith angle is  $\mu=0$  at the impact height. For limb and stellar occultation modes,  $\mu_0$  at the surface is computed following equation 2 (note that the latitude and longitude values entered in PSG refer to those of the impact height, not to the observer), while for the solar occultation configuration, the cosine of the incidence angle at the impact height is set to  $\mu_0=\mu=0$ . The path of radiation travels from TOA to the impact height to the observer.

## 6.3 Nadir

In this configuration, the observer is at a user-defined altitude looking down to a specific latitude and longitude on the planet. Similarly, to the previously described observing modes, in this

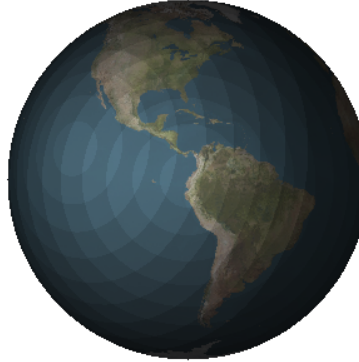
### Sub-sampling at phase 40

Sub-sampling N=5  
22 distinct regions



### Fine sampling at phase 40

Sub-sampling N=10  
74 distinct regions



### Thermal and phase 0

Sub-sampling N=10  
10 distinct regions

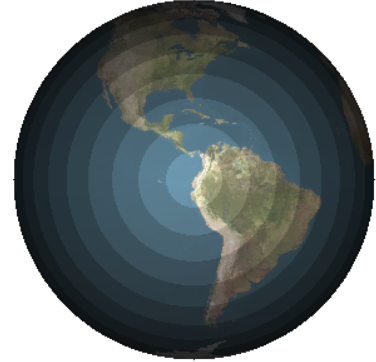


**Figure 5:** In observatory mode, the sampled region may encompass a broad range of incidence and emission angles, and in PSG a sampling algorithm determines the number of distinct regions and their weights **[Left]**. The sub-sampling N defines how fine to sample the  $\mu_0$  and  $\mu$  terms. A sampling of N=10, indicates  $\Delta\mu_0=1/10=0.1$  and  $\Delta\mu=0.1$ , which leads to a high number of 74 distinct regions. **[Right]** At phase 0 or at thermal wavelengths (where the solar fluxes are negligible), the sampling is solely organized by  $\mu$ .

configuration there is only one set of incidence and emission angles and those are relative to the observed point on the surface.

## 6.4 Observatory

In many cases, the observed planetary region by the field-of-view encompasses a broad range of incidence and emission angles, and a single set of angles does not simply fully capture the radiative transfer processes. In PSG, the geometry module will divide the planetary disk into 140 x 140 regions (19600) regions, each with its own  $\mu_0^i$  and  $\mu^i$  and will then compute an “average” incidence and emission angle across the FOV as:

$$\mu_0 = \frac{1}{n} \sum_{i=1}^n \mu_0^i \quad \mu = \frac{1}{n} \sum_{i=1}^n \mu^i \quad (3)$$

where n is the number of pixels encompassed by the FOV. In the case that the FOV encompasses the whole planetary disk, then  $\mu$  is 2/3, which corresponds to an average emission angle of 48 degrees. This algorithm will ensure that for a Lambertian surface, the resulting average  $\mu_0$  always correspond to the Lambert phase integral (see section 9 of chapter 6). This approach permits to run a single radiative transfer simulation with “average” incidence and emission angles and obtain reasonable results. In cases with strong anisotropic scattering and/or complex absorption processes, such “average” approach may not be accurate enough to capture the diversity of incidence and emissions, and for those cases we have implemented a sub-sampling algorithm that addresses this





issue. The algorithm divides the disk into “bins” of common incidence and emission angles and quantifies how many  $n$  pixels correspond to that specific  $\mu$  and  $\mu_0$  bin. For instance, in the case of  $N=10$ , the disk is organized in bins of  $\Delta\mu_0=1/10=0.1$  and  $\Delta\mu=0.1$  (all pixels with  $\mu_0$  0 to 0.1 and  $\mu$  0 to 0.1 will correspond to bin 1, etc.), which depending on the observational phase will lead to less (or more) number of distinct bins (see Figure 5). At phase 0 or at thermal wavelengths ( $\lambda > 10 \mu\text{m}$ ), only  $N$  bins are distinct, yet at more orthogonal phases, the number of bins approaches  $N^2$ . Each distinct bin will have an “average” incidence and emission angle computed following equation (3) and a “weight” determined by the projected area of the bin relative to the whole disk (distinct bins are those having a weight greater than 1%).

The benefit of this algorithm, when compared to the other sampling methods (e.g., Cahoy et al., 2010; Horak and Little, 1965) is that it takes advantage of the symmetry in the incidence and emission angles across the disk, and ensures a high fidelity (at thermal and reflected wavelengths) at a low computational cost (Saxena et al., 2021).

## 7. Description and modeling of the field-of-view (FOV)

When collecting and modeling fluxes across a planet/scene, the spatial region where one has to perform this “collection” or integration of fluxes is defined by the user provided field-of-view (FOV). The simplest form would be a circle with a diameter defined by its Full-Half-Width-Maximum (FWHM) [rad], and then the area can be calculated as  $\Omega \text{ [sr]} = \pi(\text{FWHM}/2)^2$ . In reality, the integration region may take many shapes and patterns. For instance, if operating with slit instruments, the FOV is rectangular (slit width x slit extract length) and not circular, or when operating with interferometric data (e.g., ALMA), the FOV is a “Gaussian” ellipsoid with a major and a minor axis. As we deviate from a simple circular FOV, then the orientation of the FOV with respect to the N-S axis of the planet also becomes relevant, and a rotation angle needs to be provided (see Figure 6). Furthermore, let us now consider the case of simulations with a smearing “seeing” effect, then the modelled flux is actually a collection of flux across a broader region, and weighted by a “seeing” kernel.

The field <GENERATOR-BEAM> defines the shape and properties of the FOV in PSG. When a single value is provided, PSG would interpret it as the diameter (FWHM<sub>A</sub>) of a simple “circular” beam (see example in Figure 6, first frame). By providing a second value (optional) defined as FWHM<sub>B</sub>, PSG will assume to have an irregular FOV with a major and a minor axis. While if a third value (optional) is also provided, PSG will identify this value as the rotational angle [°] of the FOV in counter-clockwise direction with respect to the N-S planetary axes (e.g., see Figure 6, second frame). If a fourth number is provided (FWHM<sub>S</sub>), PSG will switch from a step function to a Gaussian affected kernel with an additional seeing term defined by this value. The transfer function for the FOV would then correspond for an ellipsoid to:

$$\gamma(x, y) = \exp \left( -0.5 \left[ \left( \frac{x}{r_A + r_S} \right)^2 + \left( \frac{y}{r_B + r_S} \right)^2 \right] \right) \quad (4)$$

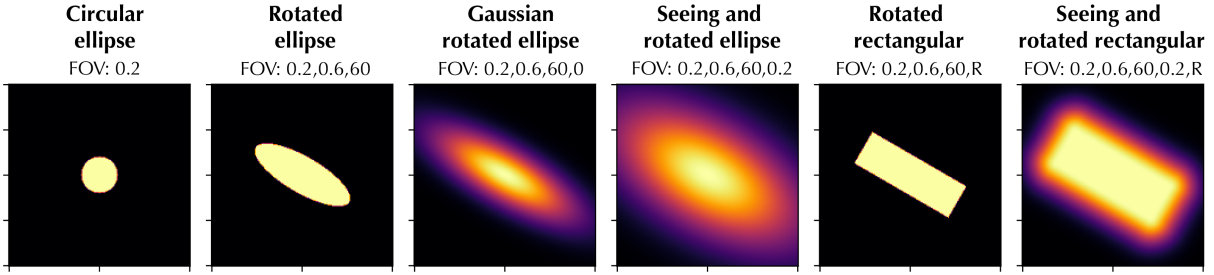
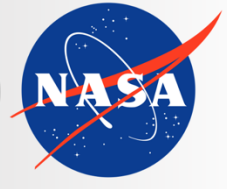


**Figure 6:** The spatial integration region across the planet/scene can take many shapes and patterns, and in PSG the properties of the field-of-view (FOV) are defined by the keyword GENERATOR-BEAM. Up to five parameters ( $FWHM_A$ ,  $FWHM_B$ , Rotation,  $FWHM_S$ , shape) establish the key elements of the response function of the FOV and its orientation with respect to the N-S axis of the planet.

where  $x$  and  $y$  are the distances from the center of the FOV across the major and minor axis respectively,  $r_A$  is sigma across the first axis ( $r_A = FWHM_A/2.355$ , where  $FWHM_A$  is the FWHM across the A-axis and it is the first user provided number),  $r_B$  is the sigma across the second axis defined ( $r_B = FWHM_B/2.355$ ), and  $r_S$  is the seeing sigma ( $r_S = FWHM_S/2.355$ ). The values  $x$  and  $y$  are in the rotated FOV frame of reference as defined by the rotational angle of the FOV (see Figure 6, third frame). A keyword “R” at the end of the field will inform PSG that this is a rectangular FOV, not an ellipsoid (see Figure 6, last two frames). For rectangular FOVs,  $\gamma=1$  is when  $x$  and  $y$  are within  $r_A$  and  $r_B$  axis, and it decays as  $\exp(-0.5 \cdot (r/r_S)^2)$  beyond that, where  $r$  is the distance from the FOV boundaries.

The area of the field of view is then calculated for an ellipsoid field of view as  $\Omega \text{ [sr]} = \pi \cdot FWHM_A \cdot FWHM_B / 4$ , and simply as  $\Omega \text{ [sr]} = FWHM_A \cdot FWHM_B$  for a rectangular field of view. Information about the weighting function across the FOV as shown in Figure 6 is solely used in the “Observatory” geometry to calculate the effective incidence and emissions (see equation 3) and the effective planetary filling factor.



**Planetary Spectrum Generator**  
National Aeronautics and Space Administration

# Chapter 3:

# **Atmospheres, exospheres and comets**

**Villanueva, Faggi, Fauchez and  
PSG team**



## 1. Types of atmospheres

PSG handles two types of atmospheres: hydrostatic equilibrated atmospheres (typical for planets) and exospheres / expanding comas (i.e., typical of comets and small bodies). Atmospheres are considered in hydrostatic equilibrium when gravity controls their vertical structure and in which the escape velocities are smaller than the kinetic atmospheric velocities. For such planetary atmospheres, gravity, molar mass, pressures, and temperatures define the vertical structure, while for exospheres, where gravity does not play a significant role in controlling the structure, they are defined by the molecular outgassing velocity and photochemical/photodissociation decay.

PSG provides the users with atmospheric templates (vertical profiles of temperature and abundances) available for the main planets of the solar system (e.g., Venus, Earth, Mars, Titan, Neptune, Uranus); and it also permits providing detailed user-defined vertical information of molecular abundances and temperatures. General atmospheric and surface parameters are available for the other bodies. For expanding atmospheres, PSG assumes isotropic outflow, constant expanding velocity and a Haser isotropic 2-steps (i.e., parent and daughter species) photodissociation scheme.

PSG provides access to several atmospheric models (e.g., chemical equilibrium, thermal radiative equilibrium, Mars GCM models, cometary heliocentric models), several databases (e.g., Earth NASA/MERRA2) and numerous templates for defining the atmospheric and surface structure and composition. As mentioned, the user can also provide any arbitrary profile of P/T and of molecular abundances by selecting "**File Template**" in the atmosphere section. The format of this file is a text file with all the entries as in the configuration file for the sections ATMOSPHERE and SURFACE. When providing user-generated profiles, the vertical parameters are provided via the ATMOSPHERE-LAYER keywords. The pressures are provided in [bars], temperatures in [K] and abundances in volume mixing ratio - [molecules / molecules] for gases (e.g., water vapor, methane) and [kg / kg] for hazes (e.g., water ice clouds, methane ice). Particle sizes in [m] are provided by adding the keyword '\_size'. The base (molecules or kg) is always wet air (all gases, including water vapor) without hazes. When no vertical profile is provided, the temperature (T) is assumed to be constant across the atmosphere, and the pressure (P) decreases with altitude (z) following the scale-height:  $P = P_{\text{surf}} \exp(-zg/RT)$ , where g is the gravity (defined in the object section) and R is the gas constant (8.3144598 [J / K / mol]).

It is important to note that only molecules included in the ATMOSPHERE-GAS and ATMOSPHERE-AEROS will be included in the simulation (and/or in the retrieval), independent of the species included in the vertical profiles. Specifically, the vertical profile/structure of the atmosphere is provided by the ATMOSPHERE-LAYER keywords, yet the connection between these profiles to the species listed in the ATMOSPHERE-GAS field is done via the "**scaler**" abundance unit in the ATMOSPHERE-UNIT keyword (see details in chapter 1 and explore an example config in PSG for further understand this connection). Note: a scaler of 1 indicates that the values as in the profile will be used, while any other unit (e.g., ppm, ppb) indicates a constant mixing ratio with altitude. If a scaler is selected for a constituent for which no profile exists, PSG will consider a scaler relative to an abundance of 100%. The surface pressure indicates where the atmosphere starts,

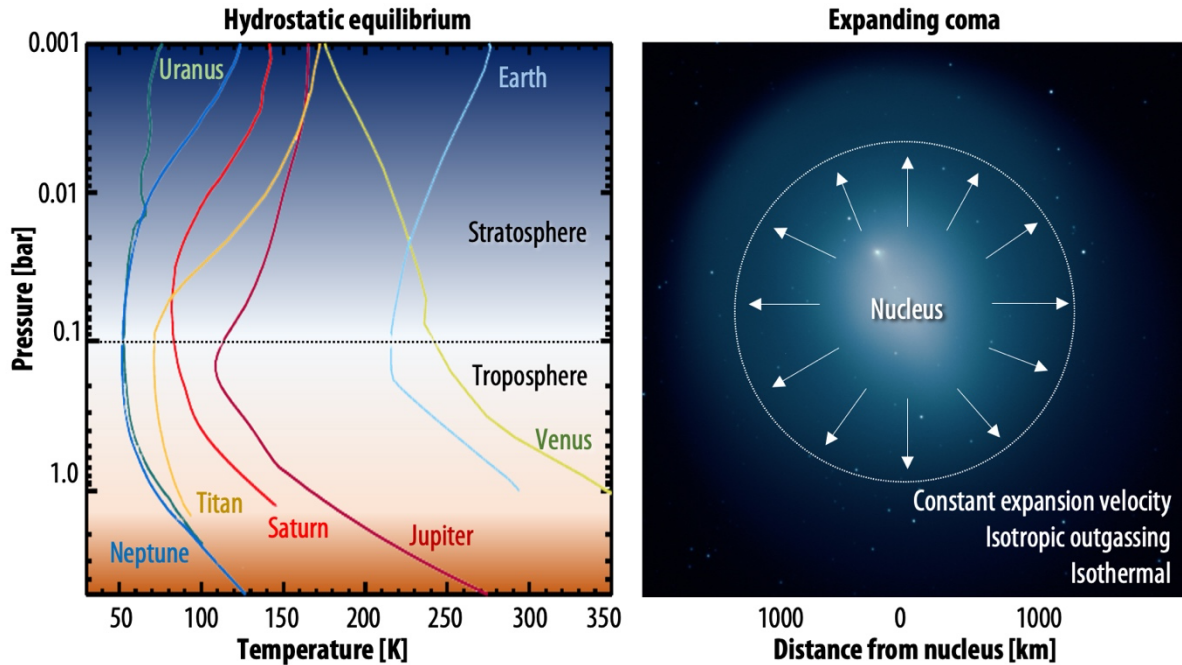


**Figure 1:** PSG handles two types of atmospheres: (1) the hydrostatic equilibrium atmosphere (typical for planets, profiles adapted from (Robinson and Catling, 2014)) and (2) the expanding coma (i.e., exospheres and typical of comets and small bodies). For the main planets, vertical profiles are available, while the user can also load any arbitrary vertical structure. For expanding atmospheres, PSG assumes isotropic outgassing, a constant temperature across the coma, and an outgassing velocity established by the heliocentric distance.

independently of the provided profile pressures, while the provided planetary diameter and gravity also refer to this pressure/surface point.

## 2. Vertical structure of an atmosphere in hydrostatic equilibrium

When considering the ideal gas law, the volume of a gas parcel is dependent on its pressure and temperature. If we consider having several parcels of gas on top of each other, all bounded to a planetary surface by the planet's gravity, the structure and "separation" of these parcels will be defined as a balance between the gravity force (trying to squeeze the parcels) and the intrinsic volumes of the parcels (defined by the parcel  $P/T$ ). The planetary gravity effect on the parcels will depend on the mass of each parcel, with the "local" gravity decaying with distance as  $g = g_{\text{surf}} ((h+R_{\text{surf}})/R_{\text{surf}})^2$ , in which  $h$  is the height of the parcel,  $R_{\text{surf}}$  is the radius of the planet, and  $g_{\text{surf}}$  is the gravity at the surface.

When the gravity is too weak to hold the parcels together, then the planetary atmosphere is no longer in hydrostatic equilibrium, and can be considered an exosphere, or as called in the case of comets, a cometary coma (see section 6). A parameter defining the limit between a planetary atmosphere in hydrostatic equilibrium and an exosphere is the escape velocity, with exospheres having outgassing velocities (identified with the variable "Expansion Velocity" in the PSG/GUI)

greater than the escape velocity. For planetary atmosphere, when non-equilibrated atmospheres are modelled the user can select “Expanding coma” in the atmosphere menu in the “Atmosphere and Surface section”, and PSG will report both the outgassing and the escape velocities of the object of interest. For hydrostatic equilibrium atmosphere simulations if the variable “Altitude” is not provided for the vertical profile in the <ATMOSPHERE-LAYERS-MOLECULES> configuration file keyword (see section 1), PSG will compute the layer altitude (h) by employing the hydrostatic equation as:

$$h_{l+1} = h_l + H \ln \left( \frac{p_l}{p_{l+1}} \right) \quad (1)$$

where l is the layer number,  $p_l$  is the pressure of the bottom layer,  $p_{l+1}$  is the pressure at the top of the layer, and H is the scaleheight. Scaleheight is a key parameter establishing the vertical structure and defines how compact the atmosphere is. It is computed at each layer based on the layer temperature (T [K]), the local molar mass ( $M_{\text{air}}$  [g/mol]) and the local gravity (g [m/s<sup>2</sup>]) as  $H = (kN_A T)/(M_{\text{air}} g)$ , where k is the Boltzmann constant and  $N_A$  is Avogadro’s constant. In PSG, we use a constant molecular weight for the whole column defined by the ATMOSPHERE-WEIGHT keyword, yet the user can operate with varying molecular mass atmospheres by providing the “Altitude” values for each layer.

### 3. Earth atmosphere

For the computation of telluric transmittances and radiances, PSG extracts atmospheric profiles and molecular abundances from the Modern-Era Retrospective Analysis for Research and Applications (MERRA-2) database (Gelaro et al., 2017). MERRA-2 is the latest atmospheric reanalysis of the modern satellite era produced by NASA’s Global Modeling and Assimilation Office, which incorporates information from hundreds of orbiters and ground stations since 1980 and provides a global three-dimensional repository of atmospheric parameters (e.g., temperature, abundance profiles, aerosols). Specifically, PSG works with the M2I3NVASM component, which provides assimilated meteorological fields (pressure, temperature, water vapor, ozone, and water ice clouds) from the surface to ~80 km (72 layers) with a cadence of 180 minutes, and spatial resolution of ~0.5 degrees (576 x 361). The values are further refined temporally and spatially to a resolution of better than 1 km employing the USGS-GTOPO30 topographic maps (Gesch and Larson, 1996) and considering a hydrostatic equilibrated atmosphere within every bin. The MERRA-2 database is constantly being updated, yet it assimilates data with a latency of approximately 2 months. For atmospheric requests before 1980, or newer than present minus 2 months, PSG will extract information for the same season / location / time-of-day but for the nearest year available in the database.

For species not contained in this repository (CO<sub>2</sub>, N<sub>2</sub>O, CO, CH<sub>4</sub>, O<sub>2</sub>, NO, SO<sub>2</sub>, NO<sub>2</sub>, NH<sub>3</sub>, HNO<sub>3</sub>, OH, HF, HCl, HBr, HI, ClO, OCS, H<sub>2</sub>CO, HOCl, N<sub>2</sub>, HCN, CH<sub>3</sub>Cl, H<sub>2</sub>O<sub>2</sub>, C<sub>2</sub>H<sub>2</sub>, C<sub>2</sub>H<sub>6</sub>, PH<sub>3</sub>), PSG will consider standard abundance profiles (Clough et al., 2005). Many of these species have long atmospheric lifetimes (e.g., CO<sub>2</sub>, CH<sub>4</sub>) and are non-condensable (e.g., CO) so they do not show strong geographical and/or temporal variability, so this assumption should be accurate enough in most cases. Yet other species are known to display strong variability (e.g., H<sub>2</sub>CO) and the provided vertical profiles should be considered solely as best-guesses.





## 4. Mars atmosphere

PSG extracts atmospheric information from the Mars Climate Database (MCD, Millour et al., 2015) and GEM General Circulation Model (Daerden et al., 2019). MCD and GEM are comprehensive repository of meteorological fields derived from General Circulation Model (GCM) numerical simulations and validated using available observational data. The MCD database has a natural spatial resolution of  $\sim 5$  degrees ( $64 \times 49$ ) and 30 layers up to  $\sim 90$  km, with 12 local times (2-hours resolution) and 12 seasons. PSG operates with the raw information contained in the NetCDF files of both models, which is later refined spatially and temporally to the specific time and latitude / longitude of the PSG calculation. In a similar procedure as done by Millour et al. (Millour et al., 2015) (and in the same way we resample the MERRA-2 database), the  $64 \times 49$  grid is refined spatially to a much finer scale ( $11520 \times 5760$ ,  $\sim 0.03$  degrees) by employing the MOLA topographic data (Smith et al., 2001). Several climatological states are possible (e.g., dust storm, cold scenario) and also for different levels of EUV radiation, with PSG extracting information only considering the typical climatological state (average dust and EUV conditions). Specifically, PSG extracts vertical profiles of pressure, temperature,  $\text{CO}_2$ ,  $\text{N}_2$ ,  $\text{O}_2$ ,  $\text{CO}$ ,  $\text{H}_2\text{O}$ , dust, dust size, water ice and ice particle size from the MCD database, while the surface albedo information is determined from the MGS/TES database (Smith, 2004).

## 5. Gas giants / Dense and hazy atmospheres

Planets in which their atmospheres are so thick, that the definition of a physical solid “surface” becomes ambiguous (e.g., Jupiter, Saturn, Uranus, Neptune), require a careful and particular parameterization of the radiative transfer. Specifically, the atmospheric layering should be as complete as possible when defining the main species that contribute to the spectroscopic opacities. In giant planets, the main opacity terms that define this optically thick “surface” are hazes (e.g.,  $\text{CH}_4$ ,  $\text{NH}_3$ ,  $\text{NH}_4\text{SH}$ ,  $\text{H}_2\text{S}$ ,  $\text{H}_2\text{O}$  hazes) and the effect of collision-induced-absorption by molecular hydrogen and helium. Beyond that, a plethora of hydrocarbon species (e.g.,  $\text{CH}_4$ ,  $\text{C}_2\text{H}_2$ ,  $\text{C}_2\text{H}_6$ ) and other trace molecules contribute to the overall atmospheric opacities.

Due to this set of numerous opacity terms, these atmospheres are rarely probed at pressures beyond 10 bars, and in PSG we have provided a basic description of the main hazes and species from 10 bars to  $\sim 10$  nbar. For the giants (i.e., Jupiter, Saturn, Uranus and Neptune), the haze profiles are based on (Sánchez-Lavega and Heimpel, 2017) while for Venus, the temperature profile is based on VIRA and the sulfuric acid haze profile is based on (Knollenberg R. et al., 1980). Molecular abundances are only prescribed for a select set of species based on (Ehrenreich et al., 2012; Lellouch et al., 2010; Marten et al., 2005; Moses et al., 2005), and it is of great importance for the user to update and validate the desired abundance / haze profiles when performing a simulation. Information about molecular line-shapes for non-terrestrial environments (e.g.,  $\text{H}_2$ , He,  $\text{CO}_2$  atmospheres) is still limited, yet with the advent of new laboratory measurements (Devi et al., 2017a, 2017b) and new modeling efforts (Gamache and Renaud, 2017; Villanueva et al., 2012b), many more line-lists are constantly added (see chapter 4).

## 6. Cometary atmospheres

A cometary atmosphere is characterized by multiple inter-related radiative processes that lead to a complex outgassing halo typically called “coma” (see Figure 2); in PSG many of these processes are included, such as (1) an expanding exosphere, (2) photodissociation processes for parent and daughter species, (3) extended icy-grains structure, (4) thermal, equilibrated and rotational emissions and (5) emissions computed from non-LTE cascade fluorescence models.

In general, cometary outgassing and molecular abundances in comets are highly variable and relatively difficult to estimate or predict. The main parameter that establishes the intensity of spectroscopic fluxes in a cometary coma is the gas production rate, or activity rate, typically identified as  $Q$  [molecules/s]. The user can provide this value as an input parameter for any molecule, but in some cases the user may not know it, and PSG will estimate the level of outgassing activity in the comet (i.e.,  $Q$ ) from other observed astronomical quantities (e.g., visual magnitude). Typically, cometary activity is driven by the water outgassing at heliocentric distances ( $r_h$ ) within 2 au, while the sublimation of more volatile ices tends to dominate cometary activity beyond 2 au, yet this is extremely dependent on composition and structure.

Within 2 au, activity ( $Q$  [molecules/s]) is mostly dominated by insolation, with outgassing rates following a  $r_h^2$  relationship ( $Q = Q_{au} / R_h^2$ , where  $Q_{au}$  is the activity at  $r_h=1$  au). Outgassing velocities also follow a heliocentric distance dependence, yet much less steep, and in PSG we employ an empirically defined relationship (valid in the collisionless region of the coma, beyond  $\sim 100$  km from the nucleus) to establish the expansion velocities:  $v_{exp}=0.8 \cdot R_h^{-0.5}$  [km/s] (Biver et al., 2002; Delsemme, 1982). In a related fashion and employing a sample of 37 comets observed from 1982 to 2004 (234 points), Jorda et al. (Jorda et al., 2008) determined an empirical relationship between visual magnitude ( $m_v$ ) and gas production rate ( $Q$ ),  $m_v = (30.675 - \log(Q))/0.2453 + 5 \cdot \log(R_g)$ . Cometary visual brightness is mainly defined by dust brightness, and such a relationship intrinsically implies a common gas to dust ratio among comets. Even considering this caveat, such a relationship is of great value when estimating cometary activity, and in PSG we use this to estimate the water production rates from visual magnitudes derived from JPL Horizon, yet the user can edit this estimate as needed.

PSG computes three brightness metrics for cometary coma, which are displayed next to the production rate field: the expected visual magnitude ( $m_v$ ), the infrared Figure-Of-Merit ( $FOM_{IR}$ ), and the radio Figure-Of-Merit ( $FOM_{Radio}$ ). These parameters are calculated based on the heliocentric distance ( $R_h$  [au]), the geocentric distance ( $R_g$ [au]), and the gas production rate ( $Q$  [molecules/s]), employing these equations:  $m_v = (30.675 - \log(Q))/0.2453 + 5 \cdot \log(R_g)$  (Jorda et al., 2008);  $FOM_{IR} = Q \cdot 1E-29 / (R_g \cdot R_h^2)$  (Mumma et al., 2003);  $FOM_{Radio} = Q \cdot 1E-28 / R_g$  (Crovisier, 2007). Molecular abundances relative to water tend to vary substantially between comets (Dello Russo et al., 2016; Lippi et al., 2021; Mumma and Charnley, 2011; Villanueva et al., 2006, 2011a), yet a “typical” set of abundance reference ratios, based on decades of observations and statistical analysis, can be assumed, and in PSG we consider as a-priori:  $H_2O/CO_2/CO/CH_4/NH_3/H_2CO/C_2H_6/HCN/CH_3OH = 100/15/12/1.5/0.5/0.3/0.6/0.4/2.4$ .



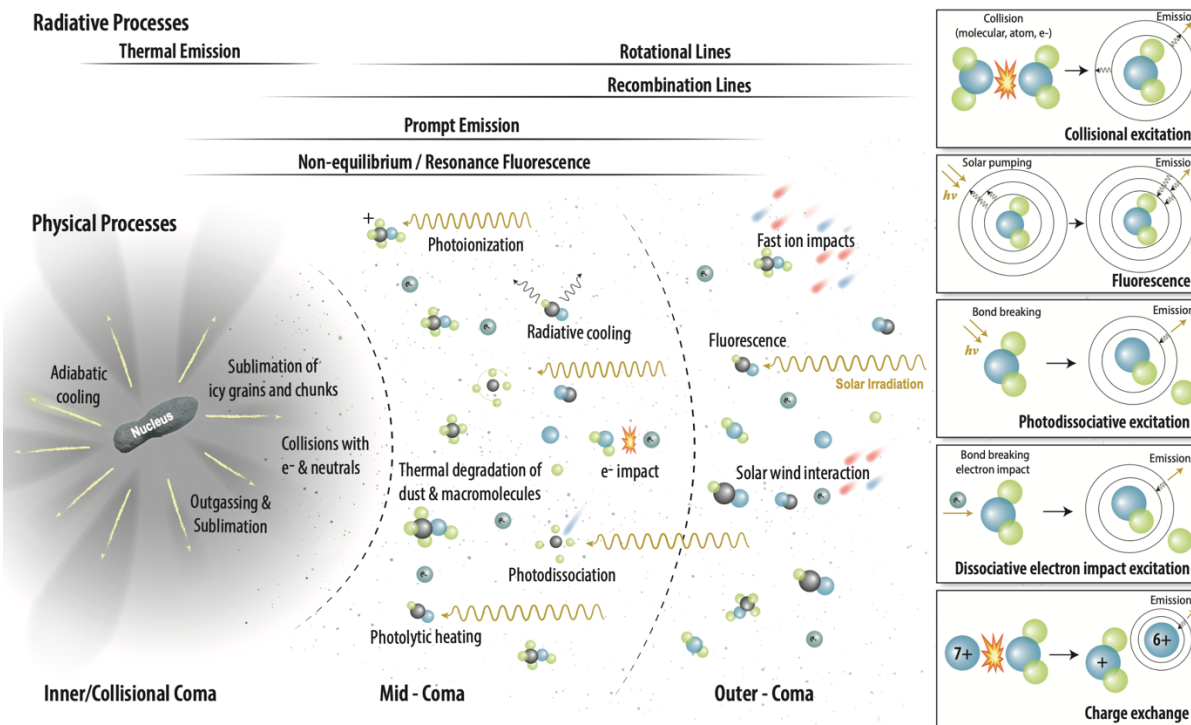


**Figure 2:** Many non-equilibrated and radiative processes take place in the atmospheres of comets, as summarized in our Comets III review (Bodewits et al., 2022). When computing cometary fluxes, PSG take many of these into account, in particular: a) an expanding and outgassed exosphere atmospheric structure, b) photodissociation processes for parent and daughter species, d) extended icy grains emissions, e) thermal, equilibrated and rotational emissions and f) fluorescence emissions via the pre-computed non-LTE cascade models for many species that include billions of lines (more details in chapter 4).

A key aspect in computing cometary fluxes is determining the number of molecules within the FOV. The total number of molecules in a coma ( $N$  [molecules]) can be calculated from the production rate ( $Q$  [molecules/second]) as  $N = Q\tau$ , in where  $\tau$  is the photo-dissociative lifetime of the molecule. In PSG, reference lifetimes  $\tau_0$  can be provided by the user via the ATMOSPHERE-TAU keyword, and these pertain to the lifetimes at 1 heliocentric distance ( $R_h=1$  au). These are scaled to the specific heliocentric distance of the comet as  $\tau = \tau_0 R_h^2$ . PSG will provide recommended values based on (Huebner et al., 1992), which the user can modify at their discretion.

To determine the actual number of molecules encompassed by the FOV ( $N_{\text{FOV}}$ ), one would need a photodissociation model and also detailed information about the shape and location of the FOV with respect to the nucleus of the comet. A metric to quantify how many of the total molecules in the coma are encompassed by the beam is by computing the cometary “filling factor” or usually called  $f(x)$ , in which 1.0 would mean all total number of molecules are within the FOV,  $N_{\text{FOV}} = N f(x)$ . There are methods for calculating  $f(x)$  for a cylindrical beam centered in a photo-dissociative atmosphere (e.g., analytical, vectorial, Monte Carlo). In PSG, we adapt the analytical methods as presented in Yamamoto (1981), which considers a Haser isotropic expansion coma under a constant expansion velocity and a multi-step photodissociate decay. Using this method, the cometary filling

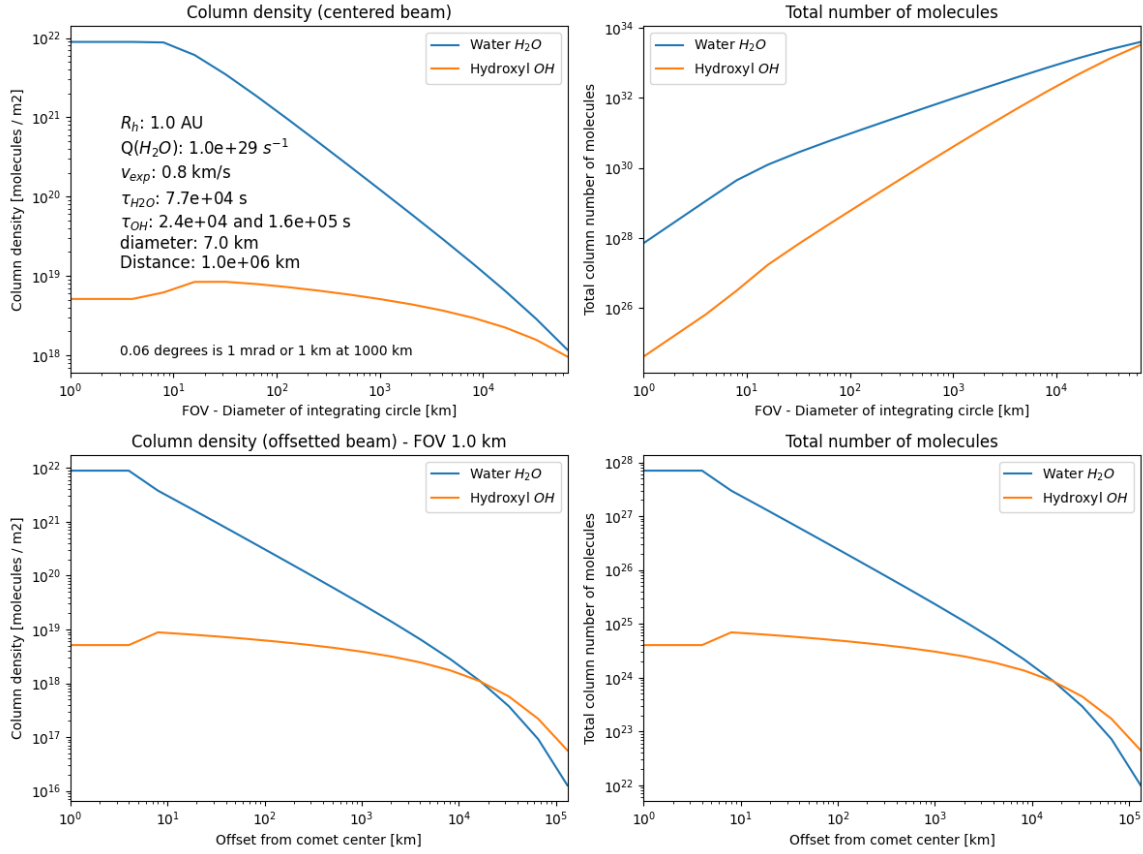


**Figure 3:** Example of the cometary model for integrating column densities across the line of sight for a centered and offset simulations. These are computed based on Bessel functions to account for photodissociation effects and employ several approximations for non-centered and embedded measurements to included nucleus occultation.

factor for parent species  $f_1(x)$  and daughter fragments  $f_2(x)$  contained in a cylindrical centered beam can be calculated as:

$$f_1(x) = xg(x) \quad (2)$$

$$f_2(x) = \frac{\mu_2}{1 - \mu_2} x[g(\mu_2 x) - g(x)] \quad (3)$$

$$g(x) = \frac{1}{x} - K_1(x) + \int_x^\infty K_0(y) dy \quad (4)$$

$$x = \frac{FOV}{2\tau_p v_{exp}} \quad (5)$$

$$\mu_2 = \tau_p / \tau_d \quad (6)$$

where  $\tau_p$  is the parent lifetime [s],  $\tau_d$  is the daughter lifetime [s],  $v_{exp}$  is the expansion velocity [km/s], FOV is the diameter of the field of the view at the comet [km],  $K_0(x)$  is the modified Bessel function



of the second kind and of zeroth order, and  $K_1(x)$  of the first order. Using this core math, filling factors for square pixels, offset beams (via concentric rings) and embedded probes (via  $1/r$  scaling) can be computed. An example of our implementation of these models into PSG is presented in Figure 3 for a parent molecule ( $H_2O$ ) and a daughter fragment ( $OH$  as produced from  $H_2O$ ). More details about the models and the python code for computing number of molecules in a cometary atmosphere are available online at PSG's GitHub site (<https://github.com/nasapsg/isocoma>). These models were initially developed in support of the ESA/Comet Interceptor mission.

## 7. Exoplanet atmospheres

The temperature, composition and structure of exoplanets vary substantially, from scorching hot giants to small rocky planets. In an attempt to provide an accurate description of this diversity, in PSG we organize the exoplanets by mass ( $M$  in Earth's mass [ $M_\oplus$ ]) and density ( $\rho$  [ $g/cm^3$ ]) into four categories (in a comparable fashion to the Kepler categorization): Earth-like planets ( $M < 2$  and  $\rho > 4$ ), super-Earths ( $2 < M < 10$  and  $\rho > 4$ , bigger than Earth but smaller than Neptune), Neptune-like ( $10 < M < 50$ , small gas giants, comparable to Neptune and Uranus), and gas-giants ( $M > 50$ , Saturn-sized and larger). Currently PSG simply assumes a terrestrial structure and composition (MERRA-2) for Earth-like planets, and a Venusian structure and composition (Ehrenreich et al., 2006) for super-Earth like planets. For gas giants, PSG employs the non-grey thermal model by Parmentier & Guillot (2014) to determine the vertical temperature profile of the planet. This analytical model is fast and matches full numerical simulations within 10% over a wide range of effective temperature, internal temperature and gravity and properly predicts the depth of the radiative/convective boundary. The equilibrium temperatures of the atmospheres are assumed to be strongly related to their composition and to the acting greenhouse gases. The model makes reasonable assumptions about composition based on gravity, distance to host star and density, and using two different opacity bands in the thermal frequency range, establishes the dual role of thermal non-grey opacities in defining the temperature profile. Opacities dominated by narrow features enable the upper atmosphere to cool down significantly compared to a grey atmosphere whereas opacities dominated by broad features lead both to a significant cooling of the upper atmosphere and a significant heating of the deep atmosphere (Parmentier and Guillot, 2014). Once the temperature profile of the exoplanet is defined, PSG employs the chemical equilibrium equations-of-state (EOS) derived by Kempton et al. (Kempton et al., 2017) for a wide range of metallicities and primordial states. This implementation provides a-priori vertical profiles for dozens of species:  $H_2O$ ,  $CO_2$ ,  $O_3$ ,  $N_2O$ ,  $CO$ ,  $CH_4$ ,  $O_2$ ,  $NO$ ,  $SO_2$ ,  $NO_2$ ,  $NH_3$ ,  $HNO_3$ ,  $OH$ ,  $HF$ ,  $HCl$ ,  $HBr$ ,  $HI$ ,  $ClO$ ,  $OCS$ ,  $H_2CO$ ,  $HOCl$ ,  $N_2$ ,  $HCN$ ,  $CH_3Cl$ ,  $H_2O_2$ ,  $C_2H_2$ ,  $C_2H_6$  and  $PH_3$ .

## 8. Three-dimensional characterization (GCM) of the atmosphere and surface

Realistic modeling of full disk and transit planetary fluxes would require capturing the heterogeneous properties of the atmosphere and the surface across the observable disk and the terminator. PSG allows to ingest General Circulation Model (GCM) 3D data of temperature, pressure, and abundance profiles, together with surface properties, such as albedo, via the GlobES app (<https://psg.gsfc.nasa.gov/apps/globes.php>). The user can upload atmospheric data from any GCM, after converting the 3D fields (typically in netCDF format) into a PSG GCM binary file. The 3D

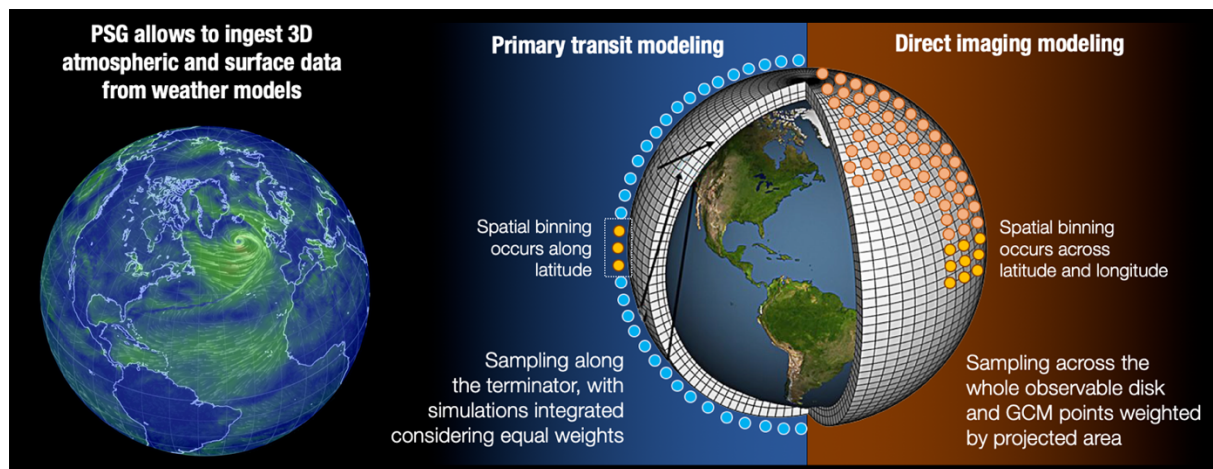


**Figure 4:** The ingestion of 3D atmospheric data is possible in PSG via the GlobES app, and this allows to accurately capture the heterogeneity of the atmospheric and the surface across the observable disk and terminator. For transit observations, the GlobES app performs radiative transfer simulations across the terminator and integrates the different spectra employing equal weights. For direct imaging and secondary eclipse simulations, the algorithm performs radiative transfer simulations across the whole observable disk, and the individual spectra are integrated considering the projected area of each bin.

and temporal atmospheric data are then aggregated and mapped into a 2D projected observationally grid that is fed to the radiative transfer modules. PSG currently provides templates and conversion scripts for several GCM models, including the ROCKE-3D terrestrial model, the Laboratoire de Météorologie Dynamique (LMD) model, the exoplanet Community Atmosphere Model (ExoCAM) model, and the Unified Model (UM). In order to ingest 3D data, these are the steps to follow:

- 1) Run the GCM model in your personal machine, and store the resulting 3D fields and parameters into a GCM formatted file (typically a netCDF file).
- 2) By employing a script (see scripts in PSG's GitHub) convert the GCM netCDF file into a PSG GCM binary file. Several example conversion scripts are available at the GlobES application site, permitting to convert netCDF output files from ROCKE-3D, LMD and ExoCAM. This script should be run at the user's local machine.
- 3) In the GlobES site, upload the PSG GCM file by clicking on "Load GCM data". If the upload process was successful, the site should display graphically the GCM outputs for the different variables.
- 4) Select the observing geometry (e.g., transit, direct imaging) directly on the GlobES site, or at the "Target and Geometry" section of PSG, and verify and update the molecules and aerosols to include in the simulation by visiting the "Atmosphere and Surface" section of PSG.



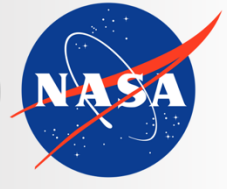
5) In the GlobES site, click on "Generate 3D spectra". For each position on the planet, the algorithm will update the atmospheric profiles, surface properties and geometry parameters and will run the radiative transfer. These results will be integrated employing the appropriate weights.

To run the GlobES module in script mode via the API, please check the python scripts available in GitHub.

**Binning:** to speed up the calculations one can horizontally bin/aggregate GCM data to have less PSG radiative-transfer calculations. Higher binning means more aggregation and less PSG radiative-transfer calculations. High "binning" numbers (above 50) should only be used when testing. A "binning" factor of 3 is typically recommended, leading to  $3 \times 3$  (lat x lon = 9) binning, and a speed up of 9 times while sacrificing a little accuracy.







**Planetary Spectrum Generator**  
National Aeronautics and Space Administration

# Chapter 4:

# **Radiative transfer modeling**

**Villanueva, Kofman, Liuzzi, Faggi and  
PSG team**

## 1. Radiative transfer modeling in PSG

In a classical radiative transfer calculation, the photons are being tracked along their path towards the observer. Two main processes occur during this transport, the photons are being absorbed by the prevailing opacity of the medium, and new photons are being generated from the local ambient (see Figure 1). Each wavelength can be treated independently if fluorescence, Raman and other non-LTE (non-Local Thermodynamic Equilibrium, see section 4) effects are ignored. In many cases, the absorbed photons will not be re-emitted and a linear integration of absorptions and thermal emissions along the path can be simply assumed. This is the case for most typical atomic/molecular absorptions, yet when Rayleigh and scattering aerosols are present, one may need to account for the multiple scattering ( $N_{MAX} > 0$ ) of the photons, requiring a specialized treatment (see chapter 5).

Even when scattering elements are active in an atmosphere, if the optical depths are small ( $\tau \ll 1$ ), one can solve the radiative transfer problem via the single-scattering approximation. This is the case because the photon has a high probability of exiting the aerosol before getting scattered a second time. In a highly absorbing environment (small scattering albedo,  $w \ll 1$ ) single scattering is also common since a photon is more likely to get absorbed than to get scattered a second time. In PSG when scattering is disabled ( $N_{MAX} = 0$ ), we employ a combination of the single scattering approximation for diffuse solar light, the Schwarzschild equation for the thermal component and an approximated multiple-scattering term for the reflected diffuse radiances. Such method does not require solving/inverting any matrix, it is computationally fast, and generally accurate for isotropic and weakly scattering regimes. In general, the equation of radiative transfer can be written as (Liou, 2002):

$$\mu \frac{dI(\tau, \mu, \phi)}{d\tau} = I(\tau, \mu, \phi) - J(\tau, \mu, \phi) \quad (1)$$

where  $I(\tau, \mu, \phi)$  is the radiance (or intensity) at optical depth  $\tau$  (proxy to altitude),  $\mu$  is the cosine of zenith angle ( $\alpha$ ) and  $\phi$  the azimuth angle. In a plane parallel atmosphere,  $\mu = \cos(\alpha)$ , with  $1/\mu$  is normally referred as the airmass scaler. In PSG, we employ a raytracing algorithm to compute  $\mu$  across the path of light in a refractive and spherical planet/atmosphere (see section 2). Calculation of the source function is at the core of the radiative transfer, and it can be expressed as:

$$J(\tau, \mu, \phi) = \frac{\omega}{4\pi} \int_0^{2\pi} \int_{-1}^{-1} I(\tau, \mu', \phi') P(\mu, \phi, \mu', \phi') d\mu' d\phi' + \frac{w}{4\pi} F_* P(\mu, \phi, -\mu_0, \phi_0) e^{-\frac{\tau}{\mu_0}} + (1 - \omega) S(\tau) \quad (2)$$

where the first term is the multiple-scattering term (solved explicitly in chapter 5 with  $N_{MAX} > 0$ ), the second term is the single-scattering contribution to the solar diffuse radiance, and last term is the thermal layer source. In LTE,  $S(\tau) = B[T(\tau)]$ , where  $B$  is the Planck function, while in PSG we allow for non-LTE sources via this term (see section 4). Regarding the other coefficients,  $w$  is the scattering albedo,  $F_*$  is the solar flux at TOA (Top of Atmosphere),  $P(\mu, \phi, \mu', \phi')$  is the phase function with incidence  $\mu', \phi'$  and emission at  $\mu, \phi$ , and  $\mu_0$  is the solar Zenith angle (negative in the phase term

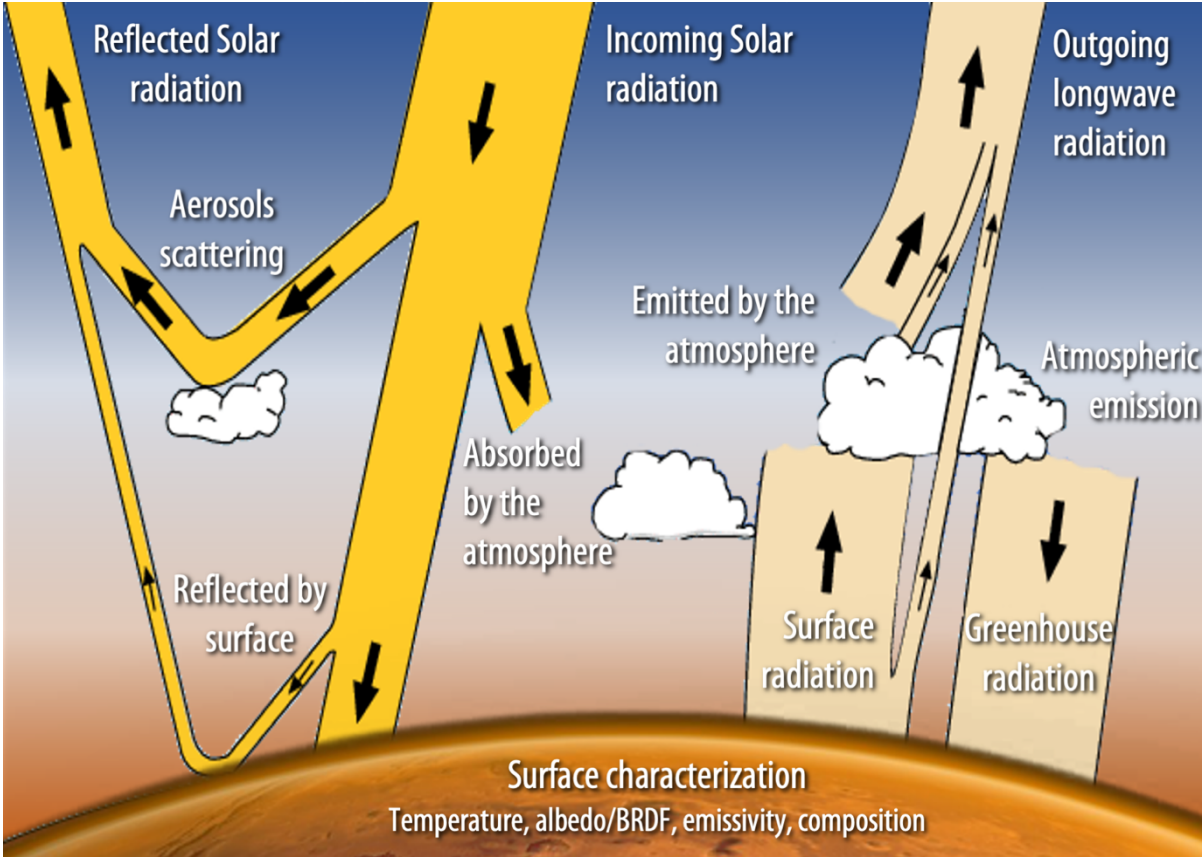


**Figure 1:** The diagram shows the different processes affecting radiation in a planetary atmosphere. Two main branches can be defined: **(left)** the photons originating from the Sun and their atmospheric scattering and reflection on the surface, **(right)** the thermal radiation. The surface plays an important role in reflecting the downward fluxes towards TOA, while multiple scattering of photons can mean solving for this system quite complex. In PSG, one can perform rapid calculations by assuming single isotropic scattering (NMAX=0), or by employing a discrete ordinate method to solve the systems of equations (NMAX>0, chapter 5).

since it defines incoming fluxes, while positive  $\mu$  indicates outgoing fluxes). Integrating equation (1) across the path of radiation ( $\tau$  dimension), one then obtains:

$$I(\tau, \mu, \phi) = I(\tau_0, \mu, \phi) e^{-\frac{\tau - \tau_0}{\mu}} + \int_{\tau_0}^{\tau} J(\tau', \mu, \phi) e^{-\frac{\tau - \tau'}{\mu}} \frac{d\tau'}{\mu} \quad (3)$$

where the first term is the radiance at the bottom of the layer attenuated by the opacity within the layer, and the second term is the integral of the radiance collected across the layer. In the case of LTE [ $S=B(T)$ ] and no scattering ( $w=0$ ), equation 3 gets reduced to the Schwarzschild equation. The integration of equation 3 is done numerically in PSG following the path of the radiation, yet the challenge is in the calculation of the source function  $J(\tau, \mu, \phi)$ .

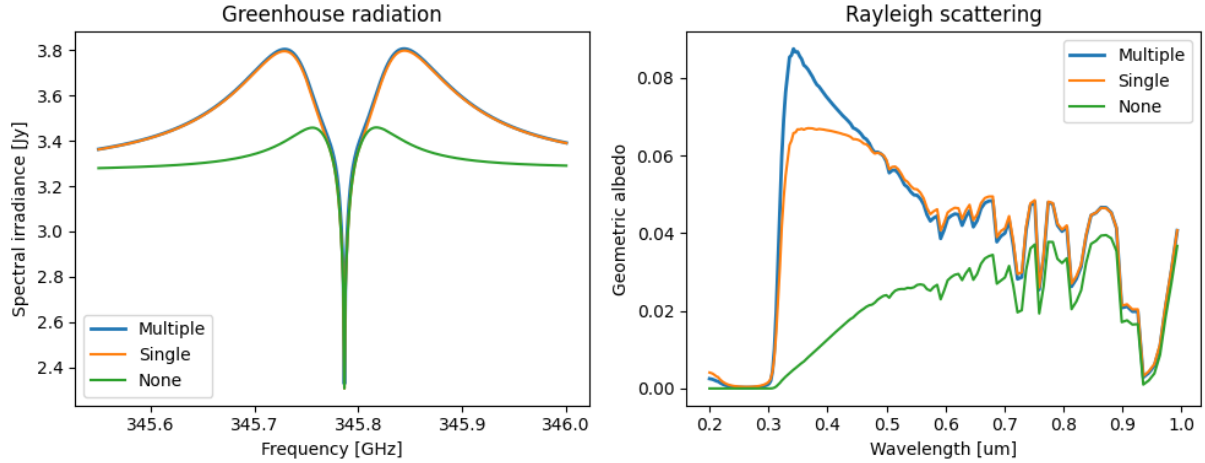


**Figure 2:** Effects of including multiple/single or no scattering in the calculations. The multiple scattering simulations were performed with NMAX=1 employing PSGDORT (a PSG adaption of DISORT, see chapter 5). **(Left)** Simulation of the CO (J=3-2) line on Mars, in which one can observe that the “scattering” effect is even relevant when operating at thermal wavelengths in a non-scattering atmosphere ( $w \approx 0$ ). The “greenhouse radiation” accounted in equation 7 has a substantial effect on the planetary signature, while the simplified methods described in section 1 reproduce well a full scattering calculation. **(Right)** In a Rayleigh atmosphere, the single scattering assumption is relatively accurate in regions of low scattering opacity, while including only extinction leads to substantial error.

Let us now consider the case of an observer at the surface [ $\tau_s = \max(\tau)$ ] looking up with a cosine of the zenith angle  $\mu$  and an azimuth angle  $\phi$ . If we neglect multiple-scattering term and assume single scattering, then the diffuse radiance can be calculated as:

$$I^\downarrow(\tau_s, \mu, \phi) = \int_0^{\tau_s} J(\tau', -\mu, \phi) e^{-\frac{\tau_s - \tau'}{\mu}} \frac{d\tau'}{\mu} \quad (4)$$

$$J(\tau, \mu, \phi) = \frac{w}{4\pi} F_* P(\mu, \phi, -\mu_0, \phi_0) e^{-\frac{\tau}{\mu_0}} + (1 - \omega) S(\tau) \quad (5)$$

In the approximation, we can use many Legendre terms in describing  $P$  (see eq. 8 in Chapter 5) with a small penalty in computation cost. As presented in Figure 1, the first term of  $J$  would be “aerosols scattering” and the second “atmospheric emission / emitted by the atmosphere”. Note the sign of the zenith angle in the source function  $J$  of equation 4, indicating downward flux so the phase function is  $P(-\mu, \phi, -\mu_0, \phi_0)$ . On a similar approach, we can now compute the radiance emanating at TOA as:

$$I^\uparrow(0, \mu, \phi) = I_s^\uparrow(\mu, \phi) e^{-\frac{\tau_s}{\mu}} + \int_0^{\tau_s} J(\tau', \mu, \phi) e^{-\frac{\tau'}{\mu}} \frac{d\tau'}{\mu} \quad (6)$$

where  $I_s(\mu, \phi)$  is the surface radiance towards the observer. For a black surface (bi-directional distribution function [BRDF]  $r=0$ , see chapter 6), the emanating surface radiance is simply  $I_s =$



$\varepsilon(\mu, \phi)B(T_s)$ , where  $\varepsilon$  is the surface emissivity towards the observer and  $T_s$  is the surface temperature. The issue is that the surface is also reflecting the radiance arriving from all possible  $\mu, \phi$  directions, and consequently one would need to solve for multiple scattering across  $\mu, \phi$ . If we now consider double Gaussian quadrature ( $\mu_q = 0.5$ ) as a first approximation for the downward direction, the total surface radiance including reflected scattered light is:

$$I_s^\uparrow(\mu, \phi) = \varepsilon(\mu, \phi)B(T_s) + r(\mu, \phi, \mu_0, \phi_0) \left[ \frac{\mu_0}{4} F_* + I^\downarrow(\tau_s, \mu_q, \phi) \right] \quad (7)$$

The first term of equation (7) is the thermal surface emission (labelled “surface radiation” in Figure (1), the following term is the reflected direct solar light (“reflected by surface”) and the last term is the reflected diffuse radiation (“greenhouse radiation”). For simplicity the BRDF for the solar flux is assumed to be the same as for the diffuse downward flux in equation (7), which is only valid for Lambert surfaces.

Calculating the radiative transfer solution under these assumptions is therefore straightforward with two numerical integrations (TOA to surface [eq. 4], and surface to observer [eq 6]). This analytical description for NMAX=0 should be only employed when operating with highly isotropic scatterers (e.g., thermal, Rayleigh), and having an optically thin medium (e.g., thin cirrus or dust layers) or a highly absorbing / non-scattering environment (see Figure 2). The user is recommended to use NMAX>0 for other cases (see chapter 5), and PSG would provide recommendations / warnings accordingly.

## 2. Raytracing in a spherical and refractive atmosphere

The definition of the direction of incidence and emission plays an important role in the calculation of the radiant intensities. As summarized in the equations of the previous section, all terms include a direction quantifier (e.g.,  $\mu, \phi$ ), which can be challenging to establish when the observed scene includes many incidence / emission angles, as when we observe a planet from afar. In PSG, the angles are computed by the geometry module, which are then fed to the radiative transfer module (see details in chapter 2). Beyond those general geometrical considerations, the path of the radiation across a spherical and refractive atmosphere is not a straight line but follows a complex curved path. On the other hand, in a plane parallel atmosphere, the incidence and emission angles across all layers are practically considered constant and simply defined as  $\mu = \cos\alpha$ ,  $\mu_0 = \cos\beta$ . On such simplified case, the amount of gas interacting across all the layers can be simply scaled to the zenith value by  $1/\mu$ , which is normally defined as the observational “airmass”. Yet in a spherical refractive atmosphere, each layer would have a distinct set of “entrance” and “exit” angles, and the amount of gas crisscrossed along the layer would not be a straight line but a curved integral.

Chapman functions (e.g., Dahlback and Stamnes, 1991) are analytical functions describing the path lengths at each layer for a spherical atmosphere, yet these solutions do not include or can model the effects of refraction. One can derive approximated curvature effects by refraction for certain incidence angles (e.g., tangential) when assuming isothermal and simple vertical profiles, yet these approximations can be quite inaccurate when modeling realistic atmospheres, since the temperatures

(and thus refractive properties) can change greatly with altitude. Ultimately, the only way to properly model and capture refraction in a spherical inhomogeneous atmosphere is via a numerical raytracing algorithm. As such in PSG, we follow the path of light from the observer all the way through the atmosphere to the surface (or TOA), and we correct the incidence angles at each layer interface by the refractive properties of the layers. The correction also captures the curved nature of the atmosphere, and each layer is divided into 10 sub-layers, permitting a finer and more accurate description of refraction/sphericity within the layers. The sub-layering method is particularly relevant when performing raytracing in limb/occultation/transit geometries.

The refraction coefficient in a medium depends on the local density, the composition, and the wavelength of the radiation. In PSG, the refractive coefficient at each layer ( $\eta$ ) is determined based on the molar mass of the atmosphere (a proxy to composition), the layer temperature/pressure (density) and the wavelength  $\lambda$  as:

$$\eta = 1 + \frac{288.15k}{1.01325} \frac{P[bar]}{T[K]} d\eta_0(\lambda) \quad (8)$$

where  $k$  is the Boltzmann constant ( $1.38064852e-23$  [m<sup>2</sup>kg s<sup>-2</sup>K<sup>-1</sup>]) and  $d\eta_0$  is the refractive coefficient minus 1 ( $d\eta_0 = \eta_0 - 1$ ) at 288.15 [K] and 1 [atm]. We employ constants and equations as tabulated in <https://refractiveindex.info> to scale  $d\eta_0$  to the corresponding simulation wavelengths. These equations are only considered for wavelengths greater than 0.15  $\mu\text{m}$  - the  $d\eta_0$  values are maximized at 0.15  $\mu\text{m}$  for shorter wavelengths.

For H<sub>2</sub> rich atmospheres:

$$d\eta_0^{H_2} = \frac{0.148956}{180.7 - \lambda^{-2}} + \frac{0.0049037}{92 - \lambda^{-2}} \quad (9)$$

For He rich atmospheres:

$$d\eta_0^{He} = \frac{0.1470091}{423.98 - \lambda^{-2}} \quad (10)$$

For CO<sub>2</sub> rich atmospheres:

$$d\eta_0^{CO_2} = \frac{6.991 \cdot 10^{-2}}{166.175 - \lambda^{-2}} + \frac{1.4472 \cdot 10^{-3}}{79.609 - \lambda^{-2}} + \frac{6.42941 \cdot 10^{-5}}{56.3064 - \lambda^{-2}} + \frac{5.21306 \cdot 10^{-5}}{46.0196 - \lambda^{-2}} \quad (11)$$

For air (N<sub>2</sub>/O<sub>2</sub>) rich atmospheres:

$$d\eta_0^{air} = 8.06051 \cdot 10^{-5} + \frac{2.48099 \cdot 10^{-2}}{132.274 - \lambda^{-2}} + \frac{1.74557 \cdot 10^{-4}}{39.32957 - \lambda^{-2}} \quad (12)$$



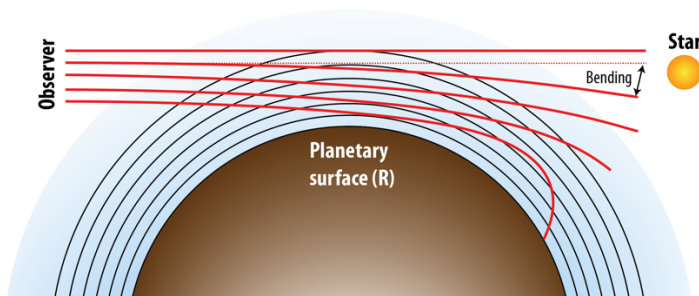


**Figure 3:** The ray-length and angles across a spherical atmosphere are different for every layer, while refraction “bends” the light across the path. The bending introduced for every ray defines if the observed radiation relates to the surface, to TOA or to the background star (e.g., transit).

At the interface between each sub-layer, the angles across the ray-path are corrected following Snell’s law,  $\sin\alpha_1 = (\eta_0/\eta_1)\sin\alpha_0$ , while the amount of gas integrated across the sub-layer in a curved path is computed numerically following Simpson’s 1/3 rule integration.

The raytracing algorithm starts at the location of the observer and follows the path of radiation across the atmosphere (see Figure 3). For instance, if the defined geometry is an occultation/limb at impact height  $H$  for a planet with radius  $R$ , then the starting path angle at  $H_{\text{TOA}}$  is computed as  $\sin\alpha_{\text{TOA}} = [(H+R)/(H_{\text{TOA}}+R)]\sin\alpha_H$ . For exoplanet transit observations, one needs to compute the raytracing for every layer, and therefore the raytracing algorithm is repeated for every layer. The algorithm also checks that the path does not curve beyond the size of the star and enters/exits the atmosphere (i.e., it does not crash on the planet surface), which would imply that no stellar light arrives to the observer for that layer.

### 3. Atmospheric opacities

As discussed in the first section, opacities are a critical component in any radiative transfer calculation. Molecules and atoms absorb light at very specific wavelengths, with the spectral lines shape of the absorption defined by the local temperature (Doppler Gaussian broadening), the ambient pressure (Collisional Lorentzian broadening) and the prevailing kinematic dispersions. One approach is to perform a line-by-line, layer-by-layer treatment, in which every line shape is modelled for every layer for all the lines in the spectral interval of investigation. Generally, the width of a line is normally quite narrow ( $<25 \text{ cm}^{-1}$ ), requiring therefore very high-resolutions ( $<0.001 \text{ cm}^{-1}$  in the near-IR) to properly model its line-shapes. Just to capture the complexity of the problem, let us consider a simulation in the  $0.2$  to  $1 \text{ }\mu\text{m}$  ( $50,000$  to  $10,000 \text{ cm}^{-1}$ ) spectral range at a resolution of  $0.001 \text{ cm}^{-1}$ . Some line-lists could contain billions of transitions on such range, so 1 billion lines and 100 layers for that range would require  $(50,000-10,000)/0.001 \times 1 \text{ billion} \times 100 = 4 \times 10^{18}$  line-shape calculations, an unachievable and impossible task. As such, several algorithms (e.g., multi grid line-shape modeling) and analytical/numerical methods (e.g., correlated-k analysis) exist, permitting to accurately calculate atmospheric opacities in practical amounts of times. In this section, we describe the methods and techniques integrated into PSG for the calculation of molecular and atomic opacities. PSG will automatically switch between the different methods and internally synthesize at the needed spectral resolutions depending on the selected spectral database and the availability of pre-computed correlate-k tables.

### 3.1 Line-by-line modeling

Line-by-line calculations are required for all calculations with resolving powers greater than 5000 ( $\lambda/\delta\lambda > 5000$ ), or when the user selects databases that PSG does not have pre-computed correlated-k tables (e.g., JPL-MolSpec, CDMS, Kurucz, GEISA). PSG will perform these calculations using an internal grid with the fine resolution needed to properly capture the shape of the lines. As such, an apparently simple calculation could mean a large internal calculation, yet PSG will take care of internally expanding / binning the spectra to ensure accurate modeling of the line-shapes. At the core of any line-by-line calculation are line-lists that tabulate the line parameters, which include: a) the line center wavelength/frequency [ $\nu_0$ ], b) the line intensity [ $S(T_{ref})$ ], c) the transition lower state energy [ $E$ ], and d) the line-shape parameters [ $w_{C0}$ ,  $ew_p$ ,  $dv_p$ ,  $ev_p$ ] for the different collision regimes (e.g., air, CO<sub>2</sub>, H<sub>2</sub>, He atmospheres). Line lists like JPL-MolSpec or CDMS do not provide line-shapes information, so the user needs to provide this information, while other line-lists only provide line-shape parameters for certain collisional regimes (e.g., air for GEISA) and would therefore be non-applicable to other environments (e.g., a CO<sub>2</sub> atmosphere). HITRAN and GEISA tabulate line intensities  $S(T_{ref})$  at  $T_{ref}=296$  K, while JPL-MolSpec and CDMS at  $T_{ref}=300$  K. These can be scaled for every layer considering the effective Curtis-Godson ray-trace temperature ( $T$ ) at the layer as:

$$S(T) = S(T_{ref}) \frac{Q(T_{ref})}{Q(T)} \frac{\exp(-hcE/kT)}{\exp(-hcE/kT_{ref})} \frac{1 - \exp(-hcv/kT)}{1 - \exp(-hcv/kT_{ref})} \quad (13)$$

where  $Q(T)$  is the partition function at temperature  $T$  (PSG contains tables for all isotopologues from 1 to 3000K),  $E$  is the lower state energy of the transition and  $\nu$  is the frequency of the transition. The Kurucz atomic database reports intensities “log  $gf$ ”, a representation of the spontaneous Einstein emission coefficient  $A_{ul}$ . Converting from “log  $gf$ ” to  $S(T_{ref})$  is done following:

$$A_{ul} = \frac{10^{\log gf}}{1.499 \cdot 10^{-14} g_u \lambda [\text{nm}]^2} \quad (14)$$

$$S(T_{ref}) = A_{ul} \frac{10^{\log hf} 10^{\log iso}}{8 \cdot \pi c \cdot 100 \cdot Q(T_{ref}) \nu^2} \left[ g_u \exp\left(-\frac{hcE}{kT_{ref}}\right) - \exp\left(-\frac{hc(E + \nu)}{kT_{ref}}\right) \right] \quad (15)$$

where “log  $hf$ ” is the hyperfine component log fractional strength, “log  $iso$ ” is the log isotopic abundance fraction and  $g_u$  the upper-state statistical weight.

The anatomy of a line-shape can be divided into three regions with two transition regions (see Figures 4 and 5): 1) a Doppler Gaussian core, 2) extended Lorentz wings, and 3) far quasi-static and exponential wings. The first two components are described via the Voigt equation, which is a convolution of a Gaussian function and a Lorentz function. There is no closed form analytical form of the Voigt equation, yet several numerical algorithms exist that achieve great accuracy. In PSG, we employ the Fadeeva function as originally implemented by (Humlíček, 1982) with the improvements suggested by (Wells, 1999). The extended wings (beyond 25 cm<sup>-1</sup> from the line



Water (H <sub>2</sub> O) ID:1								
ISO	Self	Air		CO <sub>2</sub>		H <sub>2</sub>		He
1	0.3445	0.0683	0.5826	0.0880	0.6707			
2	0.3535	0.0698	0.5971	0.1005	0.6784			
3	0.3582	0.0708	0.6054	0.1060	0.7016			
4	0.3779	0.0713	0.7783	0.0799	0.7437			
5	0.3847	0.0750	0.7824	0.0793	0.7687			
6	0.3887	0.0764	0.7840	0.0791	0.7793			
7	0.3929	0.0792	0.6200	0.1328	0.5912			
Ozone (O <sub>3</sub> ) ID:3								
1	0.0905	0.0732	0.7703					
2	0.0937	0.0751	0.7699					
3	0.0911	0.0736	0.7763					
4	0.0893	0.0732	0.7847					
5	0.0894	0.0732	0.7858					
Carbon Monoxide (CO) ID:5								
1	0.0545	0.0511	0.7065	0.0614	0.6609	0.0686	0.5811	0.0461 0.5388
2	0.0554	0.0516	0.7046	0.0621	0.6614	0.0687	0.5840	0.0462 0.5394
3	0.0553	0.0515	0.7050	0.0620	0.6614	0.0687	0.5835	0.0462 0.5392
4	0.0555	0.0517	0.7028	0.0621	0.6620	0.0687	0.5848	0.0462 0.5396
5	0.0547	0.0510	0.7010	0.0611	0.6598	0.0686	0.5795	0.0461 0.5387
6	0.0552	0.0514	0.7021	0.0619	0.6611	0.0687	0.5829	0.0462 0.5392
Oxygen (O <sub>2</sub> ) ID:7								
1	0.2109	0.0401	0.1365					
2	0.2166	0.0404	0.2460					
3	0.0379	0.0382	0.7228					
Sulfur Dioxide (SO <sub>2</sub> ) ID:9								
1	0.3925	0.0969	0.7500	0.1536	0.5879	0.1442	0.7500	0.0704 0.6400
2	0.3871	0.0986	0.7500	0.1586	0.5937	0.1449	0.7500	0.0715 0.6400
3	0.3848	0.0985	0.7500	0.1570	0.5866	0.1450	0.7500	0.0717 0.6400
4	0.3902	0.0994	0.7500	0.1610	0.5949	0.1453	0.7500	0.0720 0.6400
Ammonia (NH <sub>3</sub> ) ID:11								
1	0.4794	0.0798	0.7382	0.1435	0.7730	0.0776	0.5971	0.0282 0.3700
2	0.4742	0.0855	0.7945	0.1431	0.7730	0.0768	0.6055	0.0282 0.3700
Hydroxyl (OH) ID:13								
1	0.3000	0.0481	0.6600			0.0497	0.8600	0.0093 0.4200
2	0.3000	0.0570	0.6600			0.0589	0.8600	0.0110 0.4200
3	0.3000	0.0512	0.6600			0.0529	0.8600	0.0099 0.4200
Hydrogen Chloride (HCl) ID:15								
1	0.0932	0.0213	0.4924	0.0483	0.7500	0.0308	-0.4113	0.0124 0.7500
2	0.0931	0.0212	0.4924	0.0479	0.7500	0.0308	-0.4113	0.0124 0.7500
3	0.0891	0.0260	0.4948	0.0525	0.7500	0.0298	-0.4108	0.0110 0.7500
4	0.0892	0.0261	0.4947	0.0522	0.7500	0.0298	-0.4108	0.0110 0.7500
Hydrogen Iodide (HI) ID:17								
1	0.0445	0.0302	0.5000					
2	0.0420	0.0296	0.5000					
Carbonyl Sulfide (OCS) ID:19								
1	0.1455	0.0896	0.6038	0.1143	0.7482	0.0996	0.7500	0.0782 0.7500
2	0.1495	0.0903	0.6344	0.1153	0.7613	0.1004	0.7500	0.0785 0.7500
3	0.1485	0.0903	0.6269	0.1152	0.7588	0.1005	0.7500	0.0785 0.7500
4	0.1470	0.0901	0.6139	0.1150	0.7541	0.1003	0.7500	0.0784 0.7500
5	0.1484	0.0901	0.6258	0.1148	0.7565	0.0999	0.7500	0.0784 0.7500
6	0.1279	0.0857	0.4935	0.1075	0.6941	0.0936	0.7500	0.0761 0.7500
Hypochlorous Acid (HOCl) ID: 21								
1	0.1500	0.1000	0.7000					
2	0.1500	0.1000	0.7000					
Hydrogen Cyanide (HCN) ID:23								
1	0.6643	0.0980	0.7981			0.1127	0.9000	0.0428 0.7100
2	0.7593	0.1042	0.7989			0.1174	0.9000	0.0431 0.7100
3	0.4790	0.0869	0.7937			0.1037	0.9000	0.0425 0.7100
Hydrogen Peroxide (H <sub>2</sub> O <sub>2</sub> ) ID:25								
1	0.3000	0.1000	0.7500					

Carbon dioxide (CO <sub>2</sub> ) ID:2								
ISO	Self	Air		CO <sub>2</sub>		H <sub>2</sub>		He
1	0.0880	0.0700	0.7127	0.0880	0.6346			
2	0.0890	0.0705	0.7137	0.0890	0.6383			
3	0.0897	0.0708	0.7134	0.0897	0.6410			
4	0.0904	0.0711	0.7135	0.0904	0.6435			
5	0.0911	0.0715	0.7134	0.0911	0.6467			
6	0.0917	0.0717	0.7135	0.0917	0.6489			
7	0.0903	0.0711	0.7137	0.0903	0.6430			
8	0.0919	0.0718	0.7139	0.0919	0.6496			
9	0.0921	0.0720	0.7138	0.0921	0.6501			
10	0.0927	0.0721	0.7135	0.0927	0.6522			
11	0.0931	0.0723	0.7133	0.0931	0.6552			
12	0.0963	0.0736	0.7124	0.0963	0.6669			
Nitrogen Oxide (N <sub>2</sub> O) ID:4								
1	0.0920	0.0750	0.7449					
2	0.0933	0.0757	0.7458					
3	0.0930	0.0756	0.7466					
4	0.0933	0.0745	0.7500					
5	0.0937	0.0760	0.7459					
Methane (CH <sub>4</sub> ) ID:6								
1	0.0679	0.0519	0.6663					
2	0.0674	0.0502	0.6430					
3	0.0689	0.0512	0.7407					
4	0.0717	0.0529	0.6619					
Nitric Oxide (NO) ID:8								
1	0.0497	0.0394	0.6559					
2	0.0500	0.0395	0.6544					
3	0.0502	0.0397	0.6544					
Nitrogen Dioxide (NO <sub>2</sub> ) ID:10								
1	0.0928	0.0727	0.7046					
2	0.0950	0.0729	0.7095				π	
Nitric Acid (HNO <sub>3</sub> ) ID:12								
1	0.8057	0.1025	0.7647					
2	0.8070	0.1084	0.7500					
Hydrogen Fluoride (HF) ID:14								
1	0.1394	0.0283	0.5019	0.1135	0.5000	0.0419	0.7500	0.0077 0.5000
2	0.1136	0.0255	0.5000	0.0954	0.5000	0.0406	0.7500	0.0040 0.5000
Hydrogen Bromide (HBr) ID:16								
1	0.0693	0.0304	0.5000					
2	0.0694	0.0305	0.5000					
3	0.0669	0.0288	0.5000					
4	0.0669	0.0288	0.5000					
Chlorine Monoxide (ClO) ID:18								
1	0.1000	0.0768	0.6414					
2	0.1000	0.0768	0.6410					
Formaldehyde (H <sub>2</sub> CO) ID:20								
1	0.3386	0.0986	0.6275	0.1821	0.6275	0.1256	0.7500	0.0343 0.7500
2	0.2984	0.0992	0.5763	0.1832	0.5763	0.1256	0.7500	0.0285 0.7500
3	0.3320	0.0994	0.6306	0.1838	0.6306	0.1262	0.7500	0.0332 0.7500
Nitrogen (N <sub>2</sub> ) ID:22								
1	0.0347	0.0349	0.4009					
2	0.0348	0.0349	0.3957					
Methyl Chloride (CH <sub>3</sub> Cl) ID:24								
1	0.3748	0.0973	0.7181					
2	0.3743	0.0969	0.7169					
Acetylene (C <sub>2</sub> H <sub>2</sub> ) ID:26								
1	0.1286	0.0693	0.7500	0.0904	0.5000	0.0872	0.5880	0.0434 0.4400
2	0.1460	0.0783	0.7500	0.1030	0.5000	0.0907	0.5880	0.0444 0.4400
3	0.1236	0.0667	0.7500	0.0872	0.5000	0.0864	0.5880	0.0432 0.4400
Phosphine (PH <sub>3</sub> ) ID:28								

Ethane (C <sub>2</sub> H <sub>6</sub> ) ID:27									
1	0.1344	0.0788	0.9022						
2	0.1292	0.0760	0.8576						
Carbonyl Fluoride (COF <sub>2</sub> ) ID:29									
1	0.1750	0.0845	0.9400						
2	0.1750	0.0845	0.9400						
Hydrogen Sulfide (H <sub>2</sub> S) ID:31									
1	0.1451	0.0581	0.7500		0.0592	0.7000	0.0353	0.4600	
2	0.1480	0.0604	0.7500		0.0611	0.7000	0.0387	0.4600	
3	0.1467	0.0593	0.7500		0.0607	0.7000	0.0386	0.4600	
Hydroperoxil (HO <sub>2</sub> ) ID:33									
1	0.3000	0.1005	0.6371						
Chlorine Nitrate (ClONO <sub>2</sub> ) ID:35									
1	0.8000	0.1400	0.5000						
2	0.8000	0.1400	0.5000						
Hypobromous Acid (HOBr) ID:37									
1	0.1500	0.0600	0.6700						
2	0.1500	0.0600	0.6700						
Methanol (CH <sub>3</sub> OH) ID:39									
1	0.4000	0.1000	0.7500						
Acetonitrile (CH <sub>3</sub> CN) ID:41									
1	1.4839	0.1353	0.7200						
Diacetylene (C <sub>4</sub> H <sub>2</sub> ) ID:43									
1	0.2000	0.1000	0.7500						
Hydrogen (H <sub>2</sub> ) ID:45									
1	0.0500	0.0500	0.7500		0.0500				
2	0.0500	0.0500	0.7500		0.0500				
Sulfur trioxide (SO <sub>3</sub> ) ID:47									
1	0.1000	0.0700	0.7000						
Phosgene (COCl <sub>2</sub> ) ID:49									
1	0.3000	0.0800	0.7500						
2	0.3000	0.0800	0.7500						
Methyl fluoride (CH <sub>3</sub> F) ID:51									
1	0.3898	0.0802	0.7500						
Carbon disulfide (CS <sub>2</sub> ) ID:53									
1	0.1081	0.0862	0.7167						
2	0.1067	0.0851	0.7188						
3	0.1074	0.0856	0.7183						
4	0.1083	0.0863	0.7180						
Nitrogen trifluoride (NF <sub>3</sub> ) ID:55									
1	0.5000	0.1000	0.5500						
1	0.0927	0.0566	0.5753			0.0916	0.6255	0.0476	0.3030
Sulfur Hexafluoride (SF <sub>6</sub> ) ID:30									
1	0.0420	0.0500	0.6500						
Formic Acid (HCOOH) ID:32									
1	0.3229	0.1010	0.7500						
Oxygen atom (O) ID:34									
1	0.0500	0.0500	1.0000						
Nitric Acid Cation (NO <sup>+</sup> ) ID:36									
1	0.0500	0.0600	0.5000						
Ethylene (C <sub>2</sub> H <sub>4</sub> ) ID:38									
1	0.1138	0.0838	0.7669						
2	0.1235	0.0844	0.7609						
Methyl Bromide (CH <sub>3</sub> Br) ID:40									
1	0.2874	0.0939	0.7978						
2	0.2890	0.0939	0.7972						
PFC-14 (CF <sub>4</sub> ) ID:42									
1	0.0800	0.0780	0.6600						
Cyanoacetylene (HC <sub>3</sub> N) ID:44									
1	0.1000	0.1000	0.7500						
Carbon Monosulfide (CS) ID:46									
1	0.0659	0.0731	0.7500						
2	0.0659	0.0731	0.7500						
3	0.0659	0.0731	0.7500						
4	0.0659	0.0731	0.7500						
Cyanogen (C <sub>2</sub> N <sub>2</sub> ) ID:48									
1	0.1000	0.1066	0.7500						
Sulfur monoxide (SO) ID:50									
1	0.0311	0.0312	0.7100						
2	0.0285	0.0293	0.7100						
3	0.0284	0.0292	0.7100						
Germane (GeH <sub>4</sub> ) ID:52									
1	0.0693	0.0600	0.7500			0.1290	0.7900		
2	0.0693	0.0600	0.7500			0.1290	0.7900		
3	0.0693	0.0600	0.7500			0.1290	0.7900		
4	0.0694	0.0600	0.7500			0.1290	0.7900		
5	0.0693	0.0600	0.7500			0.1290	0.7900		
Methyl iodide (CH <sub>3</sub> I) ID:54									
1	0.2992	0.1041	0.7500						

**Table 1:** Typical line-shape information for the main isotopologues in different collisional regimes. The tabulated values are: self  $w_{CO}$ , air  $w_{CO}$ , air  $ew_P$ ,  $CO_2$   $w_{CO}$ ,  $CO_2$   $ew_P$ ,  $H_2$   $w_{CO}$ ,  $H_2$   $ew_P$ ,  $He$   $w_{CO}$ ,  $He$   $ew_P$ , which were derived by averaging the parameters in HITRAN2020 for that isotopologue (Gordon et al., 2022), supplemented with  $H_2O$  in  $CO_2$  parameters by (Devi et al., 2017; Régalia et al., 2019, compiled by Séverine Robert). The  $w_{CO}$  values are in  $[cm^{-1}/atm]$ . The line parameters are weighted layer-by-layer based on the ambient collisional regime and are supplemented with the air parameters when missing. Molecules with correlated-k tables are marked in yellow.

center) are only considered for atomic species, and are implemented in PSG following the quasi-static approximation (Burrows et al., 2000; Iro et al., 2003; Nefedov et al., 1999). The line center at each layer is calculated as:

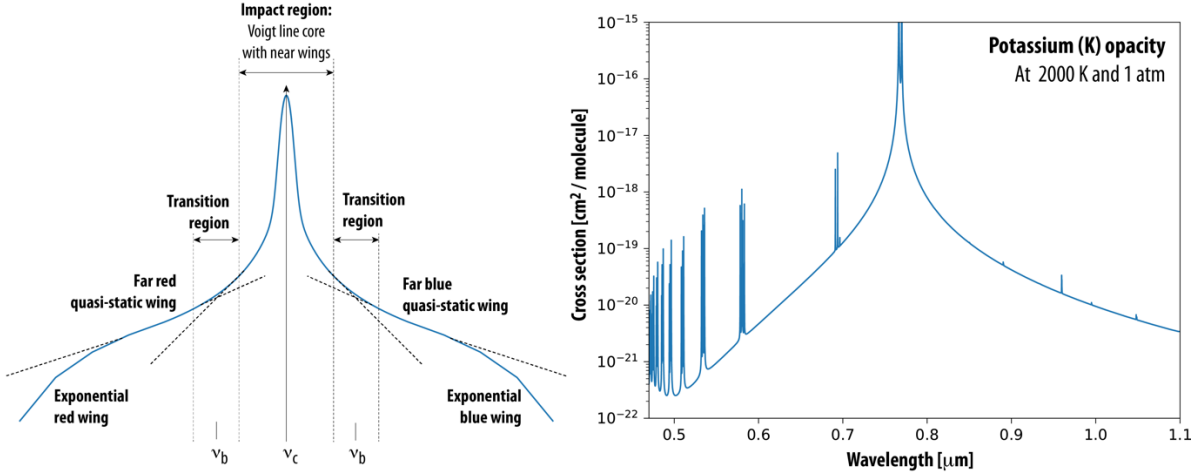


**Figure 4:** Anatomy of a spectroscopic line. **(Left)** Several regions dominate the shape of the line, in which the impact region captures the Voigt profile with Gaussian core and Lorentzian wings for molecules, while for atoms the line-shape extends greatly in frequency/wavelength into the quasi-static regime. The transition from the classical Lorentzian wing into the quasi-static region is defined by the detuning frequency ( $\nu_b$ , eq. 24), in which the extended line-shape is affected by an exponential decay term (eq. 23). The vertical scale is logarithmic. **(Right)** Example of a simulation of the opacity for Potassium (K) at 2000 [K] and at a pressure of 1 [atm] (to be compared with Figure 5 in Burrows et al., 2000), in which one can see the linear  $(\nu' - \nu)^{-3/2}$  decay of the lineshape following the quasi-static formalism (eq. 23).

$$\nu_c = \left[ \nu_0 + P \, d\nu_P \left( \frac{T_{ref}}{T} \right)^{ev_P} \right] \left[ 1 - \frac{v_l}{c} \right] \quad (16)$$

where  $\nu_0$  is the line rest frequency at 1 [atm],  $P$  is the layer pressure [atm],  $d\nu_P$  is the pressure shift of the line,  $ev_P$  is the temperature dependence of the pressure shift and  $v_l$  is the Doppler velocity towards the observer at the layer. The linewidth ( $w_D$ ) of the Gaussian Doppler core is a combination of the thermal kinetic broadening ( $w_T$ ) and the apparent velocity broadening ( $w_R$ ) introduced by the rotation of the planet:

$$w_D = \sqrt{w_T^2 + w_R^2} \quad w_T = v_c \sqrt{\frac{k_D T}{m}} \quad w_R = v_c \frac{v_R}{c} \quad (17)$$

where  $m$  is the molar mass [g/mol] of the isotopologue,  $k_D$  is the Doppler width parameter ( $1.285595 \times 10^{-13}$  [g/mol/K]) and  $v_R$  is the apparent velocity dispersion across the FOV. The Lorentzian component ( $w_L$ ) is defined by the collisional environment ( $w_C$ ) and the natural width ( $w_N$ ) of the line as:

$$w_L = w_C + w_N \quad w_C = P \, w_{C0} \left( \frac{T_{ref}}{T} \right)^{ew_P} \quad (18)$$

where  $w_{C0}$  is the linewidth at 1 [atm] and  $ew_P$  is the temperature dependence of the linewidth (see mean values for many isotopologues in Table 1). For molecular species,  $w_N$  is negligible and assumed

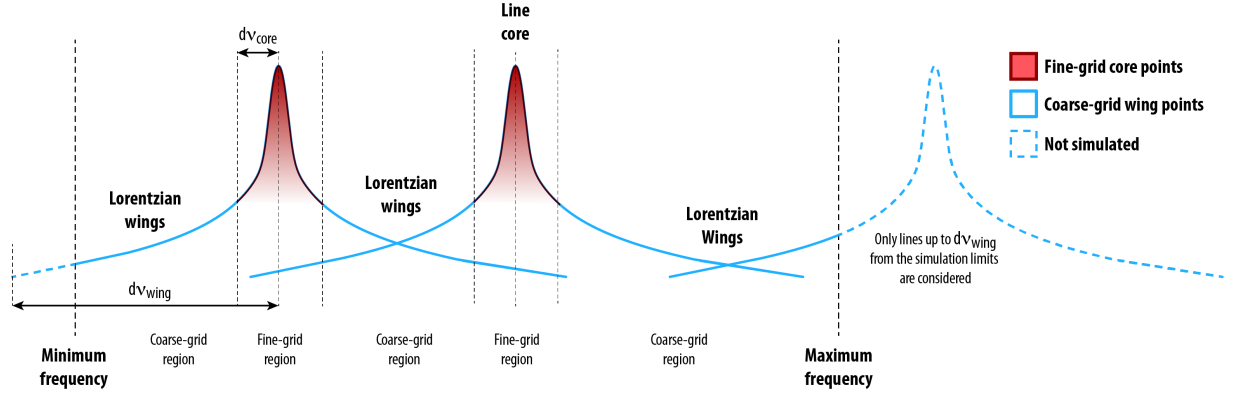


**Figure 5:** PSG employs a multi-grid scheme to simulate the line-shapes. The line cores (within  $dv_{core}$ ) are synthesized at a fine resolution (at least  $dv_{min}$ ) ensuring a proper handling of the Gaussian and Lorentzian components, while the Lorentzian wings (beyond  $dv_{core}$  and within  $dv_{wing}$ ) are synthesized at a coarser resolution ( $dv_{core}$ ) and later interpolated to the fine resolution grid. The interpolation from coarse to fine is only done once all the line shapes have been computed and PSG employs a 3-point spline interpolation scheme. Line shapes are shown on a logarithmic vertical scale.

to be zero, while  $w_N$  is calculated from the atomic radiative damping constant ( $\gamma_{RAD} [s^{-1}]$ ) as  $w_N = \gamma_{RAD} / (4\pi c)$ . Similarly, the collisional halfwidth of atoms can be derived from the Van der Waals damping constant ( $\gamma_6 [s^{-1}]$ ) as  $w_{C0} = \gamma_6 \cdot 8.62489e18 / (4\pi c)$ , with  $T_{ref}=296 [K]$  and  $ew_P=0.7$ . Within the impact region or main region of the line ( $<25 \text{ cm}^{-1}$ ), the line profile at frequency  $\nu$  for a line centered at  $\nu_C$  is a Voigt function (modelled internally in PSG via the Fadeeva function) as:

$$k(\nu) = \int_{-\infty}^{\infty} \left[ \frac{\exp(-(v' - \nu_C)^2 / 2w_D^2)}{w_D \sqrt{2\pi}} \right] \left[ \frac{w_L}{\pi((v' - \nu_C)^2 + w_L^2)} \right] dv' \quad (19)$$

For molecules, the lines shapes are assumed to extend up to  $25 \text{ cm}^{-1}$ , while for atoms the far wings beyond the detuning frequency ( $\nu_b$ ) are further extended employing the basic form of the quasi-static approximation (see Figure 4) assuming  $q=1$  as:

$$k(\nu) = (\nu - \nu_C)^{-3/2} \exp\left(-\frac{h(\nu - \nu_C)}{kT}\right) \quad (20)$$

The detuning frequency primarily depends on the collisional regime/partner and the ambient temperature. Considering the values of sodium and potassium in several collisional regimes (Nefedov et al., 1999), the  $\nu_b$  for atoms can be approximated based on the ambient temperature ( $T$ ) and atmospheric molar weight ( $m_{atm}$ ) as:

$$\nu_b [cm^{-1}] = 25 \sqrt{\frac{T[K]}{250 \cdot m_{atm}[g/mol]}} \quad (21)$$





Once the line parameters are defined for all lines across all layers, it is critical to employ a spectral grid with a sufficiently high enough resolution that properly captures the shape across all species, lines, and layers. For instance, if the core of the line has a width of  $0.001 \text{ cm}^{-1}$ , the simulation would need up to  $\sim 5$  points across the line and a synthesis grid resolution of  $0.001/5 \text{ [cm}^{-1}\text{]}$  to properly capture the opacity across the line. All lines have a Gaussian core with a width defined by equation 20, which slowly transitions to a Lorentzian shape. The user may desire a simulation at a resolution of  $dv_{\text{user}} \text{ cm}^{-1}$ , but PSG will internally oversample the radiative transfer spectral grid by  $dv_{\text{user}}/dv_{\text{min}}$  in order to ensure accurate line-shapes, in which  $dv_{\text{min}}$  is the minimum needed resolution to ensure up to  $\sim 5$  spectral points per line core. Employing equation 20,  $dv_{\text{min}}$  can be defined as:

$$dv_{\text{min}}[\text{cm}^{-1}] = v_{\text{min}}/2 \sqrt{\frac{k_D T_{\text{min}}}{m_{\text{max}}}} \quad (22)$$

where  $v_{\text{min}}$  is the minimum frequency  $[\text{cm}^{-1}]$  of the simulation,  $T_{\text{min}}$  is the minimum temperature across the atmosphere and  $m_{\text{max}}$  is the maximum molecular weight to be modelled. Far from the Gaussian core ( $>1000dv_{\text{max}}$ ), the Lorentzian wings dominate and the line-shape follows a relatively monotonic  $1/(v-v_c)^2$  dependence. As such one can employ a fine resolution grid for the line cores (within  $dv_{\text{core}} = 1000dv_{\text{max}}$  of the line core), and a coarser grid beyond this limit all the way to the  $25 \text{ cm}^{-1}$  wing limit ( $dv_{\text{wing}}$ ), see Figure 5. Once all the lines have been computed, PSG then performs a single interpolation from the coarse to the fine grid, permitting dramatic improvements in performance for line-by-line calculations with very low penalties in accuracy. Such a multi-grid scheme for modeling line-shapes was originally devised in the 80s (e.g., LINEPAK) and later integrated in many other radiative transfer codes (e.g., GENLN2, Edwards, 1992). In PSG, we have greatly improved the accuracy (typically better than  $1e-5$ ) of the coarser-fine interpolation from the original methods by performing a 3-points spline interpolation.

### 3.2 Correlated-k calculations

When considering large frequency ranges, simulating millions of lines at high-resolution can become an unattainable task. An effective approach to address this issue is to pre-compute opacities at a broad range of temperatures, pressures and collisional regimes. To do this, a first approximation to the problem is to compute cross-sections at high-resolution, but such would require billions/trillions of spectral points in order to properly capture the line-shapes ( $dv_{\text{min}}$ , eq. 25) across the full 0.2 to  $100,000 \text{ }\mu\text{m}$  wavelength range. One could store “binned” cross-sections with “average” cross-sections across spectral ranges, but that can lead to large errors when performing radiative transfer calculations. An alternative and very effective approach is the correlated-k method, in which instead of storing the “average” opacities across the spectral range, one stores the histogram or frequency of opacities across that range. For instance, in a 20-points correlated-k database, the tables would contain the probability of opacities across 20 histogram bins for every spectral range. In order to compute correlated-k tables, one first need to compute spectra at high-resolution ( $<dv_{\text{min}}$ ) for a wide range of environments, and then compute histograms across the desired database spectral grid. A challenge with correlated-k tables is that they cannot be simply transformed to any spectral grid, in contrast to cross-section tables that a simple interpolation in frequency is possible. Typically, radiative transfer models have pre-computed correlated-k tables for specific instrument resolutions,

an approach not possible in PSG, due to the generic nature of our model. When using correlated-k tables to calculate opacities, the radiative transfer has to be computed for each correlated-k bin and the radiances then added weighting by the frequency of that opacity bin. Therefore a 20 points correlated-k table, requires 20 radiative transfer calculations per spectral point.

In PSG, we have pre-computed correlated-k tables in the 0.2 to 100,000  $\mu\text{m}$  wavelength range with 20 opacity bins per spectral point for spectral resolving powers of  $\text{RP}=500$  and  $\text{RP}=5000$ . All simulations in PSG requiring resolving powers higher than 5000, are computed employing the line-by-line method, while simulations with a maximum resolving power between  $>500$  and 5000 are computed using the  $\text{RP}=5000$  tables, and using the  $\text{RP}=500$  for resolving powers lower than 500. The correlated-k tables are computed for 21 molecules (see Table 1) at a broad range of temperatures (20 cases from 40 to 2000K), pressures (17 cases,  $1\text{E}-6$  to 100 bar) and collisional regimes (e.g., air,  $\text{CO}_2$ ,  $\text{H}_2$  and He). These opacity correlated-k tables are two-dimensionally interpolated in P and T layer by layer by performing a bilinear interpolation in logarithmic scale. The opacities are converted from the natural  $\text{RP}=500/5000$  spectral grids to the simulation spectral grid by performing a transformation in the cumulative density function (CDF,  $g$ -distribution) of the opacities within the bands encompassed by each simulation grid points. The method was nicely mathematically demonstrated and validated by (Leconte, 2021), and in PSG we employ an histogram oversampling of 5 when performing the  $g$ -distribution transformation.

### *3.3 Molecular cross-sections and UV modeling*

For many species there are no available accurate Hamiltonians, and therefore linelists are not available, not permitting to perform line-by-line, nor correlated-k, computations. In addition, at high energies/frequencies (e.g., UV, optical), the energy structure of the molecules become increasingly non-quantized into a broad swath of energy levels. As such, classical linelists do not accurately characterize these high-frequency spectral regions, and laboratory measurements of molecular cross-sections are needed.

Similarly to correlated-k tables, cross-sections are needed at temperatures, pressures and collisional regimes similar to the simulation layer-by-layer parameters. This requirement is somewhat mitigated at UV wavelengths, since the effect of line-shapes and excitation properties are typically masked by the typically coarse frequency sampling at these very large frequencies. In PSG, we complement the classical line-by-line and correlated-k simulations in the UV/optical range, by ingesting UV/optical cross-sections for 44 species collected from a range of spectral databases. Most of these cross-sections originate from the MPI-Mainz Spectral Atlas (Keller-Rudek et al., 2013), which have been parsed, combined and formatted to provide a comprehensive and cohesive set of cross-sections per molecule across the 0.01 to 1  $\mu\text{m}$  wavelength range. Additional UV cross-sections include those of  $\text{O}_3$  by (Serdyuchenko et al., 2014),  $\text{CO}_2$  by (Venot et al., 2018), the Herzberg  $\text{O}_2$  continuum bands as well as the  $\text{O}_2$ – $\text{O}_2$  absorption bands (Wulf bands, 0.24 and 0.3  $\mu\text{m}$ ) by (Fally et al., 2000), and the Herzberg  $\text{O}_2$  band system (Jenouvrier et al., 1999; Mérianne et al., 2001, 2000). In PSG, we also integrate all HITRAN molecular cross-sections for trace species (Gordon et al., 2022).

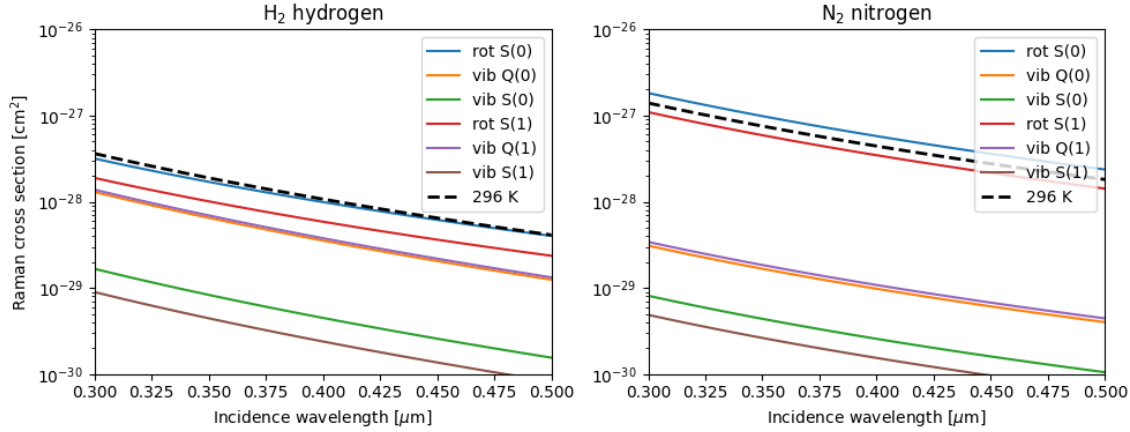


**Figure 6:** Raman cross sections for the first transitions of H<sub>2</sub> (left) and N<sub>2</sub> (right). The equivalent value at 296 [K] is computed by properly weighting the contribution from each line based on the level population at that temperature. The designation ‘vib’ refers to vibrational transitions in which the vibrational quantum number of the molecule changes from 0 to 1 (ground to first excited state), while ‘rot’ describes pure rotational transitions in which the vibrational quantum number does not change. S(i) denotes transitions in which the rotational quantum number increases by 2 (from i to i + 2), for Q(i) the rotational quantum number does not change, and for O(i) the rotational quantum number decreases by 2. These cross-sections have been computed following the methods in (Oklopčić et al., 2017), and are to be compared with the values presented in figure 14 of that paper.

### 3.4 Rayleigh and Raman scattering

At wavelengths approaching the size of the molecules, the oscillating electric field of a light wave acts on the charges within a particle, leading the molecule to become a radiating dipole. Rayleigh scattering results from the electric polarizability of the particles, and the elastically scattered radiation is at the same wavelength of the incoming radiation. Among those scattered photons, a small fraction is scattered inelastically, with the scattered photons having an energy different (usually lower) from those of the incident photons - these are Raman scattered photons. Modeling these processes can be particularly difficult, considering the wide range of possible interacting levels, the non-isotropic nature of these scattering processes, and the fact that radiation is absorbed at one wavelength and radiated at another wavelength. Furthermore, these processes depend on the molecular aggregate and environment, and numerically solving for these for a diverse set of the atmosphere compositions can be challenging.

Rayleigh cross-sections [m<sup>2</sup>/molecule] are computed as a summation of the individual molecular cross-sections (Sneep and Ubachs, 2005), which are computed at wavelength  $\lambda$  [μm] based on the polarizability  $\alpha_{\text{pol}}$  [Å<sup>3</sup>] of the encompassing molecules as:

$$\sigma_{\text{Rayleigh}}(\lambda) = \frac{\pi \cdot 8 \cdot 10^{-36}}{3} \alpha_{\text{pol}}^2 \left( \frac{2\pi}{\lambda} \right)^4 \quad (23)$$

In PSG, we employ polarizability values as compiled on the Computational Chemistry Comparison and Benchmark DataBase at NIST (<https://cccbdb.nist.gov/pollistx.asp>). The scattering parameters are defined as  $\omega=1$ ,  $g_0=1.0$  and  $g_2=0.1$  (see Chapter 5).

The effects of Raman scattering on planetary spectra are more subtle (typically a few percent), yet because the scattered radiation occurs at a different wavelength as the incidence flux, Raman scattering leads to observable spectral features in the I/F signal, which can be notably prominent at moderate/high resolutions. This also means that the scattering simulation has to be done for each specific Raman line individually, since the scattering delta-wavelength is different for each transition. Several numerical approximate methods exist to perform these calculations, yet in many cases they can be extremely computationally expensive. In PSG, we adopt a similar approach as implemented in PICASO (Batalha et al., 2019), in which the original method developed by (Pollack et al., 1986) is adapted to include the Raman cross sections for  $H_2$  and  $N_2$  computed by (Oklopčić et al., 2017). At the core of this method is the scaling of the “apparent” Raman scattering albedo at the emission wavelength by the ratio of the incoming/emitting solar fluxes. Since the scattering albedo can never exceed unity in PSGDORT, such method is only valid when other non-scattering opacity sources (e.g.,  $CH_4$ ,  $H_2O$ ,  $O_2$ ,  $O_3$ ,  $H_2$  UV/optical absorptions) are also present in the atmosphere at these wavelengths or when the difference between the impinging incidence/scattered stellar flux is small. The Raman extinction cross section (see Figure 6) is computed for each line of  $N_2$  and  $H_2$  as:

$$\sigma_{Raman}(\lambda) = \frac{C}{\lambda' \lambda^3} \quad (24)$$

where  $C$  is the cross-section factor calculated as presented in (Oklopčić et al., 2017),  $\lambda'$  is the incidence wavelength and  $\lambda^3$  is the emission/scattering wavelength. The incident ( $\lambda'$ ) and scattered ( $\lambda$ ) wavelengths are related by  $1/\lambda'^{-1} = 1/\lambda + \Delta\nu$ , where  $\Delta\nu$  is the Raman shift of the transition. In PSG, we internally recreate the Hamiltonians for  $H_2$  and  $N_2$  and compute Raman opacities layer-by-layer considering the appropriate partition functions and energy populations. The total scattering albedo including Raman is approximated to be:

$$\omega(\lambda') = \frac{\sigma_{Rayleigh}(\lambda') + \sigma_{Raman}(\lambda') \left( \frac{F_*(\lambda')}{F_*(\lambda)} \right) + \sigma_{scatt}}{\sigma_{Rayleigh}(\lambda') + \sigma_{Raman}(\lambda') + \sigma_{absorb}} \quad (25)$$

where  $\sigma_{scatt}$  is the scattering fractional opacity due to aerosols,  $\sigma_{absorb}$  is the non-scattering absorbing opacity due to aerosols and molecules (e.g., UV molecular cross-sections), and  $F^*(\lambda')/F^*(\lambda)$  is the ratio of the impinging incident to scattered solar/stellar fluxes.

### 3.5 Collision-Induced-Absorption (CIA) and the Water Continuum (MT\_CKD)

Collision-induced absorption and emission are generated by inelastic collisions of molecules in a gas. Such inelastic collisions (along with the absorption or emission of photons) may induce quantum transitions in the molecules, or the molecules may form transient supramolecular complexes with spectral features different from the underlying molecules. Collision-induced absorption and emission is particularly important in dense gases, such as hydrogen and helium clouds found in astronomical

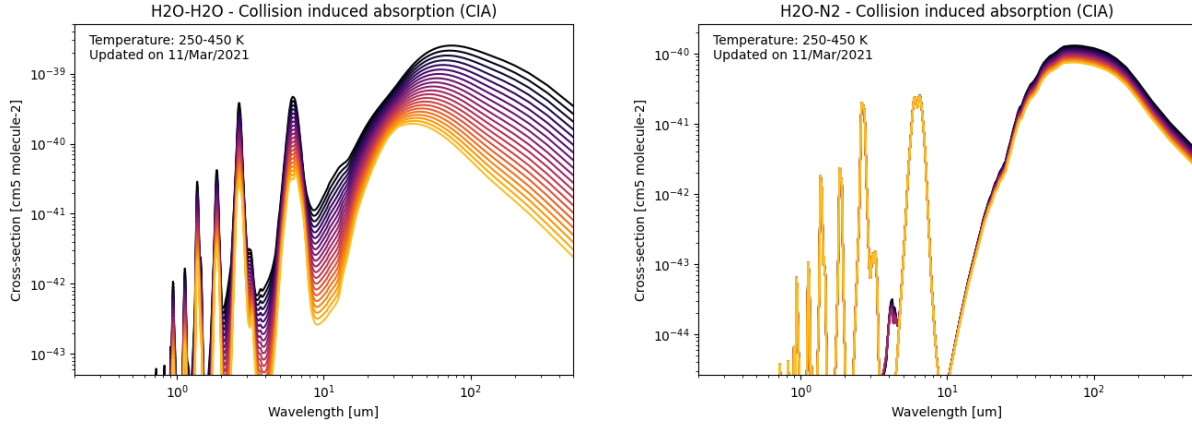


**Figure 7:** Water continuum (left: self, right: foreign) modelled as a Collision-Induced-Absorption (CIA) following the methods in (Kofman and Villanueva, 2021). The foreign values also include a known H<sub>2</sub>O-N<sub>2</sub> CIA near 4  $\mu\text{m}$  (appearing in dark blue/red on the left panel).

systems. Different to regular molecular absorptions which are dependent linearly on the molecular column density, CIAs depend quadratically on the X-Y pair column densities. In that sense, such processes are particularly relevant in deep and high-density atmospheres but can also be quite relevant even at moderate fractional atmosphere pressures. In PSG, we integrate all CIAs available in HITRAN (Gordon et al., 2022), which are complemented with several other specifically defined CIAs, including several O<sub>2</sub>-X pairs (Fauchez et al., 2020) in the infrared, the Wulf O<sub>2</sub>-O<sub>2</sub> CIAs in the UV (Fally et al., 2000), and of several CO<sub>2</sub>-X pairs (Turbet et al., 2020).

Another spectroscopic process associated molecular pairs with quite prominent and strong signatures is the water continuum, which have been historically modelled empirically employing a set for Fortran routines that form the MT\_CKD model (Mlawer–Tobin–Clough–Kneizys–Davies, Clough et al., 2005). Although the physical process underlying the water continuum as described by the MT\_CKD continuum is still under debate (Baranov and Lafferty, 2012; Shine et al., 2012), whether it is due to water dimers or collision induced absorption, both processes follow the same quadratic dependence on the water density. In PSG, we parameterize the temperature dependent MT\_CKD continuum in terms of collision induced absorption (CIA) coefficients, following the methodology presented in (Kofman and Villanueva, 2021). The MT\_CKD scripts outputs the water continuum absorbance continuum coefficient,  $C_s(\nu, T)$ , which can be expressed in unit of  $[\text{cm}^2 \text{ molecule atm}^{-1}]$ ,  $C_s^*(\nu, T)$  or in units of  $[\text{cm}^2 \text{ molecule cm}]$ ,  $C_s(\nu, T)$ . The former used most often in the literature, but the MT\_CKD work reports the units in the latter, which will be used here. Conversion between both definitions are done using (Paynter et al., 2009; Shine et al., 2016):

$$C_s(\nu, T) = C_s^*(\nu, T) \frac{T}{296} \quad (26)$$

Opacity from the water continuum coefficient is calculated as following:

$$\tau(\nu, T) = l \rho_s R(\nu, T) \left[ \frac{\rho_s}{\rho_0} C_s(\nu, T) + \frac{\rho_f}{\rho_0} C_f(\nu, T) \right] \quad (27)$$

Where  $R(\nu, T) = \nu \tanh\left(\frac{h\nu}{2k_b T}\right)$  and is the radiative term (Clough et al., 1989), with  $h$  Planck's constant,  $c$  the speed of light, and  $k_b$  Boltzmann's constant (which is  $1.36 \times 10^{-22}$  [atm molecule<sup>-1</sup> cm<sup>3</sup> K<sup>-1</sup>] for these calculations). Equations (1) and (3) can be combined to convert  $C_s(\nu, T)$  to  $k_s(\nu, T)$ :

$$l k_s(\nu, T) \rho_s^2 = l \rho_s R(\nu, T) \frac{\rho_s}{\rho_0} C_s(\nu, T) \quad (28)$$

$$k_s(\nu, T) \rho_s = R(\nu, T) \frac{\rho_s}{\rho_0} C_s(\nu, T) \quad (29)$$

$$k_s(\nu, T) = \frac{1}{\rho_0} R(\nu, T) C_s(\nu, T) \quad (30)$$

The obtained values for  $k_s(\nu, T)$  and  $k_f(\nu, T)$  are shown in Figure 7, which have been also combined with the other known H<sub>2</sub>O-N<sub>2</sub> CIAs. These are derived from the MT\_CKD  $C_s(\nu, T)$  values and include the radiative term. Note that  $k_f$  shows little temperature dependance, and mostly below 500 cm<sup>-1</sup>  $k_s$  decreases as a function of temperature.

#### 4. Non-Local Thermodynamical-Equilibrium (non-LTE) modeling

When collisions are infrequent enough to equilibrate the radiative populations of the molecules, an atmosphere is considered to be in non-local thermodynamical equilibrium (non-LTE). Then, the classical Boltzmann distribution equation describing the population of the molecular energy levels and the Planck's function assumed to describe the source radiation terms are no longer valid. This primarily occurs in the tenuous regions of the atmosphere, where collisions are infrequent and solar radiation is strong and unattenuated, leading to strong emissions as the molecules cascade back to their ground state. The radiative equilibrium equation for a two-level system can be written as:

$$\frac{n_u}{n_l} = \frac{g_u}{g_l} \exp(-h\nu/KT) \left[ \frac{1 + \rho B_{lu}/C_{lu}}{1 + A_{ul}/C_{ul}} \right] \quad (31)$$

where  $n$  are the populations of the upper (u) and lower (l) levels,  $g$  the statistical weights,  $T$  is the local kinetic temperature,  $C_{lu}$  and  $C_{ul}$  the collisional excitation and relaxation rates respectively,  $B_{lu}$  and  $A_{ul}$  are the Einstein coefficients for absorption and spontaneous emission, and  $\rho$  is the impinging excitation flux. The Einstein coefficients are radiative properties of the levels in question, while the collision rates are dependent on the local temperature ( $\propto \sqrt{T}$ ) and density. At high pressures, collisions dominate the radiative processes ( $C \gg A_{ul}$  or  $C \gg B_{lu}$ ), and the relative populations of the levels can be simply described by Maxwell-Boltzmann statistics (LTE) dependent on the local kinetic temperature. In regions with strong external radiative fields ( $\rho$ ), and more infrequent collisions ( $C \ll A_{ul}$  or  $C \ll B_{lu}$ ), the radiative parameters start to define the energy balance of the molecule and its emitting spectrum (non-LTE).

As nicely summarized by (Appleby, 1990), non-LTE starts to become relevant for methane in the mesosphere of the giant planets (e.g., Jupiter, Saturn, Uranus, Neptune, see Figure 8) at pressures less than 0.1 [mbar]. In CO<sub>2</sub> rich atmospheres (e.g., Mars, Venus), the efficient collisional rates for



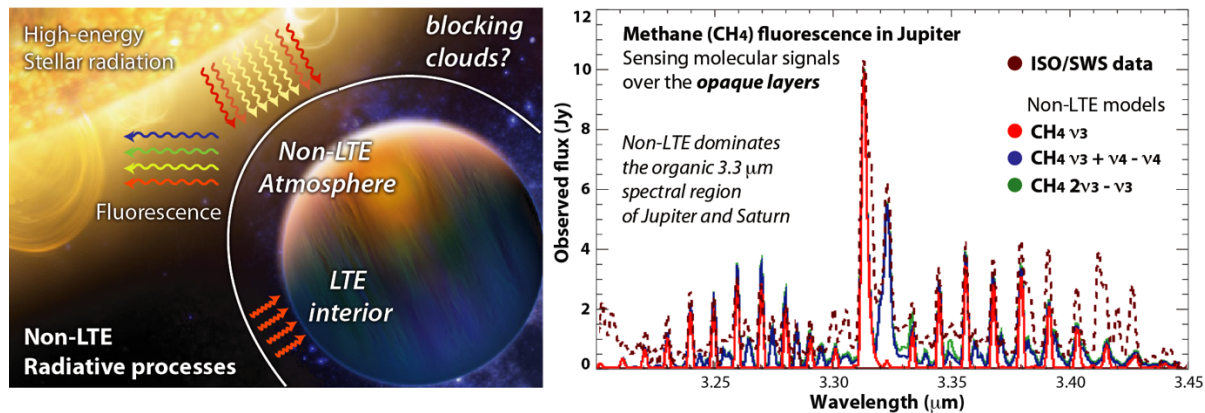


**Figure 8:** As the atmospheres are bombarded by high-energy photons from their partner stars, the upper layers efficiently emit via non-LTE processes. This disequilibrium has been observed in many planets of our solar system (shown is the detection of non-LTE methane in Jupiter, Encrenaz et al., 1996), and it is certainly active in many exoplanets' atmospheres.

this molecule, keeps LTE up to much lower densities ( $>1$  [ $\mu\text{bar}$ ], Lopez-Puertas and López-Valverde, 1995). In the atmospheres of hot-giants, stronger radiation fields will bring this limit deeper into the atmosphere, while higher kinetic temperatures will push LTE further up in the atmosphere. Chemical reactions also lead molecules into highly excited non-equilibrium states, from which diagnostic photons are released, as it is the case for the dayglow  $\text{O}_2(1\Delta)$  emission tracking the photo-destruction of  $\text{O}_3$  in terrestrial atmospheres.

Non-LTE affects two key parameters in a radiative transfer simulation, the opacity terms and the source function. Specifically, the intensity of the line no longer follows a simple LTE relationship (eq. 13), but it is computed from a non-equilibrated population. Similarly, the source function  $S(\tau)$ , typically considered to be a blackbody in equation 2, is now computed based on the specific radiative equilibrium constants for that level/wavelength. In PSG, we have implemented a method in which the user can provide non-equilibrated populations, and the radiative transfer will compute non-LTE populations and source functions accordingly. The user must provide vertical profiles of vibrational temperatures [K] (computed relative to the ground-state) for every isotopologue and vibrational band, in the form of "Tvib[MOL:ISO:IDvib]" (MOL:HITRAN molecular ID, ISO:Isotopologue ID, IDvib: vibrational band ID as defined for the isotopologue [see vibrational bands in the line-list help]). For instance "Tvib[6:1:7]" would correspond to the  $v_3=1$  level of the main isotope of  $\text{CH}_4$ .

## 5. Cometary modeling (CEM module)

In comets, non-equilibrated atmospheres are particularly prevalent due to the typical low densities across most of their coma. The structure and composition are defined as presented in chapter 3, while the emitted fluxes are computed by the PSG Cometary Emission Model (CEM).

The spectra of a comet can be divided into three main components (see Figure 9): the nucleus (reflected, emitted and absorbed radiation), coma grains or dust (reflected, emitted and absorbed radiation), and the coma gas emissions (e.g., LTE, non-LTE). The Cometary Emission Model (CEM) employs the PSG surface models, as described in chapter 6, to simulate the nucleus and the

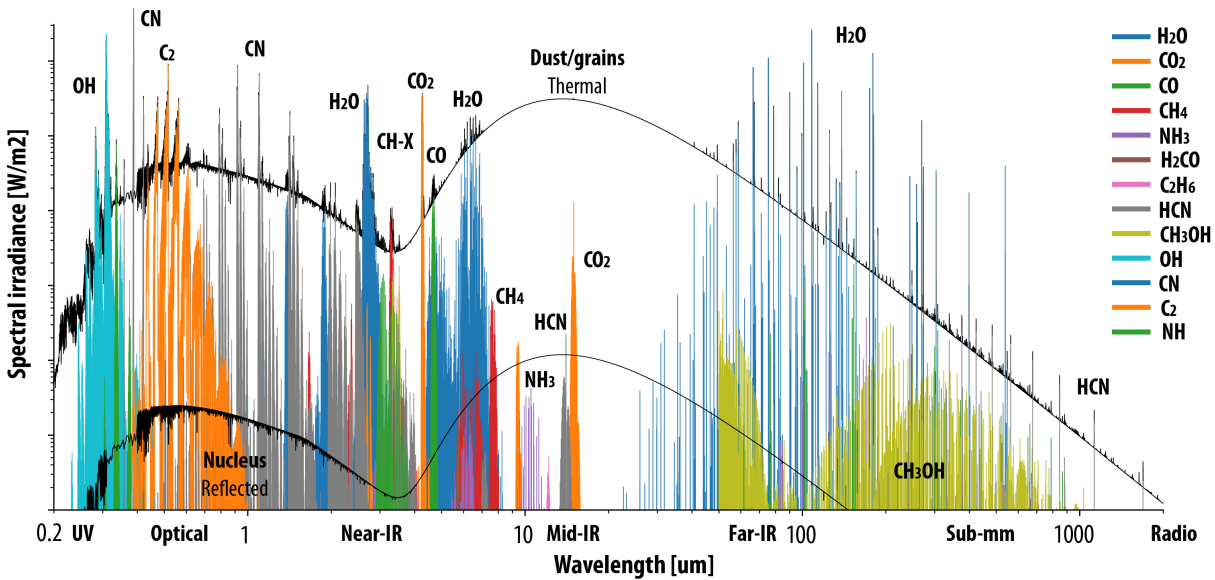


**Figure 9:** Simulated components of a cometary spectrum (the nucleus and dust coma are shown in black, while each molecular gas emission is identified with different colors) across most of the electromagnetic spectral range using PSG (see further details in our review about radiative processes in Comets III, Bodewits et al., 2022). The model includes nucleus and dust/grains emission (see chapter 6), non-LTE fluorescence emissions dominating the UV/Optical/near-IR, and thermal emissions dominating the longer wavelengths beyond the near-IR.

grains components, while the gas emissions are calculated by employing a mono-layer non-LTE and/or LTE excitation model. The nucleus is assumed to be a spherical emitting surface, while the dust in the coma is calculated as a diffuse and extended emitting component. The outgassing of dust-grains and parent molecular species is assumed to be isotropic and at constant expansion velocity, with photo-dissociation defining the lifetime and spatial extent of molecular species. Using these assumptions, the integrated number of molecules ( $N$  [molecules]) within the FOV is defined as  $N_{\text{gas}} = Q \cdot \tau \cdot f(x)$ , where  $\tau$  is the molecular lifetime [s],  $f(x)$  is the filling-factor of the FOV with respect to the total coma, and  $Q$  is the molecular production rate [molecules/s]. The definition and calculation of  $f(x)$  is complex, and we employ a combination of analytical methods that make use of Bessel functions (see chapter 3). Two possible excitation regimes are considered in PSG for the molecules: non-LTE fluorescence (typically dominating the flux in the UV-Optical-IR range) and LTE excitation (modelled using the methods as previously described in this section). In PSG, we model cometary non-LTE by ingesting fluorescence efficiencies ( $g$ -factors) which are pre-computed for a particular rotational temperature and solar radiation flux (e.g., Villanueva et al., 2013, 2012b, 2012a, 2011). These line lists can be applied to other similar exospheres of comparable low-collisional rate and high-insolation rate (see simulation example in Figure 9).

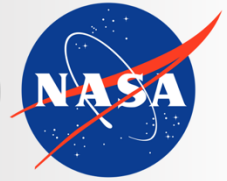
These assumptions are generally accurate enough (and widely employed by the community) to determine integrated column densities and molecular fluxes across the coma, yet the lifetime and velocity of the dust-grains can be mass/size/composition dependent and may differ from the surrounding gas environment. On the other hand, the strong relationship between visual magnitude (mainly defined by dust) and water production for 37 comets (Jorda et al., 2008) indicates that a



common dust and gas outgassing scheme should be accurate enough for most cases, and it is the method employed by CEM. In CEM, we treat dust particles as behaving like the surrounding gas and it can be demonstrated that for a dust/gas mass ratio of 1.0, the brightness relationship determined by Jorda et al. is consistent with an average particle size of  $r_{\text{dust}}=3.4 \mu\text{m}$  (when assuming a dust particle density of  $\rho=0.5 \text{ [kg/cm}^3\text{]}$  and particle albedo as the nucleus of 0.04).

When computing coma dust emission fluxes, we first derive the integrated water mass within the FOV as  $M_{\text{gas}} [\text{g}] = N_{\text{gas}} \cdot m_{\text{gas}} / A_{\text{g}}$ , where  $A_{\text{g}}$  is the Avogadro number  $6.022\text{E}23 \text{ [molecules/mol]}$  and  $m_{\text{gas}}$  is the mean molar mass of the gas ( $18 \text{ [g/mol]}$  for water), and then define the dust mass as  $M_{\text{dust}} = M_{\text{gas}} \cdot \text{DG}$ , where DG is the user-provided dust-to-gas mass ratio (`<SURFACE-GAS-RATIO>` of 1.0 is assumed to be typical, yet it is an adjustable parameter in CEM). The number of dust particles in the FOV is then  $N_{\text{dust}} = M_{\text{dust}} / (4/3 \cdot A_{\text{dust}} \cdot r_{\text{dust}} \cdot \rho)$ , where  $A_{\text{dust}}$  is the particle cross-section ( $\pi r_{\text{dust}}^2$ ), and the opacity due to dust is then  $O_{\text{dust}} = N_{\text{dust}} \cdot (A_{\text{dust}}/A_{\text{beam}})$ , where  $A_{\text{beam}}$  is the area of the FOV at the comet. Ultimately, the effective emitting dust area is  $A_{\text{em}} = A_{\text{beam}} \cdot (1.0 - \exp(-O_{\text{dust}}))$ , which is the parameter employed to compute flux densities in PSG employing standard surface radiation terms. Further details on the nucleus and grain modeling are summarized in chapter 6.





**Planetary Spectrum Generator**  
National Aeronautics and Space Administration

# Chapter 5: **Multiple Scattering Atmospheric Modeling**

**Villanueva, Liuzzi and  
PSG team**



## 1. Atmospheric scattering modeling in PSG

As light travels across an atmosphere, it is absorbed (then transformed into heat and thermally emitted) and it is also scattered into many directions. Scattering in this sense, refers to the reflection and deflection of photons in a 3D manner across an atmosphere. When this process is active in an atmosphere, it leads to an “ambient” of diffuse shine and to a peculiar light pattern when looking close to the Sun. For instance, when no scattering is active (only absorption), we would have black skies with only a disk of light at the location of the Sun. Molecular Rayleigh scattering is the reason we have blue skies, in which molecules “scatter” the photons in many directions with a specific wavelength dependance, and in which photons are scattered towards the observer even when the Sun is quite far from the observed patch of the sky. As can be quickly inferred, computing scattering is therefore a 3D problem, which can be numerically extremely difficult to solve since photons need to be tracked across the full three-dimensions (azimuth angle, polar angle, depth/altitude). In a non-scattering medium, the solution of the radiative transfer equation is straightforward, with only needing to track the photons as they go through the incidence and emission paths. For such case, PSG can solve this integral-differential equation readily and efficiently without needing to solve any multiple scattering 3D problem.

Ultimately, solving a full 3D integral-differential scattering problem for the myriad of possible incidence and emission angles would appear in principle unattainable. Several methods do exist, and these include the *doubling-adding method*, the *successive orders of scattering method*, *Gauss-Seidel iteration method*, and the *Monte Carlo approach*, among others. In particular, Chandrasekhar introduced in 1940 a pioneering method for solving radiative transfer in a scattering medium, the *discrete ordinate method*. The primary merit of this method is that it reduces the integral-differential equation to a system of ordinary differential equations, and it divides the scattering directions into numerical series. The foundation math and the proposed numerical implementation are still at the core of the most popular modern scattering methods, yet the original implementation suffered from many numerical and stability issues, and basically doomed Chandrasekhar’s analytic approach for any but the isotropic and Rayleigh scattering problems. In the 1970s, the discrete ordinate method was further improved and many numerical enhancements were developed to improve its accuracy (e.g., Liou, 1973; Wiscombe, 1977). Despite their improved accuracies and enhanced numerical methods, these codes still had instabilities and issues at high opacities, requiring a very high number of computational layers and scattering polar angles. For instance, in the popular delta-Eddington method, the high opacity instability was sidestepped by subdividing layers until each sub-layer was optically thin, which was extremely computationally expensive and probably impractical for many problems.

In the 1980s, the foundational work by Stamnes and others, led to the now widely used DISORT package (Stamnes et al., 2000, 1988), which captures the pioneering discrete ordinate math by Chandrasekhar, the improvements done in the 1970s and finally solved the many issues affecting this method (e.g., stable for high opacities, accurate for low number of polar angles). Since its inception, DISORT has been constantly updated and improved, and the core foundational concepts have not substantially changed since then. In PSG, we employ the core methods of DISORT 2.1 written in C by Dowling and colleagues (Buras et al., 2011) which we adapted for non-LTE and optimized to operate with a variety of spectral grids (e.g., line-by-line, correlated-k, surface scattering





grids) as employed by the PSG radiative transfer algorithm. The model also includes correction for pseudo-spherical geometry as described by (Dahlback and Stamnes, 1991).

## 2. Theory of radiative transfer in a scattering medium

Solving the scattering problem requires of balancing out the fluxes and radiation across the layers in order to preserve energy conservation and the pre-defined scattering properties of the medium. For this report, we will only present a summarized set of equations as those presented in Stamnes et al. (2000). Please refer to that document for a more complete and detailed mathematical description of the scattering methods. The fundamental core equation used in PSG is the following, which defines how flux is gained and lost at every layer:

$$\mu \frac{dI(\tau, \mu, \phi)}{d\tau} = I(\tau, \mu, \phi) - J(\tau, \mu, \phi) \quad (1)$$

where  $I$  is the intensity at the layer,  $\tau$  is the layer opacity (a metric for depth/altitude),  $\mu$  is the cosine of the polar angle,  $\phi$  is the azimuth angle and  $J$  is the source function. The source function includes two main terms:

$$J(\tau, \mu, \phi) = \frac{w(\tau)}{4\pi} \int_0^{2\pi} \int_{-1}^1 I(\tau, \mu', \phi') P(\tau, \mu, \phi; \mu', \phi') d\mu' d\phi' + Q(\tau, \mu, \phi) \quad (2)$$

where the first term captures the radiation being scattered into this layer from other polar ( $\mu'$ ) and azimuth ( $\phi'$ ) angles via the phase function  $P$ , and where  $w$  is the single scattering albedo of the medium. The second term is described by  $Q$  which refers to the direct beam radiation coming from the Sun, and the isotropic thermal emission emanating from this source:

$$Q(\tau, \mu, \phi) = Q^{thermal}(\tau) + Q^{beam}(\tau, \mu, \phi) \quad (3)$$

$$Q^{thermal}(\tau) = [1 - w(\tau)]S(\tau) \quad (4)$$

$$Q^{beam}(\tau, \mu, \phi) = \frac{w(\tau)}{4\pi} F_* P(\tau, \mu, \phi; -\mu_0, \phi_0) e^{-\tau/\mu_0} \quad (5)$$

where  $S(\tau)$  is simply the Planck function  $B[T(\tau)]$  in a LTE regime, yet in PSG we allow for non-LTE sources by incorporating their contribution to this term (see details in chapter 4).  $F_*$  is the solar flux at the top of the atmosphere and  $\mu_0$  and azimuth  $\phi_0$  are the polar and azimuth angles of the Sun.

### 2.1 Discretization of the azimuthal intensities, Fourier series and Legendre polynomials

Solving for  $I$  from equation (1) across all layers ( $L$ ) would involve sets of differential equations across three dimensions (see Figure 1), which are not directly solvable, so some transformations and discretizations will be required to determine the layer-by-layer intensities. Foremost, let us consider that the phase function  $P$  depends only on the angle  $\theta$  between the incident and scattered beams.

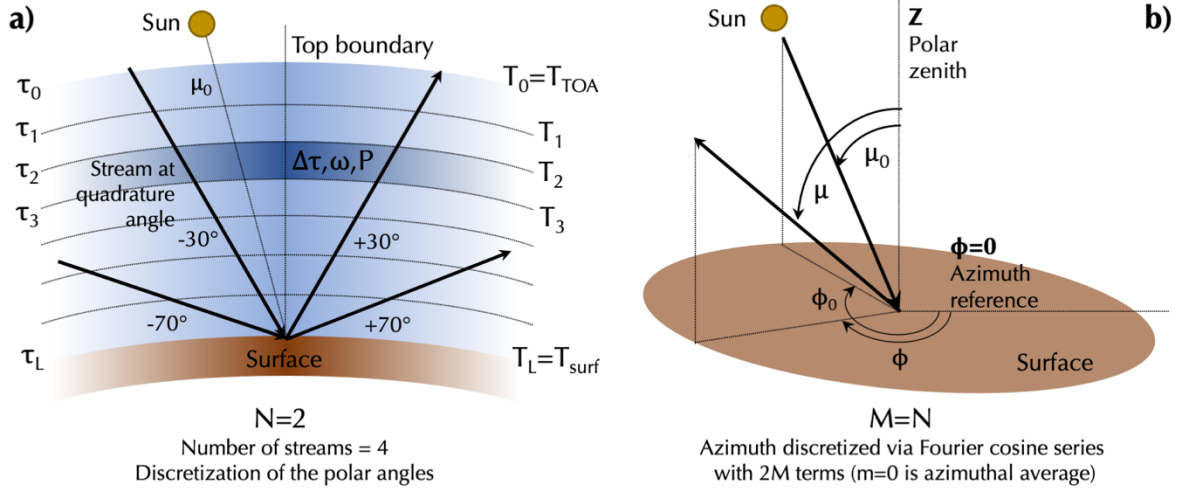


**Figure 1:** Discretization of the 3D pseudo-spherical scattering geometry. The vertical dimension is discretized in layers with specific opacities ( $\Delta\tau$ ), single scattering albedo ( $w$ ), phase function ( $P$ ) and temperature ( $T$ ). **a)** The number of streams ( $2N$ ) allows to sample the medium via a set of polar angles, which for this example of  $N=2$ , would correspond with Gaussian quadrature streams at  $\pm 30$  and  $\pm 70$  degrees. **b)** The azimuthal dependence is modeled by separating the flux in Fourier cosine series with  $m < (2M=2N)$  and the phase function in Legendre polynomials of order  $M$ .

This fact can be utilized to factor out the  $\phi$ -dependence in the equations. Let us then set that the intensity can be divided in independent terms of a Fourier cosine series as:

$$I(\tau, \mu, \phi) = \sum_{m=0}^{2M-1} I^m(\tau, \mu) \cos m(\phi_0 - \phi) \quad (6)$$

where  $2M$  is the number of azimuth components, and  $m$  the index among the series ( $\phi$  is azimuth, and  $\phi_0$  is solar azimuth angle), with  $m=0$  defining the azimuthally average intensity. In a similar fashion, we can expand the phase function ( $\Theta$  is phase) in a series of  $2M$  Legendre polynomials  $P_\ell$  as:

$$P(\tau, \mu, \phi; \mu', \phi') = P(\tau, \cos \Theta) \quad (7)$$

$$P(\tau, \cos \Theta) = \sum_{\ell=0}^{2M-1} (2\ell + 1) g_\ell(\tau) P_\ell(\cos \Theta) \quad (8)$$

$$\cos \Theta = \mu\mu' + \sqrt{(1 - \mu^2)(1 - \mu'^2)} \cos(\phi - \phi') \quad (9)$$



$$P(\tau, \cos \Theta) = \sum_{\ell=0}^{2M-1} (2\ell + 1) g_{\ell}(\tau) \left\{ P_{\ell}(\mu) P_{\ell}(\mu') + 2 \sum_{m=1}^{\ell} \Lambda_{\ell}^m(\mu) \Lambda_{\ell}^m(\mu') \cos m(\phi - \phi') \right\} \quad (10)$$

where  $g_{\ell}$  are the Legendre coefficients of the phase function, and  $\Lambda$  the normalized associated Legendre polynomial, which are defined as:

$$\Lambda_{\ell}^m(\mu) = \sqrt{\frac{(\ell - m)!}{(\ell + m)!}} P_{\ell}^m(\mu) \quad (11)$$

These transformations allow us to remove the azimuth term from the system of equations, and the scattering problem can be then decoupled in independent Fourier azimuth components as:

$$\mu \frac{dI^m(\tau, \mu)}{d\tau} = I^m(\tau, \mu) - J^m(\tau, \mu) \quad m = 0, 1, \dots, 2M - 1 \quad (12)$$

where the source function is given by the integral across polar angles of:

$$J^m(\tau, \mu) = \int_{-1}^1 D^m(\tau, \mu, \mu') I^m(\tau, \mu') d\mu' + Q^m(\tau, \mu) \quad (13)$$

and the scattering terms and direct sources are defined as:

$$D^m(\tau, \mu, \mu') = \frac{\omega(\tau)}{2} \sum_{\ell=m}^{2M-1} (2\ell + 1) g_{\ell}(\tau) \Lambda_{\ell}^m(\mu) \Lambda_{\ell}^m(\mu') \quad (14)$$

$$Q^m(\tau, \mu) = X_0^m(\tau, \mu) e^{-\frac{\tau}{\mu_0}} + \delta_{m0} Q^{thermal}(\mu) \quad (15)$$

$$X_0^m(\tau, \mu) = I_0 \frac{\omega(\tau)}{4\pi} (2 - \delta_{m0}) \sum_{\ell=m}^{2M-1} (-1)^{\ell+m} (2\ell + 1) g_{\ell}(\tau) \Lambda_{\ell}^m(\mu) \Lambda_{\ell}^m(\mu_0) \quad (16)$$

where  $\delta_{m0}$  defines if this term relevant for  $m=0$  ( $\delta_{m0}=1$  for  $m=0$ , otherwise  $\delta_{m0}=0$ ). This set of transformations removes the azimuth ( $\phi$ ) dependence and it also decouples the different Fourier component of intensity.

## 2.2 Discretization of the polar angles, Gaussian quadrature angles

In the previous section, a method to treat one of the dimensions has been identified. The next stage is addressing the polar angle integral, as presented in equation 13. This can be done by employing Gaussian quadrature angles, since it makes phase function renormalization unnecessary, implying that energy is conserved in the computation (Wiscombe, 1977). The reason for this is simply that the Gaussian rule is based on the zeros of the Legendre polynomials which are also used for expanding the phase function. Following this concept, equations 12 and 13 can be defined for a discretized polar angle scheme as:

$$\mu_i \frac{dI^m(\tau, \mu_i)}{d\tau} = I^m(\tau, \mu_i) - J^m(\tau, \mu_i) \quad m = 0, 1 \dots, 2M - 1 \quad i = \pm 1, \dots, \pm N \quad (17)$$

$$J^m(\tau, \mu_i) = \sum_{\substack{j=-N \\ j \neq 0}}^N w_j D^m(\tau, \mu_i, \mu_j) I^m(\tau, \mu_j) + Q^m(\tau, \mu_i) \quad (18)$$

where  $\mu_i$  is called a “stream”, in which this is a  $2N$ -stream solution ( $N$  is labeled NMAX in PSG). When only a limited number of streams is considered (2: NMAX=1, 4: NMAX=2), there exist analytical solutions to the systems of equations summarized above (Kylling et al., 1995; Toon et al., 1989), which are popularly employed by the planetary community. The analytical solution for NMAX=1 is effective for calculating fluxes and in energy balance calculations, but it can lead to substantial errors when computing intensities/radiances at a specific direction due to the coarse sampling of the polar angles and phase function (see section 4). We have compared the solutions obtained with NMAX=1 in PSG to the analytical method as presented in (Kylling et al., 1995; Toon et al., 1989), and obtained very good agreement when selecting the same quadrature angles.

At this stage, it is important to make a note regarding the required number of azimuthal components ( $2M$ ). As summarized above, it is related to the number of Legendre polynomials of the phase function which can be hundreds or even thousands of terms long. In practice, however, the intensity expansion is much shorter, and what practically limits the length is the number of quadrature angles. Following Chandrasekhar and DISORT, it has been customary not to extend these expansions beyond the number of quadrature angles, so for a  $2N$  calculation, we define the maximum number of terms to be  $2M=2N$ .

Following these transformations, equations 17 and 18 become a linear combination of  $I^m$  (independent for each  $m$  component) and at all quadrature angles  $\mu_i$ . At each layer, this system of differential equations can be reorganized in matrix form, and presented as for the upwelling (+) and downwelling streams (-):

$$\frac{d}{d\tau} \begin{bmatrix} I^+ \\ I^- \end{bmatrix} = \begin{bmatrix} -\alpha & -\beta \\ \beta & \alpha \end{bmatrix} \begin{bmatrix} I^+ \\ I^- \end{bmatrix} - \begin{bmatrix} Q'^+ \\ Q'^- \end{bmatrix} \quad (19)$$

where  $\alpha$  and  $\beta$  may be interpreted as layer transmission and reflection operators, respectively, and are ( $N \times N$ ) matrixes. The problem then becomes of set of  $2N \times 2N$  differential equations at each layer.



In solving this set of linear ordinary differential equations (ODEs), one can break the solution into two parts, the homogeneous and particular solution. The homogeneous solution satisfies the ODEs with no source term ( $Q^{\pm} = 0$ ), and does not have to satisfy the boundary conditions. While, the particular solution is a solution with the source terms included, it is not yet required to satisfy the boundary conditions. By reorganizing equation 19, one can solve the homogenous solution of this equation by defining  $k$  as the eigenvalues and  $G^{\pm}$  as the eigenvectors, which is customary to be expressed in the form  $G^{\pm} = I^{\pm} e^{k\tau}$ , yielding:

$$\begin{bmatrix} \alpha & \beta \\ -\beta & -\alpha \end{bmatrix} \begin{bmatrix} G^{+} \\ G^{-} \end{bmatrix} = k \begin{bmatrix} G^{+} \\ G^{-} \end{bmatrix} \quad (20)$$

This numerical solving of the homogenous system of equations is done by employing the DISORT AYMTX function, which is a version of EISPACK solver using real arithmetic. Particular solutions are then computed employing linear algebraic system of equations for every layer for solar pseudo-sources and for thermal emission allowing for linear-in-optical-depth variation of the Planck function within each layer.

### 2.3 Solving the whole system, applying boundary conditions

We have now identified the eigenvalues and eigenvectors that satisfy the differential equations at each layer, but we need to apply realistic boundary conditions to the whole system to determine the layer-by-layer intensity field. Integrating the eigenvalues and eigenvectors previously determined and re-organized the system of equations, one can establish that intensity at each layer can be described by a particular linear form in the optical depth  $\tau$ :

$$I(\tau, \mu_i) = \sum_{j=-N}^N C_j G_j(\mu_i) e^{-k_j \tau} + \delta_{m0} [Y_0(\mu_i) + Y_1(\mu_i) \tau] \quad (21)$$

where the  $C_j$  scaling coefficients for each stream are unknown. By setting this as a set of linear equations across layer ( $\tau$ ) and polar angle ( $\mu_i$ ), one can define solution boundaries and then calculate a solution to the system of linear equations. For instance, the fluxes at the top of the atmosphere ( $\tau=0$ ) are known, while the reflecting/emitting properties of the surface ( $\tau=\max$ ) are also defined. Solving  $C$  across the whole atmosphere, then constitutes a  $(2N \times L) \times (2N \times L)$  system of linear algebraic equations from which the  $2N \times L$  unknown coefficients  $C_{jp}$  ( $j=\pm 1, \dots, \pm N$ ;  $p=1, \dots, L$ ) must be determined.

This set of equations is ill-conditioned for large optical thicknesses, so a scaling transformation is applied following the methods presented in (Stamnes and Conklin, 1984), which entirely eliminates this problem at its source. Numerically, the solution to this banded matrix inversion is done with the LINPACK SGBSL algorithm.

## 2.4 Scattering numerical algorithm

The algorithm for determining the layer-by-layer scattering intensities can be organized into a sequence of nested loops (see Figure 2). Initially, the code will allocate the matrix memories, and then compute the Legendre polynomial coefficients (see equation 11) and Gauss quadrature angles / weights which are common to all calculations and wavelengths. At the center of the algorithm, the code will determine the eigenvalues and eigenvectors (layer-by-layer), which are then used for each Fourier term component to determine specific intensities for that  $m^{\text{th}}$  term. At each  $m$  iteration, the code will test for convergence by analyzing the intensity of the Fourier term with respect to the total intensity, and will stop when the required accuracy is achieved or when the maximum number of terms is reached ( $m < 2M = 2N$ ). Finally, the intensities are computed for the desired azimuth angle and corrected for delta-M (Wiscombe, 1977) and for N-stream truncation employing the IMS method (Nakajima and Tanaka, 1988). The parameter LMAX in PSG defines the number of Legendre polynomials in the description of the phase function (equation 8). As explained before, the code computes the scattering solution only using  $2M = 2N$  Legendre terms, yet by employing the IMS method, the model can add information for terms beyond  $2M$  up to the desired LMAX number of terms. In PSG, LMAX is always at least  $2 \times N_{\text{MAX}}$ .

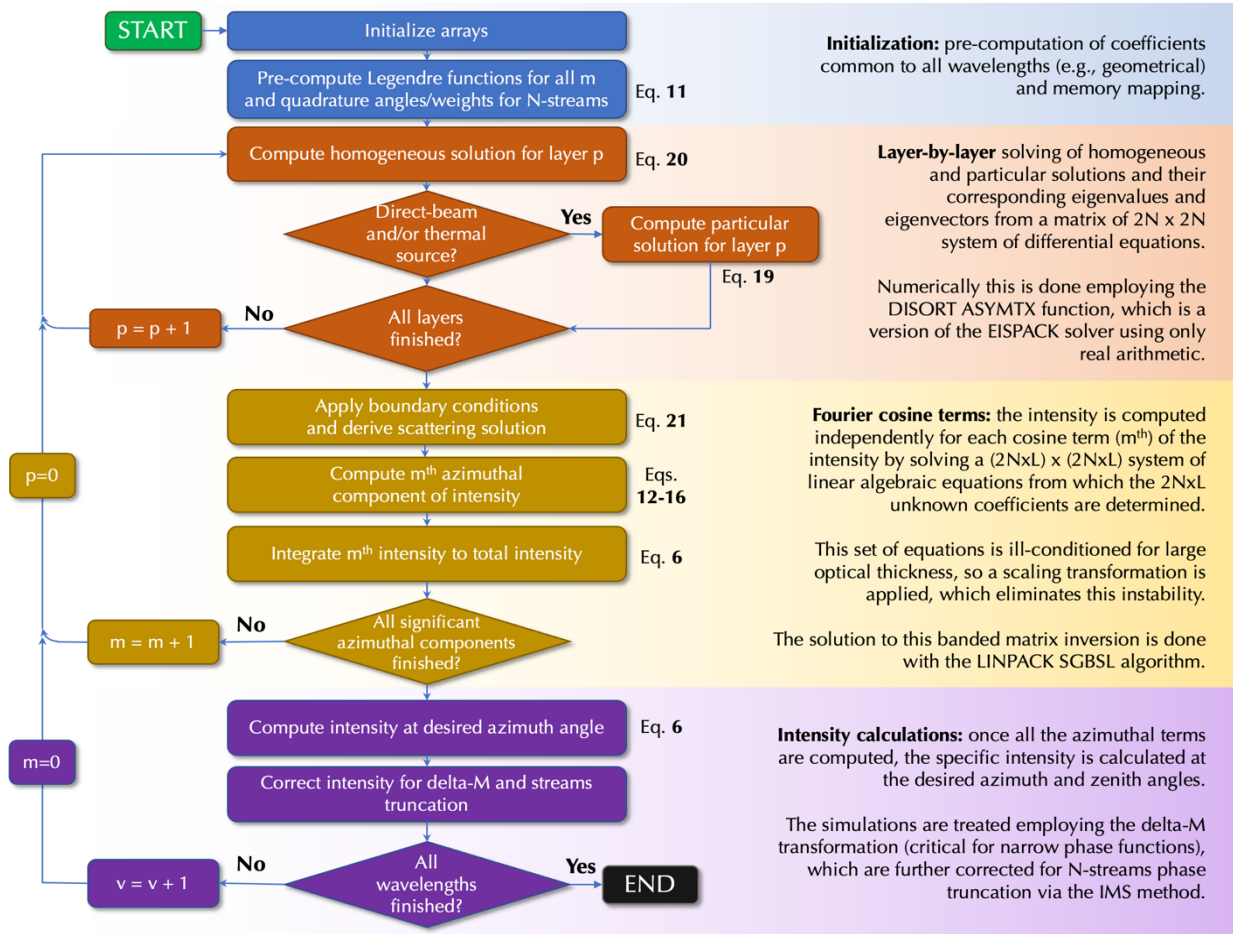


**Figure 2:** Overview of the operations performed by the scattering module. Flow chart adapted from (Stamnes et al., 2000).





### 3. Mie scattering and calculation of the aerosol models

The three key input parameters for a multiple scattering calculation are opacity ( $\tau$ , see equations 2-5), single scattering albedo ( $w$ , see equations 2-5) and the Legendre coefficients of the phase function ( $g$ , see equation 10). The opacity of an aerosol is determined by the extinction coefficient [ $\text{m}^2/\text{kg}$ ] and the mass column density [ $\text{kg}/\text{m}^2$ ] of the aerosol in the layer. For molecular Rayleigh scattering,  $\tau$  is determined from the polarizability of the molecule (Sneep and Ubachs, 2005), with  $\omega=1$ ,  $g_0=1.0$  and  $g_2=0.1$ .

The extinction coefficient, scattering albedo and Legendre coefficients are dependent on the wavelength, composition, and size/shape of the scattering particles. In PSG, scattering models for a variety of aerosols are available, which are prescribed in two forms. One form is that of wavelength [ $\mu\text{m}$ ], extinction coefficient [ $\text{m}^2/\text{kg}$ ], scattering albedo for each Legendre term, which allow for arbitrary scattering models to be used. Such models include T-matrix scattering models, which are computed for a specific particle size distribution and composition (Wolff et al., 2009). In addition, PSG has pre-computed Mie scattering models for a large variety of species and particle radius distributions. These models contain the wavelength [ $\mu\text{m}$ ], extinction coefficient [ $\text{m}^2/\text{kg}$ ], scattering albedo [ $\omega$ , 0 to 1], and Henyey-Greenstein (HG)  $g$  asymmetry factor [-1 to 1]. The HG phase function is defined as:

$$P(\theta) = \frac{1 - g^2}{(1 - 2g \cos \theta + g^2)^{3/2}} \quad (22)$$

The Mie implementation for these models is based on (Bohren and Huffman, 1983), and considers 20 angles of scattering with 200 size bins having  $\sigma_{\text{peak}}: r_{\text{eff}}/1.50833$ . The models are computed for size distributions centered at different mean size distributions (0.01, 0.05, 0.1, 0.5, 1.0, 5.0, 10.0, 50.0, 100.0  $\mu\text{m}$ ) and considering different compositions. The underlying indices of refraction of the particles is dependent on the composition of the aerosol, and in PSG we mostly employ the optical constants in the HRI database (HITRAN Refractory Index, Massie and Hervig 2013). We also complement this database with optical constants from other laboratory sources.

### 4. Selection of the number of stream pairs (NMAX) and Legendre terms (LMAX)

As we summarized in the previous sections, solving for the multiple scattering in a multi-layer atmosphere involves the discretization and separation of the problem into three dimensions: depth/ $\tau$  (L or number layers), number of stream pairs (2N) and number of azimuthal terms (2M). In PSG as in other multiple scattering solvers, we assume  $2N = 2M = 2N_{\text{MAX}}$ . We can use information of Legendre terms beyond 2M up to a desired LMAX by employing the delta-M (Wiscombe, 1977) and IMS methods (Nakajima and Tanaka, 1988).

The calculation requirement scales linearly with L, yet it grows immensely with NMAX, in the order of NMAX to the power of 3. This means that 10 times more streams would lead to factor of 1,000 longer computation time. Higher values of NMAX, LMAX and L would lead to greater accuracy but require much larger number of calculations, with perhaps minimum improvement in accuracy. In that sense, a careful definition of these parameters is critical. Importantly, the a-posteriori IMS

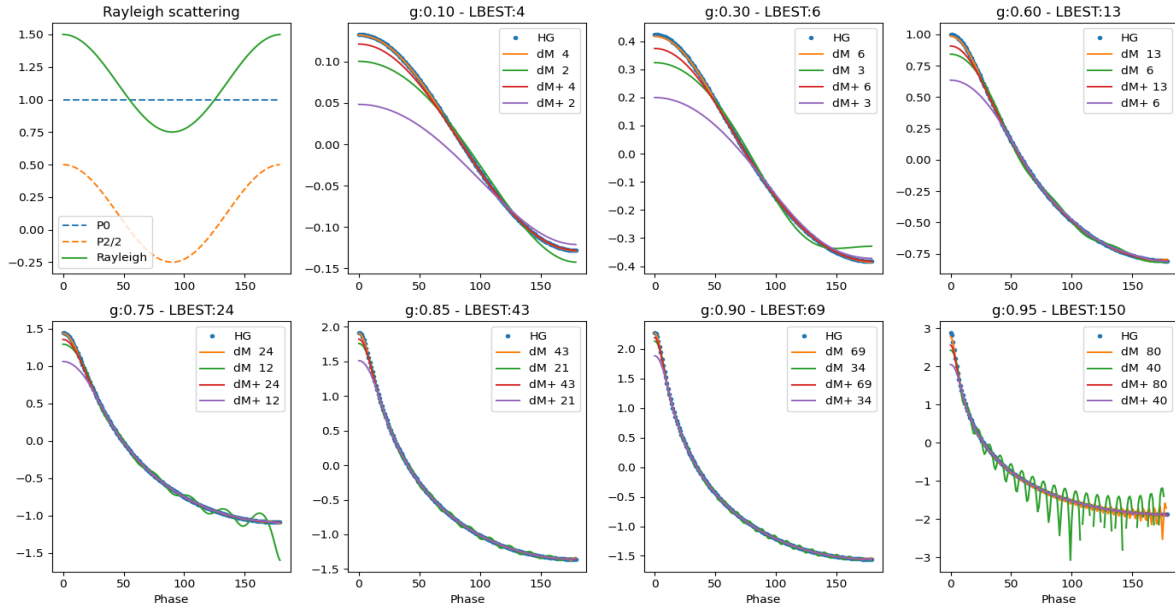


**Figure 3:** Comparison of different methods for modeling Rayleigh and Henyey-Greenstein phase functions with Legendre polynomials. LBEST is the optimum value of terms as defined in (Nakajima and Tanaka, 1988) with an accuracy of 0.5%. The y-values of the g-plots are in  $\log_{10}$  of the intensity. The plots show how the delta-M and new delta-M+ methods perform for different values LMAX and when considering the optimum LBEST value. We have capped LMAX to be 80. In general, the delta-M correction produces reasonable results even at half LMAX, while the delta-M+ solution removes the strong ringing, yet it struggles at low phase angles.

correction has been demonstrated to be quite accurate (Kokhanovsky et al., 2010) in compensating for the truncation of the Legendre terms with the delta-M method, and it is relatively inexpensive. For instance, a large increase in the number of LMAX terms (beyond 2M) would only lead to marginal (10-20%) greater computational times.

Recently, an improved phase truncation method for modeling the forward scattering peak with a Dirac delta function has been developed, the delta-M+ method (Lin et al., 2018). Compared with the original delta-M method (Wiscombe, 1977), the delta-M+ model has the same computational efficiency, but for radiance computations, its accuracy and stability are estimated to increase greatly. This new method provides generally very good results with low number of LMAX for highly asymmetrical scatterers, yet it introduces higher errors at lower phase angles. Perhaps, the IMS correction could be adapted to this new method, but this has not been demonstrated nor fully tested yet. For that reason, in PSG, we maintained the classical delta-M and IMS method, yet we will be exploring this new method more closely for a potential integration in the near future.

To showcase the effects of LMAX on the description of the phase function, we have computed phase functions for a selection of scatterers, from highly symmetrical with  $g=0.1$  to highly forward peaked scatterers with  $g=0.95$ . For numerical reasons in PSG, and also for physical reasons, the maximum value of  $g$  is capped to 0.95 (Andrews et al., 2006; Fu, 2007; Granate et al., 2016). We tested the delta-M and delta-M+ methods with a selection of different terms.

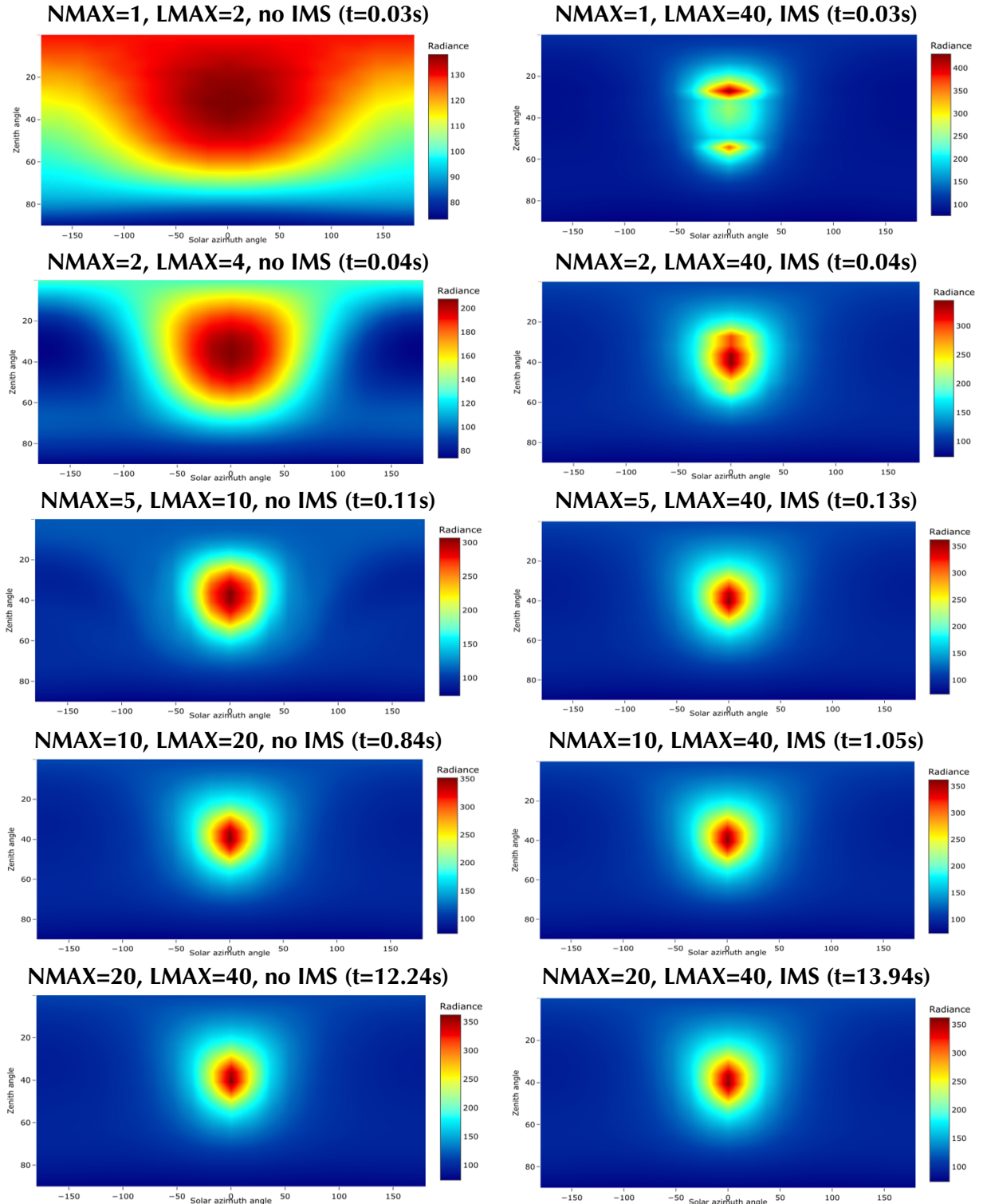


**Figure 4:** Comparison of full-sky scattering simulations (441 sky points x 100 wavelengths) for water-ice ( $g=0.85$ ) and Rayleigh for different values of NMAX, LMAX and with/without IMS. The default in PSG is with IMS. In brackets, the required computational time is presented, which grows greatly with NMAX and modestly with LMAX (compare IMS and no IMS). As shown in Figure, LBEST is 43 for  $g=0.85$ , so at LMAX=43 we should have convergence in the solution.

Level of asymmetry (g value)	Forward/backward peak ratio $P(0^\circ)/P(180^\circ)$	Number of stream pairs (NMAX) when employing IMS	Number of Legendre phase terms (LMAX)
Lower/equal to 0.1	1.0	1*	2
Greater than 0.1	1.8	2*	4
Greater than 0.3	6.4	2*	6
Greater than 0.6	64	3*	10
Greater than 0.75	343	3*	20
Greater than 0.85	729	4*	30
Greater than 0.90	6859	5*	50
Greater than 0.94	33802	5*	80

**Table 1:** Suggested minimum values of NMAX and LMAX according to asymmetry  $g$  and the corresponding forward/backward ratio  $[(1+g)/(1-g)]^3$ .  $g$ -values are internally capped to 0.95 in PSG. These are highly hypothetical, and the actual needed values will depend on the parameters of the simulation. Importantly, these have been defined favoring computational speed and performance. \*For hemispheric modeling with high sub-sampling, NMAX=1 may be sufficient.

It has been shown that errors lower than 0.5% can be achieved with  $LMAX = 3.77P(0)^{0.553}$  (Nakajima and Tanaka, 1988), where  $P(0)$  is the intensity of the phase function at phase=0. We define this metric to be LBEST, yet such number of terms can reach several hundred for highly asymmetric functions ( $g > 0.95$ ). Importantly, errors in the phase-function do not directly propagate to radiance errors. They are somewhat smoothed due to the intrinsic nature of collecting scattered light originating from many directions.

Considering that the cost of including higher LMAX values is relatively low when employing the IMS correction, one could select a relatively high number conservatively. Yet, it is always important to test the selection of NMAX and LMAX at higher values and determine when the synthesized radiances converge to the needed accuracy. One can use Figure 3 as a first guide in determining the number of LMAX as a function on the  $g$  value of the considered aerosols. PSG will also perform recommendations / warnings on the needed LMAX based on the here presented simulations.

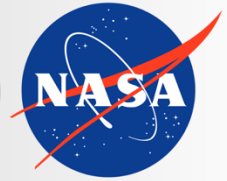
Determining NMAX is somewhat more critical considering the high computational penalty, yet an “optimum” value will depend strongly on the considered geometry and scattering elements. In the classical sense and without the IMS correction, the number of Legendre terms and azimuthal components is capped in the simulation to 2M, so  $NMAX = LMAX/2$ . For a phase function with  $g=0.95$  and  $LMAX=150$ , one would need  $NMAX=75$ . Such high NMAX would require 52000 times more time than a simulation with  $NMAX=2$ . If a simulation takes 1 second with  $NMAX=2$ , it would take ~15 hours with  $NMAX=75$ . Such requirement is astronomical, and quite impractical. Thankfully to the IMS correction, one can achieve solutions for  $LMAX=150$ , with  $NMAX=5$  at comparable accuracies. In general, a higher value of NMAX is recommended though. In Table 1, we present minimum NMAX/LMAX values based on the asymmetry  $g$  value, yet these are highly



hypothetical and would depend greatly on the problem in hand. To test for this, we have run full sky simulations with water-ice clouds having  $g=0.85$  and also including Rayleigh scattering. We compared the simulations for different levels of NMAX, and when employing the IMS correction ( $LMAX > 2NMAX$ ) or without it ( $LMAX = 2NMAX$ ). It is nicely shown that the IMS method is quite effective in correcting for the truncation of the phase function with low values of NMAX. When modeling spectra across a full planetary disk over multiple incidence/emission angles (see sub-sampling method in chapter 2), the azimuthal dependence is less relevant since it becomes “smoothed out” and a lower number of NMAX is sufficient. It has been successfully shown that the  $NMAX=1$  approach is relatively accurate in such cases (e.g., Toon et al., 1992).







**Planetary Spectrum Generator**  
National Aeronautics and Space Administration

# Chapter 6: **Surface Scattering Modeling**

**Villanueva, Protopapa, Liuzzi, Faggi and  
PSG team**



## 1. Surface modeling in PSG

As light arrives to a surface at a particular wavelength, it can either be absorbed or scattered (reflected). Processes such as surface fluorescence or Raman will transfer some of this energy to a different wavelength, but for our treatment in PSG, we simply consider this as an absorption process at this wavelength. The direction and intensity of the scattered light requires of complex modeling, and several methods exist (e.g., Lambert, Hapke, etc.). The light absorbed will heat the surface, and this together with other internal sources of heat will lead to thermal emission (with an associated directionality and effectiveness/emissivity). How effective the surface scatters light is defined by the single scattering albedo  $w$ , where 0 means the light is totally absorbed and to 1 the light is totally scattered back.

The reflected flux from an object will ultimately depend on how the surface scatters back, and we would then require information about the observing geometry, the emission direction and the geometry of the incidence fluxes. Three angles are used to define the geometry:  $i$  “incidence angle” is the angle between the Sun (or host-star) and the line perpendicular to the surface at the point of incidence, called the normal;  $e$  “emission angle” is the angle between the surface normal and the observer; and  $g$  “phase angle”, which is the angle between the source and observer (not to be confused with solar azimuth angle, which is the projection of the phase angle).

The quantity that captures how much light is being reflected towards the observer is called  $r(i,e,g)$  “bidirectional reflectance” ( $r(i,e,g)=I(i,e,g)/J$ , where  $I$  is the scattered radiance and  $J$  is the incidence radiance) which is in units of  $[sr^{-1}]$ , with steradians  $[sr]$  being a unit of solid angle. A common alternative quantity is the BRDF or “bidirectional-reflectance distribution function”  $[sr^{-1}]$ , which describes the reflectivity of the surface with respect to a Lambertian sphere, and it is simply  $r(i,e,g)/\cos(i)$ . Similarly for emission, directional emissivity  $\epsilon(e)$  is the ratio of the thermal radiance emerging at emission angle  $e$  from the surface with temperature  $T$  with respect to a black body at the same temperature.

Once the geometry ( $i,e,g$ ) and the specific scattering properties (e.g.,  $w$ ) are defined, we would then need a scattering model to accurately model the emissions from the target’s surface. In PSG, four core models are available: Lambert (isotropic scattering), Hapke (parametric surface scattering), Lommel-Seeliger (weakly scattering / diffuse surfaces) and Cox-Munk (specular glint scattering model).

## 2. Lambert model: isotropic scattering

A Lambertian surface is one that scatters isotropically, as an ideal matte or a perfectly diffusive reflecting surface. The emissivity can be defined as  $\epsilon = 1 - w$ , while the bidirectional-reflectance distribution function is defined as (adapted from Hapke, 2012a [H12 hereafter] eq. 8.12):

$$BRDF = \frac{w}{\pi} \quad (1)$$

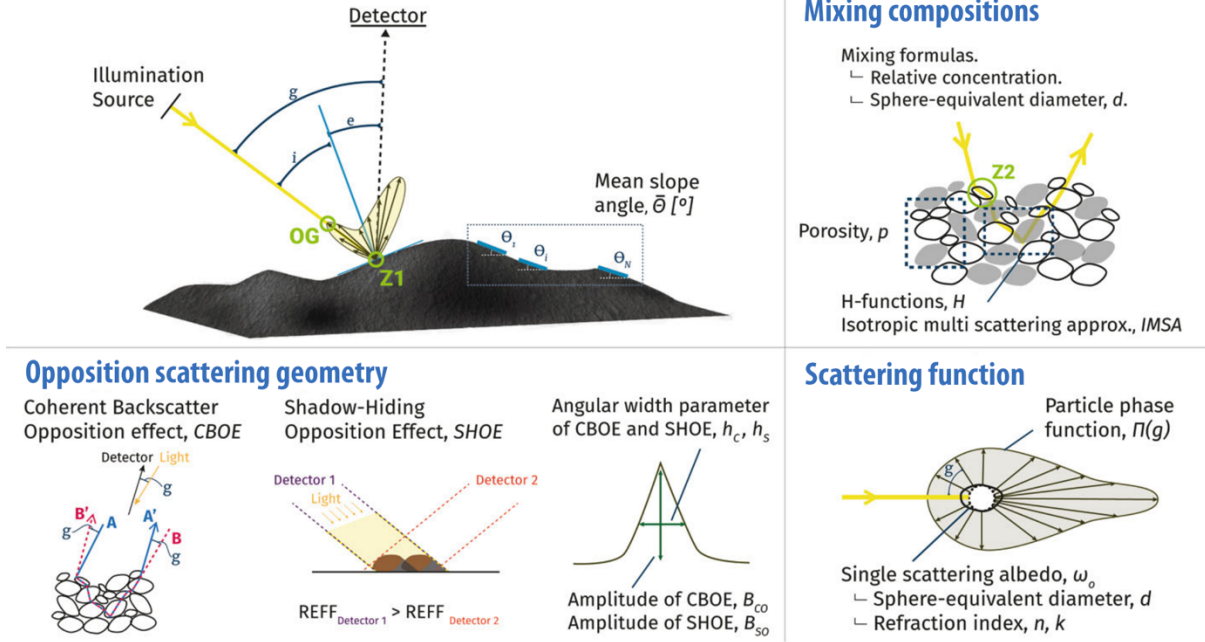


**Figure 1:** Surface scattering geometry and components of the Hapke surface model. Roughness accounts for the variability of illumination / emission angles, while by combining several components via mixing equations, the heterogeneity of the surface can be captured. The opposition effects are modeling via the CBOE and SHOE terms. Figure adapted from (Pommerol et al., 2019).

### 3. Hapke model: parametric surface modeling

The Hapke scattering model is a physically motivated model that approximates the solution for radiative transfer for a porous, irregular, and particulate surface. This model has been advancing over the last decades and captures processes and radiative transfer phenomena parameterized with approximations, which are motivated by the basic physical principles of scattering. In PSG, we implement the generic Hapke's "Isotropic Multiple-Scattering Approximation" (IMSA) model, which is useful if the surface scattering function is not too anisotropic and can be mostly described by a single-scattering term. The implementation also includes Hapke's shadow-hiding opposition effect (SHOE) factor, the coherent backscatter opposition effect (CBOE) and a compensation for surface roughness. The BRDF can be then modeled following H12 (eq. 12.55) as:

$$BRDF = K \frac{w}{4\pi \mu_{0e} + \mu_e} \left[ P(g)[1 + B_{so}B_s(g)] + H\left(\frac{\mu_{0e}}{K}\right)H\left(\frac{\mu_e}{K}\right) - 1 \right] [1 + B_{co}B_c(g)]S(i, e, g) \quad (2)$$

where  $K$  is the porosity coefficient,  $\mu_{0e}$  and  $\mu_e$  are the cosine of the effective incidence and emission angles respectively (see below),  $P(g)$  the phase function,  $B_{so}$  is the amplitude of the opposition effect (0 to 1),  $B_s(g)$  is the shadow-hiding opposition function,  $B_{co}$  is the amplitude of the coherent backscatter opposition effect (0 to 1),  $B_c(g)$  is the backscatter angular function,  $H(x)$  is the

Ambartsumian–Chandrasekhar H function, and S is the shadowing/roughness function. The phase function can be characterized using different representations, and in PSG four functions are available: HG1, HG2, HGH and LP2, described here after.

**The single lobe Henyey-Greenstein (HG1):** has one parameter  $\xi$  (asymmetry parameter, -1:backscatterer to 1:forward) defined as (H12 eq. 6.5):

$$P_{HG1}(g) = \frac{1 - \xi^2}{(1 + 2\xi \cos g + \xi^2)^{3/2}} \quad (3)$$

The sign of  $\xi$  may differ depending on the definition of the “phase”  $g$  angle and the sign of the cosine term used for the HG1 function. In PSG,  $g=0$  implies the backward direction, and therefore negative  $\xi$  numbers imply backscattering (typical).

**The double-lobed Henyey-Greenstein (HG2):** has parameters  $b$  (asymmetry parameter, 0 to 1) and  $c$  (back-scattering fraction, -1 to 1) and it is defined as (H12 eq. 6.7a):

$$P_{HG2}(g) = \frac{1+c}{2} \frac{1-b^2}{(1-2b \cos g + b^2)^{3/2}} + \frac{1-c}{2} \frac{1-b^2}{(1+2b \cos g + b^2)^{3/2}} \quad (4)$$

There are conflicting definitions of the  $c$  parameter (some use  $[1-c]$  and  $[c]$  as scalers), so please consider this carefully when entering this parameter into PSG.

**Henyey-Greenstein Hapke/hockey phase function (HGH):** It has been observed that for the HG2 function, there is an inverse relationship between the  $b$  and  $c$  parameters following a hockey stick shape. As such, the HGH phase function can be defined following Hapke, 2012b (eq. 8) as:

$$c = 3.29 \exp(-17.4b^2) - 0.908 \quad (5)$$

**The two-term Legendre polynomial function (LP2)** has parameters  $b$  and  $c$ , and it is defined as (H12 eq. 6.3 with  $P_0$ ,  $P_1$ ,  $P_2$  defined in appendix C.4):

$$P_{LP2}(g) = 1 + b \cos g + c(1.5 \cos^2 g - 0.5) \quad (6)$$

The shadow-hiding opposition function can be approximated following H12 (eq. 9.22) as:

$$B_s(g) = \frac{1}{1 + (1/h_s) \tan g/2} \quad (7)$$

where  $h_s$  is the width of the opposition surge. The backscatter angular function can be approximated following H12 (eq. 9.43) as:



$$B_C(g) = \left\{ 1 + [1.3 + K] \left[ \left( \frac{1}{h_C} \tan \frac{g}{2} \right) + \left( \frac{1}{h_C} \tan \frac{g}{2} \right)^2 \right] \right\}^{-1} \quad (8)$$

where  $h_C$  is the width of the backscatter function. The Ambartsumian–Chandrasekhar H function can be approximated with errors of less than 1% and following H12 (eq. 8.56) as:

$$H(x) = \left\{ 1 - wx \left[ r_0 + \frac{1 - 2r_0x}{2} \ln \left( \frac{1+x}{x} \right) \right] \right\}^{-1} \quad (9)$$

where  $r_0$  is the diffusive reflectance, which is calculated from the albedo factor  $\gamma = (1-w)^{1/2}$  as (H12 eq. 8.25):

$$r_0 = \frac{1 - \gamma}{1 + \gamma} \quad (10)$$

The porosity coefficient  $K$  is dependent on  $\phi$ , the filling factor or fractional volume filled by material (0: loose grains, 1: highly compacted material), given by (H12 eq. 7.45b):

$$K = \frac{-\ln(1 - 1.209\phi^{2/3})}{1.209\phi^{2/3}} \quad (11)$$

When employing the roughness term  $S$ , this implementation impacts the effective cosine of the incidence angles ( $\mu_0 \rightarrow \mu_{0e}$ ) and emission angles ( $\mu \rightarrow \mu_e$ ), where  $\mu_0 = \cos(i)$  and  $\mu = \cos(e)$ . The shadowing term and the new  $\mu_{0e}$  and  $\mu_e$  are calculated following H12 (eq. 12.63) as: when  $i \leq e$ :

$$\mu_{0e} = \chi(\theta_P) \left[ \cos i + \sin i \tan \theta_P \frac{\cos \psi E_2(e) + \sin^2(\psi/2) E_2(i)}{2 - E_1(e) - (\psi/\pi)E_1(i)} \right] \quad (12)$$

$$\mu_e = \chi(\theta_P) \left[ \cos e + \sin e \tan \theta_P \frac{E_2(e) - \sin^2(\psi/2) E_2(i)}{2 - E_1(e) - (\psi/\pi)E_1(i)} \right] \quad (13)$$

$$S = \frac{\mu_e}{\eta(e)} \frac{\mu_0}{n(i)} \frac{\chi(\theta_P)}{1 - f(\psi) + f(\psi)\chi(\theta_P)[\mu_0/\eta(i)]} \quad (14)$$

when  $e \leq i$ :

$$\mu_{0e} = \chi(\theta_P) \left[ \cos i + \sin i \tan \theta_P \frac{E_2(i) - \sin^2(\psi/2) E_2(e)}{2 - E_1(i) - (\psi/\pi)E_1(e)} \right] \quad (15)$$

$$\mu_e = \chi(\theta_P) \left[ \cos e + \sin e \tan \theta_P \frac{\cos \psi E_2(i) + \sin^2(\psi/2) E_2(e)}{2 - E_1(i) - (\psi/\pi)E_1(e)} \right] \quad (16)$$

$$S = \frac{\mu_e}{\eta(e)} \frac{\mu_0}{n(i)} \frac{\chi(\theta_P)}{1 - f(\psi) + f(\psi)\chi(\theta_P)[\mu/\eta(e)]} \quad (17)$$

Hapke parameter	Range	Hapke parameters for objects in our solar system					
		Pluto P2020	Europa B2020	Mars F2015	Moon S2014	C-type asteroids HV1989	S-type asteroids HV1989
P(g) phase function	HG1, HG2, HGH, LP2	HG1	HG2	HG2	HGH	HG1	HG1
$\xi$ or b phase coefficient	-1 to 1	-0.36	0.2 to 0.6	0.2 to 0.6	0.1 to 0.3	-0.47	-0.27
c phase coefficient	-1 to 1	-	0.1 to 0.9 alternative	0.1 to 1.0	-	-	-
B <sub>so</sub> opposition surge scaler	$\geq 0$	0.307	0.2 to 0.9		1.5 to 2.1	1.03	1.6
h <sub>s</sub> opposition surge width	$\geq 0$	0.206	0.2 to 0.7		0 to 0.12	0.025	0.08
$\theta$ roughness mean slope angle [degree]	0 to 40	20	6 to 27	5 to 25	23.4	20	20
$\phi$ filling factor	0 to 0.75	0.0	0.0	0.0	0.0	0.0	0.0
B <sub>co</sub> coherent backscattering scaler	0 to 1	0.074	0.0	0.0	0.0	0.0	0.0
h <sub>c</sub> width of coherent backscattering	$\geq 0$	0.0017	0.0	0.0	0.0	0.0	0.0

**Table 1** Summary of PSG accepted input parameters for the Hapke model. In yellow the range of each parameter is reported.

where

$$\theta_p = (1 - r_0)\theta \quad (18)$$

$$\psi = \arccos\left(\frac{\cos g - \cos i \cos e}{\sin i \sin e}\right) \quad (19)$$

$$f(\psi) = \exp(-2 \tan(\psi/2)) \quad (20)$$

$$\chi(\theta_p) = (1 + \pi \tan \theta_p^2)^{-1/2} \quad (21)$$

$$E_1(y) = \exp(-2/\pi \cot \theta_p \cot y) \quad (22)$$

$$E_2(y) = \exp(-1/\pi \cot^2 \theta_p \cot^2 y) \quad (23)$$

$$\eta(y) = \chi(\theta_p)[\cos y + \sin y \tan \theta_p (E_2(y)/(2 - E_1(y)))] \quad (24)$$





Thermal emission from a scattering surface will also have directionality, and the directional emissivity of an optically thick particulate medium can be defined following H12 (eq. 15.19) as:

$$\varepsilon = \gamma H(\mu) \quad (25)$$

Table 1 summarizes the parameters needed by PSG when performing Hapke modeling and their typical range. For comparison Hapke parameterizations and derivations for objects across our solar system are also listed, in which P2020: (Protopapa et al., 2020), B2020: (Belgacem et al., 2020), F2015: (Fernando et al., 2015), S2014: (Sato et al., 2014), HV1989: (Helfenstein and Veverka, 1989), and L2015: (Li et al., 2015).

#### 4. Lommel-Seeliger: dark and weakly scattering Lunar/asteroid/comet surfaces

For relatively dark objects with weakly scattering surfaces, the Lommel-Seeliger model performs well in capturing the variation of the scattered fluxes with respect to the source/observational angles. It is therefore the preferred model when interpreting the Moon, asteroids and other small bodies. The generalized Lommel-Seeliger is defined as (adapted from H12 eq. 8.35a):

$$\text{BRDF} = \frac{w}{4\pi} \frac{1}{\mu + \mu_o} P(g) \quad (26)$$

where  $w$  is the surface single scattering albedo and  $P(g)$  is the single-scattering phase function. Several disk-resolved models are based on this basic formalism (e.g., ROLO), and since this model is suitable for small unresolved dark bodies, it is the preferred method in PSG for modeling the disk-resolved BRDF of asteroids and comets. In the literature, there are several measurements and derivations of the “phase function” for unresolved bodies, but these refer to the integral phase function  $\Phi(g)$ , not to  $P(g)$ . We can re-normalize the empirically derived  $\Phi(g)$  to an effective surface  $P(g)$  by dividing by the integrated reflectance of a perfect Lommel-Seeliger object (adapted from H12 eq. 6.14):

$$\frac{\Phi(g)}{P(g)} = \left[ 1 - \sin \frac{g}{2} \tan \frac{g}{2} \ln \left( \cot \frac{g}{4} \right) \right] \quad (27)$$

**Lumme-Bowell phase function (HG):** The Lumme-Bowell model is a scattering model typically used in asteroid research and presented in Lumme and Bowell (1981). A simplified empirical version of the integral Lumme–Bowell model was adopted by the International Astronomical Union (IAU) in 1985 to describe the integral phase function of asteroids, and this function with slope parameter is adopted as (H12 section 12.5.2):

$$\Phi(g) = (1 - G)\Phi_1(g) + G\Phi_2(g) \quad (28)$$

$$\Phi_1(g) = \exp[-3.33(\tan g/2)^{0.63}] \quad (29)$$

$$\Phi_2(g) = \exp[-1.87(\tan g/2)^{1.22}] \quad (30)$$



**Figure 2:** Lommel-Seeliger surface modeling of the Moon with PSG. The simulation was performed employing a constant phase function,  $P(G)=1$ . The Lommel-Seeliger scattering model captures the quite homogeneous brightness observed on the Moon across the illuminated regions, while also models the significant brightening occurring at the illuminated limb.

where  $\Phi_1(g)$  is the single scattering component (steep function,  $\sim 0.043$  mag/deg),  $\Phi_2(g)$  the multiply scattered component (shallower,  $\sim 0.014$  mag/deg), and  $G$  is the slope parameter ( $0 \leq G \leq 1$ ). Considering that the geometric albedo ( $A_{\text{geo}}$ ) of a LS object is  $w/8$ , the single scattering albedo  $w$  can be determined from  $A_{\text{geo}}$  and the disk-integrated absolute magnitude  $H_0$  value and the object's diameter ( $D$ ) as (Tedesco et al., 1992):

$$A_{\text{geo}} = \frac{w}{8} = \left( \frac{1329}{D[\text{km}]} 10^{-0.2H_0} \right)^2 \quad (31)$$

**Muinsonen 3-parameters ( $HG_1G_2$ ):** over the last decades, it was observed that several bodies could not be properly described with the HG phase function, and a new system with three parameters was developed (Muinsonen et al., 2010). In 2012, the IAU replaced the HG system with the  $HG_1G_2$  system. The integral phase function, with splines coefficients listed in (Penttilä et al., 2016), is described as:

$$\Phi(g) = G_1 \Phi_1(g) + G_2 \Phi_2(g) + (1 - G_1 - G_2) \Phi_3(g) \quad (32)$$

$$\text{Splines of } \Phi_1(g) = 1 - 6g/\pi \quad (33)$$

$$\text{Splines of } \Phi_2(g) = 1 - 9g/(5\pi) \quad (34)$$

$$\text{Splines of } \Phi_3(g) = \exp(-4\pi \tan^{2/3} g/2) \quad (35)$$



**Pentilla 2-parameters (HG<sub>12</sub>):** Penttilä et al. (2016) determined an improved relationship between the G1 and G2 parameters, which is applicable to all types of asteroids with the exception of E- and D-types:

$$G_1 = 0.5351335 \cdot G_{12} \quad (36)$$

$$G_2 = 0.84293649 - 0.5351335 \cdot G_{12} \quad (37)$$

where  $G_{12}$  is only valid between 0 and 1.

**Exponential (EXP):** an exponential empirical series was investigated for the OSIRIS-REx mission to asteroid Bennu (Takir et al., 2015) as:

$$P(g) = \exp(\beta g + \gamma g^2 + \delta g^3) \quad (38)$$

**Lunar/ROLO:** The ROLO model was developed by (Buratti et al., 2011), using the USGS's ROLO data from NASA's Moon Mineralogy Mapper (M3), and the surface phase function and single scattering albedo can be described following (Buratti et al., 2011) as:

$$P(g) = C_0 \exp(-C_1 g) + A_1 g + A_2 g^2 + A_3 g^3 + A_4 g^4 \quad (39)$$

$$w = 4(A_0 - C_0) = 8 A_{geo} \quad (40)$$

The Table 2 summarizes the parameters needed by PSG when employing the LS model and their typical value ranges. For comparison, parameterizations and derivations for objects across our solar system are also listed, in which T2015: (Takir et al., 2015), C2017: (Ciarniello et al., 2017), B2011:(Buratti et al., 2011), V2015: (Vereš et al., 2015).

LS model parameter	Range	Parameters for objects in our solar system					
		Bennu T2015	67P C2017	Ceres C2017	Moon B2011	C-type asteroids V2015	S-type asteroids V2015
$\Phi(g)$ Phase function	HG, HG1G2, HG12, EXP, ROLO	EXP	HG	HG	ROLO	HG12	HG12
$G, a_1, G_{12}, \beta, C_0$	See text	-0.043	-0.09	0.02	$0.2-0.4 \cdot 10^{-2}$	0.58	0.47
$a_2, \gamma, C_1$		$2.6 \cdot 10^{-4}$			0.04 to 0.23		
$a_3, \delta, A_1$		$-9.7 \cdot 10^{-7}$			$-0.6$ to $0.1 \cdot 10^{-2}$		
$A_2$					$-1$ to $1 \cdot 10^{-4}$		
$A_3$					$-4$ to $2 \cdot 10^{-6}$		
$A_4$					$-1$ to $2 \cdot 10^{-8}$		

**Table 2** Summary of PSG accepted input parameters for the Lommel-Seeliger model. Few examples reporting small bodies of the solar system and the Moon are shown in each column.

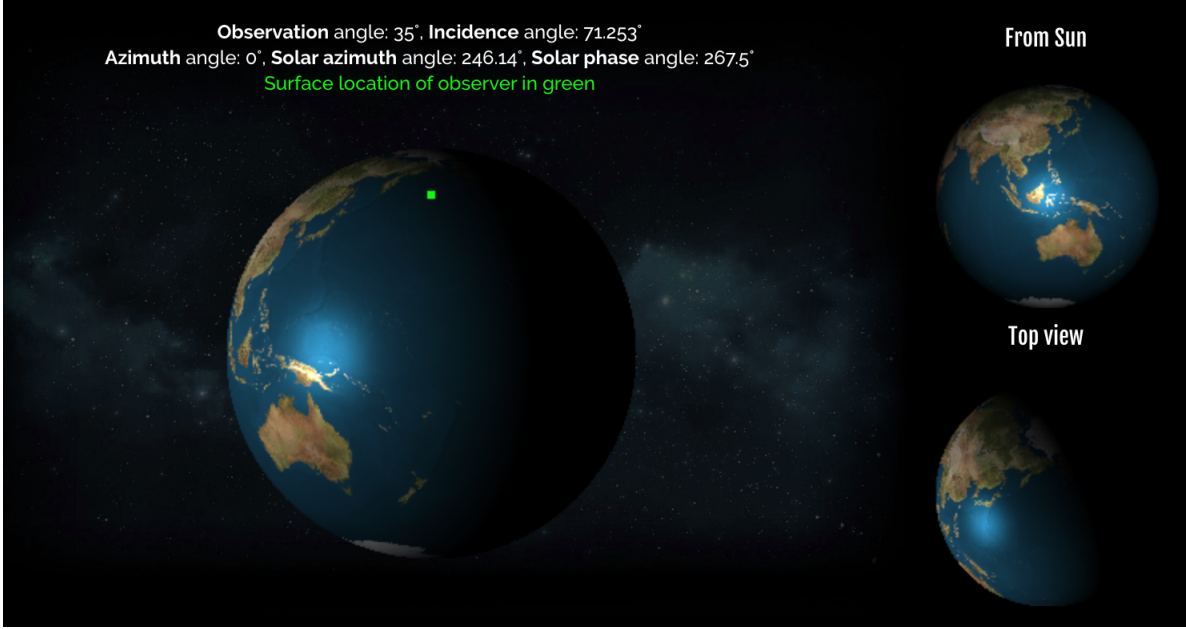


**Figure 3:** Ocean glint modeling with PSG. Typically, ocean glint leads to a notable and localized enhancement of the planetary brightness near the sub-solar point, yet the location and shape of the feature depends on the wind speed and specific observational angles. This enhancement is particularly bright and contrasted considering the typical dark / low-albedo properties of the deep oceans.

## 5. Cox-Munk model: glint and ocean's reflections

The Cox-Munk model is a scattering model of glitter on a water surface. The model employs geometric optics model with the assumption of a Gaussian distribution of the slopes of the wave facets. In the implementation of the glint model in PSG, the BRDF includes two terms, the pure glint term (Cox and Munk, 1954; Jackson and Alpers, 2010; Ma et al., 2015; Spurr, 2002), and the classical non-glint Lambert term for the surface:

$$\text{BRDF} = \text{BRDF}_{\text{glint}} + \text{BRDF}_{\text{Lambert}} \quad (41)$$

$$\text{BRDF}_{\text{glint}} = \frac{r_p s_{\Lambda} (1 + \tan^2 \beta)^2}{4 \cos e} \quad (42)$$

where  $r$  is the Fresnel reflection coefficient for an unpolarized source and computed as:

$$g_r = \text{asin}(\sin g / 1.34) \quad (43)$$

$$r = \frac{1}{2} \left[ \left( \frac{\sin(g - g_r)}{\sin(g + g_r)} \right)^2 + \left( \frac{\tan(g - g_r)}{\tan(g + g_r)} \right)^2 \right] \quad (44)$$



Cox and Munk (1954) found that the probability density function of the wave slopes depends on the wind speed ( $U_{\text{wind}}$ , assumed 4 m/s when not provided), and the probability determining glint reflections can be approximated by a Gaussian function as:

$$\sigma^2 = 0.003 + 0.00512 U_{\text{wind}}[\text{m/s}] \quad (45)$$

$$\cos \beta = \frac{\cos i + \cos e}{2 \cos g} \quad (46)$$

$$p = \frac{1}{\pi \sigma^2} \exp \left( -\frac{\tan^2 \beta}{\sigma^2} \right) \quad (47)$$

As we approach high incidence angles, not all facets are visible, and the “shadow” term compensates for this:

$$s_{\Lambda} = \frac{1}{1 + \Lambda(i) + \Lambda(e)} \quad (48)$$

$$\Lambda(x) = \frac{1}{2} \left\{ \frac{1}{\sqrt{\pi}} \frac{\sigma}{\cot x} \exp \left( -\frac{\cot^2 x}{\sigma^2} \right) - \text{erfc} \left( \frac{\cot x}{\sigma} \right) \right\} \quad (49)$$

where  $\text{erfc}(x)$  is the complementary error function.

## 6. Cometary dust/icy grains

Dust and icy particles in cometary comae are in many cases the main source of continuum/broad radiation in small bodies and in exospheres. In PSG, the single scattering albedo ( $w$ ) of the nucleus and the dust grains are assumed to be the same, yet their scattering properties are treated differently. Small particles have a very different response if compared to the solid nuclear body, with a strong forward scattering peak and a less shallow scattering phase function. PSG employs a Lambert model with the Halley-Marcus (H-M) integral phase function compiled by (Schleicher and Bair, 2011) to model the scattering properties for the dust grains, independently of the selected nucleus scattering/phase model.

The intensity of the continuum would then depend on the effective emitting area of the dust grains, and for that we employ a model as described in (Villanueva et al., 2018b), which is dependent on the comet’s activity and has been scaled to match an empirical relationship of cometary brightness and cometary activity (Jorda et al., 2008). The user can use this model and the  $A(\Theta)f_p$  method to determine the continuum intensity:

**Dust/gas ratio:** in this approach the dust particles are treated as behaving like the surrounding gas and a dust/gas mass ratio of 1.0 provides consistent continuum fluxes to the brightness vs. gas-activity relationship. The reflected sunlight flux is affected by the H-M phase curve, while the thermal emission is assumed to be isotropic and not affected by phase.

**$A(\Theta)_{fp}$** : is a quantity introduced by (A'Hearn et al., 1984) that describes continuum intensity and is generally independent of the different image-scale and measuring window sizes used in the photometry. Since this quantity intrinsically includes a phase correction, the  $A(\Theta)_{fp}$  reflected fluxes are not corrected by the H-M phase curve, yet the thermal fluxes are corrected by  $1/P_{HM}(\Theta)$ .

## 7. Mixing compositions

In PSG, mixing of components is done via the “areal” mixture principle. In an areal mixture, the surface area viewed by the detector consists of several unresolved, smaller patches, each of which consists of a pure material. In this case the total reflectance is simply the linear sum of each reflectance weighted by area. If these components abundances total than unity, then the total surface reflectance ( $BRDF_T$ ) and emissivity ( $\epsilon_T$ ) is complemented by the entered generic surface “albedo”  $a_0$  and “emissivity”  $\epsilon_0$  as (adapted from H12 eq. 10.42):

$$F_T = \sum_j F_j \quad (50)$$

$$BRDF_T = \sum_j F_j BRDF(w_j) + (1 - F_T) BRDF(a_0) \quad (51)$$

$$\epsilon_T = \sum_j F_j \epsilon(\epsilon_j) + (1 - F_T) \epsilon(\epsilon_0) \quad (52)$$

where  $F_j$  is the fractional area of this component with respect to the total sampled scene.

## 8. Calculation of the single scattering albedo: reflectances, optical constants and albedos

For each of the models described above, a key parameter is the single scattering albedo ( $w$ ). This parameter can be calculated for a specific surface from optical constants, or it can be determined from laboratory measurements of reflectance of that component, or it can be derived from astronomical measurements (e.g., geometric albedo). Scattering albedo, geometric albedo, Bond albedo, reflectance, absorptivity are all related quantities, yet they have very different meaning and their values can differ greatly for the same component. For instance, how can one use a “reflectance” laboratory spectrum with the models previously described? One would need to convert these to a wavelength dependent single scattering albedo ( $w$ ), and for that we would need the exact sample properties (e.g., compactness) and observing conditions as employed in the laboratory experiment.

**Reflectances**: if the user provides an average “albedo” or “reflectance” ( $R$ ) or employs reflectance databases (e.g., USGS), PSG will scale these to derive the representative single scattering albedo ( $w$ ), depending on the selected scattering model. For the Lambert model (and Cox-Munk Lambert component) and the Lommel-Seeliger model,  $w$  is simply assumed to be  $R$ . For the Hapke model, the single scattering albedo ( $w$ ) is calculated assuming that the laboratory/input reflectance  $R$  defines Hapke’s diffusive reflectance parameter ( $r_0$ ), and therefore:





$$w_{Hapke} = \frac{4R}{(1+R)^2} \quad R = \frac{1 - \sqrt{1 - w_{Hapke}}}{1 + \sqrt{1 - w_{Hapke}}} \quad (53,54)$$

**Alpha parameter (attenuation coefficient):** for species described with an “attenuation coefficient” ( $\alpha$ ), the single scattering albedo is calculated as  $w = \exp(-\alpha h)$ , where  $h$  is the thickness (or mean ray path length) of the material on the surface.

**Optical constants:** when optical constants ( $n$  and  $k$ ) are provided, the single scattering albedo ( $w$ ) at wavelength  $\lambda$  for a slab of thickness  $h$  is calculated following H12 (section 6.5.3,  $w$  from eq. 6.20,  $S_e$  from eq. 5.37,  $S_i$  from eq. 6.23,  $\Theta$  from eqs. 5.56 and 5.8):

$$w = S_e + (1 - S_e) \frac{1 - S_i}{1 - S_i \Theta} \Theta \quad (55)$$

$$S_e = 0.0587 + 0.8543 \Gamma + 0.0870 \Gamma^2 \quad (56)$$

$$S_i = 1 - \frac{1}{n^2} [0.9413 - 0.8543 \Gamma - 0.087 \Gamma^2] \quad (57)$$

$$\Gamma = \frac{(n - 1)^2 + k^2}{(n + 1)^2 + k^2} \quad (58)$$

$$\Theta = \exp \left[ -4\pi k \frac{h[\mu\text{m}]}{\lambda[\mu\text{m}]} \right] \quad (59)$$

**Geometric albedo ( $A_{geo}$ ) or physical albedo:** this is an apparent quantity that specifies how bright the whole planet/object appears for its size (idealized flat disk) at phase=0 (as seen from the Sun/star).  $A_{geo}=1$  means that all the light arriving is reflected back, and  $A_{geo}$  can also be greater than 1 if the object has a strong opposition effect. Considering that a planetary disk encounters the full range of incidence / emission angles, the relationship between  $A_{geo}$  and  $w$  will differ depending on the assumed surface scattering model (Shepard, 2017, H12 eq. 11.34):

$$A_{geo}^{Lambert} = \frac{2}{3} w = \frac{2}{3} R \quad A_{geo}^{LS} = \frac{1}{8} w P(0) = R P(0) \quad (60,61)$$

$$A_{geo}^{Hapke} = \left\{ \frac{w}{8} [P(0)(1 + B_{s0}) - 1] + (0.49 r_0 + 0.19 r_0^2) \right\} (1 + B_{s0}) \quad (62)$$

**Bond albedo ( $A_{bond}$ ):** this quantity defines how much radiation the surface scatters across all wavelengths and all directions. The Bond albedo is a value strictly between 0 and 1, as it includes all possible scattered light (but not radiation from the body itself). Bond albedo is particularly relevant when investigating the energy balance of a planet, yet it should not be used when predicting the

brightness of an object at a certain wavelength, since this quantity effectively describes the average response across all wavelengths.

**Emissivity ( $\epsilon$ ):** this quantity defines the efficiency of a surface in radiating its thermal energy. Considering energy conservation and Kirchhoff's law, the emissivity could be defined to be equal to 1 minus the absorptivity when integrating across all wavelengths, yet emissivity could exceed unity at certain wavelengths and directions. Absorptivity and Bond albedo are closely related, but not exactly the same, and in many cases the relationship 1-albedo can be assumed. In a general case, emissivity can have “direction” and specific response at a certain wavelength, and as reported above, for each scattering we define a method to compute emissivity from the scattering albedo.

## 9. Disk integrated quantities: albedos and phase integrals

One important aspect of the BRDF quantity is that it refers to a spatially defined location on the planet's surface, with a specific bi-directionality between the source (i angle) and the observer (e and g angles). In many cases, the observer's field-of-view (FOV) may encompass a broad range of incidence and emission angles, as when we measure the spectra of unresolved small-bodies. We would then need the integral of the bi-directional reflectance across the sampled region, or disk-integrated reflectance when the whole hemisphere is sampled. One important quantity is then the integral phase function  $\Phi(g)$ , which defines how the brightness of the planet/object changes when observed at different phases with respect to opposition ( $g=0$ ). As we discussed above, at phase  $g=0$ ,  $A_{geo}$  defines the average reflectivity at opposition, while  $\Phi(g)$  operates as a scaling factor for other phase angles and normalized to 1.0 for  $g=0$ . The phase integral is defined for each scattering modeling as following (Shepard, 2017, H12 eq 11.42):

$$\Phi(g)_{Lambert} = \frac{1}{\pi} (\sin g + (\pi - g) \cos g) \quad (63)$$

$$\Phi(g)_{LS} = P(g) \left[ 1 - \sin \frac{g}{2} \tan \frac{g}{2} \ln \left( \cot \frac{g}{4} \right) \right] \quad (64)$$

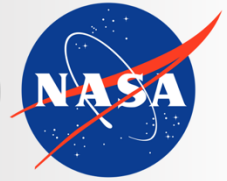
$$\begin{aligned} \Phi(g)_{Hapke} = \frac{r_0}{2A_{geo}} & \left\{ \left[ \frac{(1 + \gamma)^2}{4} \{ [1 + B_{S0} B_S(g)] P(g) - 1 \} + [1 - r_0] \right] \right. \\ & \times \left[ 1 - \sin \frac{g}{2} \tan \frac{g}{2} \ln \left( \cot \frac{g}{4} \right) \right] \\ & \left. + \frac{4}{3} r_0 \frac{\sin g + (\pi - g) \cos g}{\pi} \right\} [1 + B_{C0} B_C(g)] \end{aligned} \quad (65)$$

These integral formalisms are only provided for reference, since PSG performs the integrals across the field-of-view numerically. Specifically, the geometry module in PSG computes a scaling factor to the discrete reflectance at the (i,e,g) employed by the radiative transfer module, with respect to the integrated reflectance when diverse angles encompassed by the FOV are considered. This integration



is performed numerically for the average  $w$  by dividing the disk in  $140 \times 140$  pixels (19600 pixels), and a scaling factor between the FOV/disk-integrated and disk-resolved scattering model is determined. This allows PSG to compute accurately the radiating fluxes even when the FOV encompasses a large fraction of the disk and is offset from the object center.





**Planetary Spectrum Generator**  
National Aeronautics and Space Administration

# Chapter 7: **Mass spectrometry**

**Villanueva, Kofman and  
PSG team**



## 1. Mass spectrometry and its implementation in PSG

Mass spectrometry is a technique in which the elemental components of a sample (molecules) are described according to the mass per charge ( $m/z$ ) of its constituents (atoms/isotopes/ions) to infer its fundamental building blocks and composition. Mass spectrometers are differentiated by the choice of (1) ionization source, which converts the neutral analyte to charged fragments, (2) mass analyzer, which separates ions by  $m/z$ , and (3) detector, which measures the number of ions produced at each  $m/z$  value.

In this chapter, we focus on the interpretation and modeling of atmospheric and surface planetary samples (e.g., MAVEN/NGIMS, Rosetta/ROSINA, LADEE/NMS, Curiosity/MSL), in which the ionization and fragmentation of the species to be analyzed is induced by electron impact, a common method used by mass spectrometers for planetary missions. This consideration is mostly defined by the calibration laboratory datasets employed by the PSG/MASS module, which fundamentally relies on the electron ionization mass spectra for over 21,000 species as compiled in the NIST database.

Contrary to remote sensing techniques (e.g., molecular spectroscopy), mass spectrometry is an in-situ measurement, meaning that it requires physical access to the sample to analyze its composition. It might be surprising that a radiative transfer spectroscopic suite such as PSG has a mass spectrometry module, yet some core simulation building blocks of PSG are common to both the remote sensing techniques and the in-situ mass spectrometry. Specifically, PSG has an advanced set of orbital and atmospheric models, which provide realistic information of the local densities and kinematics at the different locations in an atmosphere. By placing a simulation “probe” at a specific location, all the needed input parameters for a mass spectrometry atmospheric simulation are provided. As we discuss further in this chapter, the fragmentation or fundamental mass spectrum of a compound also relies on laboratory and theoretical information, similar to radiative transfer simulations, and therefore similar analytical methods can be used to synthesize mass spectra for a broad range of mixtures and configurations. Furthermore, the calculation of noise in mass spectrometry measurements also relies on similar Poisson statistics as applies to the calculation of noise in measurements made by a photon counting device (e.g., imaging CCDs), so similar mathematical and physical principles can be adopted when simulating mass spectrometry noise. The PSG/MASS module includes a noise model simulator that is particularly relevant when constraining the detectability of species with a proposed space instrument or when determining the limiting factors affecting a currently available planetary mass spectral dataset.

Importantly, mass spectrometry is a common technique used by orbiters to probe planetary atmospheres, often working in tandem with remote sensing instruments. Interpretation of planetary mass spectrometry data obtained by flight mission instrumentation requires in-depth knowledge of the technological processes that lead to a mass spectrum. This also requires versatile and advanced analytical tools that can access a broad range of mass fragment databases, chemical models, and retrieval or fitting algorithms. Most of the tools employed by the community to interpret complex mass spectrometry data are based on proprietary (e.g., non-public) and expensive software packages, which are in most cases designed for industries applications or tailored to specific laboratory instruments. In many cases, the challenges affecting the interpretation and modeling of mass-

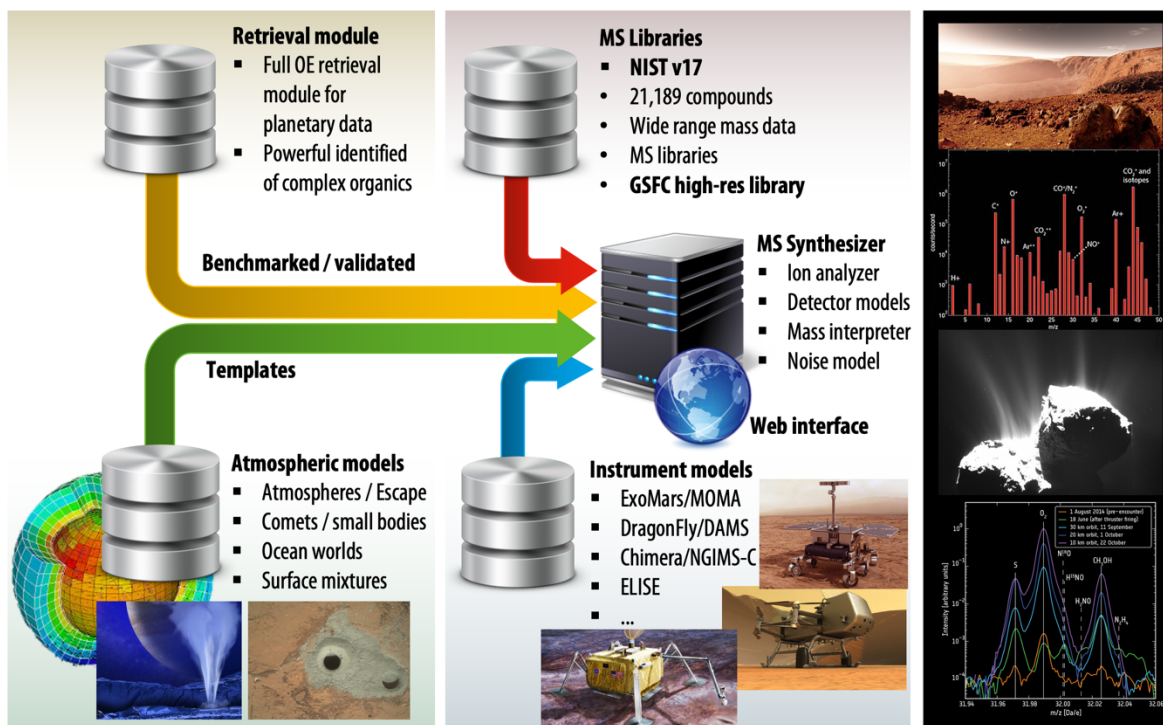


**Figure 1:** By combining an advanced set of mass-spectrometry models with the PSG versatile online planetary suite, the PSG/MASS module can greatly assist with the interpretation and simulation of planetary missions.

spectrometry for planetary science applications are poorly addressed by these industry analytical tools, and an advanced and versatile mass spectrometry planetary modeling and retrieval suite tailored to planetary science is needed. These are the founding principles and aspirations behind this module in PSG, a publicly available mass spectrometry tool specifically designed for planetary missions, which is open access and based on realistic and well-proven methods. In this initial implementation of the MASS module for PSG, we developed an algorithm that, by employing permutation theory, synthesizes all possible fragments for 21,000+ species (see Section 2). This information is then fed to the mass interpreter and modeler (see Section 3), that was exhaustively tested on data collected from several in-situ planetary missions (e.g., LADEE, MAVEN, Rosetta) – see Section 4. Finally, a retrieval or fitting method (e.g., employing the latest search engines and other statistical methods) was developed and tested on laboratory data for the identification of complex organics (see Section 4).

## 2. Fragmentation model and an accurate high-resolution mass fragment database

The advantage of having line lists in radiative transfer modeling is that it is possible to compute spectra at any resolution, ambient conditions, and radiative regime. Unfortunately, there is no equivalent publicly available fragmentation line lists applicable to mass spectrometry, only databases of mass spectra measured at modest mass resolutions ( $\geq 1$  [Da]) and collected for different species in specific ionization and fragmentation regimes. However, we can use this information in combination with a theoretical model to compute accurate an accurate high-resolution mass fragmentation



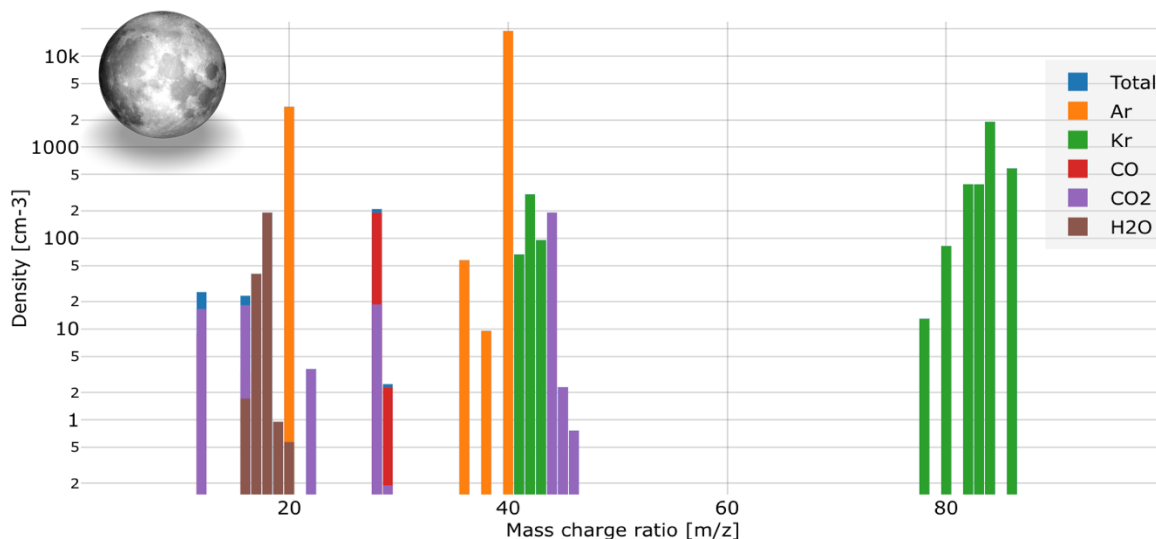


**Figure 2:** Simulated spectrum in the Moon exosphere at 55 km altitude, in the hypothetical case that it had trace amounts of H<sub>2</sub>O, CO<sub>2</sub>, and CO, while also considering probable abundances of Ar and Kr as observed with a mass spectrometer like the NMS onboard LADEE. Such theoretical investigations permit to quantify the detectability of species and their overlap with other signatures.

database for mass spectrometry. Specifically, as part of the PSG/MASS module, we developed a novel fragmentation model for mass spectrometry that generates lists of mass fragments at very high mass resolution (<1 [mDa]). At the core of our model in PSG, there is a permutation and fragmentation algorithm that divides a species into all its possible fragments. The algorithm first determines the fundamental elements of the molecule, exploring all possible isotopologues and considering natural isotopic abundances. For instance, the diatomic CO molecule would have the possible following 10 fragments (in order of increasing mass): <sup>16</sup>O<sup>+</sup> (15.994915 Da), <sup>17</sup>O<sup>+</sup>, <sup>18</sup>O<sup>+</sup>, <sup>12</sup>C<sup>+</sup>, <sup>12</sup>C<sup>16</sup>O<sup>+</sup> (27.994915 Da), <sup>17</sup>C<sup>16</sup>O<sup>+</sup> (28.999132 Da), <sup>12</sup>C<sup>18</sup>O<sup>+</sup>, <sup>13</sup>C, <sup>13</sup>C<sup>16</sup>O<sup>+</sup> (28.998269 Da), <sup>13</sup>C<sup>17</sup>O<sup>+</sup>, <sup>13</sup>C<sup>18</sup>O<sup>+</sup>. This list is obtained by taking into account only the 3 most abundant isotopes of O (with masses of 16, 17, and 18 [amu]) and 2 most abundant isotopes of C (with masses of 12 and 13 [amu]). Such lists of fragments can include thousands of possible combinations for species containing dozens of atoms with many abundant isotopes.

The probability of producing any possible fragment from a molecule will depend on the relative abundances of isotopes it may contain (fragments with many isotopic permutations are less abundant following the law of mixing) and the number of times that fragment occurs in the molecule. For instance, the CO<sub>2</sub> molecule contains two O atoms and one C atom, so if one were to fragment millions of CO<sub>2</sub> molecules in a mass spectrometer, there is twice the chance that one would observe an O<sup>+</sup> fragment than a C<sup>+</sup> fragment. Taking into consideration these two basic principles (i.e., isotopic probability of the fragment and abundance of the fragment in the molecule), the fragmentation module will compute a fragment list for each compound. Importantly, each fragment will have a precise mass (saved in a model database with a precision of 6 digits in [Da]) defined by the total mass of the fragment. Let us consider the example of CO analyzed using a spectrometer with a mass resolution of 1 [Da]. In this case, the fragments <sup>12</sup>C<sup>17</sup>O<sup>+</sup> and <sup>13</sup>C<sup>16</sup>O<sup>+</sup> would fall in the

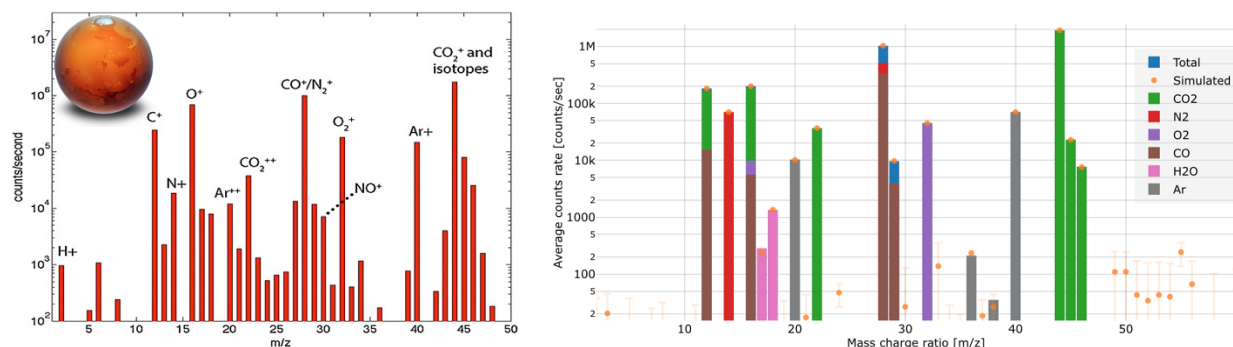


**Figure 3:** Comparison of a fully synthetic mass spectrometry PSG/MASS simulation (right) with orbital Mars data (left) as collected with MAVEN/NGIMS (Mahaffy et al., 2015). Even though the simulations were not done for the exact same conditions and the data includes background signal, the general morphology and intensity of the features is well replicated by the simulation. The noise simulated by PSG is comparable to the detection “floor” as depicted in the left panel.

same bin because both have a mass of 29 [Da], yet if the analysis is performed using a very high-resolution spectrometer, then it is possible to differentiate between the two isotopologues. This example illustrates the great advantage of having line lists of possible fragments for many species that can be used to synthesize and interpret mass spectrometry data at different resolutions.

In reality, the situation is more complex than the example described in the previous paragraph, because the selected fragmentation method and the energies involved in the ionization process will determine which fragments have a higher probability of detection. For instance, if one performs electron ionization at a specific velocity and temperature, certain fragments will be preferentially produced, and the fragmentation pattern would not be accurately reproduced by a natural occurrence probability based on the number of times a fragment exists in a molecule. On the other hand, the fragmentation pattern within constrained mass ranges can be assumed to follow the laws of isotopic mixing, so a simple a priori fragmentation model as described above could be used to determine the fragments within a 1 [Da] wide mass bin and their relative proportions. To calibrate our fragmentation model to experimentally measured mass spectra, we bin our high-resolution fragmentation database for each molecule into a spectrum with a mass resolution of 1 [Da], or in other words, we round the mass of each fragment to the nearest integer. We then take this binned line list and calibrate or scale each bin to the mass spectra reported in the NIST Standard Reference Database Number 69. NIST provides mass spectra for 21,000+ species with masses up to 200 [Da] and a mass resolution of 1 [Da]. For instance, if the proportion of fragments measured at an  $m/z$  of 20 is 0.5 in the NIST database, we scale all fragments with rounded  $m/z$  of 20 to have a total intensity of 0.5, with each fragment scaled by its relative intensity/probability within the bin. All of our mass fragments lists are normalized to the maximum in the list. This combination of theoretical and laboratory data allows for the compilation of an effective and versatile mass spectral database that can be used to synthesize a wide range of mixtures at low and high resolutions.

### 3. Simulating mass spectrometry and its noise

There are two general possible scenarios when synthesizing and interpreting mass spectrometry with PSG: (1) in-situ atmospheric measurements obtained by orbiting probes (e.g., by MAVEN/NGIMS or Rosetta/ROSINA) and (2) in-situ rover or laboratory measurements (e.g., obtained by Curiosity/MSL, by ExoMars/MOMA, or in a laboratory). Typically, mass spectrometry investigations operate with relative or dimensionless intensities, but PSG internally operates with values of [molecules/cm<sup>3</sup>] (or [cc]) which are then converted to any desired output unit by the MASS module.

For in-situ rover or laboratory measurements, the user can choose to be in “cell mode” (which refers to a gas cell) or “sample mode” (for a sample collected by a rover or a laboratory sample), which requires the user to supply the ambient atmospheric density. For in-situ atmospheric obtained by orbiting probe investigations, the MASS module will determine the input atmospheric density [molecules/cm<sup>3</sup>] at the desired probe location by passing the user-defined geometry and atmosphere information, provided in the configuration file, to the GEOMETRY and ATMOSPHERE modules (see Chapters 2 and 3).

Using the provided molecular mixing ratios [molecules/molecule], the MASS module will then compute the specific density [molecules/cm<sup>3</sup>] for each selected molecule. As presented in Chapter 3, PSG calculates the local density for each molecule by employing a realistic 2-stage photodissociation model for comets/exospheres or the hydrostatic integration to determine densities in an equilibrated planetary atmosphere. Using the selected mass ranges and resolution, the MASS module will compute a spectral grid and create a spectrum for each compound by summing the signal collected in each bin from the high-resolution reference mass fragment database as presented in section 2. The total signal will then be calculated as the integral across all species, in which each spectrum is multiplied by the specific molecular density of each component. The natural unit of the simulated spectra is then in units of [molecules/cm<sup>3</sup>] (since the line-lists are normalized to unity).

The generated mass spectrum ( $R$ ) can be converted from [molecules/cm<sup>3</sup>] to [counts/second] by multiplying the spectrum by the instrument sensitivity ( $\Gamma$ ), which is typically reported in units of [counts/second/cm<sup>3</sup>]. If the user provides the total integration time of the measurement ( $\Delta t$  in [seconds]), PSG will compute the total integrated counts (via  $S = R \cdot \Gamma \cdot \Delta t$ ) across that time and will produce a spectrum in similar format and units as reported by the instrument. For instance, a typical efficiency for MAVEN/NGIMS and LADEE/NMS is 0.03 [counts/second/cm<sup>3</sup>]. Similar to imaging CCDs, detectors used in mass spectrometers typically have strong background signatures ( $I_{\text{dark}}$  or “dark” [counts/second]) and add counts/noise upon every read ( $I_{\text{read}}$  “read” [counts/read]). This background signal can be added to the generated count rate to accurately determine and estimate the effect of noise in the data. As will be discussed in Chapter 8, in Poisson statistics, the noise follows the square root of the total measured counts [ $N = \sqrt{S_T}$ ], where  $S_T = S + n_{\text{read}}(I_{\text{read}} + I_{\text{dark}} \cdot \Delta t_{\text{read}})$ ,  $n_{\text{read}}$  is the number of reads, and  $\Delta t_{\text{read}}$  is the integration time per read [s/read]. Finally, the MASS module will compute noise following these equations and employing the specific instrument sensitivity and detector readout characteristics as described above. Performance parameters for several planetary

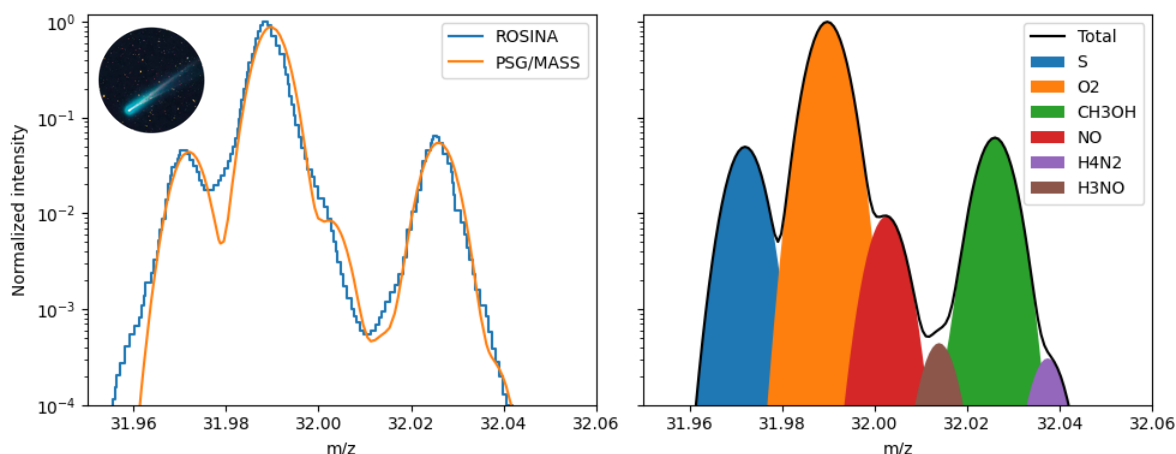


**Figure 4:** Retrieval with PSG/MASS of the composition of comet 67P as measured with the ROSINA mass spectrometer (Rubin et al., 2019) onboard Rosetta. ROSINA is a Double Focusing Mass Spectrometer (DFMS) capable of extremely high mass resolution ( $M/dM > 3000$ ), in which one can identify the multiple constituents with a mass of 32 [Da]. The PSG/MASS simulation retrieval (convolved with a Gaussian kernel) provides a very good match data and allows to properly quantify the abundance of the components found in the coma.

mass spectrometers have been collected and included as loadable instrument templates in the online PSG's instrument section.

#### 4. Mass spectrometry retrievals and complex organics identification

To demonstrate the module and explore its regimes of operability, we analyzed several important planetary mass spectrometry datasets and interpreted these data by using the MASS module. The datasets were selected to explore different input atmospheric regimes (e.g., atmosphere, comet, laboratory), different mass ranges and spectral resolutions, and these are:

**Lunar exosphere (Figure 2):** The Lunar Atmosphere and Dust Environment Explorer (LADEE) was a NASA lunar exploration and technology demonstration mission that launched in September 2013. This orbiter had a Neutral Mass Spectrometer (NMS) that targeted several species in the exosphere of the Moon, ultimately leading to the characterization of the noble gas cycle on the Moon (Benna et al., 2015) and to the discovery of several ions related to the solar wind interaction with the Moon exosphere (Halekas et al., 2015). We simulated the detectability of these noble gases together with the potential signature of other common atmospheric volatiles with PSG/MASS employing instrument parameters as those of LADEE/NMS (see Figure 2). The simulation nicely shows the strong noble signatures (for all the isotopes) and the potential overlap between the different fragments for CO, CO<sub>2</sub>, and H<sub>2</sub>O.

**Martian atmosphere (Figure 3):** The Neutral Gas and Ion Mass Spectrometer (NGIMS) onboard the Mars Atmosphere and Volatile Evolution (MAVEN) orbiter has provided key insights about the Martian atmosphere. The spectrometer targets several key Mars volatiles and enables the characterization of their vertical, spatial, and seasonal dependence by in-situ probing, in particular,

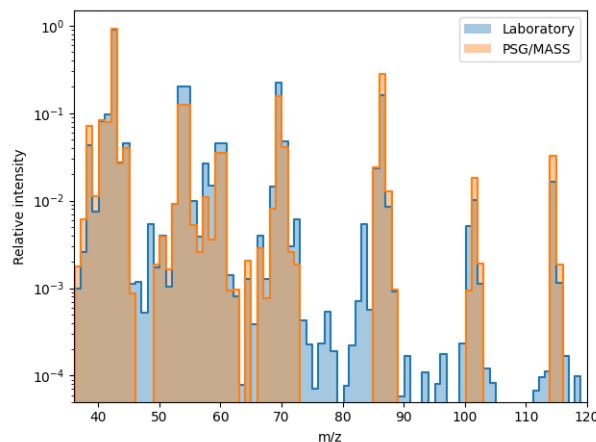


**Figure 5:** Identification of complex organics with PSG/MASS on laboratory samples. As a blind test experiment, the data were provided to us by Goddard’s Astrobiology Analytical Laboratory to determine its composition. We obtained the highest match (98.69%, right panel as shown by the retrieval web interface) with acetate 2-pentanol, consistent with the original source, while the model also identified several related species with similar structure and composition. The PSG/MASS search algorithm is extremely effective and fast (only taking ~1 second to obtain the results shown here), which enables rapid identification of complex species among a database of 21,000+ species at a broad range of masses and resolutions.

due to the “deep dip” campaigns in which the orbiter penetrated deeply into the Martian atmosphere. An example measurement is presented in (Mahaffy et al., 2015), which we compare to a simulation at a similar altitude using our tool. The conditions of the simulation are not exactly the same as those of the measurement and the simulations were not fitted to match the data, but one can see a close resemblance in the peaks’ intensity between model and data. Importantly, the PSG/MASS module provides detailed information about the contribution of the different atmospheric constituents to every mass peak, enabling analysis of overlapping signals and thus the potential significance of each individual signature.

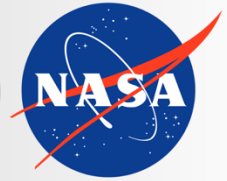
**Cometary coma of 67P (Figure 4):** Onboard the ESA/Rosetta mission orbiting around comet 67P, the ROSINA (Rosetta Orbiter Spectrometer for Ion and Neutral Analysis) mass spectrometer contained two sensors which were used to determine the composition of the comet’s atmosphere and ionosphere, the velocities of electrified gas particles, and the reactions in which they took part. A particular mode of the instrument is its double focusing mass spectrometer (DFMS) that has a mass range from 1-150 [amu] and a mass resolution higher than 3000. The DFMS channel has been optimized for very high mass resolution and large dynamic range. It can thus be an extremely useful tool for the exploration of isotopic compositions and the overlapping signatures from many species in a narrow mass range. In Figure 4, we perform a retrieval on Rosetta/ROSINA data (Rubin et al., 2019) by employing PSG/MASS, in which several species are revealed and separated. We have used a Gaussian kernel to convolve data, though this channel is known to have a peculiar/asymmetric ILS (Instrument Line Shape) function, and that would explain many of the observed differences. In particular, the unique value of having a high- resolution mass fragment database, as presented in Section 2, is nicely demonstrated in this retrieval, that a NIST 1 [Da] database would not permit.



**Complex organics and surface/laboratory samples (Figure 5):** We have added a powerful molecular search engine to PSG that allows for the comparison of observed data with a large sample of spectra. To test this capability, we asked NASA Goddard's Astrobiology Analytical Laboratory to provide us with a mass spectrum of a single large organic molecule. We asked them not to inform us of the nature or properties of the sample. We used PSG/MASS to infer and detect its composition. The search algorithm only took a second to identify an accurate match with acetate 2-pentanol among a database of 21,000+ species. The algorithm also identified several related species with similar structure and composition, which can be helpful when exploring planetary samples of processed, unknown materials.







**Planetary Spectrum Generator**  
National Aeronautics and Space Administration

# Chapter 8: **Instruments and Noise Modeling**

**Villanueva, Mandell, Liuzzi and  
PSG team**

## 1. Principles of noise modeling

Noise in an observation/measurement is introduced by a wide range of effects, and computing it requires a precise accounting of the fluxes arriving to the instrument, the instrument losses and the intrinsic components of the instrument/telescope affecting the overall sensitivity. PSG has been designed at the core to keep full accounting of the photons and fluxes at all stages of a simulation, ensuring a proper tracking of signals and their respective associated noises. In particular, the noise simulations in PSG are done by the GENERATOR module after performing the integration of the spectral radiances across the corresponding selected simulation field-of-view, spectral wavelengths range and instrument properties (see Figure 1).

The total noise in a simulation can be generally defined as a linear combination, typically a sum of squares, of three main noise sources: scene (or target) fluxes (planetary and stellar fluxes), background fluxes (e.g., zodiacal, telluric) and detector or systematic instrument sources. At short wavelengths (e.g., optical or near IR), the background photon counts follow a Poisson distribution, and the fluctuations are given by the square root of the mean number of photons received (Tables 1 and 2). A Poisson distribution holds only in the case that the mean photon mode occupation number is small,  $n \ll 1$ . For a thermal background, the occupation number is given by the Bose-Einstein formula,  $n_{th}(v, T) = [\exp(hv/kT) - 1]^{-1}$ , so the opposite classical limit  $n \gg 1$  is the usual situation at longer wavelengths for which  $h\nu \ll kT$ . When  $n \gg 1$ , the photons do not arrive independently according to a Poisson process but instead are strongly bunched, and the fluctuations are linearly related to the received photons. Therefore, the Dicke equation is used to calculate sensitivities for the receiver temperature mode (e.g., ALMA and sub-mm receivers), which states that the noise is proportional to the background power rather than its square root. The formalism employed for this mode in PSG is based on the ALMA sensitivity calculator (Table 1).

As we explore the concept of noise calculations in this chapter, it is important to establish a key parameter affecting the calculations,  $R$  as number of photons per second arriving to the detector (see additional details in Table 2). If we know the integration time ( $T$ ), then the total number of observable photons is simply  $S = RT$ . Let us now consider that we have calculated an effective spectral radiance  $L$  [ $W/m^2/\mu m/sr$ ] for our simulation scene, then  $R$  is calculated as:

$$R [\text{photons} / s] = \eta \cdot L [W/m^2/\mu m/sr] \cdot A_{tele} [m^2] \cdot \Delta\lambda [\mu m] \cdot \Omega [sr] \cdot (\lambda/hc) [\text{photons} / s / W] \quad (1)$$

where  $\eta$  is the instrument throughput (1.0 is a perfect instrument),  $A_{tele}$  is the collecting area of the telescope (bigger telescopes collect more photons),  $\Delta\lambda$  is the spectral width of the simulation pixel,  $\Omega$  is the steradian area of the field-of-view (FOV), and the last term is simply a scaler of the number of photons/s for every Watt. A few key important points are to be made here:  $R$  is independent of distance to the object (that is captured in  $L$ ); the per  $/\mu m$  in  $L$  refers to the width of the pixel, not to its wavelength (wider or lower “resolution” pixels collect more photons); wide FOVs (greater  $\Omega$ ) leads to higher photon rates, but only if  $L$  is constant across the FOV. It is then key that we capture the differences in  $L$  for an extended source versus a point source. If the FOV is smaller or within the size of an extended source (e.g., large nearby planets or a background source like the zodiacal dust), then  $L$  does not change. In that sense, having a larger FOV that still encompasses the source will lead

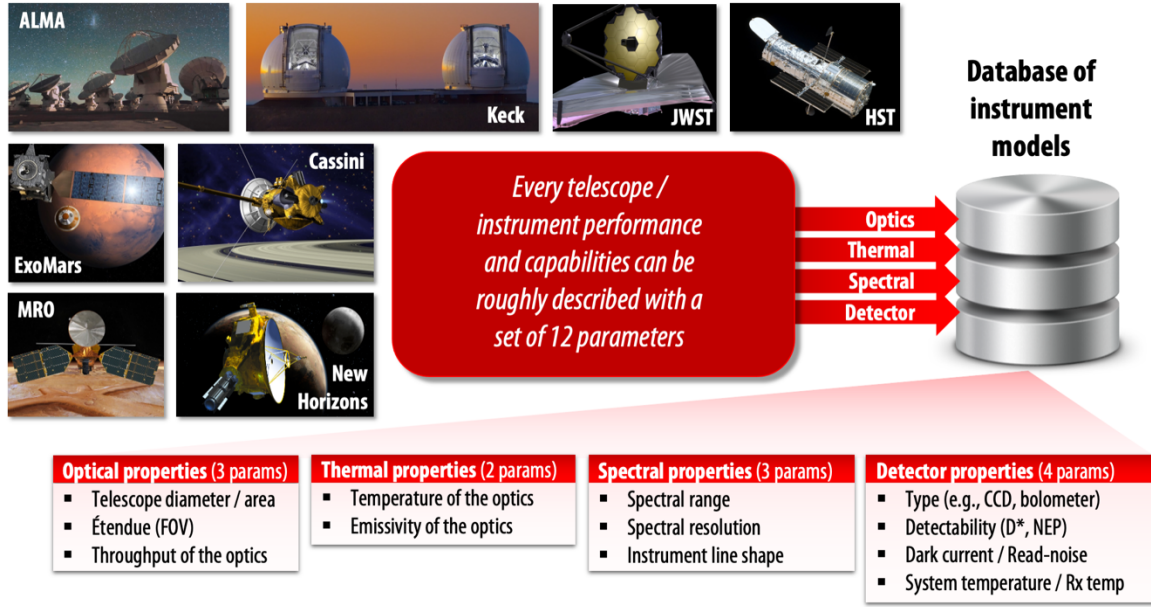


**Figure 1:** The basic elements of any noise simulation require 12 core parameters as summarized in this figure. In PSG, we have prepared templates for a wide range of instruments, observatories and missions that capture their noise performances, which can be selected/uploaded in the instrument section of PSG. A user-custom instrument simulator can also be created.

to a higher count rate. On the other hand, if the source is smaller than the FOV (e.g., a point source or a distant star), then  $L$  will scale with inversely with  $\Omega$ , and then the count rate will remain the same (more details in section 2). Another key metric identified in equation 1 is  $\eta$ , or the total throughput of the instrument. The higher the number the more photons from the source we collect ( $S$ ), and then the higher the  $S/N$ . For instance, if a mirror in an instrument optical setup has a transmissivity of 0.95, having 10 reflecting surfaces will lead to a total transmissivity of  $0.95^{10} = 0.6$ . Furthermore, some instruments may be designed to greatly reduce the signal for only certain regions of the scene, as in a coronagraph, where the stellar signatures have a particular  $\eta_{\text{star}}$  and the planet/background signatures has a different  $\eta_{\text{planet}}$  (more details in section 6).

With equation 1, we have identified the core formalism for computing the first two components of noise (planetary, stellar and background sources, more details in Table 2), now remaining the modeling of detector and systematic instrumental noise. Each detector technology introduces noise in a particular way, and it also responds differently to the observed fluxes. As such in PSG, several detector and instrument models are available to capture this diversity (see Table 1). Imaging sensors (e.g., CCDs) introduce noise upon reading the detector (read noise, typically quantified in e-/pixel/read) and via a background current which increments over time (dark current, quantified as e-/pixel/s). The dark current is added to any frame, but can be removed by doing (science frame – dark frame), in which dark is a no-signal frame taken over the same exposure time as the data. The dark current can be then removed, but not its noise, and therefore this type of detector noise needs to be included in any astronomical simulation. In the case of read noise, it can be reduced for certain detectors by performing multiple reads before emptying the detector well, a process normally defined

Type of noise	Parameters	Detector specific noise equations
<b>TRX</b> Receiver temperature (radio)	$T_{RX}$ [K]: noise of receiver $g$ : sideband (0:SSB, 1:DSB) $n_{pol}$ : 1 (# of polarizations) $f_N$ : 1 (# of baselines)  <b>For interferometric systems</b> (e.g., ALMA): $n_{pol}$ : 2 (assuming dual / full configuration) $f_N = n_{tele} \cdot (n_{tele}-1)$	$L_{RJ} = 1E-18 \cdot \lambda^4 / 2kc$ $T_{source} = L \cdot L_{RJ}$ $T_{back} = L_{back}L_{RJ} + T_{ground}(1 - trn_{ground})$ $k_{sys} = (1+g)/(\eta_{Total} trn_{ground})$ $T_{sys} = k_{sys} [T_{RX} + \epsilon_{optics}T_{optics} + T_{source} + T_{back}]$ [K]  $f_{\Omega} = (\Omega_{Tele} / \Omega)$ Diffraction / FOV correction $D_v = 1E6 \cdot c \cdot d\lambda / \lambda^2$ $N_{total} = T_{sys} \cdot f_{\Omega} / \sqrt{(f_N \cdot n_{pol} \cdot d_v \cdot n_{exp} \cdot t_{exp})}$ [K]
<b>NEP</b> Noise Equivalent Power	NEP [W / $\sqrt{Hz}$ ]: sensitivity	$N_D = n_{pixels} \cdot n_{exp} \cdot t_{exp} \cdot (NEP \cdot \lambda \cdot 1E-6 / hc)^2$ [e <sup>-2</sup> ]
<b>D*</b> - Detectivity	$D^*$ [cm $\sqrt{Hz}$ / W]: detectivity $S$ [ $\mu m$ ]: pixel size	$N_D = n_{pixels} \cdot n_{exp} \cdot t_{exp} \cdot ((S \cdot 1E-4 / D^*) \cdot \lambda \cdot 1E-6 / hc)^2$
<b>NETD</b> Noise-Equivalent Temperature difference	NETD [mK] at $T=300K$ , $f=50$ Hz and $\Delta\lambda=1 \mu m$ $S$ [ $\mu m$ ]: pixel size  <i>This value is measured by the detector manufacturer by performing a defined measurement on a source of temperature <math>T</math> (e.g., 300K), with a repetition <math>f</math> (e.g., 50 Hz). The noise will be dependent on the operating spectral coverage of the detector (e.g., <math>\Delta\lambda=1 \mu m</math> for a 12-13 <math>\mu m</math> response).</i>	<i>To convert from a NETD obtained with another source temperature <math>T</math> [K], sampling frequency <math>f</math> [Hz] or detector bandwidth <math>\Delta\lambda</math> [<math>\mu m</math>]:</i>  $NETD = NETD(T, f) \cdot dPB/dT(300, 50) / dPB/dT(T, f) \cdot \sqrt{(50/f) \cdot \Delta\lambda}$  $dPB/dT = hc/(\lambda kT^2) \cdot PB$ $PB = A \cdot \Omega \cdot \Delta\lambda \cdot 2hc^2/\lambda^5 \cdot [\exp(hc/(\lambda kT)) - 1.0]^{-1}$ $A = S^2$ (area of pixel) $\Omega = \pi/(4F\#^2 + 1)$ (solid angle of pixel) $NEP = NETD \cdot dPB/dT / \sqrt{f}$
<b>Imager</b> – (e.g., CCD, CMOS, EMCCD, ICCD / MCP)	Read-noise [e- / pixel] Dark [e- / s / pixel]	$N_D = n_{pixels} \cdot n_{exp} \cdot [N_{read}^2 + (Dark \cdot t_{exp})]$ [e <sup>-2</sup> ]

**Table 1:** Mathematical formalisms for the different detector models.

as multiple nondestructive readout (NDR). This can lead to a reduction of the read noise by  $\sqrt{K}$  (where  $K$  is the number of reads), yet this may also notably increase the read/integration times leading to other systematic (e.g., saturation) issues. In summary when performing noise calculations, it is critical to validate the detector parameters used for the simulation and to define an optimum integration method (i.e., number of exposures, and integration per exposure).

## 2. Field-Of-Views (FOVs), diffraction limits and planetary filling factors

The GEOMETRY module of PSG will compute several key parameters which permits to accurately quantify the relationship between the size and location of the planet and stars (e.g., host-star and any stellar background) with respect to the FOV. As shown in Figure 1 of chapter 2, if the distance to



### General formalism for the noise components under Poisson statistics (i.e., UV, optical, IR)

$$\begin{aligned}
 L_{e-} &= \Omega \cdot A_{\text{Tele}} \cdot \eta_{\text{eff}} \cdot d\lambda \cdot \lambda \cdot t_{\text{exp}} \cdot n_{\text{exp}} \cdot 1\text{E-6} / hc \quad \text{Radiance to detector electrons conversion factor} \\
 N_{\text{source}} &= L \cdot L_{e-} \quad \text{Noise introduced by the source itself [e-}^2\text{]} \\
 N_{\text{back}} &= (L_{\text{back}} + n_{\text{ezo}} \cdot L_{\text{zodi}}) \cdot L_{e-} \quad \text{Noise introduced by background sky sources [e-}^2\text{]} \\
 N_{\text{optics}} &= \epsilon_{\text{optics}} \cdot L_{e-} \cdot (2E24 \cdot h \cdot c^2 / \lambda^5) / (\exp(1E6 \cdot h \cdot c / (k \cdot T_{\text{optics}} \cdot \lambda)) - 1) \quad \text{Noise by the telescope [e-}^2\text{]} \\
 N_{\text{ground}} &= L_{e-} \cdot (1 - \text{trn}_{\text{ground}}) \cdot (2E24 \cdot h \cdot c^2 / \lambda^5) / (\exp(1E6 \cdot h \cdot c / (k \cdot T_{\text{ground}} \cdot \lambda)) - 1) \quad \text{Noise for ground [e-}^2\text{]} \\
 N_{\text{Total}} &= \sqrt{(2N_D + N_{\text{source}} + 2N_{\text{back}} + 2N_{\text{optics}} + 2N_{\text{ground}})} \quad \text{Total noise [e-]}
 \end{aligned}$$

#### Parameters and constants:

$L$  [W / sr / m<sup>2</sup> / μm]: spectral radiance of the source  
 $L_{\text{back}}$  [W / sr / m<sup>2</sup> / μm]: spectral radiance of the background sources  
 $t_{\text{exp}}$  [s]: time per exposure  
 $n_{\text{exp}}$ : total number of exposures  
 $n_{\text{pixels}}$ : total number of pixels for  $\Omega$  and  $d\lambda$ .  
 $n_{\text{ezo}}$ : Exozodiacal dust scaler relative to Solar System zodiacal dust  
 $T_{\text{optics}}$  [K]: temperature of the optics  
 $\epsilon_{\text{optics}}$ : emissivity of the optics  
 $\eta_{\text{eff}}$ : total throughput of the system (including quantum efficiencies)  
 $\Omega$  [steradian]: is the solid angle of the observations. It is wavelength dependent.  
 $A_{\text{Tele}}$  [m<sup>2</sup>]: is the total collecting area of the observatory ( $n_{\text{Tele}} \cdot \pi \cdot [D_{\text{Tele}}/2]^2$ )  
 $\lambda$  [μm]: is the wavelength in microns  
 $\text{trn}_{\text{ground}}$ : terrestrial transmittance  
 $T_{\text{ground}}$  [K]: temperature of the terrestrial atmosphere - 280  
 $h$  [W s<sup>2</sup>]: is Planck's constant - 6.6260693E-34  
 $c$  [m / s]: is the speed of light - 299792458  
 $k$  [J / K]: is Boltzmann's constant - 1.380658E-23

**Table 2:** Mathematical formalisms for the computation of noise for Poisson statistics detectors.

the system is greater than 0.1 parsec, PSG will compute the planetary orbit and the projected distance between the planet and the host-star in the observer's reference frame. This information is recorded in the field GEOMETRY-STAR-DISTANCE ( $\Delta_{\text{star}}$ ), in which a negative value (e.g., -1) would indicate the star is not in the scene (all cases with distances < 0.1 pc), a 0 value indicates that star is fully in the FOV, and a value larger than 0 indicates the distance in arcseconds between the center of the FOV and the center of the star. If the star is within the FOV ( $\Delta_{\text{star}}=0$ ), the planet may too, and it may cover the star (e.g., primary transit), in which the field GEOMETRY-STAR-FRACTION indicates the fraction of the star being covered by the planet. The GEOMETRY module employs a full 3D orbital calculation of the orbit, the star, and the planet, to determine the exact fraction of the star being covered by the planet. These parameters are used to determine the amount of stellar background flux to include in the simulation by the GENERATOR module.

As discussed in section 1, the definition of the average spectral radiance of the scene ( $L$  [W/m<sup>2</sup>/μm/sr]) and the area of the FOV ( $\Omega$  [sr]) defines the actual total integrated fluxes and ultimately the count rates. The field GEOMETRY-PLANET-FRACTION ( $f_{\text{planets}}$  sometimes referred as the “filling factor”, a value ranging from 0 to 1) quantifies how much of the planet surface area is included in the FOV, which is computed by the GEOMETRY module and includes information regarding the shape/orientation of the FOV, distance to the object, size of the planet

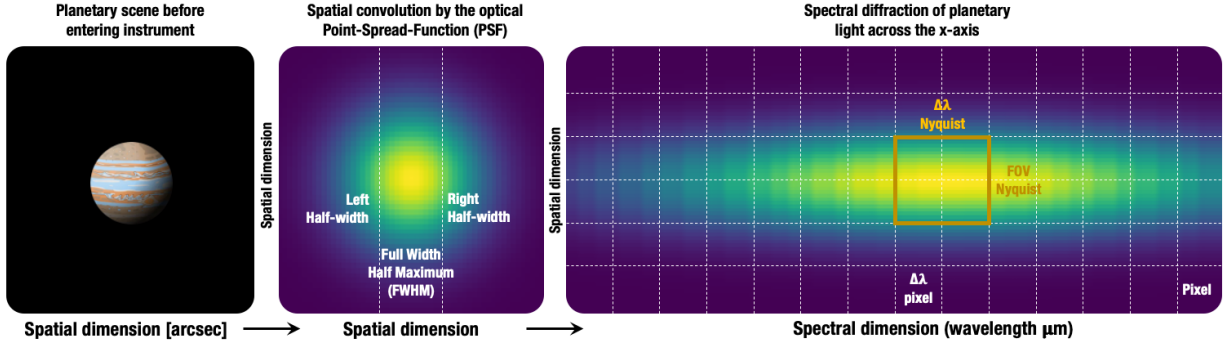


**Figure 2:** As the planetary light enters the instrument and it is sampled by the detector, the signal is first convolved spatially, then diffracted spectrally and ultimately projected on the detector. The spectral width of every detector pixel depends on the specific instrument configuration, which samples the optical resolution with at least two detector pixels. In this configuration, a “boxcar” pixel as simulated with PSG would correspond to the orange box with 4 detector pixels per instrumental resolution.

and any possible offsets. If the planet is bigger than the FOV, then in principle  $f_{\text{planet}} = \Omega / \Omega_{\text{planet}}$ . The effective scene spectral radiance is then  $L = f_{\text{planet}} \cdot (\Omega_{\text{planet}} / \Omega) \cdot L_{\text{planet}}$ , where  $L_{\text{planet}}$  is the intrinsic radiance of the planet. This is consistent with what was discussed in section 1, in which for extended objects  $L$  remains constant and equal to  $L_{\text{planet}}$  since the first terms cancel out. For diffraction limited telescopes, the FOV [rad] of a telescope of diameter  $D$  scales with wavelength  $\lambda$  as  $\text{FOV} \sim 1.22 \lambda / D$ , and therefore  $\Omega = (\pi/4)\text{FOV}^2$  scales quadratically with wavelength. Such considerations are taken into account by PSG when computing filling factors and count rates (equation 1) for each simulation pixel.

### 3. Spectral grids, sampling and convolutions

Equation 1 and those in tables 1 and 2 make use of finite and quantifiable parameters, all derivable from the simulation input parameters or from the specifications of the instrument. Yet a challenging parameter to conceptualize is “number of pixels”. As summarized in section 1 and in Table 1, the detector noise is per/pixel, and for that one needs to fully understand how the simulated spectra projects onto the detector. If one selects “**boxcar**” for the resolution type in the PSG/GUI Telescope and Instrument section, the separation/spacing between each simulation spectral point will be as defined by the resolution. For instance, if the user chooses a “boxcar” and a resolution of  $0.1 \mu\text{m}$ , then each simulation point will be spaced by  $0.1 \mu\text{m}$ , and  $\Delta\lambda$  in equation 1 will be  $0.1 \mu\text{m}$ . However, if the user selects “**gaussian**” for the resolution type, then in PSG the spectral points will be computed at intervals of the selected resolution divided by 10, so at spacings of  $0.01 \mu\text{m}$  for this example, and the spectra will be convolved with a Gaussian kernel having a Full-Width-Half-Maximum (FWHM) of  $0.1 \mu\text{m}$ . In spectroscopic terms, this means that for the “boxcar” method the sampling resolution is equal to the spectral resolution, and for the “gaussian” method the sampling resolution is 10 times higher than the spectral resolution. This higher sampling rate for the gaussian method is needed to ensure proper characterization of the instrument line shape in PSG and it is





well beyond the Nyquist limit (sampling at least twice as the resolution). Yet, this also means that for the “gaussian” method,  $\Delta\lambda$  in equation 1 will be  $0.01 \mu\text{m}$ , and the count rates 10 times lower.

Now that we have introduced the concepts of “sampling” and “resolution” pixels, we can proceed further with the interpretation of instrument (or optical) and simulation pixel (see Figure 2 for a graphical interpretation of these concepts). It is highly recommended that the user chooses “boxcar” pixels for noise simulations in PSG, so resolution in PSG would then mean “optical” or actual instrument resolution (as reported in their specification tables). Then we need to understand what is the sampling rate that the instrument has for that optical resolution, defining the “number of pixels” ( $n$ ) entry in PSG Telescope and Instrument section. Most instrument developers, try to squeeze as much information in an array as possible, so this means making the instrumental sampling rate as close to the Nyquist limit as possible. This would mean  $n=2$ , yet many instruments project into 2D arrays, and herewith we would have  $n \sim 2 \times 2 = 4$  pixels per “boxcar” PSG resolution or instrument’s actual resolution. For grating instruments, a value of  $n=8$  is recommended (to allow for a typical spread among more pixels), while for linear dispersive instruments  $n=2$  to  $4$  is recommended.

Depending on the dispersive/diffractive method used by the instrument to separate light, some wavelengths may project onto less or more pixels. In PSG, the keyword GENERATOR-NOISEPIXELS allows to provide the number of pixels (e.g.,  $n_A$ ,  $n_B$ ,  $n_Z$ ) at specific wavelengths (e.g.,  $\lambda_A$ ,  $\lambda_B$ ,  $\lambda_Z$ ) of the instrument, in the format  $n_A@ \lambda_A, n_B@ \lambda_B \dots, n_Z@ \lambda_Z$  (see example of JWST/MIRI-LRS template configuration file for details). If this information is not provided, and a diffraction limited configuration is defined, PSG assumes that the number of pixels grows with wavelength due to the larger diffraction pattern, and herewith the number pixels scales as  $\lambda^2$ .

#### 4. Radiation and intensity output units

In PSG, the user can select from a wide variety of generally used astronomical units for the calculated fluxes, radiances and output intensities (see full table at <https://psg.gsfc.nasa.gov/helpmodel.php#units>). When employing absolute units, the output intensities are specific and clearly defined, yet there are some ambiguities for certain units, and in this section we will establish the formalisms for each of them as defined in PSG:

**Spectral radiances (e.g.,  $[\text{W}/\text{m}^2/\mu\text{m}/\text{sr}]$ ):** this is the baseline of the simulation units, in which the instrument parameters less affect the output results. The reported values by PSG will contain corrections for filling factors/planet fraction (see section 2), so the spectral radiances will depend on the assumed size of the FOV and the projected size of the planet in it. This unit is convenient when comparing simulation results between different instruments or configurations (e.g., independent of spectral resolution or collecting area).

**Radiances, intensities, and fluxes:** as the spectral radiances get multiplied by specific properties of the instrument – by FOV resulting in spectral irradiance (e.g.,  $[\text{Jy}]$ ); by collecting area resulting in spectral intensity (e.g.,  $[\text{W}/\text{cm}^2/\text{sr}]$ ); by FOV, collecting area and spectral resolution [photons/second] as in equation 1 – they start to resemble more the values actually measured by an instrument/observatory. Jansky  $[\text{Jy}]$  is a particular useful unit when reporting integrated fluxes of



small and distant objects (e.g., asteroids, exoplanets, stars, or objects having filling factor = 1 as described in see section 2), since it is generally invariant with FOV (when larger than the object), resolution and collecting area, and the numerical values are normally “legible” and closer to 1 for many sources.

**Brightness temperature [K]:** is a typical unit used in radio astronomy, which refers to the effective blackbody temperature of the observed flux, if the source would fill the FOV and it would have an emissivity of 1. Effectively, brightness temperature is the inverse of the Planck function, yet this inverse transformation is highly non-linear and rather numerically instable, so it should be used only for specific and selected cases. An alternative and more stable transformation is the Rayleigh-Jeans Brightness temperature [K], which is based on the first Taylor term of the Planck function and relates linearly with spectral radiance [L]. The Rayleigh-Jeans approximation starts to depart greatly from the Planck function at wavelengths shorter than the sub-mm, and it should be only considered at radio wavelengths.

**Magnitude (m):** this logarithmic unit normalizes the simulated irradiances to those of the star Vega, considering a radius of  $1.65e9$  [m], a distance of  $7.68$  [pc], and a spectral energy distribution closely approximating that of a black body for a temperature of  $11,000$  [K].

**Contrast:** when a star is in the simulation scene (e.g., transit, coronagraphy, occultation, object  $> 1$  [pc]), PSG can compute the fluxes with respect to the background star ( $I = L/L_{\text{star}}$ ). In transit mode (see section 2), the values report the relative stellar flux lost due to the transit as,  $I = (R_p / R_{\text{star}})^2$  equivalent in fluxes as  $I = (T \cdot L_{\text{star}} - L) / L_{\text{star}}$ , where  $T$  is the transit transmittance. It is important to note that  $L$  is the intrinsic self-emitted flux of the planet, and this means that the “total” column in PSG contains the net lost flux, which is the sum of the lost flux ( $T \cdot L_{\text{star}}$ ) minus the self-emitted flux ( $L$ ). The “transit” column reports  $T$ . By definition,  $R_p$  and  $T$  include the solid surface radius ( $R_{\text{surf}}$ ) and the opaque component of the atmosphere ( $R_p = R_{\text{surf}} + H_{\text{atm}}$ ). In that sense, when requesting the unit [ppm], PSG will only report the  $H_{\text{atm}}$  component in parts-per-million so  $I = 1e6 (H_{\text{atm}}/R_{\text{star}})^2$ , while the unit [km] will report  $H_{\text{atm}}$  in [km], which is determined algebraically from the radiative transfer computed “transit”  $T$  term.

**Apparent albedo (I/F):** is the ratio of the planet brightness relative to that one of an idealized flat, fully reflecting, and perfectly emitting ( $\epsilon=1$ , with temperature as  $T_{\text{surf}}$ ) disk with the same cross-section as the planet. If the planet/object is at phase=0 and the FOV encompasses the whole planet, this unit then corresponds to the “geometric albedo”. In PSG, fluxes always include reflected and thermal emitted fluxes, and in that sense I/F provides a metric to the reflective and emitting properties of the planet. If the simulation includes leaked star/stellar fluxes (e.g., coronagraphy), these are removed from the “Total” column to provide solely planetary I/F values.

## 5. Zodiacal light, exozodii, telluric and background sources

As we observe our target planetary object (and possible stellar companion), we also observe several background sources, which are not included in the reported radiances, but they do impact the overall sensitivity of the simulations. Effectively when performing observations, one first samples the object

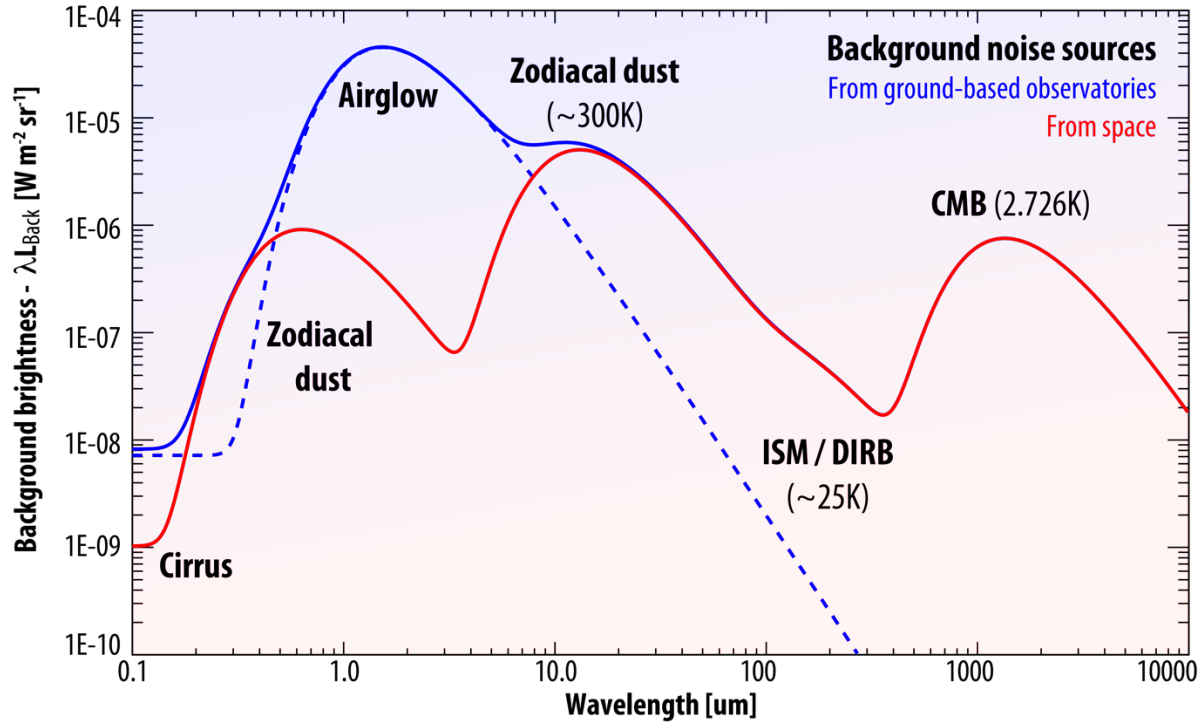


**Figure 3:** When observing faint astronomical sources, the sensitivity is affected by the shot noise introduced by background and diffuse sources. From space, the background is dominated by the faint and diffuse emission (thermal and scattered sunlight) from zodiacal dust, while airglow (a mixture of photoionization emissions, chemiluminescence and scattered sunlight) dominates the background for ground-based observations. PSG also employs a rudimentary (as shown), yet relatively effective, approximation for atmospheric airglow.

and the background in the A position, then switches to a B position in which only the background is sampled, and then performs the A-B difference to eliminate the background flux from the observations. An optimum sky / background method is to observe in an ABBA sequence to enable second order background cancellation. Even though the observations would no longer include background fluxes, they do unfortunately retain the noise associated with them. This background noise is also added twice (since it exists in the A and B positions), and therefore it must be included twice (see  $N_{\text{total}}$  equation in Table 2).

There are 3 major sources of background noise:

**Instrumental optics ( $N_{\text{optics}}$ ):** this is noise originating due to the thermal emission by the instrumental/telescope optics. This value is typically constrained by the temperature and emissivity of the main mirror of the telescope, and it is why so much care is taken to shield the observatory from sunlight when pursuing sensitive infrared observations (e.g., JWST). This term is parameterized in PSG by defining the emissivity and temperature of the optics.

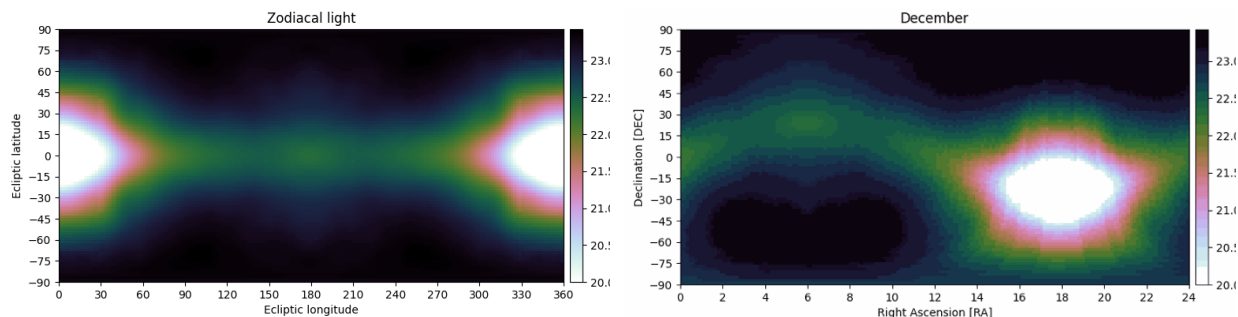


**Figure 4:** The zodiacal flux decreases notably when away from the Sun, and as the Sun moves across the sky (RA/DEC) during the year, the zodiacal levels change for the same RA/DEC. It is therefore of importance to properly define the zodiacal level at the time of the observations or at the most favorable time/month. The levels shown in these figures were computed by combining data from (Kwon et al., 2004) and from (Leinert et al., 1998). A zodi calculator in PSG (<https://psg.gsfc.nasa.gov/helpmodel.php#noise>) permits to estimate the zodiacal level and the scaler to be used in PSG.

**Ground-based background sources ( $N_{\text{tel}}$ ):** when performing ground-based observations, thermal emission and airglow by our own atmosphere lead to strong background signatures. Thermal emission and absorption are parameterized in PSG via the definition of the location of the observatory and the total telluric water column for the simulation. PSG works with a database of pre-computed telluric transmittances, that includes 5 altitude regimes (Maunakea/Hawaii [4200 m], Paranal/Chile [2600 m], SOFIA [14,000 m] and balloon observatories [35,000 m]) and 4 water columns established by scaling the tropical water profile by a factor of 0.1, 0.3 and 0.7 and 1. Airglow is a particular important source of radiation at short wavelengths originating from a mixture of photoionization emissions, chemiluminescence and scattered sunlight, and it is modeled in PSG via a simple yet effective parameterization as presented Figure 3.

**Background astronomical sources ( $N_{\text{back}}$ ):** several background and diffuse sources (e.g., zodiacal dust, exozodi, Cirrus, ISM/DIRB, CMB, Leinert et al., 1998) introduce noticeable levels of noise. Zodiacal light is the faint and diffuse radiation across the ecliptic plane originating from scattered sunlight by interplanetary dust. The brightness of the zodiacal light decreases with distance from the Sun, with a notable increase at opposition due to backscattered sunlight ("gegenschein"). This background radiation is typically the main background radiation term impacting space observations of faint objects, and it is highly dependent on the RA/DEC of the target and the time of the observations. In PSG, the parameterization of the zodiacal level is done by a scaling factor with respect to the polar ecliptic value (23.3 V [mag/arcsec<sup>2</sup>]), with a scaling of 2 (22.5 [mag/arcsec<sup>2</sup>]) being the default and the typical value for a general observatory. For exozodis, the surface brightness increases because of the geometry and preferable scattering with an average value of 22 V [mag/arcsec<sup>2</sup>]. In coronagraphy, the user can scale this by a multiplier (1 being 22 [mag/arcsec<sup>2</sup>]).



## 6. Coronagraphic modeling

Coronagraphic simulations are relatively complex simulations, in which several components of a scene are integrated into a cohesive simulated spectrum with a corresponding associated noise (see Figure 5). In practice, these simulations are integrated into PSG by adding a “coronagraph” layer on top of the classical instrument modeling discussed in the previous sections. This layer will provide specific throughputs ( $\eta$ ) for the planet and background signals, and another for the stellar signature. These throughputs will depend on the wavelength of the pixel, the diameter of the telescope, the separation between the planet and star and considered coronagraph and contrast transfer curves. The main objective of a coronagraph is to maximize the throughput of the planetary signature and to minimize the fluxes from the stellar companion. This is achieved by placing a blocking element (e.g., star-shade, vortex coronagraph that relies on a phase mask forming a spiraling blocking phase) in front of the star, while also keeping the planet away from this blocking element. The distance between the star and planet then defines how much of the planet flux is permitted to go through.

There are four important parameters in a coronagraph:

**Core throughput ( $\eta_{\text{core}}$ ):** this is the maximum throughput of the coronagraph for the planetary signature. The greater this value the higher the performance of the instrument. In figure 5, for instance  $\eta_{\text{core}}$  is 0.27 for LUVOIR-A.

**Inner Working Angle (IWA):** this defines the star-planet separation, defined in radians as  $\lambda/D$ , at which the throughput is half of the core throughput and towards the star. The lower this value, the closer we can observe the planet from the star. In Figure 5, we see that the IWA for LUVOIR-B is 3.5.

**Outer Working Angle (OWA):** this defines the  $\lambda/D$  at which the throughput drops below half the core throughput beyond the core region. In Figure 5, the OWAs are beyond the limits of the  $14 \lambda/D$  shown limit, yet we only show a simplified transfer curve in this figure. The greater this value, the further we can observe the planet from the star.

**Contrast (C):** defines how much stellar leakage remains, and it is defined with respect to the core throughput. In PSG, we assume  $\eta_{\text{star}}$  to be constant in wavelength, and only dependent on the reported contrast and the coronagraph core throughput in the form of  $\eta_{\text{star}} = \eta_{\text{core}} \cdot C$ . For instance, considering the case of LUVOIR-A with C defined as  $1e-10$ , the stellar throughput is then  $\eta_{\text{star}} = 0.27 \cdot 1e-10 = 2.7e-11$ .

A particular confusing term is  $\lambda/D$  (as presented in the coronagraph chart in Figure 5), and why it depends on wavelength. This is because coronagraphy is primarily done via interference patterns (not the case of star-shades though), and therefore it is wavelength dependent. For instance, a  $\lambda/D$  of 9 for a 15 meters telescope ( $D=15$  [m]) at a wavelength of  $0.5 \mu\text{m}$  ( $\lambda = 5e-7$  [m]) is  $9 \cdot 5e-7 / 15 = 3e-7$  [rad], which is equivalent to a separation of  $0.06$  [arcsec] ( $3e-7 \cdot 3600 \cdot 180 / \pi$ ). For a planet at  $5$  [pc], this would correspond to a separation of  $0.3$  [au] ( $5 \cdot 3e-7 / 4.84814e-6$ ) between the planet

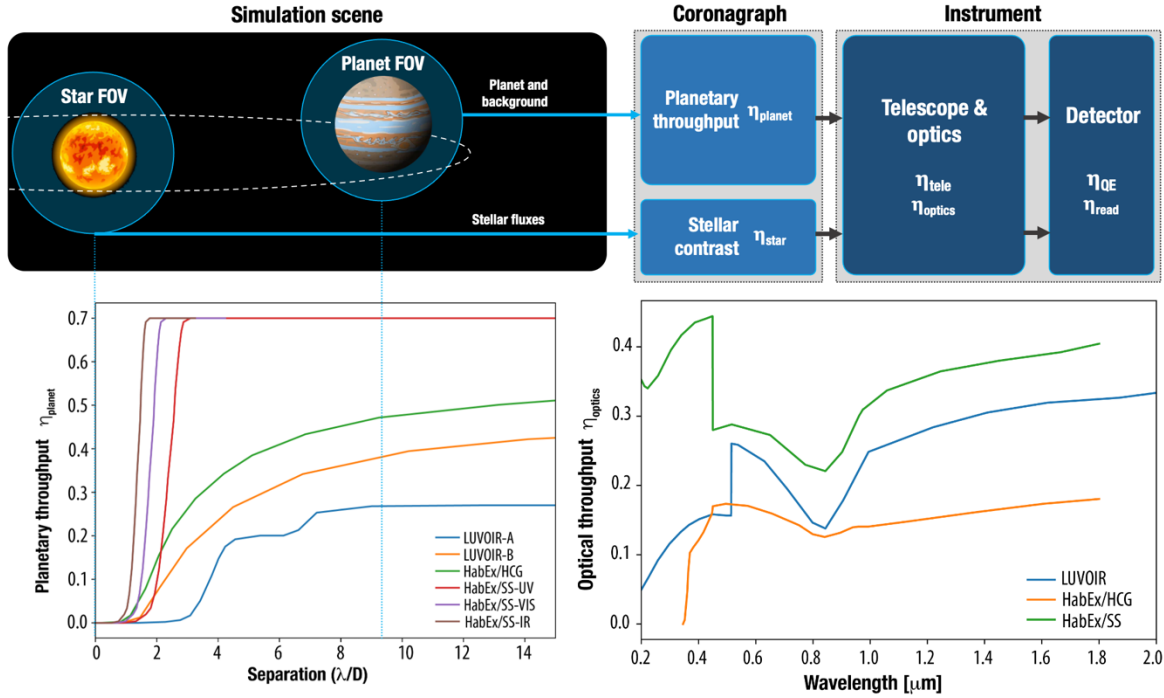


**Figure 5:** Elements involved in a coronagraphic simulation, and example throughput curves for several blocks as considered by the LUVOIR (A and B) and HabEx concept missions (star-shade/SS and coronagraph/HCG). The “coronagraph” acts as an additional layer to the standard “instrument” model blocks of PSG, in which the planetary (and background) fluxes are affected by the coronagraph transfer function ( $\eta_{\text{planet}}$ ), while the stellar fluxes are heavily reduced by orders of magnitude ( $\eta_{\text{star}}$ ). All these parameters can be provided as inputs to PSG as described in section 6. The value of  $\eta_{\text{planet}}$  will depend on the star-planet separation (in radians), the wavelength ( $\lambda$  [m]), the telescope diameter ( $D$  [m]) and the planetary throughput curve.

and the star. Then, if we are observing a planet at 5 [pc] separated by 0.3 [au] from the star with LUVOIR-A (corresponding to  $\lambda/D = 9$ ), then the throughput would be 0.27.

In the case of star-shades (e.g., HabEx/starshade), the blockage is not done by interference but by physically blocking the stellar light with a spacecraft flying in formation in front of the observatory. As such, the blockage is primarily defined by the physical properties of the star-shade, and it is in principle wavelength independent. The transfer function is then not reported in  $\lambda/D$ , but in actual units of separation [radians] or [arcseconds]. In PSG, the coronagraph transfer function can be provided in units of  $\lambda/D$  or in [arcseconds] depending on the sign of the x-axis – please refer to the LUVOIR and HabEx templates for examples in how to upload your own coronagraph transfer function. If no coronagraph function is provided, PSG assumes that the throughput is minimum (contrast) within half the inner-working-angle (IWA), it reaches 0.5 at the IWA, and reaches 1.0 at 1.5 times the IWA.

Beyond the coronagraph transfer function, several instrument elements will lead to losses in the light path. The more important are:  $\eta_{\text{tele}}$  is the telescope main mirror efficiency (0.95 is a typical value);



$\eta_{\text{optics}}$  is the optical throughput which is typically wavelength dependent (as shown in Figure 5);  $\eta_{\text{QE}}$  is the detector quantum efficiency and depends on the detector technology and sampled wavelength (typically ranges from 0.7 to 0.9); and  $\eta_{\text{read}}$  is the read-out efficiency which can be considered 1.0 in many cases, yet a value of 0.75 is commonly used for certain EMCCD detectors. The total instrument throughput includes all these losses, and therefore  $\eta_{\text{inst}} = \eta_{\text{tele}} \cdot \eta_{\text{optics}} \cdot \eta_{\text{QE}} \cdot \eta_{\text{read}}$ . In PSG, the provided total throughput efficiency refers to this quantity and should include all losses beyond those of the coronagraph.

For further details on coronagraphic simulations with PSG and comparisons to other coronagraph simulators, please refer to Checlair et al., 2021 (LUVOIR/HabEx), Kopparapu et al., 2021 (LUVOIR) and Saxena et al., 2021 (Roman). Importantly, when operating in coronagraphy mode, the noise output of PSG (“**noi**” file) will include the calculated planetary coronagraphy ( $\eta_{\text{planet}}$ ) for every simulation pixel, while PSG will also provide the count rates for the different sources in the “**cps**” file. The count rates allow to quantify the relevance of the different sources arriving to the detector, of key relevance when comparing to other coronagraph models (e.g., Robinson et al., 2016) or when investigating the dominating sources impacting the noise levels.

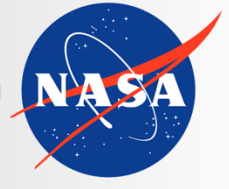
## 7. AOTF and grating modeling

Acousto Optical Tunable Filters (AOTF) allow to select a certain wavelength range of the light traversing an optical path by injecting a specific frequency to a tunable crystal. These filters are relatively compact and quick flexible, and therefore a common feature in many instruments, in particular, for mass/volume/power efficient space instruments (e.g., ExoMars-TGO/NOMAD). When performing simulations of AOTF images in PSG, there is no need to select this mode – simply selecting a resolution that corresponds to the spectral width of the filter is sufficient. The AOTF mode in PSG refers to a special configuration, in which the AOTF operates as an order sorting device for a high-resolution grating system. In an echelle grating spectrometer, all diffraction orders overlap at the same location, and a cross-disperser or filter is used to select the main order of interest. The challenge in an AOTF + grating system is that the AOTF has a complex transfer function, and the contribution of nearby orders overlap to the main selected order. This would mean that when modeling a spectrum for order X, one sees lines spanning a broad range +/- N orders around X.

In PSG, we have implemented a realistic AOTF and grating model that captures the subtleties of order addition and allows for a complex AOTF transfer function scheme. Specifically, the AOTF function is modelled as an asymmetric sinc function complemented by a Gaussian core and a systematic offset. For further details regarding the implementation and modeling of the AOTF in PSG, please refer to (Liuzzi et al., 2019; Villanueva et al., 2021).







**Planetary Spectrum Generator**  
National Aeronautics and Space Administration

# Chapter 9: **Retrieval Methods**

**Liuzzi, Villanueva, Mandell and  
PSG team**

## 1. Retrievals general elements

Retrieving information from planetary observations can be approached in many ways, which can rely to a different degree on radiative transfer or the data themselves. In any case, any retrieval problem is defined in terms of an input (the “data”), a series of unknown variables to retrieve (the “parameters”) and a model that correctly accounts for the physics of the observed system. The objective of a retrieval scheme is to minimize the difference between the data and the model, and to find the corresponding set of parameters.

In most cases, as many inverse problems, this is an ill-posed problem, as many different solutions could represent the observations as well: a classical example is the problem of simultaneously estimating the surface temperature and emissivity of a planetary body, which even in absence of atmospheric absorption does not have an obvious solution. Therefore, one of the main challenges in retrievals is to resort proper ways to optimize the solution towards a set of parameters that is physically coherent with the observed system. Modern algorithms and schemes are accustomed to providing such optimal solutions, by using statistical constraints and heavily relying on climate models as a starting point for the search of the solution.

According to the degree of constraint that can be applied to the search for the optimal solution, retrieval schemes can be roughly divided into two large categories: 1) (pseudo-)analytical schemes, which foresee the possibility to work with strong constraints to the solution, and 2) statistical schemes, in which the search for the solution is performed by exploring a large region of the parameters space and minimizing proper metrics related to the difference between data and model.

PSG currently has two packages that implement two of the most widely used retrieval techniques for each category: an Optimal Estimation (OE) method module (Rodgers, 2000), which has been widely applied and well consolidated in the context of Earth and the other planetary bodies of the Solar System; and a Nested Sampling (NS) scheme (Buchner, 2021) which is widely employed in the context of exoplanetary research to, e.g., look for signatures of molecular absorption in atmospheres.

## 2. Optimal Estimation

OE retrievals are particularly suitable in cases where a wealth of prior information about the parameters to retrieve is available and can be used to constrain the solution of the parameters. In fact, any OE algorithm and its variations include the necessity to use **a-priori** as an integral part of the mathematical equations that yield the minimization of the residuals between the model and the data; this objective is always sought in an iterative fashion through a Gauss-Newton approach, via the minimization of a chosen cost function  $Q$  that can be customized according to the specific application.

The OE package in PSG is fully integrated with the radiative transfer model, meaning that they are completely inter-operable, and that the data and the parameters set in PSG can be part of the set of parameters to retrieve. The OE scheme in PSG is based on the original formulation of OE (Rodgers, 2000) and some extra regularization mechanisms (e.g., Liuzzi et al., 2016) which are summarized



here. The principle of OE is to analytically link the **data space** with the **parameter space** by a set of analytical equation that are derived from the minimization of a cost function.

PSG adopts the simplest choice for the cost function, which is the  $\chi^2$  (chi-square) of the spectral residuals. Let us suppose that the data  $\mathbf{R}$  (i.e., a spectrum) consist of an array of  $M$  spectral channels, and that  $\mathbf{r}$  is the model spectrum. Let  $\boldsymbol{\sigma}$  be an array of length  $M$  representing the uncertainty (i.e., the noise) affecting the measurement  $\mathbf{R}$ . The  $\chi^2$  will be calculated as follows:

$$\chi^2 = \sum_{i=1}^M \frac{(r_i - R_i)^2}{\sigma_i^2} \quad (1)$$

**Parameter space:** In a more general formulation, OE equations are expressed in a matrix form, summarizing all the parameters of the problem. Let  $\mathbf{v}$  be an array of length  $N$  which contains all the parameters corresponding to the “true” set of values for the data. This array could include, e.g., the surface parameters (temperature, reflectance), the atmospheric parameters in terms of the total column observed of a particular constituent (gas, aerosol, temperature), or the full, or a portion of the vertical profile of those parameters along the line of sight. At first, one also must define an initial guess for the values of the parameters, which is denoted as  $\mathbf{v}_0$ . Furthermore, OE works by properly constraining the solution by tying it to a background array, denoted as  $\mathbf{v}_a$ , which usually contains values for the parameters tuned on a-priori information, such as climate models, or educated guesses on the parameters from past observations. However, as discussed later, the choice of the background is very critical only when the data do not contain enough information to independently constrain the value of a specific parameter. The final quantity in the parameter space is their covariance matrix  $\mathbf{S}_a$ , which determines what is the expected variability of the parameters and their degree of correlation. The simplest choice for it is a diagonal matrix, which corresponds to assuming total independence of all the parameters from each other. Yet, in many cases, this is a non-realistic assumption, especially when dealing with vertical profiles of atmospheric parameters, which will be characterized by a certain vertical correlation scale.

**Data space:** the modeled data  $\mathbf{r}$  results directly from the radiative transfer model, which can be synthetically indicated as a function  $F$ :  $\mathbf{r} = F(\mathbf{v}')$ . Similarly to the parameter space, data comes with a prescribed noise  $\boldsymbol{\epsilon}_R$ , which is quantified according to the observing instrument and the conditions, or can be also estimated by the statistical properties of the analyzed dataset (e.g., Serio et al., 2018). In OE, the noise comes in form of a signal covariance matrix  $\mathbf{S}_y = \boldsymbol{\epsilon}_R \boldsymbol{\epsilon}_R^t$  in its simplest diagonal form, with  $t$  standing for transpose. This is the formulation adopted in PSG and corresponds to neglecting any possible component of correlated noise; yet, in the more general case, complex formulations considering effects such as inter-channel correlations can be adopted.

With these definitions, the most general form of the cost function minimized by OE is the following:

$$Q = [\mathbf{R} - F(\mathbf{v}')]_t \mathbf{S}_y^{-1} [\mathbf{R} - F(\mathbf{v}')] + \gamma [\mathbf{v}' - \mathbf{v}_a]_t \mathbf{S}_a^{-1} [\mathbf{v}' - \mathbf{v}_a] \quad (2)$$

where  $\gamma$  is the additional Levenberg-Marquardt regularization parameter (Liuzzi et al., 2016; Carissimo et al., 2005), which acts as a tradeoff between the background values given to the parameters to be retrieved and the observations. Large values of  $\gamma > 1$  will constrain the retrieval scheme more to the a-priori parameter value. As  $\gamma$  approaches 0, the solution scheme tends to a constrained least-square with Eq. (2) tending to the (1). For  $\gamma = 1$ , the Rodgers' classical scheme is run. In PSG, for the sole calculation of the  $\chi^2$ , the formulation with  $\gamma = 0$  is adopted.

**The link between data and parameters:** At a first degree, OE is built to search the optimal solution by computing gradients of the cost function in the parameter space. This is naturally done by using the Jacobian matrix  $\mathbf{K} = \left. \frac{\partial F(\mathbf{v})}{\partial \mathbf{v}} \right|_{\mathbf{v}=\mathbf{v}'}$ ; the matrix will have size  $M \times N$ , and will contain the derivatives of the model with respect to the parameters to retrieve evaluated around the current solution. If we also define  $\mathbf{x} = \mathbf{v} - \mathbf{v}_0$ ,  $\mathbf{x}_a = \mathbf{v}_a - \mathbf{v}_0$  and  $\mathbf{y} = \mathbf{R} - F(\mathbf{v}_0) - \mathbf{K}\mathbf{x}_a$ , Eq. (2) can be developed into the formal retrieval equation:

$$\mathbf{x}(\gamma \mathbf{S}_a^{-1} + \mathbf{K}_t \mathbf{S}_y^{-1} \mathbf{K}) = \mathbf{y}(\mathbf{K}_t \mathbf{S}_y^{-1}) \quad (3)$$

This equation is solved iteratively, by re-evaluating the cost function at every step where a new  $\mathbf{x}$  is obtained. At the  $n$ -th iteration, the solution implemented in PSG is in the following form:

$$\mathbf{x}_n = (\gamma \mathbf{S}_a^{-1} + \mathbf{K}_t \mathbf{S}_y^{-1} \mathbf{K})^{-1} [\mathbf{K}_t \mathbf{S}_y^{-1} \mathbf{y} + \gamma \mathbf{S}_a^{-1} \mathbf{x}_a] \quad (4)$$

where the Jacobian matrix and the parameters array are evaluated based on the result of the previous iteration  $n-1$ . In PSG, as in any OE scheme, it is customary to internally normalize the parameters' array and the matrices associated with that, such that calculations and matrices inversion is performed avoiding numerical instabilities as much as possible. After a certain number of iterations, convergence is reached when the  $\chi^2$  is lower than a fixed threshold; there are also occurrences when convergence is not reached, and those are characterized by divergence in the  $\chi^2$  value, or by situations in which the retrieved values for some of the parameters are not properly constrained.

The OE scheme also provides a natural quantification of some a-posteriori quantities that are useful to characterize the information content of the data and the statistical uncertainty affecting the retrieved parameters. the uncertainty affecting the retrieved parameters, which we denote here with  $\tilde{\mathbf{v}}$ , by computing the a-posteriori covariance matrix:

$$\mathbf{S}_{\tilde{\mathbf{v}}} = (\gamma \mathbf{S}_a^{-1} + \mathbf{K}_t \mathbf{S}_y^{-1} \mathbf{K})^{-1} (\gamma^2 \mathbf{S}_a^{-1} + \mathbf{K}_t \mathbf{S}_y^{-1} \mathbf{K}) (\gamma \mathbf{S}_a^{-1} + \mathbf{K}_t \mathbf{S}_y^{-1} \mathbf{K})^{-1} \quad (5)$$

Another important quantity is the Averaging Kernel (AK) matrix of the derived parameters, which is defined as the sensitivity of the retrieved parameters with respect to their "real" value:

$$\mathbf{AK} = \frac{\partial \tilde{\mathbf{v}}}{\partial \mathbf{v}} = (\gamma \mathbf{S}_a^{-1} + \mathbf{K}_t \mathbf{S}_y^{-1} \mathbf{K})^{-1} \mathbf{K}_t \mathbf{S}_y^{-1} \mathbf{K} \quad (6)$$

The diagonal of the AK matrix contains values between 0 and 1, which indicate the sensitivity of the retrieval to each parameter. Low values could indicate either poor intrinsic sensitivity of the data

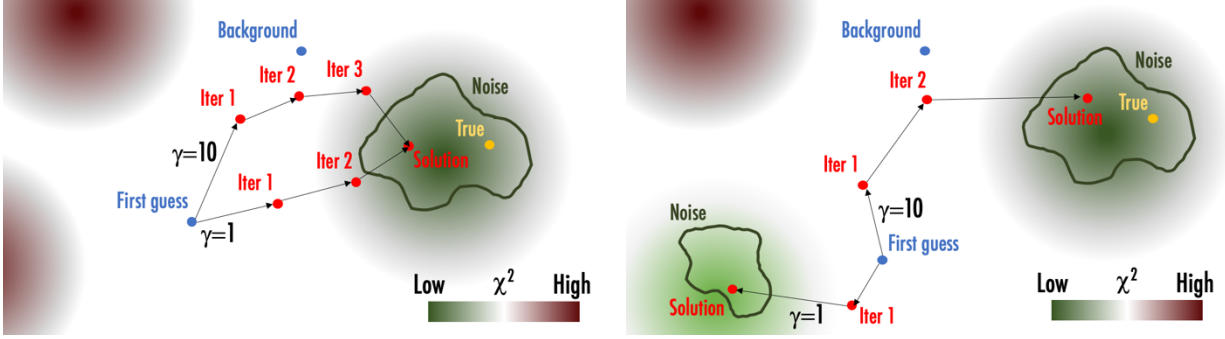


**Figure 1:** Scheme to illustrate the walk of OE between the First Guess and the solution. The background color represents the  $\chi^2$ , while the green lines represent the limit at which the solutions are all equal within the spectral noise (i.e., every model in that contour differs from the data by at most the noise). According to the value of gamma, the walk to the solution happens in different paths at different distances from the background. **Left:** a case in which the First Guess is relatively close to the truth. **Right:** a case where the First Guess is closer to another local minimum in the  $\chi^2$ , where other settings in the OE can steer the walk to the solution to the correct one.

themselves to the retrieval parameters (low  $K$ ), or too stringent constraints imposed to the variability of the retrieved parameters (very high  $\gamma S_a^{-1}$ ), and that the retrieved information will be dominated by the background. Instead, diagonal elements of  $AK$  equal to 1 will indicate that the retrieved values are fully constrained by the data. The non-diagonal elements indicate the degree of correlation between parameters; ideally, these values are close to 0, or negligible with respect to the diagonal elements.

The behavior of the OE scheme can be conceptually summarized in the scheme in Figure 1. Depending on the value of  $\gamma$ , the walk between the first guess and the solution is influenced by the background and can be slower or faster. However, it is important to note that the OE works at its best only when the first guess is reasonable with respect to the truth. When this is not the case, the presence of local minima in the  $\chi^2$  close to the first guess could yield the solution to collapse into such local minima, unless the background is properly chosen to make sure that the solution ends up in a domain close to the truth.

### 3. Implementation of OE in PSG

The implementation of OE in PSG benefits of some extra elements borrowed from simpler approaches, such as the regularized Levenberg-Marquardt (LM) minimization method. PSG relies on defining many parameters in the previous equations implicitly in the code, with minimal input from the user. The scheme for the implementation of OE in PSG is shown in Figure 2. Specifically, the following aspects and variables are implicitly defined in the code:

- For every retrieved parameter, PSG accepts in input from the user minima and maxima for their variability,  $v_{min}$  and  $v_{max}$ , similarly to what is usually done in a LM regularized approach. Those are then used to define the a-priori covariance matrix  $S_a$ , whose diagonal elements are computed as 10% of the difference between  $v_{max}$  and  $v_{min}$ .

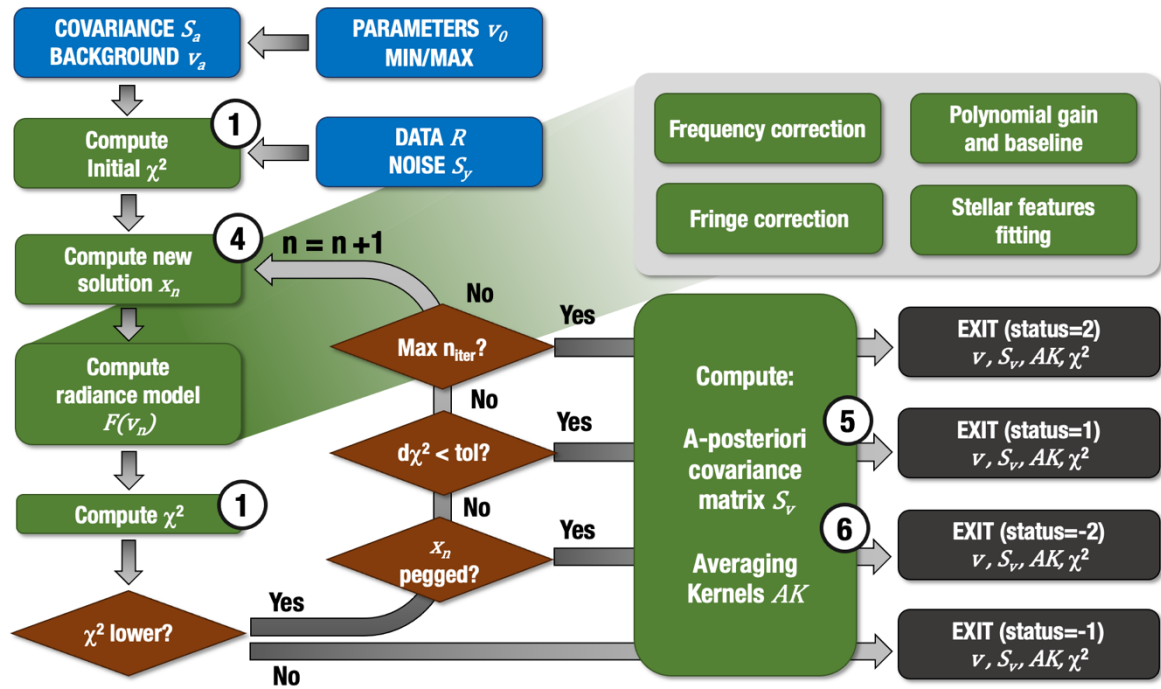


**Figure 2:** Scheme summarizing how OE is implemented in PSG. The blue boxes represent the user inputs, the green boxes are the internal PSG operations (and related equation numbers in the circle), in grey the outputs are shown.

- The same extremes are used to define the background  $v_a$  as the average of the extremes:  $1/2(v_{max} + v_{min})$ .
- To make the convergence and the inversion of the matrices smoother, the variables in the parameter space are all normalized using either the extremes provided by the user, or a-priori information related to the type of parameters. For example, in the case of temperature (atmospheric or surface), the elements of  $x$  corresponding to temperature are divided by 300 (K).
- The maximum number of iterations is 20. While it is common for OE to rely on a fixed threshold for the  $\chi^2$  below which the scheme exits with the solution, this would imply relying on accurate knowledge of the input noise. Given the general applicability of PSG, this is not always the best choice. Instead, it is checked whether the  $\chi^2$  at the  $n$ -th iteration is lower than the one at the  $(n-1)$ -th iteration by a factor.
- Retrieved parameters are checked by looking at whether the retrieval pegs them to their extremes. If that occurs several consecutive times the scheme excludes them from the retrieval.

The retrieval module can also correct for specific instrumental effects, which are iteratively accounted for through the radiative transfer function. This is necessary as at every iteration the model corresponding to the updated retrieval parameters changes, and with that the estimation of instrument-induced effects (more on this in Villanueva et al., 2013). A schematic view of such effects is given in Figure 3:



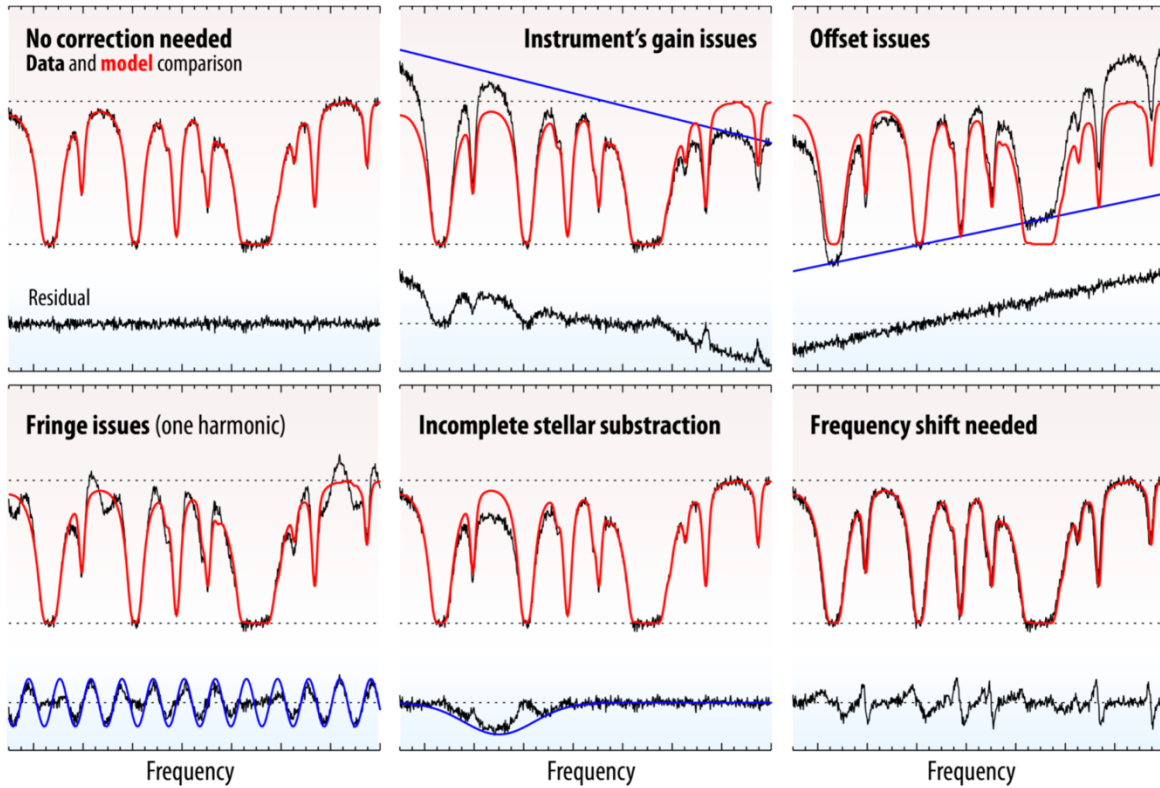


**Figure 3:** Illustration that shows the corrections that the PSG retrieval module is capable of accounting for and modeling.

**Frequency correction:** frequency shifts can be induced by a myriad of instrumental effects, such as flexing of detectors and gratings caused by temperature changes. Correction of this effect is performed in PSG via a brute-force approach. Once the radiative transfer produces a model at the same spectral resolution as the data, the model is interpolated on the same sampling points as the data. To search for eventual frequency corrections, the data spectral grid is shifted, stretched and bended in regular steps, circling to the optimal solution which is sought by evaluating the correlation coefficient between the data and the frequency-corrected model.

**Fringe correction:** Several types of data (e.g., grating-based spectrometers, interferometers) are commonly affected by fringing. Spectral fringes arise from multiple reflections between two optical surfaces, and interference of the resulting wave fronts. The fringe spacing is  $1/nL$ , ('n' is the index of refraction in the medium, and L is the separation of the two surfaces). When this happens multiple times in an instrument, multiple fringes of different frequency will show up in the data. Correction for spectral fringing is performed as follows. First, a Lomb–Scargle periodogram analysis on the residual spectra is performed, from which period, amplitude, and phase are determined for each fringe. This information is used to compute a synthetic model for each fringe, whose amplitude is fitted to the spectra through a LM fit and subtracted from the spectra pixel-by-pixel.



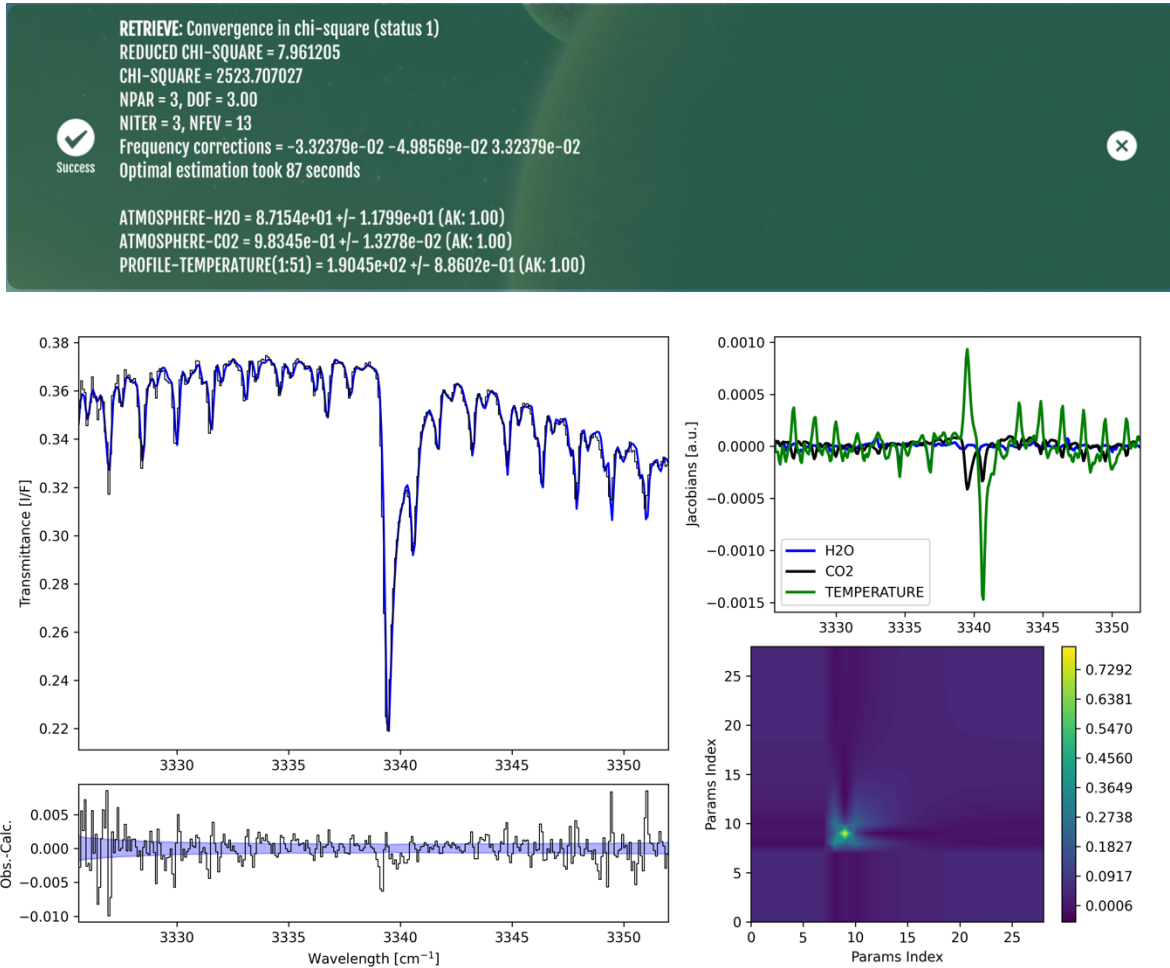


**Figure 4.** Sample results of a retrieval of water vapor, CO<sub>2</sub> column and average temperature along the line of sight for ExoMars NOMAD data (as in Liuzzi et al., 2021). **Top:** summary of the retrieved values and the main metrics computed by PSG. **Middle left:** data R (black) and best fit model  $F(v_n)$  (blue). **Bottom left:** spectral residuals (black) and noise envelope  $\epsilon_R$  (blue). **Middle right:** Jacobians, a.k.a. the derivatives of the model with respect to the parameters to retrieve (lines of the matrix K). **Bottom right:** Averaging Kernels of the temperature profile.

**Polynomial gain and offset:** Gain effects are oscillations in the continuum around an average value and are quite common in observed spectra from any kind of instrument and at any wavelength. Excluding those modeled by radiative transfer as intrinsic to the observed system (e.g., emissivity or reflectance of the surface, atmospheric aerosols), the residual continua are modeled by PSG by LM fitting of a polynomial of degree specified by the user, which multiplies the model. An offset, instead, occurs as external flux added in the observations (e.g., by straylight), and is fitted by LM as a polynomial additive component to the model.

**Stellar features fitting:** in some cases, such as ground-based or nadir observations of a rocky planet, stellar lines and features can show up in the data if not previously corrected, and there are cases in which fitting their amplitude can give information about atmospheric absorption (as stellar

Parameter	Brief description	Optimal value	Optional?
$\chi^2$	As in Eq. (1)	$<N$ (residuals average is $<\epsilon_R$ )	NO
Reduced $\chi^2$	$\chi^2/(N- M)$	$<1$	NO
DOF	$\sum_{i=1}^N AK(i, i)$	$M$ (Information fully constrained by data)	It is 0 if no parameters are retrieved
NITER NFEV	Number of iterations Number of forward calculations	Max NITER is 20 The lower, the faster	NO
Status	Status of convergence	-2: all variables pegged to limits -1: Divergence in $\chi^2$ (does not decrease) 0: bad input /nothing to retrieve 1: convergence in $\chi^2$ (OPTIMAL) 2: max. NITER reached	NO
Frequency correction	Polynomial coefficients for shift, stretch and bending of the freq. correction	0 for all (i.e., the frequency solution is already optimal)	YES
AK	As in Eq. (6)	Unity matrix (Information fully constrained by data, parameters independent of each other)	NO

**Table 1:** List of the PSG retrieval output parameters, their definitions, and their significance.

radiation transverses two paths before reaching the observer in many geometries), or surface reflectance. There are also cases in which stellar lines are previously subtracted from the data, but the subtraction is not complete or generates micro-dispersion features related to incorrect frequency calibration. In any case, the forward module in the retrieval is capable of modeling and taking out stellar features by LM fitting of their amplitude.

Examples of retrieval applications are shown in Figure 4. In the examples of ExoMars Trace Gas Orbiter data, the single components of the retrieval scheme in PSG are highlighted. On the bottom we also show a sample calculation of Averaging Kernels of the atmospheric temperature profile. Since these data are taken in Solar Occultation geometry at a specific altitude (13 [km]), the Averaging Kernels show that no information related to the temperature is present below that altitude, and that most of the information is concentrated in the proximity of the tangent altitude. PSG does not output the full a-posteriori covariance matrix, showing only the estimated uncertainty of each parameter (square root of the diagonal elements of  $\mathbf{S}_{\hat{p}}$ ). A summary of the quantities that are provided in output by PSG is given in Table 1. This serves as reference to interpret the results of a retrieval, to clarify what outputs are optional, and to have a clear idea of what is the optimal value of each quantity in relation to the quality of the data and resulting fit.

## 4. Retrieval of vertical profiles

Retrievals of vertical profiles can be quite more complicated than cases when OE is applied to retrieve scalar parameters across the full atmosphere. Complications arise essentially because of three reasons: (1) the retrieval of vertical profiles require a significant increase in the number of parameters to retrieve (hence in the computational load); (2) the vertical sensitivity of the data to the properties of the atmosphere may not necessarily be obvious, and could depend on the specific spectral interval and observation geometry; (3) the value of a specific parameter in an atmospheric layer depends on the value of – at the very least – that parameter in nearby layers, and this must be properly accounted for in the OE equations. This is at the core of any *regularization* strategy, whose aim is to obtain physically meaningful vertical profiles of the specific parameter of interest.

As an example, let us suppose that one wants to retrieve the vertical temperature profile of a terrestrial planet from nadir observations. The same data could be as well represented by a smooth vertical profile centered around an average value, but also by a vertical profile with large unphysical fluctuations, layer by layer, around the same average value. The objective of regularization is to correctly establish the solution filtering unphysical fluctuations out, yielding a profile at a desired vertical resolution.

There is a variety of methods for regularization of vertical profiles, based either on weighing the information from different spectral intervals (e.g., Serio et al., 2016), or on a-posteriori smoothing of the solution (e.g., Quémerais et al., 2006). The latter approach is particularly useful to limit unphysical and amplified oscillations in the retrieved profile, by imposing a smoothness constraint which will decrease the effect of the noise in the profile. At the core of any regularization there is a proper choice of the covariance matrix  $\mathbf{S}_a$ . It is particularly important that  $\mathbf{S}_a$  is structured to contain all the information related to the expected variability of the vertical profiles of the parameters to retrieve, and properly enhances the elements of the profile to which the data are less sensitive to. This last specific aspect will depend on the observation geometry and the wavelength of the observation.

As an example, let us consider the case of data acquired in nadir-looking geometry, and that one wants to retrieve the vertical profiles of temperature and of a specific gas, together with  $n$  scalar parameters (i.e., column amounts of other gases, aerosols, or surface temperature). If possible, a full covariance matrix for these parameters could be derived directly from climatology or circulation models, by selecting a subset of locations and times, and computing the covariance of the vertical profiles and scalar parameters of interest. This approach would also account for correlations between different parameters and profiles, producing a non-diagonal covariance matrix, and it is customary in many Earth science applications (e. g., Masiello & Serio (2013); Yang & Liu (2019)).

In absence of climatology-specific a-priori information about the covariance of the profiles,  $\mathbf{S}_a$  takes the form of a block-diagonal matrix, that for the specific example considered here has the following structure:

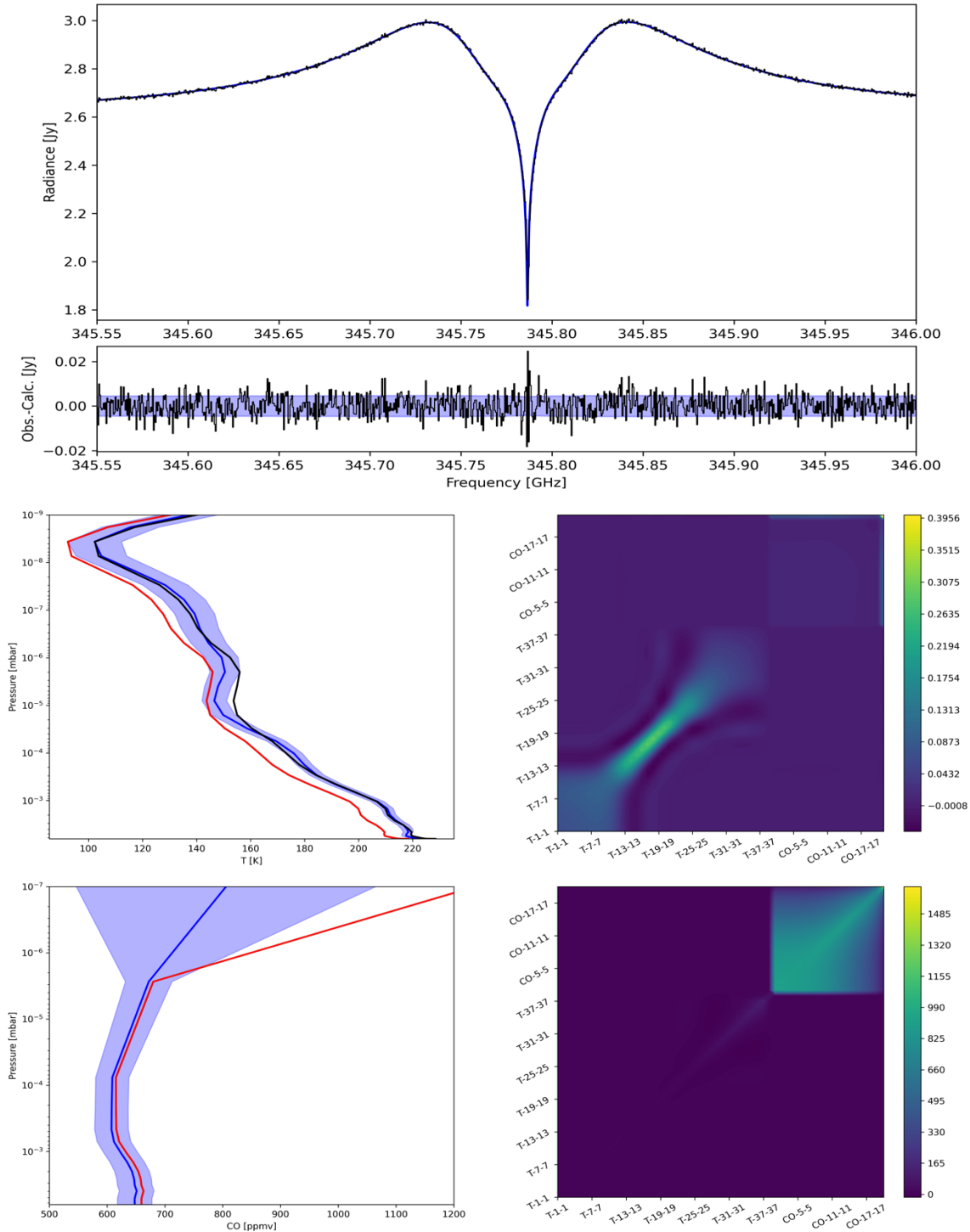


**Figure 5:** Vertical profile retrievals with PSG. **Top:** best fit to simulated ALMA data (black) and residuals on the bottom compared to the simulated noise. **Bottom left:** vertical profiles of temperature and CO: true (black), first guess and background (coincident: red) and retrieved with error bars (blue with the shaded area). **Bottom right:** a-posteriori Averaging Kernel matrix (top), and covariance matrix (bottom). It can be seen the block structure divided between the temperature profile (also on the axis with the layer number) and the CO one. The latter is less constrained (lower AK values, higher covariance).

$$\mathbf{S}_a = \begin{pmatrix} \mathbf{S}_T & \mathbf{0} & \mathbf{0} \\ \mathbf{0} & \mathbf{S}_{gas} & \mathbf{0} \\ \mathbf{0} & \mathbf{0} & s_1 & \cdots & 0 \\ & & \vdots & \ddots & \vdots \\ & & 0 & \cdots & s_n \end{pmatrix} \quad (7)$$

where the values  $s_{i=1,\dots,n}$  represent the variances of the scalar parameters,  $\mathbf{S}_T$  is the covariance matrix of the temperature profile, and  $\mathbf{S}_{gas}$  is the covariance matrix of the gas profile, both of them of sizes  $N_L \times N_L$ , where  $N_L$  is the number of atmospheric layers on which the profile is retrieved.

To regularize retrievals, these two matrices need to be structured in a way that each atmospheric layer has some degree of dependency from the nearby layers. A good way to do that is to assign a Markovian formalism to these matrices (as done, e. g., in Irwin et al. (2008); Serio et al. (2019)), such that their elements of  $\mathbf{S}_T$  (or  $\mathbf{S}_{gas}$ ) can be written as:

$$\mathbf{S}_T(i, j) = s_T(i) \cdot s_T(j) \cdot \exp \left( - \frac{\| \log (p_i/p_j) \|}{\alpha} \right) \quad (8)$$

where  $s_T(i)$  is the standard deviation assigned to the parameter in the  $i$ -th layer,  $p_i$  the pressure of that layer, and  $\alpha$  is a scaling factor that defines the scale of the correlation between nearby layers, in units of atmospheric scale heights. The higher the value of  $\alpha$ , the more the profile will be vertically correlated and tend to a constant with altitude. Typical choices of  $\alpha$  are around 1.5 for most temperature profiles, while there are also cases in which  $\alpha$  varies with the pressure itself to account for expected local steep gradients of the profile to retrieve. The values of  $s_T(i)$ , instead, depend strictly on the nature of the parameter (its vertical variability), the observation geometry (e.g., nadir vs. looking up), and the specific wavelength (i.e., the expected information content) of the observation. According to these aspects, one could choose to increase the standard deviation values with the altitude, keep it constant, or decrease it, and this is a very problem-specific decision.

Without any further specific modification these terms can be plug into the OE retrieval equations to obtain a solution. An example of retrieval is given in Figure 5, where a vertical profile of temperature and CO is retrieved from simulated ALMA observations of a CO line of Mars. It can be seen that the T vertical profile is well constrained to the true one, and because the CO and T are heavily interdependent, it is difficult to obtain vertically resolved CO measurements. This is also indicated by the Averaging Kernel matrix, which shows low information content for CO.

## 5. Nested retrievals: principles

The mathematical basis of OE theory is centered on the idea that a solution for the geophysical parameters can be sought by exploiting a-priori information derived from circulation models or other sources of knowledge. The a-priori plays an essential role in driving the solution to the most likely one and in the way the parameter space is explored, and when no reliable a-priori information is available, or when the First Guess is poorly constrained, OE can struggle in finding a physical



solution. In these cases, other approaches that rely less on a-priori knowledge, can be adopted to explore the parameter space. A large class of these models are based on randomly sampling the parameter space, to iteratively establish a region of likely solutions. While the OE seeks to minimize the number of iterations and maximizes the constraints to get to the solution, such statistical methods use large numbers of random realizations in the parameter space with little to no a-priori constraints.

The simplest framework in this sense is the Markov-Chain Monte-Carlo (MCMC, see van Ravenzwaaij et al. (2018)). A Monte-Carlo approach consists in drawing several random samples from a normal distribution and calculate their sample average. The benefit of working in this way is that, instead of computing the mean from the distribution properties, which may be unknown, the mean is computed directly by probing its statistical properties. The Markov-Chain property of MCMC, instead, consists in generating the random samples in a specific sequential framework: each random sample is in fact the steppingstone to draw the following random sample (therefore, the *chain*). The “Markov” property of the chain is that each new sample depends on the previous one, but new samples are independent of any samples before the previous.

As said, MCMC comes particularly in handy in Bayesian inference, because MCMC is focused on posterior distributions which are often difficult to handle by analytic examination (van Ravenzwaaij et al., 2018). In this sense, MCMC allows the user to approximate aspects of posterior distributions that cannot be directly calculated. If we consider the context of planetary observation, Bayesian inference uses the *information* provided about a set of planetary parameters, that is the *likelihood*, to update a prior state of beliefs about those parameters to become a posterior state of knowledge about them. The fact that many samples are drawn allows to evaluate the likelihood on the average of them and to estimate their standard deviation as an analog for uncertainty.

Let us continue to consider only the problem of retrieving planetary parameters from observed spectra. The MCMC essentially performs a walk, point by point, from an initial random realization of the parameters to the final solution. Depending on the number of parameters and the complexity of the radiative transfer, the convergence of the MCMC to a solution could be quite slow and require many iterations. With time, several more refined approaches have been resorted to make MCMC more efficient. One way to do that is to initialize the exploration of the parameter space with a larger number of points, and then use them to iteratively increase the likelihood of their average. This is the basic principle behind *nested sampling* (NS, Skilling, 2006). Let us introduce some elements of the NS; first, let us indicate with  $\theta$  a set of  $N$  parameters (e.g., atmospheric and surface parameters of interest), and with  $D$  the  $M$ -dimensional observed data array (a spectrum). Let us also indicate with  $H$  some model or hypothesis for the data  $D$ . This is clearly the nexus between data and parameters.



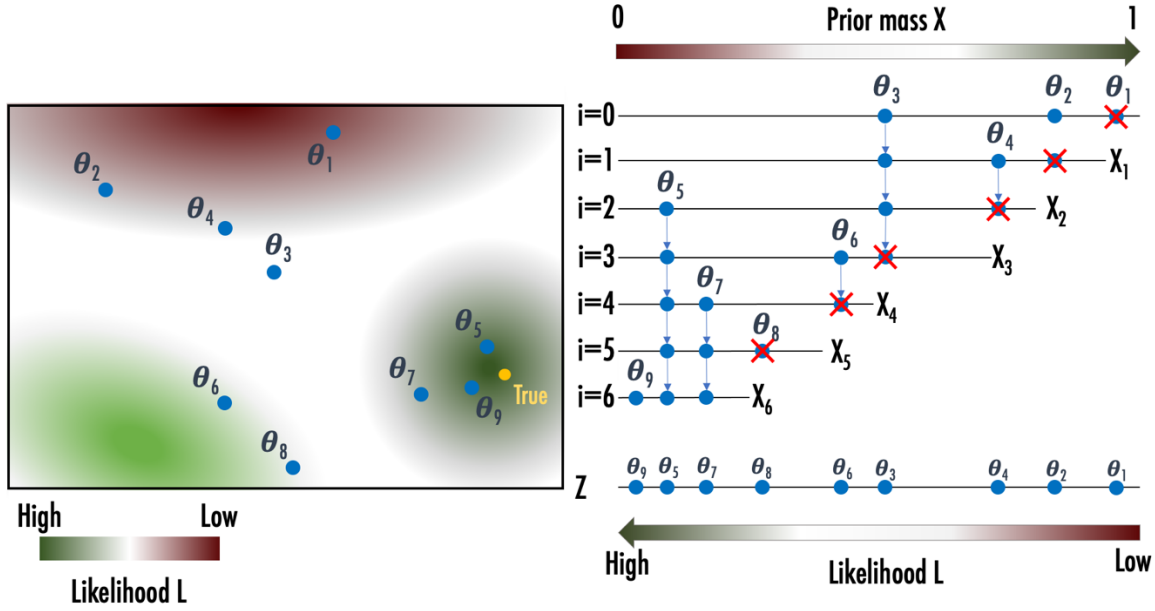


**Figure 6:** Schematic representation of the NS method. On the left, a simple parameter space (two-dimensional,  $N=2$ ) is represented, in which the solution (yellow) is in a high-likelihood region (color scale on the bottom). On the right, it is shown how high likelihood regions correspond to low mass ones and vice versa. At initialization, the scheme is started with  $n=3$  live points, each one characterized by a set of parameters  $\theta_j$ . At each iteration, the lowest-likelihood point is replaced with a new one, until convergence. Adapted from Skilling (2006).

According to the Bayes' theorem:

$$\Pr(\boldsymbol{\theta}|\mathbf{D}, H) = \frac{\Pr(\mathbf{D}|\boldsymbol{\theta}, H) \Pr(\boldsymbol{\theta}|H)}{\Pr(\mathbf{D}|H)} = \frac{L(\boldsymbol{\theta})\pi(\boldsymbol{\theta})}{Z} = P(\boldsymbol{\theta}) \quad (9)$$

where:

- $\Pr(\boldsymbol{\theta}|\mathbf{D}, H)$  is the posterior probability distribution of the parameters  $\boldsymbol{\theta}$ , given the data  $\mathbf{D}$ . This represents also the final result of the retrieval, and can be synthetically indicated with  $P(\boldsymbol{\theta})$ .
- $\Pr(\mathbf{D}|\boldsymbol{\theta}, H)$  is the likelihood of the data  $\mathbf{D}$  given the parameters  $\boldsymbol{\theta}$ , and responds to the question: how likely are the data  $\mathbf{D}$  to be reproduced by the parameters  $\boldsymbol{\theta}$  with the model hypothesis  $H$ ? It can be indicated with  $L(\boldsymbol{\theta})$ . *To trace a parallel with OE, this has a similar role as the cost function, or a chi-square.*
- $\Pr(\boldsymbol{\theta}|H)$  is the prior state of knowledge of the parameters  $\boldsymbol{\theta}$  before analyzing the data. For example, it can be an  $N$ -dimensional uniform distribution limited by ranges in which the parameters are searched, and it can be indicated with  $p(\boldsymbol{\theta})$ .
- $\Pr(\mathbf{D}|H)$  is the evidence. This is a key quantity in NS, as it represents not only a normalization factor for the posteriors, but also a natural quantification of the progression of NS retrievals through the solution, as it inherently tells how well data  $\mathbf{D}$  are reproduced under hypotheses  $H$ . It is commonly indicated with  $Z$ .



The question that NS tries to answer is: which set of models best describe the data? The key quantity to get to an answer is the evidence  $Z$ . From Eq. (9), for a set of models  $\theta$ ,  $Z$  can be defined as:

$$Z = \int L(\theta)\pi(\theta)d\theta \quad (10)$$

which is particularly challenging given the multi-dimensionality of the problem. To limit this complexity, NS starts from  $n$  initial models, each one specified by a set of planetary parameters  $\{\theta\}_{i=1,\dots,n}$  sampled from the prior distribution. For these initial set of models, let us compute their hyper-volume  $X$  in the parameter space including only those sets of parameters whose likelihood is above a certain threshold  $L'$ :

$$X(L') = \int_{L(\theta) > L'} \pi(\theta)d\theta \quad (11)$$

This integral sometimes is also referred to as (*cumulant*) *prior mass* including all likelihood values greater than  $L'$ . If one imagines the variable  $L'$  to increase, the integral in Eq. (11) goes from 1 to 0 (because of the normalization in Eq. (9) that is not explicitly reported). The introduction of the prior mass allows to simplify greatly the calculation of  $Z$ , which now becomes a one-dimensional integral:

$$Z = \int_0^1 L(X)dX \quad (12)$$

In this way, also, the problem regularizes naturally, as the likelihood calculation is not done on single samples, but on volumes in the parameter space, making  $L$  a monotonic, well-behaved function. Its integration then becomes easy to discretize as a sum over finite elements in the space of mass  $X$ . The NS objective becomes to modify in successive steps the initial sample to increase the evidence, and given the relation established between  $X$  and the parameter space  $\pi(\theta)$ , this can be done in one of the two spaces equivalently. The basic scheme of NS to work this out is summarized in the following and illustrated graphically in Figure 6, which can be compared to Figure 1 for OE.

- Start with  $n$  initial sets of parameters  $\{\theta\}_{j=1,\dots,n}$  randomly from the parameter space  $\pi(\theta)$ .
- Set the initial conditions:  $i=0$ ;  $X_0=1$ ;  $Z=0$  (or a very small value).

Until convergence is reached:

- Calculate the likelihoods  $\{L\}_{j=1,\dots,n}$  of  $\{\theta\}_{j=1,\dots,n}$  and record the lowest likelihood  $L_i'$ . Eliminate this point from the sample.
- Under the hypothesis that the mass function is of gaussian form, with most of the mass concentrated in a small region of the parameter space, set  $X_i = e^{-i/n}$ . One can also not consider this hypothesis and directly compute Eq. (11) by sampling the parameter space.
- Because the lowest-likelihood point has been canceled out from the sample, one needs to compute how much the evidence has increased from this cancellation. Using the discrete form of (12), one calculates the finite element  $\Delta X_i = w_i = (X_{i-1} - X_{i+1})/2$ . Then, the evidence is increased by  $L_i w_i$ .
- Now the lowest-likelihood point is replaced with a new one, which is drawn from the prior distribution  $\pi(\theta)$  with the condition that its likelihood is higher than  $L_i'$ .

At the end, the evidence  $Z$  can be incremented by  $n^{-1}[L(\theta_1) + L(\theta_2) + \dots + L(\theta_n)]X_i$ , to account for the missing intervals in the integral in (12) for all the surviving points in the parameter space. However, this last adjustment is usually less important if either the number of samples  $n$  is large, or if the number of steps to convergence is large.

There are two important aspects to clarify about NS mechanics: the choice of the convergence criterion and the choice of the likelihood functional form. For the first one, while the simplest choice would be to terminate NS when a certain number of iterations  $n$  is reached, there are much cleverer possible choices that account for the statistical properties of the evidence  $Z$  and the likelihood of the samples. While there are no universally valid conditions to terminate NS that ensures always to find the “best” solution, the general idea is to have a condition that translate into “continue the NS iterations until most of the evidence  $Z$  has been found” (Skilling, 2006). Two possible criteria to satisfy this are the following:

- Continue until even the largest current likelihood, taken over the current  $X_i$ , would not increase the current evidence by more than some small fraction (chosen by the user)  $\alpha$ :  $\max(L_1, \dots, L_n)X_i < \alpha Z_i$
- If an upper bound to the likelihood can be found (or is plausible) and can be quantified with  $L_{up}$ , a possible stopping condition would be given by  $L_{up}X_i < \alpha Z_i$ . This is particularly applicable in a planetary context, when a tolerance could be established by estimating the noise affecting the observations and used to estimate the maximum likelihood achievable.

The second problem is the definition of the likelihood. As said before, the likelihood could be considered the equivalent of a cost function for OE. Using the same notations adopted for OE, in the context of retrieving planetary parameters from observed spectra a commonly adopted form for the likelihood is using its log (Feroz and Hobson, 2008), as follows:

$$L = -\frac{1}{2}\chi^2 - \sqrt{2\pi} \sum_{i=1}^M \sigma_i \quad (13)$$

## 6. MultiNest and its implementation: PSGnest

The theory of NS and Bayesian retrievals more in general can be greatly refined and improved under many aspects, which have to do with the way in which the sampling is performed, and samples are selected towards convergence. It is known that NS becomes highly inefficient for multimodal posteriors, namely cases where regions of comparable (high) likelihood exist in the parameter space. This led to introducing the notion of clustered nested sampling (Shaw et al., 2007), in which multiple modes in the posterior are detected and defined, and distinct ellipsoidal bounds are constructed around each one of them (Feroz and Hobson, 2008). This approach has a significant positive impact on the sampling efficiency. On this work, Feroz built the MultiNest model (Feroz et al., 2009), which is currently the standard for nesting algorithms applied to cosmology and planetary science.



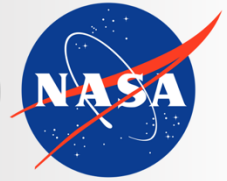
**Figure 7:** Example of retrieval with PSGnest of a gas-rich exoplanet using the ATMO grid. **Top:** spectrum and best fit (orange). **Middle:** list of retrieved parameters and their uncertainty, evidence, and runtime. **Bottom:** typical corner-plot used to represent posterior distribution of sampled points.

Compared to the initial work by Skilling, MultiNest can handle cases like the one schematized in Figure 6 more efficiently, as it is able to identify multiple regions of local maximum likelihood, each one corresponding to a degenerate solution. This is usually done by inserting additional steps in the NS basic scheme, which consist in identifying distinct clusters of live points that are well separated and constructing an individual ellipsoid for each cluster. The fact that the evidence is linear allows to consider each cluster individually and sum the single contributions, provided the correct assignment of prior volumes to each cluster and region of maximum likelihood (Feroz and Hobson, 2008).

In PSG, the tool PSGnest (<https://psg.gsfc.nasa.gov/apps/psgnest.php>) implements the most recent version of MultiNest, and is designed to analyze any kind of planetary data, with particular attention for exoplanets, for which NS is particularly suitable given the frequent lack of background information. Retrievals of exoplanetary parameters usually require tens to hundreds of live points and many iterations, yielding a total of sampled sets of parameters of the order of several thousands. Such large number make it somewhat unpractical to compute the spectra corresponding to the sampled parameters using a full radiative transfer model in real time.

For this reason, it is common to apply this technique drawing the samples from a pre-computed set of spectra organized in the form of a grid. More specifically, once a sample set of parameters  $\theta_j$  is drawn, PSGnest performs a tri-linear interpolation within the grid to compute an interpolated spectrum corresponding to  $\theta_j$ . As long as the grid points are distributed in such a way that their variation between couples of them has an effect almost linear on the radiance, this is an effective way to produce synthetic radiances without the need of working directly with radiative transfer. Examples of widely used grids include the ATMO grid (Goyal et al., 2018) applicable to transit observations of giants.

PSGnest provides in output the log evidence  $\log(Z)$ , the output parameters and their uncertainties, which are estimated from the posterior distribution of the sampled points and their standard deviation. An example of results is shown in Figure 7 on a synthetic spectrum of a hot Jupiter using the ATMO grid (Goyal et al., 2018). The PSGnest can capture multimodal solutions as they occur in exploring the parameter space.



**Planetary Spectrum Generator**  
National Aeronautics and Space Administration

# Chapter 10: **Application Program Interface (API) and Installation**

**Villanueva, Liuzzi and  
PSG team**



### 1. Application Program Interface

PSG allows to perform operations remotely by employing a versatile online Application Program Interface (API). The API operates by sending a configuration file to the PSG servers, that can be modified on the user local machine as needed. Upon reception of the configuration file, PSG will compute the spectra and send back the planetary spectra. The great value of the API is that the user does not need to install / update the radiative transfer modules and databases on his/her computer, and by simply performing a 'curl' command, the user will run the simulations on high-performance NASA servers.

The configuration file is a relaxed form of XML (eXtensible Markup Language), the now preferred file type across applications. The spectrum is provided in standard ASCII columns. The resulting units for the columns can be defined with the configuration XML file, while which type of data to provide (e.g., radiance, transmittance, noise) is provided by a POST command.

The communication with the server is performed via HTTPS, and this can be implemented via the 'curl' terminal command. A single line of 'curl', in which the user inputs are provided via a config.txt (example) will lead to spectra. The figure below better explains the inner workings of the PSG modules, and how the user can enable / disable the different modules, and request for different spectral outputs.

### 2. Calling the API

To compute spectra, one first needs to create / modify a PSG configuration file. The user can choose to edit this file with any text editor or scripting language.

**1.** Obtain a template configuration file (e.g., config.txt). The easiest way to obtain a configuration file is by parameterizing PSG via the web interface until a desired spectrum is obtained. On the main page of PSG, then click on "Download config-file", this will download the XML configuration file.

**2.** Modify the config.txt configuration file using a text-editor (e.g. J-edit, Atom, etc), or by using any scripting / programming language. In order to understand what each parameter means, please refer to the PSG documentation.

**3.** Open a terminal window and type the following command:

```
curl --data-urlencode file@config.txt https://psg.gsfc.nasa.gov/api.php
```

**4.** By default, the API will run all PSG modules employing this configuration file, and will return the total radiance spectra (**rad** file). One can run only certain modules and request for a different type of spectral output. This is achieved by providing several POST keywords (see section 4). For instance:

To return planetary transmittances (**trn** file) without the header information:



```
curl -d type=trn -d whdr=n --data-urlencode file@config.txt  
https://psg.gsfc.nasa.gov/api.php
```

To return only stellar (**str** file) transmittances (the API will only run the module 'continuum'):

```
curl -d type=str --data-urlencode file@config.txt https://psg.gsfc.nasa.gov/api.php
```

5. With the API, the user can also compute ephemerides and/or atmospheric parameters. For instance:

a) Create a text file config.txt with this content:

```
<OBJECT-DATE>2017/01/15 14:30  
<OBJECT-NAME>Mars  
<GEOMETRY-REF>MRO[74]
```

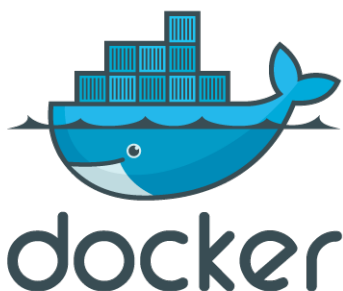
b) Call the API with this command:

```
curl -d type=cfg -d wephm=y -d watm=y --data-urlencode file@config.txt  
https://psg.gsfc.nasa.gov/api.php
```

### 3. Installing a personal version of PSG in your computer

The user can also install and run a local version of PSG via the Docker system. PSG is a complex suite of spectroscopic models and databases, coordinated by a general radiative-transfer scheme. Installing the whole suite on a personal system can be a daunting process and would entail a great deal of resources / memory / time. Instead, by employing the Docker virtualization system, the user is saved from this complexity and can easily install a pre-configured Virtual Machine with PSG that provides web/API access as the normal PSG suite.

In order to provide flexibility, the PSG personal suite is organized in packages. By default, the personal suite of PSG comes with the PROGRAMS and BASE packages, yet the user can install many additional packages, expanding the capabilities of the local version. Specifically, the correlated-k tables for low/moderate spectral resolutions can be quite large, and should be installed only when strictly necessary. The local PSG site also keeps track of any updates of these packages with respect to the current PSG suite, and it will inform you if you are required to update the packages.



**Docker virtualization system:** PSG can run in any personal computer (Mac, Linux or Windows based) with the Docker software. Docker containers wrap up software and all its dependencies (including the operative system) into a standardized package that includes everything it needs to run: code, runtime, system tools and libraries. This guarantees that PSG will always run the same and Docker makes its installation as simple as pulling a container image. This also means that PSG can be easily deployed in cloud computing environments (e.g., Google Cloud, Amazon Web Services).





1. Install the Docker application in your computer. This is relatively easy, and it will establish a virtualization system in which PSG will run. Visit the Docker site at [www.docker.com](http://www.docker.com).

2. From the command line / terminal, enter the following commands to pull the PSG container from the publicly available Docker hub repository:

```
docker logout
docker pull nasapsg/psg
docker tag nasapsg/psg psg
```

3. To run PSG and enable its API interface (add the keyword '--restart always' to keep PSG always running, even after re-booting):

```
docker run -d --name psg -p 3000:80 psg
```

4. To visit the local site of PSG, open your browser and go to **http://localhost:3000**, while to run the local version of the Application-Program-Interface (API), enter the following command:

```
curl --data-urlencode file@config.txt http://localhost:3000/api.php
```

5. The user can install, upgrade and remove packages by visiting **http://localhost:3000**. For performing this from the command line (e.g., inside a VM instance) follow these commands (where 'package' is the package name, all in lower case):

```
curl http://localhost:3000/index.php?install=package
curl http://localhost:3000/index.php?update=package
curl http://localhost:3000/index.php?remove=package
```

Some useful docker commands are:

<code>docker stop psg</code>	Stops the current PSG container.
<code>docker restart psg</code>	Restarts the PSG service.
<code>docker start psg</code>	Starts the PSG service if stopped.
<code>docker rm psg</code>	Removes the current container of PSG from docker memory. This operation deletes all updates/installed packages since its initial run, and resets PSG.
<code>docker ps -a</code>	Lists the status (e.g., stopped, started, exited) of all currently available containers. Containers cannot be re-run if they have already been created and therefore appear in this list (independently of the status). Restart, if necessary, while if the user wants to reset PSG to its original image, remove the container (docker rm) and re-run it (docker run).



<code>docker image ls</code>	Lists all the available docker images. The user can spawn multiple instances/containers from the same image. When the user pulls the PSG image from the docker hub, then this image will appear in this list.
<code>docker image rm psg</code>	Deletes the PSG image from memory. Any new PSG container/instance will require a re-pull of the image from the docker hub.
<code>docker system prune -af</code>	Deletes all images and containers/instances from docker memory, fully resetting docker.

#### 4. Types of planetary spectra and special keywords

Requested spectra (type keyword)	
<b>rad</b>	Integrated fluxes, incorporating all planetary and stellar transmittances, and considering the specific instrument / observatory parameters. This file is computed by the module generator. This is the default output setting.
<b>noi</b>	Synthetic observational noise, including the noise introduced by the planet itself, its star (if present within the field), background sources (e.g., exozodii, local zodiacal dust, CMB), the terrestrial atmosphere (if observing from ground), and the instrument performance. This file is computed by the module generator.
<b>trn</b>	Integrated planetary transmittance spectra, including all geometry considerations and requested atmospheric parameters. This file is computed by the module PUMAS only.
<b>atm</b>	Integrated planetary fluxes as observed at the planet in units of $[W/m^2/sr/um]$ . This file is computed by the modules PUMAS and CEM.
<b>str</b>	Stellar transmittance spectrum. This file is computed by the module continuum.
<b>tel</b>	Terrestrial transmittance spectrum (telluric). This file is computed by the module continuum.
<b>srf</b>	Surface reflectance and emissivity spectra. This file is computed by the module continuum.
<b>cfg</b>	The API will return the updated configuration file. This file is computed by the modules geometry and atmosphere.
<b>ret</b>	The API will perform a retrieval on the provided data and return all available output and input files.
<b>all</b>	This keyword will return all the resulting spectra, and the configuration file.

Requested spectra (type keyword)	
<b>wgeo</b>	The geometry module computes the observational angles (GEOMETRY-SOLAR-ANGLE, GEOMETRY-OBS-ANGLE) and the beam/planet ratio (GEOMETRY-PLANET-FRACTION) employing the geometry information provided by the user in the XML configuration file. For exoplanets, it also computes the planet transit factor (GEOMETRY-STAR-FRACTION), and the planet-star distance (GEOMETRY-STAR-DISTANCE). This information is then saved into the configuration file to be used by the other modules. The default is wgeo=y, yet one can disable this computation with wgeo=n.
<b>wephm</b>	<p>This keyword enables the calculation of ephemeris parameters based on the object name and the provided date:</p> <ul style="list-style-type: none"> <li>• <b>wephm=y</b> computes ephemeris for the date provided.</li> <li>• <b>wephm=N</b> computes ephemeris for the current date/time.</li> <li>• <b>wephm=T</b> for exoplanets, it searches the next primary transit event, while for Solar System bodies it computes the ephemeris for [date - one day].</li> <li>• <b>wephm=S</b> for exoplanets, it searches the next secondary transit event, while for Solar System bodies it computes the ephemeris for [date + one day].</li> <li>• <b>wephm=P</b> for exoplanets, it searches the next periastron event.</li> <li>• <b>wephm=n</b> disables the ephemerides module (<i>default</i>).</li> </ul>
<b>watm</b>	This keyword enables / disables the atmosphere module - Default watm=n.
<b>whdr</b>	This keyword allows to disable outputting the header information - Default whdr=y.
<b>app</b>	Name of the PSG app to call (e.g., globes)

## 5. Architecture of the API system and setting up a cluster system

The basic principles of remote operation via the API allow for expansion and adaption to a broad range of operational regimes (see Figure 1). As discussed before, the operation of the public PSG server and of the installable Docker version is the same, with only changing the URL in the curl command. The Docker operational scheme can be viewed as a layering system, in which the PSG Docker service “layer” sits above the user’s computer operative system (OS). The interface with the system is done via http ports in all cases. The default port of any http request is via port 80, and in many cases, the local computers may already have a http server running on them (e.g., Apache daemons) or have other services operating at other ports. That is why the PSG Docker system is configured to employ a high port number as default (3000), to avoid interface with local IP ports on the computer. The PSG public server employs Secure Sockets Layer (SSL) certificates for enhanced security, and that is why the communication is done via the encrypted “https” protocol, and not via the classical “http” protocol.

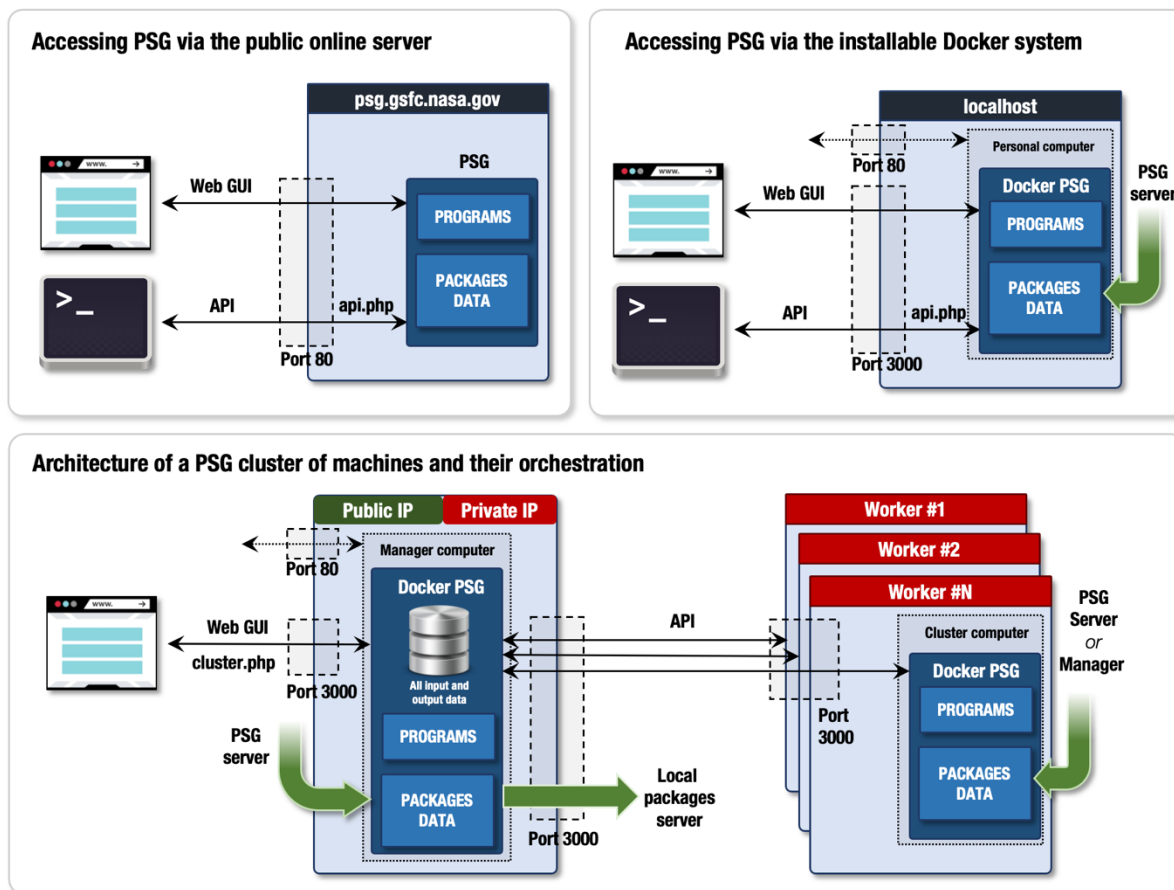


**Figure 1:** Architectures of three possible PSG configurations controlled via web GUI and API commands: for running the public online server (**upper-left**), for operating locally via the installable Docker system (**upper-right**), and for handling a cluster of PSG machines (**lower panel**). In all cases, the control is done via the HTTP protocol, yet using different ports (80 or 3000), IP addresses, and encryption schemes (e.g., with or without SSL certificates). In a cluster architecture, the manager and workers all operate within a closed intranet network with private IP addresses, yet the manager has an open port with a public address that allow access to the cluster from anywhere in the world. The systems are kept up to date with the latest PSG developments by the installation / update / removal of spectroscopic packages.

The PSG API commands have been designed to allow for maximum control of the PSG Docker instances, allowing for further automation of the system. For instance, one can have many machines running PSG Docker and organize for them to analyze spectra and data in a coordinated manner. Orchestrating many Docker machines is not a trivial process, and some architectures do exist, such as Kubernetes, yet they can be complex to setup and their configuration for running PSG instances would involve a further layer of customization and setup. For that purpose, we have developed a PSG cluster management tool and integrated it to the PSG Docker service (see Figure 2). The tool is accessible at the page “cluster.php” and it is password (default is “cluster”) controlled to allow for secure remote access.

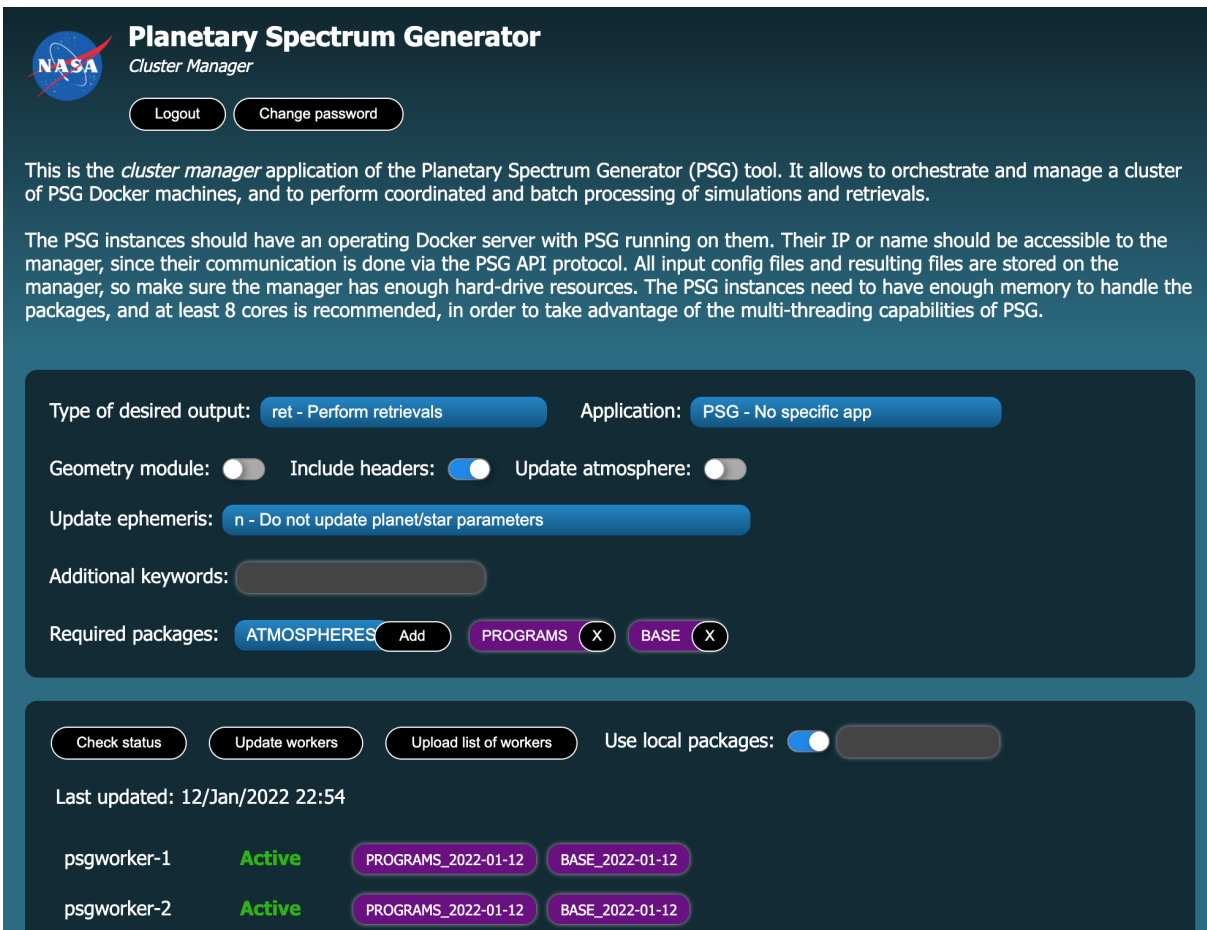


**Figure 2:** Example of the PSG cluster management interface. The user can select what specific PSG modules to run and which packages to use. The tool also permits to handle and update the packages on the workers and keeps track of their functionality when performing orchestrated operations.

The manager does not run PSG calculations itself but organizes and sends API requests to the workers in a coordinated manner. The PSG instances should have an operating Docker server with PSG running on them. Their IP or name should be accessible to the manager, since their communication is done via the PSG API protocol. All input config files and resulting files are stored on the manager, so make sure the manager has enough hard-drive resources. The PSG instances need to have enough memory to handle the packages, and at least 8 cores is recommended, in order to take advantage of the multi-threading capabilities of PSG.

The system is configured by providing a list of accessible IP addresses and a tarball containing all the configuration files to process. Only files with extensions “cfg”, “txt” and “set” will be processed. The configs with extension “set” will force a “type=set” API call for those files, while for the others the selected type in the GUI will be used. The manager will uncompress/unpack this tarball, and sequentially go through all the files in the package by sending it to any available machine in the list of PSG computers. The manager keeps track of which machine is free and operating and removes machines from the list if they fail to return valid outputs upon an API call. The GUI to the manager



allows to define specifics about the particular batch of PSG operations, types of desired outputs, special keywords and to select specific modules and apps. It is important to note that the manager operations are done via PSG API commands, so no detailed administration of the workers is possible from the manager GUI. One would need to administer them from the specific computer management tool, AWS as described in the next section, or via bash commands with password access to the workers.

An optimum way to handle many workers is to give them a sequential name (e.g., psgworker-1, psgworker-2), so they can all be controlled via a single command from the manager. As such, the pdsh Linux command is quite powerful for this, since pdsh being a variant of the remote shell rsh, pdsh can run multiple remote commands in parallel. Below we provide some common commands that can be done sent from the terminal of the manager:

```
pdsh -w centos@psgworker-[1-10] systemctl start docker.service
pdsh -w centos@psgworker-[1-10] docker start psg

pdsh -w centos@psgworker-[1-10] docker stop psg
pdsh -w centos@psgworker-[1-10] yum -y update --skip-broken
pdsh -w centos@psgworker-[1-10] shutdown -r now

pdsh -w centos@psgworker-[1-10] systemctl start docker.service
pdsh -w centos@psgworker-[1-10] docker stop psg
pdsh -w centos@psgworker-[1-10] docker system prune -af
pdsh -w centos@psgworker-[1-10] docker logout
pdsh -w centos@psgworker-[1-10] docker pull nasapsg/psg
pdsh -w centos@psgworker-[1-10] docker tag nasapsg/psg psg
pdsh -w centos@psgworker-[1-10] docker run -d --restart always --name psg -p
3000:80 psg
```

## 6. Setting up a PSG cluster system with AWS

As an example on how to setup a cluster system with PSG machines, we describe in this section how to setup a system with the Amazon Web Services (AWS), yet the same principles can be implemented on many other computational networks. AWS is a collection of computational, storage and web services that allow registered users to perform a wide array of tasks that require scalable and flexible computing resources. In the following paragraphs, we present a series of instructions and indications to work with the EC2 (Elastic Compute Cloud) resources and see how to setup a series of instances.

AWS offers the possibility to create a Free-Tier account as a starting point to learn how to use the AWS resources and to use the basic tier of those resources. To create an AWS account, the user needs to go on the AWS portal and follow the steps of the automated procedure. Once the account is created, it is time to do the first login. By default, the creation of the AWS account does not come with pre-defined users, therefore we need to define them. The starting point is to login as a root user only for the first login. For the following times, logging as root is generally not recommended, as for the inexperienced user this could result into taking unwanted actions. Once logged in, the user needs to create the first administrator IAM user, which will use to login all the other times. It is important to save the password, the user number (a 12-digit code), and the username (typically



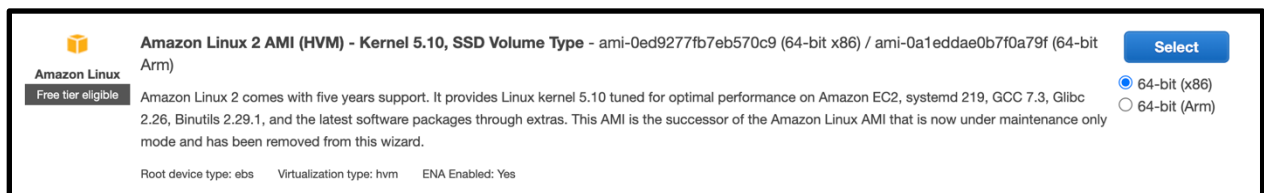
“Administrator” if the instructions are followed to the letter): those are the three things we will need to login anytime in the future.

### 6.1 Structure of the AWS console and instances

Once logged in as admin, the console is our entry point to all the services offered by AWS. The console allows to control the creation of tasks, instances, repositories of memory, clusters, and to check the billing for the services used. From the console we can start creating a single EC2 instance. All the instances we create form the Virtual Private Cloud (VPC) of the user. An instance works effectively as a machine with its own memory and computational resources. Every instance is assigned with:

- **A public IP address**, which makes the machine accessible from users as selected by the security groups (see later). By default, the public IP changes every time the instance is stopped and subsequently restarted.
- **A private IP**, which is not accessible from outside and is only used to communicate with eventual other instances in the VPC. This is static, meaning that once the machine is created, it does not change.

Every EC2 instance comes with basic software and tools already pre-installed, such as python3, and is fully ready to work with Docker containers and functionalities. To create an instance, let's start from the console and click on “Launch a virtual machine” in the “build a solution” panel.



The first screen shows a list of possible architectures for the instance. Among all of them, in the free tier, an Amazon Linux 2 AMI is available at no charge. This configuration is the default one and is good for most basic tests and applications.

Currently selected: t2.micro (- ECUs, 1 vCPUs, 2.5 GHz, -, 1 GiB memory, EBS only)								
	Family	Type	vCPUs	Memory (GiB)	Instance Storage (GB)	EBS-Optimized Available	Network Performance	IPv6 Support
<input type="checkbox"/>	t2	t2.nano	1	0.5	EBS only	-	Low to Moderate	Yes
<input checked="" type="checkbox"/>	t2	t2.micro <small>Free tier eligible</small>	1	1	EBS only	-	Low to Moderate	Yes

The second screen lets us choose the resources to use. They vary according to the type of application we want to build. The t2 micro instance comes for free and uses a basic, yet adequate configuration for most starting-level applications. A good guide for other types of applications can be found at the AWS site (<https://aws.amazon.com/ec2/instance-types/>).





Number of instances	<input type="text" value="1"/>	<a href="#">Launch into Auto Scaling Group</a>
Purchasing option	<input type="checkbox"/> Request Spot instances	
Network	<input type="text" value="vpc-"/> (default)	<a href="#">Create new VPC</a>
Subnet	<input type="text" value="No preference (default subnet in any Availability Zone)"/>	<a href="#">Create new subnet</a>
Auto-assign Public IP	<input type="text" value="Enable"/>	
Hostname type	<input type="text" value="Use subnet setting (IP name)"/>	
DNS Hostname	<input checked="" type="checkbox"/> Enable IP name IPv4 (A record) DNS requests <input checked="" type="checkbox"/> Enable resource-based IPv4 (A record) DNS requests <input type="checkbox"/> Enable resource-based IPv6 (AAAA record) DNS requests	

Next, we choose the network settings. The first parameter is the number of instances, we can create as many as we want of the same type. Each one will be a machine with its own public and private IP. We can choose the VPC for the instance (typically the same for all of them, yet a user can have more than one VPC). If two instances belong to different VPCs, they will be able to communicate only through their public IP address, and not their private (more on this can be found later).

In the next screen (step 3) we can also choose to create an instance that comes with pre-installed software or some commands to be executed at its creation. For example, we would wish to create an instance that comes with PSG already installed and running. To do that, on the bottom of the page there is a “User data” field. In the space, we can paste the code that we would use in a bash session:

```
#!/bin/bash
yum update -y
yum install docker -y
sudo service docker start
sudo docker pull nasapsg/psg
sudo docker tag nasapsg/psg psg
sudo docker run -d --name psg -p 3000:80 psg
echo 'sudo service docker start' >> /etc/rc.local
echo 'sudo docker start psg' >> /etc/rc.local
sudo chmod +x /etc/rc.d/rc.local
```

at startup, the machine will come with PSG already running on port 3000. The last 3 commands are used to paste in the file rc.local the instructions to restart the docker daemon and the PSG container anytime the instance is restarted after stopping.

Volume Type	Device	Snapshot	Size (GiB)	Volume Type	IOPS	Throughput (MB/s)	Delete on Termination	Encryption
Root	/dev/xvda		<input type="text" value="8"/>	General Purpose SSD (gp2)	100 / 3000	N/A	<input checked="" type="checkbox"/>	Not Encrypt

We can then choose the storage amount for the instance. This is equivalent to choosing the amount of space that the machine has in the SSD. There is a 30 GB limitation in the free tier.

Inbound rules for sg-0c1ad65dfa2d317b0 (Selected security groups: sg-0c1ad65dfa2d317b0)

Type ⓘ	Protocol ⓘ	Port Range ⓘ	Source ⓘ	Description ⓘ
HTTP	TCP	80	0.0.0.0/0	
SSH	TCP	22	0.0.0.0/0	
Custom TCP Rule	TCP	3000	0.0.0.0/0	

Before launching the instance, we need to create a security group for the instance. This is crucial since it defines the rules and restrictions to access the instance. Configuring these rules depends only on what we want to do with the instance. For example, if we are not interested in running a website on the instance to be accessed with the https protocol, we won't need to add any HTTPS rule. Adding any extra rule other than those strictly needed will likely result in errors when trying to access the instance. The default given by AWS is the sole SSH, as that is the primary way to access an instance.

Select an existing key pair or create a new key pair

A key pair consists of a **public key** that AWS stores, and a **private key file** that you store. Together, they allow you to connect to your instance securely. For Windows AMIs, the private key file is required to obtain the password used to log into your instance. For Linux AMIs, the private key file allows you to securely SSH into your instance. Amazon EC2 supports ED25519 and RSA key pair types.

Note: The selected key pair will be added to the set of keys authorized for this instance. Learn more about [removing existing key pairs from a public AMI](#).

Choose an existing key pair

Select a key pair

myfirstkey | RSA

☐ I acknowledge that I have access to the corresponding private key file, and that without this file, I won't be able to log into my instance.

Cancel

Launch Instances

The above configuration is quite simple and suitable to run PSG on the instance, and it offers the possibility to access the instance via SSH, HTTP and a custom rule in TCP that opens the port 3000 to listen inbound traffic from any address (0.0.0.0/0).

The next screen gives a review of the properties and the possibility to edit them. Once clicking on “launch”, there is a last important step to complete. The AWS will ask either to generate a key for the instance, or to use a previously generated one. The key is our code of access to enter and use the instance via SSH, and it is possible to generate it and download it ONLY in this moment. For the creation of the first instance, we will need to create a key, and save it as a .pem file, which will be put in a secure location on our computer. For OSX and UNIX, a suitable secure location is ~/.ssh .



Instances (1/3) <a href="#">Info</a>									
<input type="text" value="Search"/> <span>1</span>									
<input checked="" type="checkbox"/>	Name	Instance ID	Instance state	Instance type	Status check	Alarm status	Availability Zone	Publ	
<input checked="" type="checkbox"/>	Original		<span>Running</span>	t2.micro	<span>2/2 checks passed</span>	No alarms	us-east-1d	ec2-	
<input type="checkbox"/>	Clone1		<span>Stopped</span>	t2.micro	-	No alarms	us-east-1d	-	
<input type="checkbox"/>	Clone2		<span>Stopped</span>	t2.micro	-	No alarms	us-east-1d	-	

**Instance summary for**  **(Original)** [Info](#)
Connect Instance state Actions

Updated less than a minute ago

**Instance ID**  
 (Original)

**IPv6 address**  
 -

**Hostname type**  
 IP name: ip-.ec2.internal

**Instance type**  
 t2.micro

**AWS Compute Optimizer finding**  
 ⓘ Opt-in to AWS Compute Optimizer for recommendations. | [Learn more](#)

**Public IPv4 address**  
 | [open address](#)

**Instance state**  
Running

**Private IP DNS name (IPv4 only)**  
 ip-.ec2.internal

**Elastic IP addresses**  
 -

**IAM Role**  
 -

**Private IPv4 addresses**  

**Public IPv4 DNS**  
 .amazonaws.com | [open address](#)
**Answer private resource DNS name IPv4 (A)**  
 -
 
**VPC ID**  
 | [open address](#)
**Subnet ID**  
 | [open address](#)

[Details](#) [Security](#) [Networking](#) [Storage](#) [Status checks](#) [Monitoring](#) [Tags](#)

ⓘ You can now check network connectivity with Reachability Analyzer. Run Reachability Analyzer ×

**Networking details** [Info](#)

**Public IPv4 address**  
 | [open address](#)

**Public IPv4 DNS**  
 .amazonaws.com | [open address](#)

**IPv6 addresses**  
 -

**Carrier IP addresses (ephemeral)**  
 -

**Answer RBN DNS hostname IPv4**  
Enabled

**Private IPv4 addresses**

**Private IP DNS name (IPv4 only)**

**Secondary private IPv4 addresses**  
 -

**Outpost ID**  
 -

**VPC ID**  
 | [open address](#)
**Subnet ID**  
 | [open address](#)
**Availability zone**  
us-east-1d
**Use RBN as guest OS hostname**  
Disabled

Now we can launch our instance and check its status on the AWS console at “EC2” under “AWS services”. In the above series of screens, we can see the ID of the instance, the IP addresses and the links to security protocols established for the instance, the subnet and the VPC on which it is running. Clicking on these will open other windows with details about the connectivity for



diagnosing purposes as needed. Many network settings can also be accessed by “VPC” under “AWS services”. Once created, the instance can be left running for as much time as we need to perform operations on its computing resources. Then, we have three options, once clicking on “Instance state”:

- **Stop** the instance: this will be the equivalent of turning off the machine. All the content of the instance, the software installed is fully preserved. When restarted, the instance will be assigned a different public IP though by default, unless a static (also known as elastic) public IP is requested. For more info on this see [this guide](#).
- **Reboot** the instance: this is the equivalent of restarting the machine. The same considerations apply as for “stop”.
- **Terminate** the instance: this kills the instance for good. Once terminated, an instance cannot be turned on, and all the content on it is lost.

### 6.2 Accessing the instances

Any instance in the VPC can be accessed through SSH via its public IP. The private IP is used only once in an instance to access to any other instance in the VPC. To access the instance, we need to use the key that was created with it. Once in the SSH, we can add the key to the keychain:

```
cd ~/.ssh
ssh-add -K mykey.pem # add the key to the keychain
```

and then the instance can be accessed via SSH:

```
ssh -A ec2-user@ec2-pub-lic-IP-add.compute-1.amazonaws.com
```

the address is in the form of the public Ipv4 DNS taken from the screens shown previously. Once in the machine, we can run any command typical of UNIX terminal. It is good practice to update the instance at the first login.

```
~/ssh > ssh -A ec2-user@ec2- .compute-1.amazonaws.com
Last login: Thu Jan 6 23:42:04 2022 from pool- .net

  _| _|_ )
 _| ( /   Amazon Linux 2 AMI
 _|\_|_|_|

https://aws.amazon.com/amazon-linux-2/
```

As previously seen, AMI Linux instances use yum as utility to manage packages on the instance. Once connected by SSH, yum can be used to install, update, and remove packages. More information on this and the options can be found on at the redhat site ([https://access.redhat.com/sites/default/files/attachments/rh\\_yum\\_cheatsheet\\_1214\\_jcs\\_print-1.pdf](https://access.redhat.com/sites/default/files/attachments/rh_yum_cheatsheet_1214_jcs_print-1.pdf)).



To verify that the PSG docker container that was installed and started when the instance was created is accessible from any source (internal and external to the VPC) we can check whether the public IP currently in use by the instance directs us to the PSG personal suite page. On the SSH, or on any terminal not connected to the SSH, we can type:

```
curl http://my.pub.lic.IP
```

If the security protocols are correct, that should always give

```
PROGRAMS - Using latest version (2022-01-03)
BASE - Using latest version (2022-01-03)
```

If no other PSG package has been installed. The PSG will be also accessible on any browser by typing

```
http://my.pub.lic.IP:3000/api.php
```

As said, if other instances are in the VPC, they can be accessed by their private IP from the SSH session open, by SSH through their private IP:

```
ssh ec2-user@pri.va.te.IP
```

## 6.2 Configuring AWS on the ssh

It may be quite inconvenient and tedious to look for private and public IPs when many instances are active. To automatize this and other procedures and exploit to the highest level the capabilities of AWS, the aws utility must be configured on the instance. To do that, we need first to obtain a new personal key from the AWS interface. This can be done from the top-right of the AWS console, accessing “security and credentials” once clicking on the user ID. Then, under “AWS IAM credentials” we can click on “Create Access Key” and save it in a .csv file in the local ~/.ssh directory or any other directory. Once we have the key, we can type in the SSH session on the instance

```
aws configure
```

which will ask for the public key, the private key (both just generated) and the region (us-east-1 for the East coast and the DC area). The fourth prompted argument is optional. If no output is returned, the procedure is successful. Now we can quickly obtain all the private or the public IP addresses of all the instances on the VPC by typing on the SSH instance:

```
aws ec2 describe-instances --region your-region --instance-ids --
query "Reservations[*].Instances[*].PrivateIpAddress" --output text
```

```
aws ec2 describe-instances --region your-region --instance-ids --
query "Reservations[*].Instances[*].PublicIpAddress" --output text
```



The first IP returned will be the one of the instance we are running on, followed by a single row with all the other IPs of the other instances.

#### *6.2 Cloning an instance*

When we need a lot of instances that do the same job, and on which a lot of packages and software needs to be installed on each of them, it may be extremely tedious and inconvenient to create them one by one. In this case, the smartest thing to do is to create a single ec2 instance, customize it with all the software needed, and then from there create an image of the instance. To do that, we need first to stop the instance. Once stopped, under “actions” we can select “Image and template” and then “create image”. The following screen will be used to name the image, select the volumes to copy (if more than one) and then create it. The image will be available under “Images -> AMIs” in the EC2 dashboard. By entering this menu, we can then launch as many instances as desired from the image, following the exact same procedure as for the creation of the first image.

## References

- A'Hearn, M.F., Schleicher, D.G., Millis, R.L., Feldman, P.D., Thompson, D.T., 1984. Comet Bowell 1980b. *The Astronomical Journal* 89, 579–591. <https://doi.org/10.1086/113552>
- Andrews, E., Sheridan, P.J., Fiebig, M., McComiskey, A., Ogren, J.A., Arnott, P., Covert, D., Elleman, R., Gasparini, R., Collins, D., Jonsson, H., Schmid, B., Wang, J., 2006. Comparison of methods for deriving aerosol asymmetry parameter. *Journal of Geophysical Research: Atmospheres* 111. <https://doi.org/10.1029/2004JD005734>
- Appleby, J.F., 1990. CH<sub>4</sub> nonlocal thermodynamic equilibrium in the atmospheres of the giant planets. *Icarus* 85, 355–379. [https://doi.org/10.1016/0019-1035\(90\)90123-Q](https://doi.org/10.1016/0019-1035(90)90123-Q)
- Baranov, Y.I., Lafferty, W.J., 2012. The water vapour self- and water-nitrogen continuum absorption in the 1000 and 2500 cm<sup>-1</sup> atmospheric windows. *Philosophical Transactions of the Royal Society of London Series A* 370, 2578–2589. <https://doi.org/10.1098/rsta.2011.0234>
- Batalha, N.E., Marley, M.S., Lewis, N.K., Fortney, J.J., 2019. Exoplanet Reflected-light Spectroscopy with PICASO. *ApJ* 878, 70. <https://doi.org/10.3847/1538-4357/ab1b51>
- Belgacem, I., Schmidt, F., Jonniaux, G., 2020. Regional study of Europa's photometry. *Icarus* 338, 113525. <https://doi.org/10.1016/j.icarus.2019.113525>
- Benna, M., Mahaffy, P.R., Halekas, J.S., Elphic, R.C., Delory, G.T., 2015. Variability of helium, neon, and argon in the lunar exosphere as observed by the LADEE NMS instrument. *Geophysical Research Letters* 42, 3723–3729. <https://doi.org/10.1002/2015GL064120>
- Biver, N., Bockelée-Morvan, D., Colom, P., Crovisier, J., Henry, F., Lellouch, E., Winnberg, A., Johansson, L.E.B., Gunnarsson, M., Rickman, H., Rantakyö, F., Davies, J.K., Dent, W.R.F., Paubert, G., Moreno, R., Wink, J., Despois, D., Benford, D.J., Gardner, M., Lis, D.C., Mehringer, D., Phillips, T.G., Rauer, H., 2002. The 1995 2002 Long-Term Monitoring of Comet C/1995 O1 (HALE BOPP) at Radio Wavelength. *Earth* 90, 5–14. <https://doi.org/10.1023/A:1021599915018>
- Bodewits, D., Bonev, B.P., Cordiner, M.A., Villanueva, G.L., 2022. Radiative processes as diagnostics of cometary atmospheres. *Comets III* Under review.
- Bohren, C.F., Huffman, D.R., 1983. *Absorption and scattering of light by small particles*, New York: Wiley.
- Buras, R., Dowling, T., Emde, C., 2011. New secondary-scattering correction in DISORT with increased efficiency for forward scattering. *Journal of Quantitative Spectroscopy and Radiative Transfer* 112, 2028–2034. <https://doi.org/10.1016/j.jqsrt.2011.03.019>
- Buratti, B.J., Hicks, M.D., Nettles, J., Staid, M., Pieters, C.M., Sunshine, J., Boardman, J., Stone, T.C., 2011. A wavelength-dependent visible and infrared spectrophotometric function for the Moon based on ROLO data. *J. Geophys. Res.* 116, E00G03. <https://doi.org/10.1029/2010JE003724>
- Burrows, A., Marley, M.S., Sharp, C.M., 2000. The Near-Infrared and Optical Spectra of Methane Dwarfs and Brown Dwarfs. *ApJ* 531, 438–446. <https://doi.org/10.1086/308462>



- Cahoy, K.L., Marley, M.S., Fortney, J.J., 2010. Exoplanet Albedo Spectra and Colors as a Function of Planet Phase, Separation, and Metallicity. *ApJ* 724, 189. <https://doi.org/10.1088/0004-637X/724/1/189>
- Carissimo, A., De Feis, I., Serio, C., 2005. The physical retrieval methodology for IASI: the  $\delta$ -IASI code. *Environmental Modelling & Software* 20, 1111–1126. <https://doi.org/10.1016/j.envsoft.2004.07.003>
- Checlair, J.H., Villanueva, G.L., Hayworth, B.P.C., Olson, S.L., Komacek, T.D., Robinson, T.D., Popović, P., Yang, H., Abbot, D.S., 2021. Probing the Capability of Future Direct-imaging Missions to Spectrally Constrain the Frequency of Earth-like Planets. *AJ* 161, 150. <https://doi.org/10.3847/1538-3881/abdb36>
- Ciarniello, M., De Sanctis, M.C., Ammannito, E., Raponi, A., Longobardo, A., Palomba, E., Carrozzo, F.G., Tosi, F., Li, J.-Y., Schröder, S.E., Zambon, F., Frigeri, A., Fonte, S., Giardino, M., Pieters, C.M., Raymond, C.A., Russell, C.T., 2017. Spectrophotometric properties of dwarf planet Ceres from the VIR spectrometer on board the Dawn mission. *A&A* 598, A130. <https://doi.org/10.1051/0004-6361/201629490>
- Clough, S.A., Kneizys, F.X., Davies, R.W., 1989. Line shape and the water vapor continuum. *Atmospheric Research* 23, 229–241. [https://doi.org/10.1016/0169-8095\(89\)90020-3](https://doi.org/10.1016/0169-8095(89)90020-3)
- Clough, S.A., Shephard, M.W., Mlawer, E.J., Delamere, J.S., Iacono, M.J., Cady-Pereira, K., Boukabara, S., Brown, P.D., 2005. Atmospheric radiative transfer modeling: a summary of the AER codes. *Journal of Quantitative Spectroscopy and Radiative Transfer* 91, 233–244. <https://doi.org/10.1016/j.jqsrt.2004.05.058>
- Cox, C., Munk, W., 1954. Measurement of the Roughness of the Sea Surface from Photographs of the Sun's Glitter. *J. Opt. Soc. Am., JOSA* 44, 838–850. <https://doi.org/10.1364/JOSA.44.000838>
- Crovisier, J., 2007. Cometary diversity and cometary families. *ArXiv Astrophysics e-prints* arXiv:astro-ph/0703785.
- Daerden, F., Neary, L., Viscardy, S., García Muñoz, A., Clancy, R.T., Smith, M.D., Encrenaz, T., Fedorova, A., 2019. Mars atmospheric chemistry simulations with the GEM-Mars general circulation model. *Icarus* 326, 197–224. <https://doi.org/10.1016/j.icarus.2019.02.030>
- Dahlback, A., Stamnes, K., 1991. A new spherical model for computing the radiation field available for photolysis and heating at twilight. *Planetary and Space Science* 39, 671–683. [https://doi.org/10.1016/0032-0633\(91\)90061-E](https://doi.org/10.1016/0032-0633(91)90061-E)
- Dello Russo, N., Kawakita, H., Vervack, R.J., Weaver, H.A., 2016. Emerging trends and a comet taxonomy based on the volatile chemistry measured in thirty comets with high-resolution infrared spectroscopy between 1997 and 2013. *Icarus* 278, 301–332. <https://doi.org/10.1016/j.icarus.2016.05.039>
- Delsemme, A.H., 1982. Chemical composition of cometary nuclei. Presented at the IAU Colloq. 61: Comet Discoveries, Statistics, and Observational Selection, pp. 85–130.
- Devi, V.M., Benner, D.C., Sung, K., Crawford, T.J., Gamache, R.R., Renaud, C.L., Smith, M.A.H., Mantz, A.W., Villanueva, G.L., 2017a. Line parameters for CO<sub>2</sub> broadening in the

- v2 band of HD16O. *Journal of Quantitative Spectroscopy and Radiative Transfer* 187, 472–488. <https://doi.org/10.1016/j.jqsrt.2016.10.004>
- Devi, V.M., Benner, D.C., Sung, K., Crawford, T.J., Gamache, R.R., Renaud, C.L., Smith, M.A.H., Mantz, A.W., Villanueva, G.L., 2017b. Line parameters for CO<sub>2</sub>- and self-broadening in the v1 band of HD16O. *Journal of Quantitative Spectroscopy and Radiative Transfer* 203, 133–157. <https://doi.org/10.1016/j.jqsrt.2017.01.032>
- Edwards, D.P., 1992. GENLN2: A General Line-by-Line Atmospheric Transmittance and Radiance Model. The National Center for Atmospheric Research: Technical Note 367-STR.
- Ehrenreich, D., Tinetti, G., Lecavelier des Etangs, A., Vidal-Madjar, A., Selsis, F., 2006. The transmission spectrum of Earth-size transiting planets. *Astronomy and Astrophysics* 448, 379–393. <https://doi.org/10.1051/0004-6361:20053861>
- Ehrenreich, D., Vidal-Madjar, A., Widemann, T., Gronoff, G., Tanga, P., Barthélemy, M., Lilensten, J., des Etangs, A.L., Arnold, L., 2012. Transmission spectrum of Venus as a transiting exoplanet. *Astronomy and Astrophysics* 537, L2. <https://doi.org/10.1051/0004-6361/201118400>
- Encrenaz, T., de Graauw, T., Schaeidt, S., Lellouch, E., Feuchtgruber, H., Beintema, D.A., Bézard, B., Drossart, P., Griffin, M., Heras, A., Kessler, M., Leech, K., Morris, P., Roelfsema, P.R., Roos-Serote, M., Salama, A., Vandenbussche, B., Valentijn, E.A., Davis, G.R., Naylor, D.A., 1996. First results of ISO-SWS observations of Jupiter. *Astronomy and Astrophysics* 315, L397–L400.
- Fally, S., Vandaele, A.C., Carleer, M., Hermans, C., Jenouvrier, A., Mérianne, M.-F., Coquart, B., Colin, R., 2000. Fourier Transform Spectroscopy of the O 2 Herzberg Bands. III. Absorption Cross Sections of the Collision-Induced Bands and of the Herzberg Continuum. *Journal of Molecular Spectroscopy* 204, 10–20. <https://doi.org/10.1006/jmsp.2000.8204>
- Faucher, T.J., Villanueva, G.L., Schwieterman, E.W., Turbet, M., Arney, G., Pidhorodetska, D., Kopparapu, R.K., Mandell, A., Domagal-Goldman, S.D., 2020. Sensitive probing of exoplanetary oxygen via mid-infrared collisional absorption. *Nat Astron* 4, 372–376. <https://doi.org/10.1038/s41550-019-0977-7>
- Fernando, J., Schmidt, F., Pilorget, C., Pinet, P., Ceamanos, X., Douté, S., Daydou, Y., Costard, F., 2015. Characterization and mapping of surface physical properties of Mars from CRISM multi-angular data: application to Gusev Crater and Meridiani Planum. *Icarus* 253, 271–295. <https://doi.org/10.1016/j.icarus.2015.03.012>
- Feroz, F., Hobson, M.P., 2008. Multimodal nested sampling: an efficient and robust alternative to Markov Chain Monte Carlo methods for astronomical data analyses: Multimodal nested sampling. *Monthly Notices of the Royal Astronomical Society* 384, 449–463. <https://doi.org/10.1111/j.1365-2966.2007.12353.x>
- Feroz, F., Hobson, M.P., Bridges, M., 2009. MultiNest: an efficient and robust Bayesian inference tool for cosmology and particle physics. *Monthly Notices of the Royal Astronomical Society* 398, 1601–1614. <https://doi.org/10.1111/j.1365-2966.2009.14548.x>
- France, K., Loyd, R.O.P., Youngblood, A., Brown, A., Schneider, P.C., Hawley, S.L., Froning, C.S., Linsky, J.L., Roberge, A., Buccino, A.P., Davenport, J.R.A., Fontenla, J.M., Kaltenegger, L.,

- Kowalski, A.F., Mauas, P.J.D., Miguel, Y., Redfield, S., Rugheimer, S., Tian, F., Vieytes, M.C., Walkowicz, L.M., Weisenburger, K.L., 2016. The MUSCLES Treasury Survey. I. Motivation and Overview. *The Astrophysical Journal* 820, 89. <https://doi.org/10.3847/0004-637X/820/2/89>
- Fu, Q., 2007. A New Parameterization of an Asymmetry Factor of Cirrus Clouds for Climate Models. *Journal of the Atmospheric Sciences* 64, 4140–4150. <https://doi.org/10.1175/2007JAS2289.1>
- Gamache, R.R., Renaud, C.L., 2017. Modified Complex Robert-Bonamy (MCRB) calculations of H<sub>2</sub>O transitions broadened by H<sub>2</sub> for applications to planetary and exoplanet atmospheres. *J. Phys.: Conf. Ser.* 810, 012032. <https://doi.org/10.1088/1742-6596/810/1/012032>
- Gelaro, R., McCarty, W., Suarez, M.J., Todling, R., Molod, A., Takacs, L., Randles, C.A., Darmenov, A., Bosilovich, M.G., Reichle, R., Wargan, K., Coy, L., Cullather, R., Draper, C., Akella, S., Buchard, V., Conaty, A., da Silva, A.M., Gu, W., Kim, G.-K., Koster, R., Lucchesi, R., Merkova, D., Nielsen, J.E., Partyka, G., Pawson, S., Putman, W., Rienecker, M., Schubert, S.D., Sienkiewicz, M., Zhao, B., 2017. The Modern-Era Retrospective Analysis for Research and Applications, Version 2 (MERRA-2). *Journal of Climate* 30, 5419–5454. <https://doi.org/10.1175/JCLI-D-16-0758.1>
- Gesch, D.B., Larson, K.S., 1996. Techniques for development of global 1-kilometer digital elevation models, in: *Pecora Thirteen, Human Interactions with the Environment - Perspectives from Space*. Sioux Falls, South Dakota.
- Gordon, I.E., Rothman, L.S., Hargreaves, R.J., Hashemi, R., Karlovets, E.V., Skinner, F.M., Conway, E.K., Hill, C., Kochanov, R.V., Tan, Y., Wcisło, P., Finenko, A.A., Nelson, K., Bernath, P.F., Birk, M., Boudon, V., Campargue, A., Chance, K.V., Coustenis, A., Drouin, B.J., Flaud, J. –M., Gamache, R.R., Hodges, J.T., Jacquemart, D., Mlawer, E.J., Nikitin, A.V., Perevalov, V.I., Rotger, M., Tennyson, J., Toon, G.C., Tran, H., Tyuterev, V.G., Adkins, E.M., Baker, A., Barbe, A., Canè, E., Császár, A.G., Dudaryonok, A., Egorov, O., Fleisher, A.J., Fleurbaey, H., Foltynowicz, A., Furtenbacher, T., Harrison, J.J., Hartmann, J. –M., Horneman, V. –M., Huang, X., Karman, T., Karns, J., Kass, S., Kleiner, I., Kofman, V., Kwabia-Tchana, F., Lavrentieva, N.N., Lee, T.J., Long, D.A., Lukashchuk, A.A., Lyulin, O.M., Makhnev, V.Yu., Matt, W., Massie, S.T., Melosso, M., Mikhailenko, S.N., Mondelain, D., Müller, H.S.P., Naumenko, O.V., Perrin, A., Polyansky, O.L., Raddaoui, E., Raston, P.L., Reed, Z.D., Rey, M., Richard, C., Tóbiás, R., Sadiek, I., Schwenke, D.W., Starikova, E., Sung, K., Tamassia, F., Tashkun, S.A., Auwera, J.V., Vasilenko, I.A., Vigasin, A.A., Villanueva, G.L., Vispoel, B., Wagner, G., Yachmenev, A., Yurchenko, S.N., 2022. The HITRAN2020 molecular spectroscopic database. *Journal of Quantitative Spectroscopy and Radiative Transfer* 107949. <https://doi.org/10.1016/j.jqsrt.2021.107949>
- Goyal, J.M., Mayne, N., Sing, D.K., Drummond, B., Tremblin, P., Amundsen, D.S., Evans, T., Carter, A.L., Spake, J., Baraffe, I., Nikolov, N., Manners, J., Chabrier, G., Hebrard, E., 2018. A library of ATMO forward model transmission spectra for hot Jupiter exoplanets. *Mon Not R Astron Soc* 474, 5158–5185. <https://doi.org/10.1093/mnras/stx3015>
- Granate, P., Coelho, P.J., Roger, M., 2016. Radiative heat transfer in strongly forward scattering media using the discrete ordinates method. *Journal of Quantitative Spectroscopy and*

- Radiative Transfer, Eurotherm Conference No. 105: Computational Thermal Radiation in Participating Media V 172, 110–120. <https://doi.org/10.1016/j.jqsrt.2015.12.011>
- Halekas, J.S., Benna, M., Mahaffy, P.R., Elphic, R.C., Poppe, A.R., Delory, G.T., 2015. Detections of lunar exospheric ions by the LADEE neutral mass spectrometer. *Geophysical Research Letters* 42, 5162–5169. <https://doi.org/10.1002/2015GL064746>
- Hapke, B., 2012a. *Theory of Reflectance and Emittance Spectroscopy*, 2nd ed. Cambridge University Press, Cambridge. <https://doi.org/10.1017/CBO9781139025683>
- Hapke, B., 2012b. Bidirectional reflectance spectroscopy 7. *Icarus* 221, 1079–1083. <https://doi.org/10.1016/j.icarus.2012.10.022>
- Helfenstein, P., Veverka, J., 1989. Physical characterization of asteroid surfaces from photometric analysis 557–593.
- Horak, H.G., Little, S.J., 1965. Calculations of Planetary Reflection. *The Astrophysical Journal Supplement Series* 11, 373. <https://doi.org/10.1086/190119>
- Huebner, W.F., Keady, J.J., Lyon, S.P., 1992. Solar photo rates for planetary atmospheres and atmospheric pollutants. *Astrophysics and Space Science (ISSN 0004-640X)* 195, 1–289. <https://doi.org/10.1007/BF00644558>
- Humlíček, J., 1982. Optimized computation of the Voigt and complex probability functions. *Journal of Quantitative Spectroscopy and Radiative Transfer* 27, 437–444. [https://doi.org/10.1016/0022-4073\(82\)90078-4](https://doi.org/10.1016/0022-4073(82)90078-4)
- Iro, N., Gautier, D., Hersant, F., Bockelée-Morvan, D., Lunine, J.I., 2003. An interpretation of the nitrogen deficiency in comets. *Icarus* 161, 511–532. [https://doi.org/10.1016/S0019-1035\(02\)00038-6](https://doi.org/10.1016/S0019-1035(02)00038-6)
- Irwin, P.G.J., Teanby, N.A., de Kok, R., Fletcher, L.N., Howett, C.J.A., Tsang, C.C.C., Wilson, C.F., Calcutt, S.B., Nixon, C.A., Parrish, P.D., 2008. The NEMESIS planetary atmosphere radiative transfer and retrieval tool. *Journal of Quantitative Spectroscopy and Radiative Transfer* 109, 1136–1150. <https://doi.org/10.1016/j.jqsrt.2007.11.006>
- Jackson, Christopher.R., Alpers, W., 2010. The role of the critical angle in brightness reversals on sunglint images of the sea surface. *J. Geophys. Res.* 115, C09019. <https://doi.org/10.1029/2009JC006037>
- Jenouvrier, A., Mérienne, M.-F., Coquart, B., Carleer, M., Fally, S., Vandaele, A.C., Hermans, C., Colin, R., 1999. Fourier Transform Spectroscopy of the O<sub>2</sub> Herzberg Bands . I. Rotational Analysis. *Journal of Molecular Spectroscopy* 198, 136–162. <https://doi.org/10.1006/jmsp.1999.7950>
- Jorda, L., Crovisier, J., Green, D.W.E., 2008. The Correlation Between Visual Magnitudes and Water Production Rates. *Asteroids, Comet, Meteors* 2008 8046.
- Keller-Rudek, H., Moortgat, G.K., Sander, R., Sörensen, R., 2013. The MPI-Mainz UV/VIS Spectral Atlas of Gaseous Molecules of Atmospheric Interest. *Earth System Science Data* 5, 365–373. <https://doi.org/10.5194/essd-5-365-2013>
- Kempton, E.M.R., Lupu, R., Owusu-Asare, A., Slough, P., Cale, B., 2017. Exo-Transmit: An Open-Source Code for Calculating Transmission Spectra for Exoplanet Atmospheres of

- Varied Composition. Publications of the Astronomical Society of the Pacific 129, 044402-.  
<https://doi.org/10.1088/1538-3873/aa61ef>
- Knollenberg R., Travis L., Tomasko M., Smith P., Ragent B., Esposito L., McCleese D., Martonchik J., Beer R., 1980. The clouds of Venus: A synthesis report. *Journal of Geophysical Research: Space Physics* 85, 8059–8081.  
<https://doi.org/10.1029/JA085iA13p08059>
- Kofman, V., Villanueva, G.L., 2021. Absorption in exoplanet atmospheres: Combining experimental and theoretical databases to facilitate calculations of the molecular opacities of water. *Journal of Quantitative Spectroscopy and Radiative Transfer* 270, 107708.  
<https://doi.org/10.1016/j.jqsrt.2021.107708>
- Kokhanovsky, A.A., Budak, V.P., Cornet, C., Duan, M., Emde, C., Katsev, I.L., Klyukov, D.A., Korkin, S.V., C-Labonnote, L., Mayer, B., Min, Q., Nakajima, T., Ota, Y., Prikhach, A.S., Rozanov, V.V., Yokota, T., Zege, E.P., 2010. Benchmark results in vector atmospheric radiative transfer. *Journal of Quantitative Spectroscopy and Radiative Transfer* 111, 1931–1946. <https://doi.org/10.1016/j.jqsrt.2010.03.005>
- Kopparapu, R., Arney, G., Haqq-Misra, J., Lustig-Yaeger, J., Villanueva, G., 2021. Nitrogen Dioxide Pollution as a Signature of Extraterrestrial Technology. *ApJ* 908, 164.  
<https://doi.org/10.3847/1538-4357/abd7f7>
- Kurucz, R.L., 2009. Including All the Lines, in: *AIP Conference Proceedings*. Harvard-Smithsonian Center for Astrophysics, Cambridge, MA 02138, USA, pp. 43–51.  
<https://doi.org/10.1063/1.3250087>
- Kwon, S.M., Hong, S.S., Weinberg, J.L., 2004. An observational model of the zodiacal light brightness distribution. *New Astronomy* 10, 91–107.  
<https://doi.org/10.1016/j.newast.2004.05.004>
- Kylling, A., Stamnes, K., Tsay, S.-C., 1995. A reliable and efficient two-stream algorithm for spherical radiative transfer: Documentation of accuracy in realistic layered media. *J Atmos Chem* 21, 115–150. <https://doi.org/10.1007/BF00696577>
- Leconte, J., 2021. Spectral binning of precomputed correlated- k coefficients. *A&A* 645, A20.  
<https://doi.org/10.1051/0004-6361/202039040>
- Leinert, Ch., Bowyer, S., Haikala, L.K., Hanner, M.S., Hauser, M.G., Levasseur-Regourd, A.-Ch., Mann, I., Mattila, K., Reach, W.T., Schlosser, W., Staude, H.J., Toller, G.N., Weiland, J.L., Weinberg, J.L., Witt, A.N., 1998. The 1997 reference of diffuse night sky brightness. *Astronomy and Astrophysics Supplement Series* 127, 1–99.  
<https://doi.org/10.1051/aas:1998105>
- Lellouch, E., Hartogh, P., Feuchtgruber, H., Vandenbussche, B., Graauw, T. de, Moreno, R., Jarchow, C., Cavalié, T., Orton, G., Banaszkiewicz, M., Blecka, M.I., Bockelée-Morvan, D., Crovisier, J., Encrenaz, T., Fulton, T., Küppers, M., Lara, L.M., Lis, D.C., Medvedev, A.S., Rengel, M., Sagawa, H., Swinyard, B., Szutowicz, S., Bensch, F., Bergin, E., Billebaud, F., Biver, N., Blake, G.A., Blommaert, J. a. D.L., Cernicharo, J., Courtin, R., Davis, G.R., Decin, L., Encrenaz, P., Gonzalez, A., Jehin, E., Kidger, M., Naylor, D., Portyankina, G., Schieder, R., Sidher, S., Thomas, N., Val-Borro, M. de, Verdugo, E., Waelkens, C., Walker, H., Aarts, H., Comito, C., Kawamura, J.H., Maestrini, A., Peacocke, T., Teipen, R., Tils,

- T., Wildeman, K., 2010. First results of Herschel-PACS observations of Neptune. *A&A* 518, L152. <https://doi.org/10.1051/0004-6361/201014600>
- Li, J.-Y., Helfenstein, P., Buratti, B.J., Takir, D., Clark, B.E., 2015. Asteroid Photometry. arXiv:1502.06302 [astro-ph]. [https://doi.org/10.2458/azu\\_uapress\\_9780816532131-ch007](https://doi.org/10.2458/azu_uapress_9780816532131-ch007)
- Lin, Z., Chen, N., Fan, Y., Li, W., Stamnes, K., Stamnes, S., 2018. New Treatment of Strongly Anisotropic Scattering Phase Functions: The Delta-M+ Method. *Journal of the Atmospheric Sciences* 75, 327–336. <https://doi.org/10.1175/JAS-D-17-0233.1>
- Liou, K.-N., 2002. *An Introduction to Atmospheric Radiation*, 2nd Edition. ed. Academic Press - Elsevier.
- Liou, K.-N., 1973. A Numerical Experiment on Chandrasekhar's Discrete-Ordinate Method for Radiative Transfer: Applications to Cloudy and Hazy Atmospheres. *Journal of the Atmospheric Sciences* 30, 1303–1326. [https://doi.org/10.1175/1520-0469\(1973\)030<1303:ANE OCD>2.0.CO;2](https://doi.org/10.1175/1520-0469(1973)030<1303:ANE OCD>2.0.CO;2)
- Lippi, M., Villanueva, G.L., Mumma, M.J., Faggi, S., 2021. Investigation of the Origins of Comets as Revealed through Infrared High-resolution Spectroscopy I. Molecular Abundances. *The Astronomical Journal* 162, 74. <https://doi.org/10.3847/1538-3881/abfdb7>
- Liuzzi, G., Masiello, G., Serio, C., Venafrà, S., Camy-Peyret, C., 2016. Physical inversion of the full IASI spectra: Assessment of atmospheric parameters retrievals, consistency of spectroscopy and forward modelling. *Journal of Quantitative Spectroscopy and Radiative Transfer* 182, 128–157. <https://doi.org/10.1016/j.jqsrt.2016.05.022>
- Liuzzi, G., Villanueva, G.L., Mumma, M.J., Smith, M.D., Daerden, F., Ristic, B., Thomas, I., Vandaele, A.C., Patel, M.R., Lopez-Moreno, J.-J., Bellucci, G., 2019. Methane on Mars: New insights into the sensitivity of CH<sub>4</sub> with the NOMAD/ExoMars spectrometer through its first in-flight calibration. *Icarus* 321, 671–690. <https://doi.org/10.1016/j.icarus.2018.09.021>
- Liuzzi, G., Villanueva, G.L., Trompet, L., Crismani, M.M.J., Piccialli, A., Aoki, S., Lopez-Valverde, M.A., Stolzenbach, A., Daerden, F., Neary, L., Smith, M.D., Patel, M.R., Lewis, S.R., Clancy, R.T., Thomas, I.R., Ristic, B., Bellucci, G., Lopez-Moreno, J.-J., Vandaele, A.C., 2021. First Detection and Thermal Characterization of Terminator CO<sub>2</sub> Ice Clouds With ExoMars/NOMAD. *Geophysical Research Letters* 48, e2021GL095895. <https://doi.org/10.1029/2021GL095895>
- Lopez-Puertas, M., López-Valverde, M.A., 1995. Radiative Energy Balance of CO<sub>2</sub> Non-LTE Infrared Emissions in the Martian Atmosphere. *Icarus* 114, 113–129. <https://doi.org/10.1006/icar.1995.1047>
- Lumme, K., Bowell, E., 1981. Radiative transfer in the surfaces of atmosphereless bodies. I - Theory. II - Interpretation of phase curves. *The Astronomical Journal* 86, 1694–1721. <https://doi.org/10.1086/113054>
- Ma, L.X., Wang, F.Q., Wang, C.A., Wang, C.C., Tan, J.Y., 2015. Investigation of the spectral reflectance and bidirectional reflectance distribution function of sea foam layer by the Monte Carlo method. *Appl. Opt.* 54, 9863. <https://doi.org/10.1364/AO.54.009863>

- Mahaffy, P.R., Benna, M., Elrod, M., Yelle, R.V., Bougher, S.W., Stone, S.W., Jakosky, B.M., 2015. Structure and composition of the neutral upper atmosphere of Mars from the MAVEN NGIMS investigation. *Geophysical Research Letters* 42, 8951–8957. <https://doi.org/10.1002/2015GL065329>
- Marten, A., Matthews, H.E., Owen, T., Moreno, R., Hidayat, T., Biraud, Y., 2005. Improved constraints on Neptune's atmosphere from submillimetre-wavelength observations. *Astronomy and Astrophysics* 429, 1097–1105. <https://doi.org/10.1051/0004-6361:20041695>
- Masiello, G., Serio, C., 2013. Simultaneous physical retrieval of surface emissivity spectrum and atmospheric parameters from infrared atmospheric sounder interferometer spectral radiances. *Applied Optics* 52, 2428. <https://doi.org/10.1364/AO.52.002428>
- Masiello, G., Serio, C., Carissimo, A., Grieco, G., Matricardi, M., 2009. Application of  $\phi$ -IASI to IASI: retrieval products evaluation and radiative transfer consistency. *Atmospheric Chemistry and Physics* 9, 8771–8783.
- Massie, S.T., Hervig, M., 2013. HITRAN 2012 refractive indices. *Journal of Quantitative Spectroscopy and Radiative Transfer* 130, 373–380. <https://doi.org/10.1016/j.jqsrt.2013.06.022>
- Mérienne, M.-F., Jenouvrier, A., Coquart, B., Carleer, M., Fally, S., Colin, R., Vandaele, A.C., Hermans, C., 2001. Improved Data Set for the Herzberg Band Systems of  $^{16}\text{O}_2$ . *Journal of Molecular Spectroscopy* 207, 120–120. <https://doi.org/10.1006/jmsp.2001.8314>
- Mérienne, M.-F., Jenouvrier, A., Coquart, B., Carleer, M., Fally, S., Colin, R., Vandaele, A.C., Hermans, C., 2000. Fourier Transform Spectroscopy of the  $\text{O}_2$  Herzberg Bands. II. Band Oscillator Strengths and Transition Moments. *Journal of Molecular Spectroscopy* 202, 171–193. <https://doi.org/10.1006/jmsp.2000.8126>
- Millour, E., Forget, F., Spiga, A., Navarro, T., Madeleine, J.B., Montabone, L., Pottier, A., Lefèvre, F., Montmessin, F., Chaufray, J.Y., López-Valverde, M.A., González-Galindo, F., Lewis, S.R., Read, P.L., Huot, J.-P., Desjean, M.-C., Team, M.G. development, 2015. The Mars Climate Database (MCD version 5.2). *European Planetary Science Congress 2015* 10, EPSC2015-438.
- Moses, J.I., Fouchet, T., Bézard, B., Gladstone, G.R., Lellouch, E., Feuchtgruber, H., 2005. Photochemistry and diffusion in Jupiter's stratosphere: Constraints from ISO observations and comparisons with other giant planets. *Journal of Geophysical Research* 110, 8001. <https://doi.org/10.1029/2005JE002411>
- Muinenen, K., Belskaya, I.N., Cellino, A., Delbò, M., Levasseur-Regourd, A.-C., Penttilä, A., Tedesco, E.F., 2010. A three-parameter magnitude phase function for asteroids. *Icarus* 209, 542–555. <https://doi.org/10.1016/j.icarus.2010.04.003>
- Mumma, M.J., Charnley, S.B., 2011. The Chemical Composition of Comets – Emerging Taxonomies & Natal Heritage. *Annual Review of Astronomy and Astrophysics* 49, 471–524.
- Mumma, M.J., Disanti, M.A., Dello Russo, N., Magee-Sauer, K., Gibb, E.L., Novak, R., 2003. Remote infrared observations of parent volatiles in comets: A window on the early solar



- system. *Advances in Space Research* 31, 2563–2575. [https://doi.org/10.1016/S0273-1177\(03\)00578-7](https://doi.org/10.1016/S0273-1177(03)00578-7)
- Nakajima, T., Tanaka, M., 1988. Algorithms for radiative intensity calculations in moderately thick atmospheres using a truncation approximation. *Journal of Quantitative Spectroscopy and Radiative Transfer* 40, 51–69. [https://doi.org/10.1016/0022-4073\(88\)90031-3](https://doi.org/10.1016/0022-4073(88)90031-3)
- Nefedov, A.P., Sinel'shchikov, V.A., Usachev, A.D., 1999. Collisional Broadening of the Na-D Lines by Molecular Gases. *Phys. Scr.* 59, 432–442. <https://doi.org/10.1238/Physica.Regular.059a00432>
- Oklopčić, A., Hirata, C.M., Heng, K., 2017. How Does the Shape of the Stellar Spectrum Affect the Raman Scattering Features in the Albedo of Exoplanets? *ApJ* 846, 91. <https://doi.org/10.3847/1538-4357/aa8630>
- Parmentier, V., Guillot, T., 2014. A non-grey analytical model for irradiated atmospheres. I. Derivation. *Astronomy and Astrophysics* 562, A133. <https://doi.org/10.1051/0004-6361/201322342>
- Paynter, D.J., Ptashnik, I.V., Shine, K.P., Smith, K.M., McPheat, R., Williams, R.G., 2009. Laboratory measurements of the water vapor continuum in the 1200–8000  $\text{cm}^{-1}$  region between 293 K and 351 K. *Journal of Geophysical Research (Atmospheres)* 114, D21301. <https://doi.org/10.1029/2008JD011355>
- Penttilä, A., Shevchenko, V.G., Wilkman, O., Muinonen, K., 2016. H, G1, G2 photometric phase function extended to low-accuracy data. *Planetary and Space Science* 123, 117–125. <https://doi.org/10.1016/j.pss.2015.08.010>
- Pollack, J.B., Rages, K., Baines, K.H., Bergstrahl, J.T., Wenkert, D., Danielson, G.E., 1986. Estimates of the bolometric albedos and radiation balance of Uranus and Neptune. *Icarus* 65, 442–466. [https://doi.org/10.1016/0019-1035\(86\)90147-8](https://doi.org/10.1016/0019-1035(86)90147-8)
- Pommerol, A., Jost, B., Poch, O., Yoldi, Z., Brouet, Y., Gracia-Berná, A., Cerubini, R., Galli, A., Wurzel, P., Gundlach, B., Blum, J., Carrasco, N., Szopa, C., Thomas, N., 2019. Experimenting with Mixtures of Water Ice and Dust as Analogues for Icy Planetary Material. *Space Sci Rev* 215, 37. <https://doi.org/10.1007/s11214-019-0603-0>
- Protopapa, S., Olkin, C.B., Grundy, W.M., Li, J.-Y., Verbiscer, A., Cruikshank, D.P., Gautier, T., Quirico, E., Cook, J.C., Reuter, D., Howett, C.J.A., Stern, A., Beyer, R.A., Porter, S., Young, L.A., Weaver, H.A., Ennico, K., Ore, C.M.D., Scipioni, F., Singer, K., 2020. Disk-resolved Photometric Properties of Pluto and the Coloring Materials across its Surface. *AJ* 159, 74. <https://doi.org/10.3847/1538-3881/ab5e82>
- Quémerais, E., Bertaux, J.-L., Korabiev, O., Dimarellis, E., Cot, C., Sandel, B.R., Fussen, D., 2006. Stellar occultations observed by SPICAM on Mars Express. *Journal of Geophysical Research: Planets* 111. <https://doi.org/10.1029/2005JE002604>
- Régalia, L., Cousin, E., Gamache, R.R., Vispoel, B., Robert, S., Thomas, X., 2019. Laboratory measurements and calculations of line shape parameters of the H<sub>2</sub>O–CO<sub>2</sub> collision system. *Journal of Quantitative Spectroscopy and Radiative Transfer* 231, 126–135. <https://doi.org/10.1016/j.jqsrt.2019.04.012>

- Robinson, T.D., Catling, D.C., 2014. Common 0.1 bar tropopause in thick atmospheres set by pressure-dependent infrared transparency. *Nature Geoscience* 7, 12–15.  
<https://doi.org/10.1038/ngeo2020>
- Robinson, T.D., Stapelfeldt, K.R., Marley, M.S., 2016. Characterizing Rocky and Gaseous Exoplanets with 2 m Class Space-based Coronagraphs. *PASP* 128, 025003.  
<https://doi.org/10.1088/1538-3873/128/960/025003>
- Rodgers, C.D., 2000. Inverse Methods for Atmospheric Sounding | Series on Atmospheric, Oceanic and Planetary Physics [WWW Document]. URL  
<https://www.worldscientific.com/worldscibooks/10.1142/3171> (accessed 6.14.19).
- Rubin, M., Altwegg, K., Balsiger, H., Berthelier, J.-J., Combi, M.R., De Keyser, J., Drozdovskaya, M., Fiethe, B., Fuselier, S.A., Gasc, S., Gombosi, T.I., Hänni, N., Hansen, K.C., Mall, U., Rème, H., Schroeder, I.R.H.G., Schuhmann, M., Sémon, T., Waite, J.H., Wampfler, S.F., Wurz, P., 2019. Elemental and molecular abundances in comet 67P/Churyumov-Gerasimenko. *Monthly Notices of the Royal Astronomical Society* 489, 594–607.  
<https://doi.org/10.1093/mnras/stz2086>
- Sánchez-Lavega, A., Heimpel, M., 2017. Atmospheric Dynamics of Giants and Icy Planets, in: *Handbook of Exoplanets*. Springer, Cham, pp. 1–32. [https://doi.org/10.1007/978-3-319-30648-3\\_51-1](https://doi.org/10.1007/978-3-319-30648-3_51-1)
- Sato, H., Robinson, M.S., Hapke, B., Denevi, B.W., Boyd, A.K., 2014. Resolved Hapke parameter maps of the Moon. *J. Geophys. Res. Planets* 119, 1775–1805.  
<https://doi.org/10.1002/2013JE004580>
- Saxena, P., Villanueva, G.L., Zimmerman, N.T., Mandell, A.M., Smith, A.J.R.W., 2021. Simulating Reflected Light Exoplanet Spectra of the Promising Direct Imaging Target, up Andromedae d, with a New, Fast Sampling Method Using the Planetary Spectrum Generator. *AJ* 162, 30. <https://doi.org/10.3847/1538-3881/abf657>
- Schleicher, D.G., Bair, A.N., 2011. The Composition of the Interior of Comet 73P/Schwassmann-Wachmann 3: Results from Narrowband Photometry of Multiple Components 141, 177.  
<https://doi.org/10.1088/0004-6256/141/6/177>
- Serdyuchenko, A., Gorshelev, V., Weber, M., Chehade, W., Burrows, J.P., 2014. High spectral resolution ozone absorption cross-sections – Part 2: Temperature dependence. *Atmos. Meas. Tech.* 7, 625–636. <https://doi.org/10.5194/amt-7-625-2014>
- Serio, C., Masiello, G., Camy-Peyret, C., Jacquette, E., Vandermarcq, O., Bermudo, F., Coppens, D., Tobin, D., 2018. PCA determination of the radiometric noise of high spectral resolution infrared observations from spectral residuals: Application to IASI. *Journal of Quantitative Spectroscopy and Radiative Transfer* 206, 8–21. <https://doi.org/10.1016/j.jqsrt.2017.10.022>
- Serio, C., Masiello, G., Camy-Peyret, C., Liuzzi, G., 2019. CO<sub>2</sub> spectroscopy and forward/inverse radiative transfer modelling in the thermal band using IASI spectra. *Journal of Quantitative Spectroscopy and Radiative Transfer* 222–223, 65–83.  
<https://doi.org/10.1016/j.jqsrt.2018.10.020>

- Serio, C., Masiello, G., Liuzzi, G., 2016. Demonstration of random projections applied to the retrieval problem of geophysical parameters from hyper-spectral infrared observations. *Appl. Opt.*, AO 55, 6576–6587. <https://doi.org/10.1364/AO.55.006576>
- Shaw, J.R., Bridges, M., Hobson, M.P., 2007. Efficient Bayesian inference for multimodal problems in cosmology. *Monthly Notices of the Royal Astronomical Society* 378, 1365–1370. <https://doi.org/10.1111/j.1365-2966.2007.11871.x>
- Shepard, M.K., 2017. *Introduction to Planetary Photometry*. Cambridge University Press, Cambridge. <https://doi.org/10.1017/9781316443545>
- Shine, K.P., Campargue, A., Mondelain, D., McPheat, R.A., Ptashnik, I.V., Weidmann, D., 2016. The water vapour continuum in near-infrared windows - Current understanding and prospects for its inclusion in spectroscopic databases. *Journal of Molecular Spectroscopy* 327, 193–208. <https://doi.org/10.1016/j.jms.2016.04.011>
- Shine, K.P., Ptashnik, I.V., Rädcl, G., 2012. The Water Vapour Continuum: Brief History and Recent Developments. *Surveys in Geophysics* 33, 535–555. <https://doi.org/10.1007/s10712-011-9170-y>
- Skilling, J., 2006. Nested sampling for general Bayesian computation. *Bayesian Analysis* 1, 833–859. <https://doi.org/10.1214/06-BA127>
- Smith, D.E., Zuber, M.T., Frey, H.V., Garvin, J.B., Head, J.W., Muhleman, D.O., Pettengill, G.H., Phillips, R.J., Solomon, S.C., Zwally, H.J., Banerdt, W.B., Duxbury, T.C., Golombek, M.P., Lemoine, F.G., Neumann, G.A., Rowlands, D.D., Aharonson, O., Ford, P.G., Ivanov, A.B., Johnson, C.L., McGovern, P.J., Abshire, J.B., Afzal, R.S., Sun, X., 2001. Mars Orbiter Laser Altimeter: Experiment summary after the first year of global mapping of Mars. *Journal of Geophysical Research* 106, 23689. <https://doi.org/10.1029/2000JE001364>
- Smith, M.D., 2004. Interannual variability in TES atmospheric observations of Mars during 1999–2003. *Icarus* 167, 148–165. <https://doi.org/10.1016/j.icarus.2003.09.010>
- Sneep, M., Ubachs, W., 2005. Direct measurement of the Rayleigh scattering cross section in various gases. *Journal of Quantitative Spectroscopy and Radiative Transfer* 92, 293–310. <https://doi.org/10.1016/j.jqsrt.2004.07.025>
- Spurr, R., 2002. Simultaneous derivation of intensities and weighting functions in a general pseudo-spherical discrete ordinate radiative transfer treatment. *Journal of Quantitative Spectroscopy and Radiative Transfer* 75, 129–175. [https://doi.org/10.1016/S0022-4073\(01\)00245-X](https://doi.org/10.1016/S0022-4073(01)00245-X)
- Stamnes, K., Conklin, P., 1984. A new multi-layer discrete ordinate approach to radiative transfer in vertically inhomogeneous atmospheres. *Journal of Quantitative Spectroscopy and Radiative Transfer* 31, 273–282. [https://doi.org/10.1016/0022-4073\(84\)90031-1](https://doi.org/10.1016/0022-4073(84)90031-1)
- Stamnes, K., Tsay, S.C., Jayaweera, K., Wiscombe, W., 1988. Numerically stable algorithm for discrete-ordinate-method radiative transfer in multiple scattering and emitting layered media. *Applied Optics* 27, 2502–2509. <https://doi.org/10.1364/AO.27.002502>
- Stamnes, K., Tsay, S.-C., Laszlo, I., 2000. *DISORT, a General-Purpose Fortran Program for Discrete-Ordinate-Method Radiative Transfer in Scattering and Emitting Layered Media: Documentation of Methodology* (No. DISORT Report v1.1).

- Takir, D., Clark, B.E., Drouet d'Aubigny, C., Hergenrother, C.W., Li, J.-Y., Lauretta, D.S., Binzel, R.P., 2015. Photometric models of disk-integrated observations of the OSIRIS-REx target Asteroid (101955) Bennu. *Icarus* 252, 393–399. <https://doi.org/10.1016/j.icarus.2015.02.006>
- Tedesco, F., Veeder, J., Fowler, W., Chillemi, R., 1992. The IRAS Minor Planet Survey 456.
- Toon, O.B., McKay, C.P., Ackerman, T.P., Santhanam, K., 1989. Rapid calculation of radiative heating rates and photodissociation rates in inhomogeneous multiple scattering atmospheres. *Journal of Geophysical Research: Atmospheres* 94, 16287–16301. <https://doi.org/10.1029/JD094iD13p16287>
- Toon, O.B., McKay, C.P., Griffith, C.A., Turco, R.P., 1992. A physical model of Titan's aerosols. *Icarus* 95, 24–53. [https://doi.org/10.1016/0019-1035\(92\)90188-D](https://doi.org/10.1016/0019-1035(92)90188-D)
- Turbet, M., Boulet, C., Karman, T., 2020. Measurements and semi-empirical calculations of CO<sub>2</sub> + CH<sub>4</sub> and CO<sub>2</sub> + H<sub>2</sub> collision-induced absorption across a wide range of wavelengths and temperatures. Application for the prediction of early Mars surface temperature. *Icarus* 346, 113762. <https://doi.org/10.1016/j.icarus.2020.113762>
- van Ravenzwaaij, D., Cassey, P., Brown, S.D., 2018. A simple introduction to Markov Chain Monte–Carlo sampling. *Psychon Bull Rev* 25, 143–154. <https://doi.org/10.3758/s13423-016-1015-8>
- Venot, O., Bénilan, Y., Fray, N., Gazeau, M.-C., Lefèvre, F., Es-sebbar, E., Hébrard, E., Schwell, M., Bahrini, C., Montmessin, F., Lefèvre, M., Waldmann, I.P., 2018. VUV-absorption cross section of carbon dioxide from 150 to 800 K and applications to warm exoplanetary atmospheres. *A&A* 609, A34. <https://doi.org/10.1051/0004-6361/201731295>
- Vereš, P., Jedicke, R., Fitzsimmons, A., Denneau, L., Granvik, M., Bolin, B., Chastel, S., Wainscoat, R.J., Burgett, W.S., Chambers, K.C., Flewelling, H., Kaiser, N., Magnier, E.A., Morgan, J.S., Price, P.A., Tonry, J.L., Waters, C., 2015. Absolute magnitudes and slope parameters for 250,000 asteroids observed by Pan-STARRS PS1 – Preliminary results. *Icarus* 261, 34–47. <https://doi.org/10.1016/j.icarus.2015.08.007>
- Villanueva, G.L., Bonev, B.P., Mumma, M.J., Magee-Sauer, K., Disanti, M.A., Salyk, C., Blake, G.A., 2006. The Volatile Composition of the Split Ecliptic comet 73P/Schwassmann-Wachmann 3: A Comparison of Fragments C and B. *The Astrophysical Journal* 650, L87–L90. <https://doi.org/10.1086/508806>
- Villanueva, G.L., Disanti, M.A., Mumma, M.J., Xu, L.-H., 2012a. A Quantum Band Model of the  $\nu_3$  Fundamental of Methanol (CH<sub>3</sub>OH) and its Application to Fluorescence Spectra of Comets. *The Astrophysical Journal* 747, 1–11. <https://doi.org/10.1088/0004-637X/747/1/37>
- Villanueva, G.L., Liuzzi, G., Crismani, M.M.J., Aoki, S., Vandaele, A.C., Daerden, F., Smith, M.D., Mumma, M.J., Knutsen, E.W., Neary, L., Viscardy, S., Thomas, I.R., Lopez-Valverde, M.A., Ristic, B., Patel, M.R., Holmes, J.A., Bellucci, G., Lopez-Moreno, J.J., NOMAD team, 2021. Water heavily fractionated as it ascends on Mars as revealed by ExoMars/NOMAD. *Sci. Adv.* 7, eabc8843. <https://doi.org/10.1126/sciadv.abc8843>

- Villanueva, Geronimo L, Magee-Sauer, K., Mumma, M.J., 2013. Modeling of nitrogen compounds in cometary atmospheres: Fluorescence models of ammonia (NH<sub>3</sub>), hydrogen cyanide (HCN), hydrogen isocyanide (HNC) and cyanoacetylene (HC<sub>3</sub>N). *Journal of Quantitative Spectroscopy and Radiative Transfer* 129, 158–168.  
<https://doi.org/10.1016/j.jqsrt.2013.06.010>
- Villanueva, G.L., Mumma, M.J., Bonev, B.P., Novak, R.E., Barber, R.J., Disanti, M.A., 2012b. Water in planetary and cometary atmospheres: H<sub>2</sub>O/HDO transmittance and fluorescence models. *Journal of Quantitative Spectroscopy and Radiative Transfer* 113, 202–220.  
<https://doi.org/10.1016/j.jqsrt.2011.11.001>
- Villanueva, G.L., Mumma, M.J., Disanti, M.A., Bonev, B.P., Gibb, E.L., Magee-Sauer, K., Blake, G.A., Salyk, C., 2011a. The Molecular Composition of Comet C/2007 W1 (Boattini): Evidence of a Peculiar Outgassing and a Rich Chemistry. *Icarus* 216, 227–240.  
<https://doi.org/10.1016/j.icarus.2011.08.024>
- Villanueva, G.L., Mumma, M.J., Magee-Sauer, K., 2011b. Ethane in planetary and cometary atmospheres: Transmittance and fluorescence models of the  $\nu_7$  band at 3.3  $\mu\text{m}$ . *Journal of Geophysical Research* 116, 1–23. <https://doi.org/10.1029/2010JE003794>
- Villanueva, G.L., Mumma, M.J., Novak, R.E., Radeva, Y.L., Käufel, H.U., Smette, A., Tokunaga, A., Khayat, A., Encrenaz, T., Hartogh, P., 2013. A sensitive search for organics (CH<sub>4</sub>, CH<sub>3</sub>OH, H<sub>2</sub>CO, C<sub>2</sub>H<sub>6</sub>, C<sub>2</sub>H<sub>2</sub>, C<sub>2</sub>H<sub>4</sub>), hydroperoxyl (HO<sub>2</sub>), nitrogen compounds (N<sub>2</sub>O, NH<sub>3</sub>, HCN) and chlorine species (HCl, CH<sub>3</sub>Cl) on Mars using ground-based high-resolution infrared spectroscopy. *Icarus* 223, 11–27.  
<https://doi.org/10.1016/j.icarus.2012.11.013>
- Villanueva, G.L., Smith, M.D., Protopapa, S., Faggi, S., Mandell, A.M., 2018a. Planetary Spectrum Generator: An accurate online radiative transfer suite for atmospheres, comets, small bodies and exoplanets. *Journal of Quantitative Spectroscopy and Radiative Transfer* 217, 86–104.  
<https://doi.org/10.1016/j.jqsrt.2018.05.023>
- Villanueva, G.L., Smith, M.D., Protopapa, S., Faggi, S., Mandell, A.M., 2018b. Planetary Spectrum Generator: An accurate online radiative transfer suite for atmospheres, comets, small bodies and exoplanets. *Journal of Quantitative Spectroscopy and Radiative Transfer* 217, 86–104.  
<https://doi.org/10.1016/j.jqsrt.2018.05.023>
- Wells, R.J., 1999. Rapid approximation to the Voigt/Faddeeva function and its derivatives. *Journal of Quantitative Spectroscopy and Radiative Transfer* 62, 29–48.  
[https://doi.org/10.1016/S0022-4073\(97\)00231-8](https://doi.org/10.1016/S0022-4073(97)00231-8)
- Wiscombe, W.J., 1977. The Delta-M Method: Rapid Yet Accurate Radiative Flux Calculations for Strongly Asymmetric Phase Functions. *Journal of the Atmospheric Sciences* 34, 1408–1422.  
[https://doi.org/10.1175/1520-0469\(1977\)034<1408:TDMRYA>2.0.CO;2](https://doi.org/10.1175/1520-0469(1977)034<1408:TDMRYA>2.0.CO;2)
- Wolff, M.J., Smith, M.D., Clancy, R.T., Arvidson, R., Kahre, M., Seelos, F., Murchie, S., Savijarvi, H., 2009. Wavelength dependence of dust aerosol single scattering albedo as observed by the Compact Reconnaissance Imaging Spectrometer. *Journal of Geophysical Research* 114, E00D04. <https://doi.org/10.1029/2009JE003350>
- Yamamoto, T., 1981. On the photochemical formation of CN, C<sub>2</sub>, and C<sub>3</sub> radicals in cometary comae. *Moon and the Planets* 24, 453.

Yang, K., Liu, X., 2019. Ozone profile climatology for remote sensing retrieval algorithms. *Atmos. Meas. Tech.* 12, 4745–4778. <https://doi.org/10.5194/amt-12-4745-2019>